Dissertation

submitted to the

Combined Faculty of Natural Sciences and Mathematics

of the Ruperto Carola University Heidelberg, Germany

for the degree of

Doctor of Natural Sciences

Presented by

M. Sc. Laura-Christin Förster

born in: Langenfeld (Rheinland)

Oral Examination: 05.04.2019

Analysis of protein-sphingolipid interactions in Influenza A-infected cells

Referees: Prof. Dr. Britta Brügger

Prof. Dr. med. Hans-Georg Kräusslich

To my beloved ones

Table of Contents

List of Figures

List of Tables

Abbreviations

a-	Alpha, here: anti-
A549	Adenocarcinomic human alveolar basal epithelial cells
aa	Amino acid
ACER2	Acid ceramidase 2
AcOH	Acetic acid
acyl-CoA	Acyl-Coenzyme A
ANXA2	Annexin 2
aPC	Ester-linked PC
APS	Ammoniumperoxodisulfat
Aqua (H_2O) dest.	Aqua destillata (lat.), distilled water
Arg	Arginine
ASAH1	Acid ceramidase 1
Asgr1	Asialoglycoprotein receptor 1
aSMSase	Acid sphingomyelinase
ATII	Alveolar epithelial type II
Atg	Autophagy-related gene
BECN1	Beclin-1
BCA	Bicin choninic acid
BMP	Bis(monoacylglycerol)phosphate
bp	Base pairs
BSA	Bovine serum albumine
C	Carbon atom
°C	Degree celsius
$CaCl_2$	Calcium chloride
CAG	CMV early enhancer/chicken beta-actin
CARC	See CRAC
CAV	Caveolin
CBD	CAV1-binding domain
CCM	Cholesterol-consensus motif
CD	Cluster of differentiation
CD4	T-cell surface glycoprotein CD4
CD63	CD63 antigen
CD81	CD81 antigen
cDNA	Copy DNA
CE	Cholesterol ester
Cer	Ceramide
CerK	Ceramide Kinase
CerS	Ceramide synthase
CERT	Ceramide transfer protein
CGT	Galactosyltransferase
$CHCl_3$	Chloroform
Chol	Cholesterol
CIP	Alkaline phosphatase, calf intestinal
CLICK	Click reaction
cm	Centimeter
CMV	Cytomegalovirus
COPI	Coat-protein I
C1P	Ceramide-1-phosphate
CPSF	*Cleavage and polyadenylation specificity factor*
CR1	Chromosomal maintenance 1 (Exportin 1)
CRAC	Cholesterol-recognition amino acid consensus
CRISPR	Clustered Regularly Interspaced Short Palindromic Repeats

cRNA	Complementary RNA
CRP	Ceramide-enriched platforms
CT	Cytoplasmic tail
Ct	Threshold cycle
C-terminal	Carboxy-terminal
CuAAC	Copper (I)-catalysed azide alkyne cycloaddition
$CuBF_4$	Tetrakis(acetonitrile)copper(I) tetrafluoroborate
$CuSO_4$	Here: Copper(II) sulfate pentahydrate
CXN	Calnexin
DAG	Diacylglycerol
DAPI	4',6-diamidino-2-phenylindole
DB	Double bond
DC	Dendritic cell
ddH_2O	Double-distilled water
Des	DihydroceramideΔ4 desaturase
DHCer	Dihydroceramide
DHSL	Dihydrosphingolipid
DHSM	Dihydrosphingomyelin
DTT	Dithiothreitol
DMEM	Dulbecco's modified Eagle's medium
DMP	Dimethyl pimelimidate
DMSO	Dimethyl sulfoxide
DNA	Deoxyribonucleic acid
DNase	Desoxyribonuclease
DRM	Detergent-resistant membrane
dsRNA	Double-stranded RNA
DTT	Dithiotreitol
ECM	Extracellular matrix
E. coli	*Escherichia coli*
EDTA	Ethylenediaminetetraacetic acid
EE	Early endosome
e.g.	Exempli gratia (lat.), for example
EGFP	Enhanced GFP
EGFR	Epidermal growth factor receptor
ELOVL1	Elongation of very long chain fatty acids protein 1
EM	Electron microscope
EMT	Epithelial- to mesenchymal transition
EndoH	Endoglycosidase H
ePC	Ether PC (PC O-)
ER	Endoplasmic reticulum
ERC	Cholesterol-enriched endocytic recycling compartments
ESCRT	Endosomal sorting complex required for transport
esiRNA	Endo-ribonuclease prepared siRNA
et al.	And others (lat.)
EtOH	Ethanol
FA	Fatty acid
FACS	Fluorescence activated cell sorting
FAPP2	Four-phosphate adaptor protein 2
FB1	Fumonisin B1
FC	Fold change
FCS	Fetal calf serum
FG	FuGene® HD
Fig.	Figure
FIP2	FH protein interacting protein FIP2
FT	Flow-through
FW	Forward
g	Gram

GA2	Asialo-ganglioside GM2
GALC	Galactocerebrosidase
GalCer	Galactosylceramide
GAPDH	Glycerinaldehyd-3-phosphat-Dehydrogenase
Gb3	Globotriaosylceramide
GCS	Glucosylceramide synthase (also UGCG)
GD1a	Disialoganglioside 1A
GD1b	Disialoganglioside 1B
GFP	Green fluorescent protein
GlcCer	Glucosylceramide
GM1	Monosialoganglioside
GM3	Monosialotrihexosylganglioside
GM4	Monosialoganglioside GM4
GPI	Glycosylphosphatidylinositol
GPL	Glycerophospholipid
GRAMD1C	Protein Aster-C
gRNA	Guide RNA
GSL	Glycosphingolipid
h	hour
H(A)	Hemagglutinin
HBE	Human bronchial epithelial cells
HCl	Hydrochloric acid
HDAC6	Histone deacetylase 6
HEK	Human Embryonic Kidney
HeLa	Henrietta Lacks Human epithelial carcinoma cells
HEPES	2-[4-(2-Hydroxyethyl)piperazin-1-yl]ethanesulfonic acid
HexCer	Hexosylceramide (Glc- or GalCer)
Hex2Cer	Dihexosylceramide
HIV	Human immunodeficiency virus
HK68	A/Hong Kong/1/1968
hLRT	human lower respiratory tract
hpi	Hours post-infection
4-HPR	Retinoic acid p-hydroxyanilide
hURT	human upper respiratory tract
IAV	Influenza A virus
ID	Identifier
i.e.	Id est (lat.), that is
IF	Immunofluorescence
IFIT1	Interferon-induced protein 1
IFITM3	Interferon-induced transmembrane protein 3
IFN	Interferon
IN	Input
in vitro	In glass (lat.)
in vivo	Within the living (lat.)
IP	Immunoprecipitation
ITGA4	Integrin alpha 4
ITGAV	Integrin alpha 5
ITGB1	Integrin beta 1
ITGB1BP	Integrin beta 1 binding protein
Kan	Kanamycin
kb	Kilobases
KD	Knock-down
kDa	Kilodalton
KDS	3-Ketodihydrosphingosine reductase
KO	Knock-out
Lab	Laboratory
LacCer	Lactosylceramide
LAMP	Lysosome associated protein

LAPTM4B	Lysosomal Protein Transmembrane 4 Beta
LB	Lysogenic broth or Luria Bertani
LBPA	Lysobisphospatidic acid
LC	Long chain
Lc3	N-acetyl-D-glucosaminyl-1,3-beta-D-galactosyl-1,4-beta-D- glucosylceramide
LC3	Autophagy marker
L_D	Liquid-disordered
LE	Late endosome
Lec2	Lectin 2
LFQ	Label-free quantification
L_O	Liquid-ordered
Log_2	Binary logarithm
LP	Lipofectamine®2000
LPA	Lyso-PA
LPC	Lyso-PC
LPP	Lipid phosphate phosphatase family
Lys	Lysine
M1/2	Matrix protein 1/2
M	Molar
m	Meter
MCC	Microcrystalline cellulose
mCherry	Monomeric Cherry (fluorescent protein)
MDCK	Madin-Darby Canine Kidney
MEF	Mouse Embryonic Fibroblasts
MeOH	Methanol
µg	Microgram
mg	Milligram
$MgCl_2$	Magnesium chloride
MHC	Major histocompatibility complex
min	Minute
µM	Micromolar
MOI	Multiplicity of infection
MOPS	3-(N-Morpholino)propansulfonsäure
mRNA	Messenger RNA
MS	Mass spectrometry
MVB	Multivesicular body
MW	Molecular weight
n	Sample size
N(A)	Neuraminidase
NaCl	Sodium chloride
NaOH	Sodium hydroxide
NCL	Nucleolin
NEP	Nuclear export protein (also: NS2)
NHEJ	Nonhomologous end-joining
N-linked	Asparagine-linked
NLS	Nuclear localisation signal
nm	Nanometer
nM	Nanomol
NP	Nucleoprotein
NP40	Nonidet P40
NPC	Niemann-Pick disease type C
NS	Non-structural protein 1
N-terminal	Amino-terminal
OH	Hydroxyl
ON	Overnight
ORMDL	ORM1-like protein
P	Here: phosphorylated
p24 (TMED2)	Transmembrane emp24 domain-containing protein 2 (p24)

PA	Phosphatidic acid
PA	Plaque assay
p.a.	Analytical purity
pac	Photoactivatable- and clickable
pacSL	Pac-sphingolipid
PAGE	Polyacrylamide gel electrophoresis
PB	Polymerase basic
PBMC	Peripheral blood mononuclear cell
PBS	Phosphate buffered saline
PBST	Phosphate buffered saline Tween20
PC	Phosphatidylcholine
PC-PLC	PC-specific phospholipase C
PCR	Polymerase chain reaction
PCYOX1	Prenylcysteine oxidase 1
PD	Pulldown
pDNA	Plasmid DNA
PE	Phosphatidylethanolamine
PFA	Paraformaldehyde
PFU	Plaque forming unit
PG	Phosphatidylglycerol
pH	Potentia hydrogenii (lat.)
PI	Phosphatidylinositol
PIC	Protease Inhibitor Cocktail
PIP	Phosphatidylinositolphosphate
$PI(4,5)P_2$	Phosphatidylinositol-4,5-bisphosphate
pI/P-	plasmalogen
PM	Plasma membrane
PNGase F	Peptide:N-glycosidase F
PNS	Post-nuclear supernatant
PPARy	Peroxisome proliferator-activated receptor y
PR8	A/Puerto Rico/8/1934
PS	Phosphatidylserine
P/S	Penicillin/Streptomycin
qRT-PCR	Real-time quantitative PCR
Rab	Ras-related in brain
RAB11A	Ras-related protein Rab-11A
RD6	A/Regensburg/D6/2009
RE	Recycling endosome
Rep	Replicate
RGEN	RNA-guided endonuclease
RIG-I	Retinoic acid inducible gene I
RNA	Ribonucleic acid
RNase	Ribonuclease
rpm	Rounds per minute
RQ	Relative quantification
RT	Room temperature
RV	Reverse
s	Second
SA	Sialic acid
SC	Short chain
SDS	Sodium dodecyl sulfate
SDS-PAGE	Sodium dodecyl sulfate polyacrylamide gel electrophoresis
SEM	Standard error of mean
SFV	Semliki Forest Virus
SGPP1	S1P phosphatase 1
SILAC	Stable isotope labeling by/with amino acids in cell culture
siRNA	Silencing RNA
SL	Sphingolipid

SLC	Solute carrier
SLC1A5	Neutral amino acid transporter B(0)
SLC25A11	Mitochondrial 2-oxoglutarate/malate carrier protein
SLC46A1	Solute Carrier Family 46 Member 1
SM	Sphingomyelin
SMPD	Sphingomyelin phosphodiesterase
SMS	Sphingomyelin synthase
SMSase	Sphingomyelinase
SN	Supernatant
SNP	Single-nucleotide polymorphism
S1P	Sph/Spg-1-phosphate
SP3	Single-Pot Solid-Phase-enhanced Sample Preparation
SPC	Sphingosylphosphorylcholine
Spg	Sphinganine
Sph	Sphingosine
SphK	Sphingosine kinase
S1PL	Sphingosine-1-phosphate lyase
SPP	S1P phosphohydrolase
S1PR	S1P-receptors
SPT	Serine palmitoyltransferase
SPTLC	Serine palmitoyltransferase
SPTSSA	Serine palmitoyltransferase small subunit A
SPTSSB	Serine palmitoyltransferase small subunit B
Srt	Sortase
ss	Single-stranded
SV40	Simian virus 40
svRNA	Small-viral RNA
T2A	Porcine teschovirus-1 2A
TAE	Tris acetate EDTA
TAG	Triacylglycerol
TBTA	Tris[(1-benzyl-1*H*-1,2,3-triazol-4-yl)methyl]amine
TEA	Triethylamine
TCEP	Tris(2carboxyethyl)phosphine hydrochloride
TEM	Tetraspanin-enriched microdomain
TEMED	Tetramethylethylendiamine
TF	TurboFect®
TFA	Trifluoroacetic acid
TfR	Transferrin receptor
TGN	*trans*-Golgi network
TLC	Thin layer chromatographie
TLR	Toll-like receptor
TM	Transmembrane
TMD	Transmembrane domain
TMEM41B	Transmembrane protein 41B
TMS	Trimethylsilyl
TM9SF3	Transmembrane 9 superfamily member 3
TRAM1	Translocating chain-associated membrane protein 1
Tris	Tris(hydroxymethyl)aminomethane
TSPAN	Tetraspanins
TX-100	Triton X-100
U	Enzyme activity (µmol/min)
UGCG	Glucosylceramide synthase (also GCS)
(U)HPLC	(Ultra) High Performance Liquid Chromatography
UTR	Untranslated region
UV	Ultraviolet

UZ	Ultrazentrifugation
V	Volt
VDAC1	Voltage-dependent anion-channel 1
VIM	Vimentin
VLC	Very long chain
VLP	Virus-like particle
vRdRP	Viral RNA-dependent RNA polymerase
vRNA	Viral RNA
vs.	versus
VSV	Vesicular stomatitis virus
v/v	Volume per volume
WDR33	WD Repeat Domain 33
WHO	World Health Organisation
w/o	without
WT	Wild type
w/v	Weight per volume
g	Acceleration of gravity
Δ	Delta, here: deficient

1 Summary/Zusammenfassung

Influenza A virus (IAV) is a human respiratory pathogen causing seasonal endemic and irregular pandemic flu infections. The ability to undergo rapid antigenic changes is a reason for the persistent clinical relevance of IAV as continuously novel subtypes emerge, severely compromising vaccine effectiveness.

IAV budding is initiated by the viral glycoproteins hemagglutinin (HA) and neuraminidase (NA) and occurs at apical plasma membrane regions, referred to as microdomains or membrane rafts, which are enriched in cholesterol and (glyco)sphingolipids. Sphingolipids (SLs) derive from the amino alcohol sphingosine and represent major building blocks of cellular membranes and important cell signaling molecules. SLs seem to play a crucial role in viral assembly as a defect in sphingomyelin (SM) biosynthesis has been shown to compromise cell surface transport of HA and NA, as well as budding and release of progeny virions. In addition, SLs are significantly enriched in the viral envelope. However, direct evidence for an IAV-triggered modulation of SL metabolism and the contribution of specific SL classes, species, metabolites or SL metabolising enzymes to viral propagation is still lacking.

The aim of this thesis was to shed light on the role of SLs and SL-binding host proteins in the IAV replication cycle. Photoactivatable and clickable sphingosine (pacSph) was employed to monitor protein-SL interactions in sphingosine-1-phosphate lyase (S1PL)-deficient cells. Here, the goal was i) to analyse the SL-binding potential of viral proteins, especially HA and NA, of different IAV subtypes, ii) to perform a proteome-wide mapping of protein-sphingolipid interactions at early and late stages of infection, and iii) to study roles of long-chain SL species for IAV propagation using CRISPR/Cas9-mediated ceramide synthase 2 (CerS2) knock-out (KO) cells.

Transfection and infection experiments suggest that HA and NA homologues display different SL-binding efficiencies. Employing a SILAC-based proteomic approach, a set of proteins was identified showing altered SL-interaction dynamics in infected cells. Here, integrin beta-1 (ITGB1) was further investigated as a potential pro-viral SL-binding host target. Knock-out cell models showed that loss of CerS2 resulted in increased infection efficiency in HeLa cells. Notably, the KO of CerS2

correlated with an elevation of dihydro-SL (DHSL) levels. DHSLs have been reported to increase upon IAV and other viral infections, and might thus also be responsible for the observed pro-viral effect. How the absence of CerS2 affects cellular DHSL levels and how this alters host cell infectivity remains to be studied in future experiments.
Together these data provide novel insights into the role of sphingolipids in the IAV replication cycle and might eventually paving the path for new therapeutic targets in the combat against IAV.

Das Influenza A Virus (IAV) ist ein respiratorischer Krankheitserreger, welcher saisonal endemische und spontan auftretende pandemische Grippeinfektionen beim Menschen hervorruft. Durch die kontinuierlichen Veränderungen der antigenen Eigenschaften des Virus entstehen fortlaufend neue IAV Subtypen, welche sich drastisch auf die Effektivität von Grippeimpfstoffen auswirken können und zu der persistierenden klinischen Relevanz von IAV beitragen.
Der Zusammenbau des Viruspartikels wird durch die viralen Glykoproteine Hämagglutinin (HA) und Neuraminidase (NA) initiiert. Die virale Morphogenese findet in spezifischen, apikalen Plasmamembranregionen der Wirtszelle statt, welche auch Mikrodomänen oder „Lipid Rafts“ (Lipidflöße) genannt werden. Diese sind durch eine Anreicherung an Cholesterol und (Glyko-)Sphingolipiden charakterisiert. Sphingolipide (SL) sind Derivate des Aminoalkohols Sphingosin und Hauptbestandteile zellulärer Membranen sowie bedeutende Signaltransduktionsmoleküle. SL scheinen zudem eine essentielle Rolle in der Morphogenese viraler IAV Partikel zu besitzen, da Defekte im Biosyntheseweg von Sphingomyelin (SM) den Transport von HA und NA zur Zelloberfläche sowie den Aufbau und die Freisetzung von Nachfolgeviren beeinträchtigen. Zudem weist die Virushülle eine Anreicherung an SL auf. Ob das IAV einen direkten Einfluss auf den Stoffwechsel von SL besitzt und welche Klassen, Spezies, Metaboliten oder SL-metabolisierende Enzyme für die virale Replikation von Signifikanz sind ist jedoch weitgehend unbekannt.
Das Ziel dieser Doktorarbeit war es, die Rolle von SL und SL-bindenden Wirtsproteinen, die für den Replikationszyklus des IAV eine Rolle spielen könnten, näher zu untersuchen. Hierfür wurde **p**hotoaktivierbares und klickbares („**c**lickable“)

Sphingosin (pacSph) verwendet, um Protein-SL Interaktionen in Sphingosine-1-phosphat-Lyase (S1PL)-defizienten Zellen zu detektieren. So sollte (i) das SL-bindende Potential viraler Proteine, speziell von HA und NA, verschiedener IAV Subtypen analysiert werden, (ii) durch Proteomanalyse Protein-SL Interaktionen von Wirtszellproteinen mit SL in verschiedenen Infektionsstadien untersucht werden und (iii) die Rolle von langkettigen SL Spezies in der IAV Replikation mit Hilfe eines CRISPR/Cas9-basierten Knock-outs der Ceramid-Synthase 2 (CerS2) erforscht werden.

Transfektions- und Infektionsexperimente ergaben, dass homologe Proteine von HA und NA unterschiedliche SL-bindende Potentiale besitzen könnten. Des Weiteren konnten durch eine SILAC-basierte Proteomuntersuchung verschiedene Proteine identifiziert werden, die eine unterschiedliche SL-Interaktionsdynamik in infizierten Zellen aufweisen. In diesem Rahmen wurde der Zusammenhang des SL-Interaktionspotentials von Integrin-beta 1 (ITGB1) und dessen proviralen Effektes näher untersucht. Zudem führte der Verlust von CerS2 zu einer verminderten Infektionseffizienz in HeLa Zellen. Der Knock-out hat jedoch auch zu einer Erhöhung von Dihydro-SL (DHSL) geführt. In anderen Studien wurde gezeigt, dass die Menge an DHSL in IAV und anderen viralen Infektionen ansteigt und dies die Ursache für den beobachtete proviralen Effekt in CerS2-defizienten HeLa Zellen sein könnte. Inwiefern die Abwesenheit von CerS2 zelluläre DHSL Level beeinflusst, und damit verbunden die Suszeptibilität gegenüber IAV erhöht, muss daher weiterhin experimentell untersucht werden.

2 Introduction

2.1 The cellular lipidome: lipid diversity and distribution

Lipids play a crucial role in a wide range of physiological processes and are therefore essential components for all organisms. The total amount of lipids within a cell, tissue or organism is designated the lipidome[1]. The study of lipid metabolic pathways and corresponding enzymes is an emerging field of interest, as a variety of diseases, such as cancer, diabetes or infectious diseases, correlate with aberrations in the lipidome. Hence, the field of lipidomics aims at elucidating lipid-interacting networks, and largely depends on mass spectrometry and liquid chromatography as analytical tools[2]. Originally, lipids have been simply described as organic compounds only soluble in organic solvents, but not water[3]. However, this does not account for the complexity of lipids. According to the most prominent classification system initiated by the LIPID MAPS consortium, lipids are e.g. divided into 8 general categories, further subdivided into classes, subclasses and 4th-level classes, yielding far over 40,000 unique lipid structures[1,4].

Approximately 5% of the human genome encodes for lipid synthesising, metabolising and transporting enzymes, thus underlying their biological function as cellular building blocks, signalling molecules, energy storage, protein-organising entities and molecules for post-translational protein modification [5-8]. The diverse function of lipids is reflected by the variable lipid composition ("compositional diversity") within or between lipid bilayer leaflets, cell types, tissues or organelles[5,9,10]. Specific physical properties are defined by the vast, heterogenous molecule composition of lipids ("chemical or structural diversity")[1,10]. As an example, structural diversity of lipids is achieved by the combination of (hydrophobic) fatty acid side chains and (polar) functional head groups, linked to a specific glycerol, sphingosine or sterol backbone[2,5].

Cellular lipids such as triacyglycerols (TAGs) and cholesterol ester (CE) are e.g. part of cytosolic lipid droplets and circulating lipoproteins; yet, most of the lipidome is contributed to membranes[9,11].

2.1.1 Membrane lipids

A major physical property of membrane lipids is their amphiphilic nature, the presence of a hydrophilic and a hydrophobic part, which enables them to spontaneously self-associate in aqueous environments[6]. In addition, the "intrinsic shape" of lipids, defined by the headgroup and the chemical composition of the acyl chain, enables lipid mono-or bilayers to induce positive or negative membrane curvature, which can be further modulated by membrane proteins[12]. Consequently, membrane lipids promote fission and fusion events as well as budding and tubulation processes, or impact protein localisation and function via protein-lipid interactions[6,10]. Membrane lipids are consistent of three main classes: glycerophospholipids (GPLs), sphingolipids (SLs) and sterols (Figure 2.1)[10]. GPLs comprise the classes phosphatidylcholine (PC), which accounts for over 50% of membrane GPLs, phospatidylglycerol (PG), phospatidylethanolamine (PE), phosphatidylserine (PS), phosphatidylinositol (PI) and phosphatidic acid (PA). The common backbone of all GPLs is glycerol with an O-acylated fatty acid (FA) at *sn-1* and/or *sn-2* position (=diacylglycerol, DAG), whereas the attached head group at the *sn-3* position defines the GPL class (Figure 2.1)[6]. SLs harbour a sphingoid backbone. Prominent SL classes are ceramide (Cer), the phospho-SL sphingomyelin (SM) and glycosphingolipids (GSLs)[6,13]. They will be further discussed in **section 2.2**. In contrast to GPLs and SLs, sterols (such as cholesterol) only harbour a polar head group that is oriented to the interphase of the cell-enclosing lipid bilayer (=plasma membrane, PM). At PMs, cholesterol molecules are presumably protected from the aqueous environment by interaction with phospholipids ("umbrella model")[6,14,15].

FAs attached to GPLs and SLs contribute to the chemical diversity of membrane lipids, differing in length, double bond number and position as well as hydroxylation[10]. Membrane-bound GPLs and SLs can also be hydrolysed upon initiation of various signal cascades, resulting in messenger or bioactive lipid molecules, which act in an autocrine or paracrine fashion. GPL-derived messenger lipids include lyso-PC and -PA (LPC/LPA), PA and DAG, whereas bioactive SLs comprise sphingosine (Sph), Sph/Spg-1-phosphate (S1P), sphingosylphosphorylcholine (SPC), Cer and Cer-1-phosphate (C1P)[6].

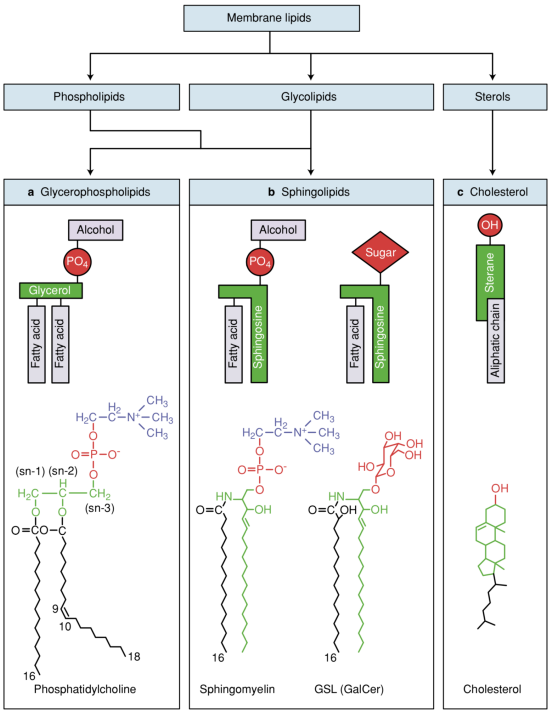

Figure 2.1: Classification of membrane lipids based on their structure.

Plasma membrane lipids comprise glycerophospholipids, sphingolipids and sterols (see **section 2.1.1**). Modified from Fantini *et al*., 2002; license number 4476421014066[16].

2.1.2 Cellular lipid distribution

Enzymes involved in lipid synthesis are compartmentalised at subcellular and even sub-organellar level. As a result, the lipid composition of organelles is always distinctive and specific[10].

The secretory pathway involves the endoplasmic reticulum (ER), the intermediate compartment, the Golgi apparatus and the PM[17]. These organelles are not only engaged in the synthesis and delivery of (transmembrane) protein cargoes to their destinations, but are also implicated in *de novo* bulk membrane lipid synthesis *de novo* and creation of (lipid) compositional diversity (Figure 2.2)[6,17,18]. The ER is the major site of synthesis of GPLs, cholesterol, triacylglycerol (TAG), CEs and the sphingolipid Cer. In some cell types a significant amount of galactosylceramide (GalCer) is also produced in the ER[6,19,20]. The Golgi apparatus is the central station for protein sorting, and the site of synthesis for (complex) SLs (see **section 2.2**)[6]. SLs are also considered to be involved in sorting of lipids and membrane proteins between certain organelles, as well as in their transport to the PM via SL-enriched microdomains (see **section 2.1.3**)[6,13,21-23]. In epithelial cells, SL-based protein and

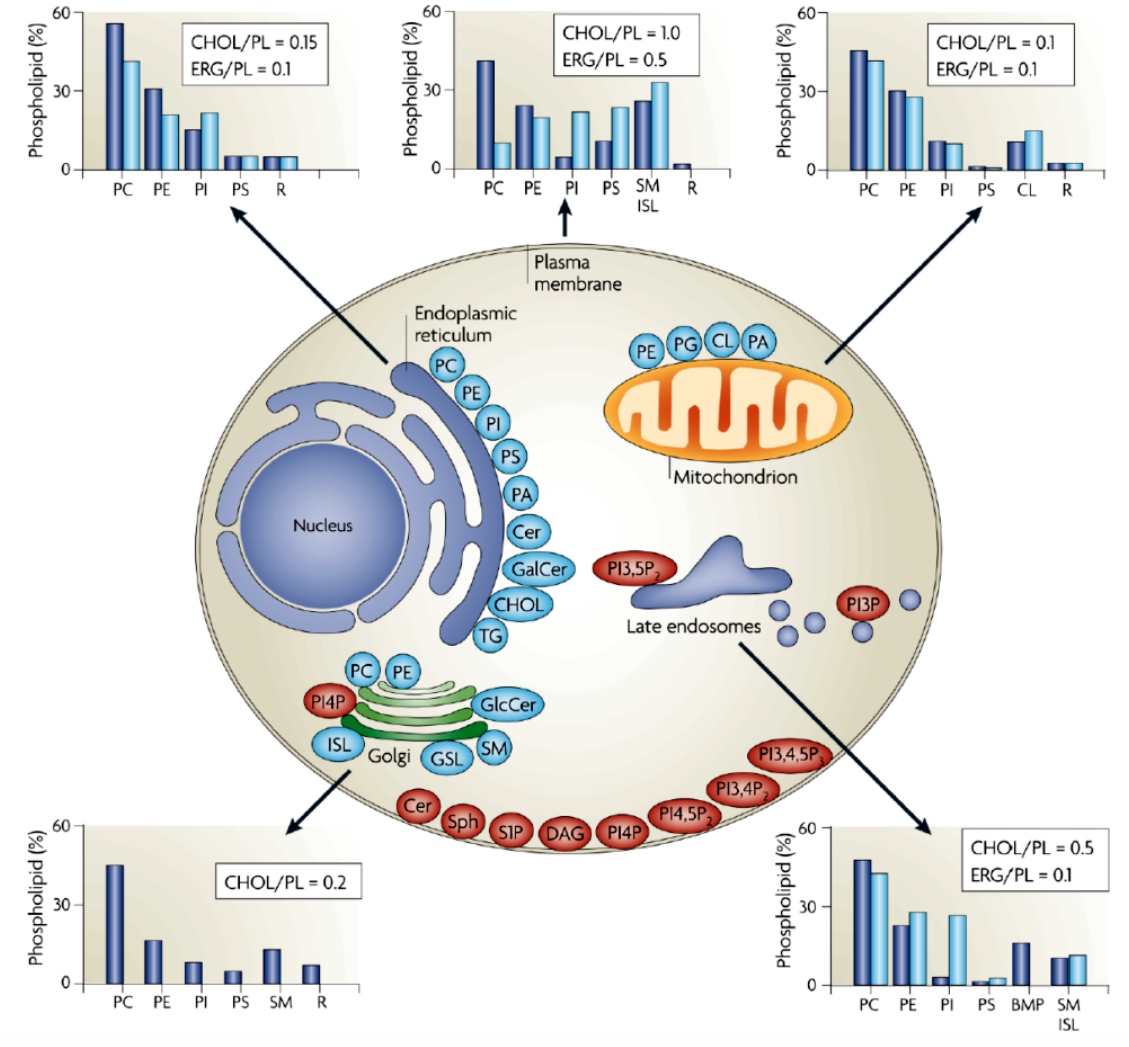

Figure 2.2: Cellular lipid distribution in organelles and plasma membranes.

The main panel depicts the synthesis sites of major cellular lipids (light blue) and lipids which are involved in cell signalling or serve as specific organelle markers (red). Also shown is the percentage of total phospholipid (PL; GSLs and SM, respectively) levels in either mammalian cells (dark blue) or yeast (light blue) within each organelle or at PMs, and the ratio of cholesterol (CHOL) or ergosterol (ERG) relative to the PL content. For detailed description, see **section 2.1.1** and **section 2.1.2**. Note: the lipid cardiolipin (CL) is restricted to mitochondrial membranes, bis(monoacylglycerol)phosphate (BMP) to late endosomes. Abbreviations not explained in text: ISL= yeast inositol sphingolipid, R= remaining lipids, TG= TAG. Figure taken from van Meer *et al.*, 2008; license number: 4463530355221[6].

lipid sorting is deployed to establish cell polarity, namely the differentiation into an apical and a basolateral membrane domain[24,25]. Together with cholesterol, SLs are most abundant at the PM as compared to other subcellular organelles[6].

The PM harbours enzymes involved in the synthesis or degradation of various lipids, further serving as signalling molecules, such as GPL-derived phosphatidylinositol-4,5-bisphosphate (PI(4,5)P_2). Other PIPs serve as characteristic organelle markers and interact with cytosolic proteins important for e.g. vesicular trafficking processes[6,26]. Together with parts of the surrounding medium, PM-localised macromolecules, large particles or fluids are eventually taken up by a process called

endocytosis, and internalised material is either recycled or targeted for degradation[27]. The lipid profile of the early endosome (EE) is similar to the PM profile, yet upon maturation to late endosomes (LE)/multivesicular bodies (MVBs), the cholesterol amount decreases with a concomitant increase in bis(monoacylglycerol)phosphate (BMP), and (complex) SLs are degraded[6,28]. Mitochondria are not part of the secretory pathway; however, ER and mitochondrial membranes are connected by transient contact sites and mitochondria possess a distinctive set of enzymes involved in mitochondrial lipid biosynthesis[29].

2.1.3 Lipid rafts

Except for the membranes of the early secretory pathway, membrane bilayers are characterised by an asymmetric lipid distribution (Figure 2.2), which contributes to certain functions such as phagocytosis or budding processes[6]. Lipid asymmetry is a result of segregation of specific lipids along the secretory pathway due to preferential interactions[30,31] PE and PS e.g. are mostly located towards the cytosolic side, whereas complex PC, SM and GSLs are enriched at the luminal side or the exoplasmic leaflet of the PM[32,33]. The latter require vesicle-mediated transport to the PM, however, PC and SLs are most probably transported separately along the secretory pathway[6]. Cholesterol that is interacting with phospholipids at PMs[34], is mainly shuttled from the ER to the PM via non-vesicular transport, and recently the GRAMD1- or Aster-A, B and C proteins have been shown to be implicated in cholesterol removal from PMs[31,35,36]. Interaction of cholesterol, (mostly saturated) G(S)Ls and especially SM at the exoplasmic PM leaflet has been initially postulated to drive lateral heterogeneity within the same bilayer at nanoscale, forming so-called SL/cholesterol rafts, PM microdomains or lipid rafts[31,37]. The physical principle underlying lipid raft formation was suggested to be based on “liquid-liquid-phase separation”[38]. The higher the degree of saturation and the length of acyl chains, the more likely will lipids separate into densely packed, ordered domains, called liquid-ordered (L_O) domains[6,39]. In contrast, lipids with more unsaturated and/or shorter acyl chains (rather found in GPLs) segregate into liquid-disordered (L_D) domains[6,40,41]. In addition, temperature and protein-lipid interactions can also contribute to driving phase separation[42]. The investigation of lipid rafts *in vivo* is still hampered by experimental limitations, but a common accepted definition is that

they are “heterogenous”, temporal and spatial “dynamic, cholesterol-and SL-enriched nanodomains (10-200 nm)”, which are able to “form microscopic domains (>300 nm) upon clustering induced by protein-protein and protein-lipid interactions”[43]. They can further be “present in (…) the inner and the outer leaflets of an asymmetric cell membrane, are presumably coupled across leaflets and form functional platforms for the regulation of cellular processes”[43-45] (summarised in[42]).
Interactions of SLs and cholesterol in microdomains can occurs via strong hydrogen bonding[46,47]. Although the initial raft hypothesis was based on preferential interactions of SLs together with cholesterol, the engagement of cholesterol in raft formation is still a matter of debate[42,48]. Recent findings suggest the additional presence of sphingomyelinase (SMSase)-induced high-ordered ceramide-enriched platforms (CRPs), which presumably lack cholesterol[49-52]. An emerging alternative raft model postulates that the cortical actin cytoskeleton, including associated proteins, is a key determinant for PM segregation and lipid raft stability *in vivo*[45,53]. However, although the presence of cholesterol in lipid rafts might be obscure, a large body of evidence implicates that SLs are key components of these microdomains, and that different SL species might form distinctive rafts with a specific, function-related specific protein environment (summarised in[54]). Therefore, the SL biosynthetic pathway shall be closer elucidated prior discussing protein recruitment to rafts.

2.2 Sphingolipid metabolism

The *de novo* biosynthetic pathway of SLs begins in the cytosolic leaflet of the ER with the condensation of L-serine and activated palmitate (palmitoyl-CoA) to 3-ketodihydrosphingosine/3-ketosphinganine. The reaction is catalysed by the enzyme serine palmitoyltransferase (SPT) and results in a 18 carbon (C) atom amino-alcohol. Reduction of the product by 3-ketodihydrosphingosine reductase (KDS) yields the sphingoid backbone sphinganine (Spg) (Figure 2.3, left panel)[55,56]. N-acylation of the sphingoid backbone at the C2-position by a N-acyl transferase, (dihydro)ceramide synthase (CerS), generates dihydroceramide (DHCer)[54,57]. Six different isoforms of CerS exist, all of which have a distinctive specificity towards the length of the activated FA substrate[56]. The Spg-backbone of *de novo* generated DHCer is reduced to sphingosine (Sph) by the ER-resident dihydroceramideΔ4

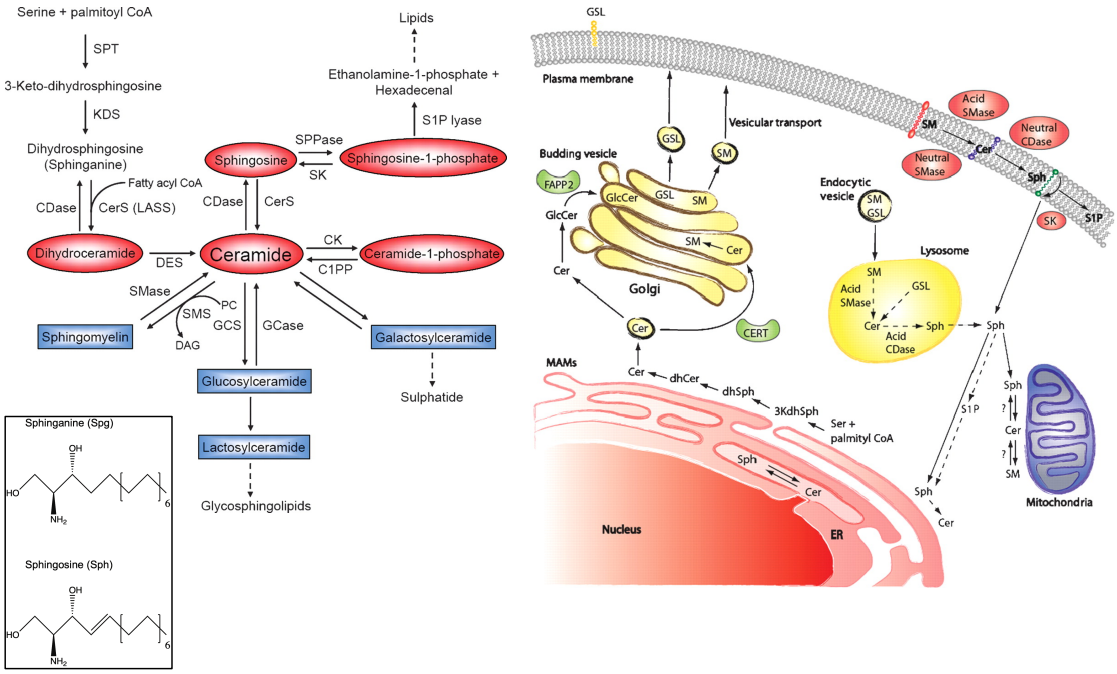

Figure 2.3: The Sphingolipid metabolic pathway.

The *de novo* and recycling biosynthetic pathway of SLs is shown in the left panel. SL messengers are shown in red, the sphingoid backbones Spg and Sph are framed. Note that CerS were originally annotated LASS (longevity assurance) genes. Different intracellular stages of SL synthesis and degradation are depicted in the right panel. For detailed description, see **section 2.2**. CDase= ceramidase, C1PP= C1P-phosphatase, CK= ceramide kinase, SPPase= SPP. Image modified from Bartke & Hannun, 2009; Copyright © 2009 by the American Society for Biochemistry and Molecular Biology, Inc.[58].

desaturase (Des1 in most tissues) to obtain Cer, which is considered the hub of SL metabolism, and gives rise to complex SLs[55,59]. Importantly, DHCer is only generated during *de novo* synthesis from Spg, but CerS also accept the sphingoid backbone Sph as substrate, mainly derived from the SL degradation pathway[57]. CerSs do not show a preference for Spg or Sph, yet the amount of cellular dihydro-SLs (DHSLs) is significantly lower than the amount of Sph-containing SLs, as the Des reaction is one of the few irreversible reactions in the SL biosynthetic pathway[60].

Cer is transported either by vesicular transport or the Cer transfer protein (CERT) to the Golgi apparatus (Figure 2.3, right panel)[55]. CERT transports DHCer and Cer, yet it displays specificity for Cer with acyl chains below 22 C-atoms[55,61,62]. CERT-transported Cer is rather incorporated into SMs than GSL, both obtained by modification of Cer at the C1-hydroxyl (OH) group[55,63,64].

GSLs can be subdivided either into galactosylceramide (GalCer) or glucosylceramide (GlcCer) and are produced from Cer and an activated sugar unit (UDP-galactose or glucose, respectively)[60]. GalCer is synthesised by the ER-resident

enzyme galactosyltransferase (CGT) and serves as a precursor for sulfatides (sulfogalactolipids), or is sialylated to produce GM4 ganglioside[60,65]. GlcCer is the product of the glucosylceramide synthase (GCS/UGCG) reaction in the *cis*-Golgi compartment and indispensable for mammalian development; most GSLs derive from GlcCer[60,66,67]. In contrast, GalCer is implicated in less widespread functions, such as oligodendrocyte functionality or myelination processes, and the GalCer-synthesising enzyme CGT is expressed only in a few tissues[55]. Newly synthesised GlcCer is transported by the lipid transporter four-phosphate adaptor protein 2 (FAPP2) to sites of complex GSL synthesis in the luminal membrane leaflet of the *trans*-Golgi network (TGN) complex[60,63,68,69]. Alternatively, GlcCer can also pass the Golgi complex by vesicular trafficking and shuttled to sites of enzymatic modification by an unknown transporter[70]. The initial step of complex GSL synthesis involves galactosylation of GlcCer to produce lactosyl-Cer (LacCer), which is consequently trapped in the Golgi and serves as the key molecule for various types of SL-glycosylation, yielding asialo-ganglioside GM2 (GA2), globotriaosyl-Cer (Gb3), monosialodihexosylganglioside (GM3) and N-acetyl-D-glucosaminyl-1,3-beta-D-galactosyl-1,4-beta-D- glucosylceramide (Lc3) as precursors for GSLs assigned to the respective asialo, globo/iso-globo, ganglio and lacto/neo-lacto series[71]. Membrane-embedded complex GSLs (and also SM) are transported via carrier proteins to the PM, where they can be trimmed by glycosidases[6,72]. In total, a combination of over 400 sugar residue (glycan) combinations are found among complex GSLs, made up of 1 to 20 sugar units[71]. After endocytosis, degradation of PM-bound GSLs occurs in lysosomes via distinctive exohydrolases, stripping off glycan moieties until Cer remains[6,73,74].

Although GSLs are crucial for mammalian development, SM depicts the major cellular SL class and is essential for cellular viability[55,75]. CERT transported Cer is used for SM synthesis in the TGN via sphingomyelin synthases (SMSs)[55,64]. To produce SM, the phosphocholine headgroup of PC is transferred to Cer, yielding DAG and SM[3]. Hence SMSs regulate the levels of PC, Cer, DAG and SM simultaneously, enabling the enzyme to influence cellular homeostasis as Cer and DAG have (opposing) bioactive properties[55]. There are two SMSs, SMS1 and SMS2, both present in the *trans*-Golgi, but only SMS2 is also localised to the PM[55].

SLs, specifically Cer, can also be generated by sphingomyelinase (SMSase) activity or the salvage/recycling pathway[74]. This pathway contributes to

approximately 50-90% of SL synthesis. Whereas free Spg ("dihydrosphingosine") is mostly generated *de novo*, free Sph mainly derives from the breakdown of complex SLs[74,76,77]. Complex GSL and SM are degraded to Cer in lysosomal compartments by the action of either glycohydrolases or acid sphingomyelinase (aSMSase)[75,78]. Hydrolysis of SM also releases free phosphocholine that can be used, together with DAG, for PC synthesis[3]. The breakdown product Cer is further converted by acid ceramidases to Sph and the respective free FA, which, in contrast to Cer, can leave the lysosome and be recycled for Cer synthesis or the generation of bioactive SL molecules[79,80].

Ceramide generated from the *de novo* or the recycling pathway can be converted to C1P by Cer kinase (CerK) in the *trans*-Golgi[55,81]. C1P is dephosphorylated by C1P phosphatase, presumably at the PM[55,58]. Ceramidase-obtained Sph in turn can be metabolised via C1-phosphorylation to S1P, a reaction catalysed by cytosolic or membrane-associated Sph-kinases 1 and 2 (SphK1/2)[55]. Cytosolic SphK1 can be transported to the nucleus, associate with the PM or be secreted, and is pro-survival[55,82]. In contrast, SphK2, assumed to be pro-apoptotic, is mainly localised in the nuclear region and exhibits a broader specificity for sphingoid backbones[55,83]. S1P can be degraded by several enzymes, such as the cell-surface localised lipid phosphate phosphatase family (LPP1-3) or the ER-resident S1P phosphohydrolase (SPP1/2)[55]. Both enzyme families might be able to attenuate S1P signalling, yet LPPs also modulate PA levels and hence SK1 localisation[55,84-86]. SPPs specifically regulate the re-entry of Sph for Cer synthesis in the recycling pathway[87,88]. Another S1P-metabolising enzyme is S1P lyase (S1PL), which converts S1P irreversibly to hexadecanal and phosphoethanolamine in the ER[55,89,90]. Importantly, Cer, C1P as well as Sph and S1P are interconvertible messenger molecules, mainly derived from the salvage pathway, which display opposite signalling functions within the cell and thus modulate cell fate[74,91]. Non-phosphorylated Cer and Sph accumulation promotes cell death, whereas their phosphorylated counterparts act anti-apoptotic, pro-inflammatory and induce cell proliferation[91]. This "SL-rheostat" is further complicated as dihydro-SL (DHSL) messengers also exhibit aberrant bioactive functions compared to Spg-containing molecules, such as inducing autophagy and coping with oxidative stress[59].

Exchange of SL by its DHSL counterpart has also a significant effect on biophysical membrane properties, specifically lipid packing and fluidity[92]. Saturation of the Spg

backbone results in a stronger interaction with cholesterol and hence the formation of domains with enhanced rigidification, which has impacts on membrane physiology[93,94]. Raft formation and physiology is, however, not only influenced by variable lipid interaction affinities but also modulated by (membrane) proteins[37].

2.2.1 Raft domain organisation: raft-targeting of proteins

Lipid-lipid interaction as a principle of raft self-assembly, as described in **section 2.1.3**, has been initially postulated to be solely dependent on interaction of (G)SLs and cholesterol[47]. The situation *in vivo* is, however, presumably way more complex, as the cortical actin cytoskeleton and its associated protein network have been considered to be a key factors for raft clustering, although the molecular machinery underlying these cluster formation is not elucidated yet[53,95]. Protein-lipid interactions are indeed essential initiators of lipid heterogeneity. Association of proteins with raft-lipids can be supported by protein lipidation, such as lipid anchors (Figure 2.4)[42]. Posttranslational modifications include prenylation, cholesteroylation, palmitoylation, myristoylation or a glycosylphosphatidylinositol (GPI) anchor[96]. Proteins modified with branched or unsaturated FA chains, like prenyl chains, are more likely to be incorporated into L_D domains; in contrast, saturated lipid anchors, e.g. GPI, myristate or palmitoyl moieties, as well as cholesteroylation, presumably recruit proteins to L_O domains[42,97-99]. Still, the amount of "raftophilic" proteins exceeds the amount of lipidated proteins. Approximately one third of these proteins are not lipidated, but are recruited by other mechanisms to raft domains[42]. These might include, beside protein oligomerisation, e.g. the length of the transmembrane domain (TMD)[100,101]. Mammalian membrane lipids usually harbour acyl chain lengths between 12 and 24 C-atoms, and lipids with similar acyl chain length tend to aggregate within membranes to evade the energetically unfavorable exposure of hydrophobic moieties to the aqueous environment ("hydrophobic

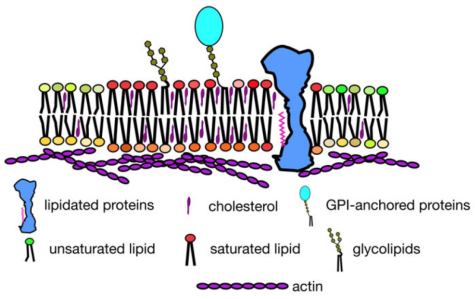

Figure 2.4: Lipid raft domain organisation.

Lipid raft domains are assemblies of cholesterol and mainly saturated lipids (such as SLs, G(S)Ls and phospholipids). Certain modifications can target proteins to these domains. The cortical actin cytoskeleton presumably plays a central role in lipid raft organisation. For detailed description, see **section 2.1.3** and **section 0.** Modified from Sezgin *et al*, 2017, license number: 4466351099331[42].

mismatch")[42,102]. Similarly, the length of the TMD determines to which membrane regions proteins preferably insert, and longer TMDs preferably tend to associate with L_O domains[42,101,103]. Another raft-targeting feature is the presence of (raft)lipid-binding domains. Cholesterol-binding motifs include CRAC (cholesterol-recognition amino acid consensus) or the inversed CARC motifs[104]. Proteins might also interact with SLs[42]. The human epidermal growth factor receptor (EGFR) has been demonstrated to associate with a specific GSL of the ganglioside series, GM3, and the coat-protein I (COPI)-machinery protein p24 has been illustrated to specifically interact with SM C18:0 species[22,105,106]. Recent findings suggested a SL-binding signature sequence within the TMD of membrane proteins, which could be identified in p24 as a prerequisite for SM interaction[22,106,107]. Notably, most proteins harbouring the SL-binding signature motif were assigned to the PM, and a substantial number might be localised to raft domains, as has been shown for a significant amount of palmitoylated proteins[42,107,108].

2.2.2 Lipid rafts in pathogenesis

Lipid rafts are, among other physiological functions, implicated in the pathogenesis of bacterial and viral infections, and over 100 pathogens are known to interact with raft domains[42,109]. Several bacterial pathogens exploit lipid rafts, such as caveolae (a specific raft type containing the protein caveolin, CAV), for bacterial uptake and subsequent dissemination[110,111]. Furthermore, numerous studies illustrated that both non-enveloped and enveloped viruses from various virus families employ lipid rafts during entry and budding of the viral replication cycle. Most non-enveloped viruses use rafts rather for entry processes, such as simian virus 40 (SV40), echovirus type 1, rotavirus, enterovirus, rhinovirus or rotavirus. In contrast, Ebola and Marburg virus, human immunodeficiency virus (HIV) and Influenza (A) virus (IAV) do not only involve lipid rafts in viral entry, but also in assembly and budding processes[112]. Specifically for HIV and IAV it was demonstrated that viral envelopes, deriving from the (apical) PM of host cells, exhibit a raft-like lipid composition[113,114]. Envelopes of HIV and IAV showed an enrichment of (G)SLs and cholesterol compared to the total host cellular lipidome, and defects and/or inhibition of certain stages in SL metabolism severely impaired infectivity and/or assembly as well as budding processes[113,115]. The presence of the putative SL-binding signature motif

in the neuraminidase protein of IAV subtype 1, which exhibited an accelerated PM targeting compared to other NA subtypes, further underlines that raft lipids might play a crucial role in viral pathogenesis[116]. In the following, the biology of IAV shall be explained in more detail.

2.3 Influenza A biology

IAV is a human and animal-infecting pathogen and causative agent for seasonal "flu" epidemics, resulting in mild up to severe, acute respiratory illness (WHO)[117]. Annual epidemics depict not only health and economic burdens, but have also the potential to evolve to lethal global pandemics, of which six have been recorded in the 20th century[118,119]. IAV belongs to the family of *Orthomyxoviridae* and is characterised by a single-stranded (ss), negative-sensed (-) RNA genome[120]. Among the three genera A, B and C, mostly A and B are clinically relevant for human infections, especially IAV. The assignment to various subtypes is based on the combination of the viral envelope glycoproteins hemagglutinin (HA or H) and neuraminidase (NA or N)[121]. Further descriptive elements of a specific IAV strain include the species origin, the geographical place of 1st isolation, the number of the strain and year of isolation (summarised in[122]).

Aquatic bird species are the natural host reservoir for influenza viruses, yet adaption to a variety of hosts has taken place, including dogs, horses, bats, pigs, birds and humans[121,123,124]. Human-adapted IAV has its zoonotic origin in birds and swine. So far 18 HA and 11 NA subtypes have been characterised in birds, of which subtype A/H1N1, A/H2N2 and A/H3N2 have clinical relevance for human infections[125,126]. Vaccination is a measure to counteract the spread of seasonal endemics, however, protective efficiency is hampered by the continuous evolution of the virus, enabling IAV to evade vaccine-driven immunity and also immunity established after prior Influenza infections[125]. Especially nucleotide (nt) changes and amino acid (aa) substitutions in HA and NA give rise to novel antigenic variants or strains, commonly referred to as antigenic drift[125]. In addition, the genome of Influenza viruses is comprised of gene segments (Figure 2.5, upper panel) which can be easily exchanged if two or more distinct virus strains infect the same host cell. This process, called gene reassortment or antigenic shift, has been the major cause for the establishment of global pandemics[127]. Due to the dynamic change in

viral surface glycoproteins and the lack of proofreading activity of the error-prone viral RNA-dependent RNA polymerase (vRdRP), IAV constantly exists in a population of "quasispecies"[128]. In particular, mutations in the HA protein determine if a specific antigenic variant successfully propagates, as it is responsible for host receptor binding and the primary immune target[129,130].

2.3.1 Function and pathogenicity of viral proteins

The IAV genome is comprised of eight gene segments (Figure 2.5, upper panel). The (-)ssRNA is converted to (+)ssRNA by the vRdRP in order to enable transcription of viral genes by the host cell machinery[131]. Importantly, several gene products can be derived from one gene segment due to alternative splicing, ribosomal frameshift or the usage of alternative initiation codons, yielding more viral proteins than gene segments (Figure 2.5)[123,132]. Except for the nonstructural protein NS1, all viral proteins depict structural proteins, including the polymerase basic 1 (PB1), polymerase basic 2 (PB2) and polymerase acidic (PA) protein, which together form the vRdRP complex, the nucleoprotein (NP), the matrix protein M1 and ion channel/surface protein M2 as well as HA and NA[125].

Replication and transcription take place in the nucleus of the infected host cell and are mediated by PB1, PB2 and the PA[133]. PB1 functions as catalytic subunit of the vRdRP; PB2 binds to 5' caps of host pre-messenger RNAs (pre-mRNA), which are subsequently removed by endonucleolytic cleavage of the PA protein[133-135]. This mechanism called "cap-snatching" is essential for priming of viral transcription, as the viral polymerase is not able to produce 5' caps on its own[133,134,136]. Heterotrimers of PB1, PB2 and PA are associated with the 5' and 3' untranslated regions (UTRs) of the viral RNA (vRNA) segments, and the NP is associated with both vRNA and the RdRP, forming the viral ribonucleoprotein (vRNP) complex. Beside replication and transcription, the vRNP complex is also involved in intracellular transport of vRNA, genome packaging of viral genomes in newly synthesised virions, as well as gene reassortment[137]. Notably, the PB1 gene segment variably encodes for other proteins, PB1-F2, PB1-S1 and PB1-N40[132,138,139]. PB1-F2 has pro-apoptotic and anti-inflammatory properties. It targets the inner membrane potential which results in the inhibition of innate immune responses, namely interferon (IFN) signalling and inflammasome formation[140,141]. PB1-S1, similar to PB2-F2,

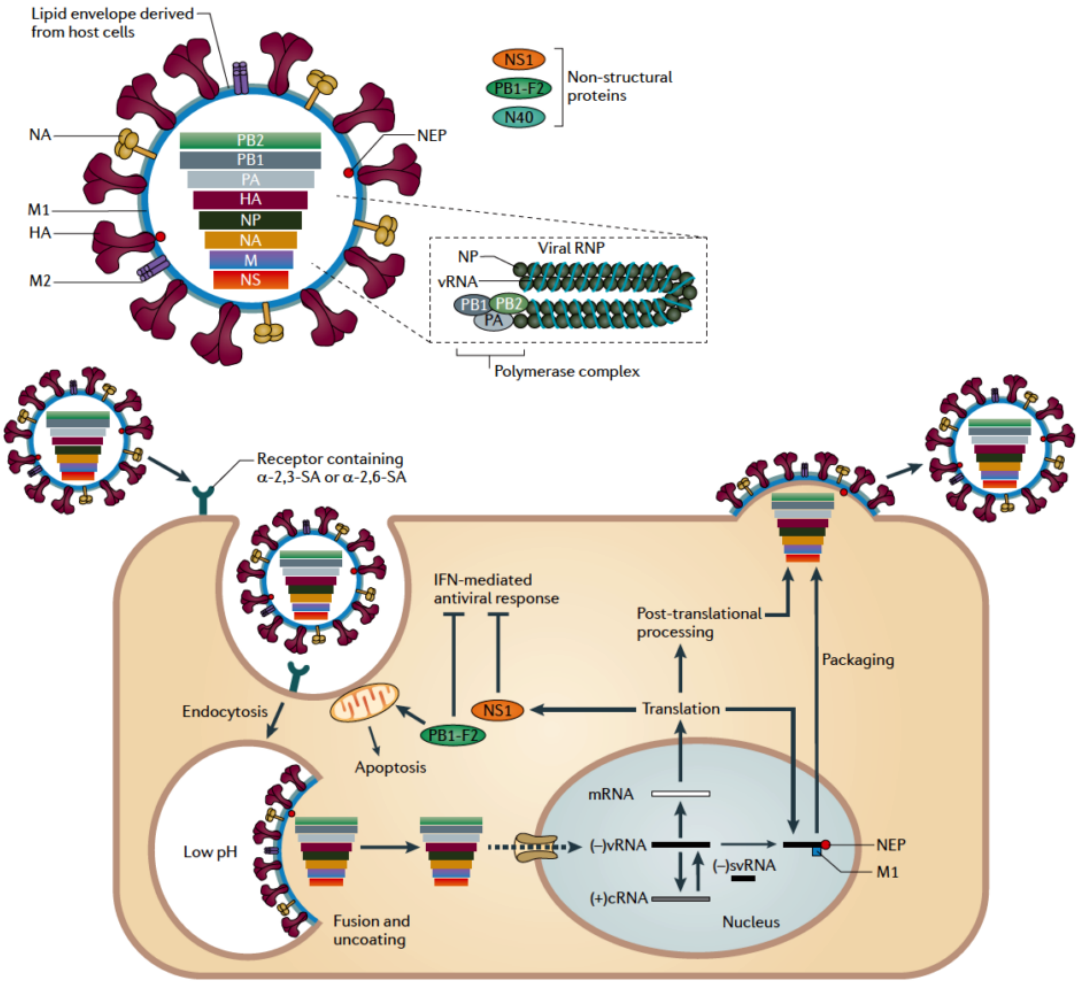

Figure 2.5: The Influenza A virion morphology and replication cycle.

The virion structure of IAV is depicted in the upper panel, the replication cycle including entry, uncoating, transcription and translation as well as assembly and budding processes in the lower panel. For detailed description, see **section 2.3.1** and **section 2.3.2**. Not mentioned in text: PB-F1 and (PB1-)N40 are additional non-structural proteins. (-)vRNA= negative-sense viral RNA [ss(-)RNA]; (+)cRNA= positive sense, complementary RNA [(+)ssRNA]. Modified from Medina & Sastre, 2011; license number: 4463531401658[142].

localises to mitochondria and inhibits retinoic acid inducible gene I (RIG-I)-dependent IFN signalling pathways[132]. The expression of PB1-N40 is interdependent on PB1 and PB1-F2 expression, but its function for viral pathogenicity is still elusive[139]. PA-related alternative gene products include PA-N155 & PA-N182 as well as PA-X, which have been implicated in viral replication efficiency and the ability to shut off host immune responses[143-145]. The NS gene segment encodes for the NS1 and NS2 proteins which are generated by differentially spliced mRNAs[146]. The NS1 protein possesses a N-terminal double-strand (ds)RNA binding domain with a nuclear localisation signal (NLS), an effector domain containing a nuclear export signal and a C-terminal protein interaction domain (PDZ domain)[147]. NS1 is able to augment viral translation and simultaneously impair host mRNA transcription as

well as translation. This is achieved by intervention with the host cellular splicing machinery and interaction with the cellular CPSF 30 kDa domain protein (also known as CPSF4), respectively[148,149]. NS1 is also implicated in the restriction of lipid metabolism pathways and especially an effective modulator of host defence mechanisms[147,150]. It counteracts both innate as well as adaptive immune responses, such as suppression of RIG-I/TRIM25-mediated sensing of vRNA and thus type I IFN signalling, attenuation of antiviral signaling or attenuation of dendritic cell (DC) maturation[151-153]. The interplay of NS1 with either PB1-F2 or the PA-X protein has been demonstrated to suppress IFN signalling and host protein synthesis[140,154]. In contrast, the NS2 (or nuclear export protein, NEP) of Influenza is involved in the export of vRNP complexes and presumably enhances polymerase activity, and is part of the viral particle[155,156]. Recently, a third splice variant of the NS gene segment has been discovered, termed NS3, which has been associated with host adaption processes[157].

The matrix protein M1 protein is the most abundant viral protein and builds the inner layer of the viral lipid envelope[158,159]. It builds a “scaffold” for other viral proteins[160]. Hence, M1 plays a crucial role in virus assembly and budding and presumably determines IAV morphology[160,161] The second gene product from the M gene, M2, is a proton-selective ion channel embedded in the viral envelope. After the virus has been internalised by the host cell, M2 is responsible for the release of viral genomes and proteins into the host cytoplasm[162]. It additionally serves as a “scission” protein in order to release new virus particles from the cell, and has been demonstrated to block autophagosome maturation[163,164]. Another splice variant from the M gene, M42, also seems to function as a proton channel[165].

The glycoproteins HA and NA both undergo ER- and Golgi-mediated N-linked glycosylation upon secretory transport towards the PM, which facilitates not only the proper folding and stability of viral proteins, but also enables immune evasion[166,167]. The most abundant viral glycoprotein in in the viral envelope (≈80%) is HA, the key determinant for host tropism and pathogenesis[123]. The main receptors for seasonal H1 and H3 strains are sialic acid (SA)-alpha-2,6-Gal-terminated saccharides found on the cell surface of sialoglycans (=glycoproteins and gangliosides with a terminal SA residue), expressed from non-ciliated, bronchial epithelial cells within the human upper respiratory tract (hURT)[168-170]. In contrast, avian-adapted HA proteins mainly recognise the isomeric SA-alpha-2,3-Gal-terminated glycosidic bond that is

rather found in the human lower respiratory tract (hLTR) on ciliated cells[170,171]. Animals harbouring both isoforms of SA-linked receptors, e.g. pigs, serve as mixing vessel for antigenic shift variants and potential pandemic Influenza strains[172,173]. The internal carbohydrate structure of sialogylcans probably also plays a role in receptor recognition[174]. GSLs of the ganglioside series, like GM3 and GD1a, have been implicated in IAV entry[175,176]. Yet, evidence exists that IAV can also bind to cell-surface receptors independent of SA. It has been shown that HA is also able to bind to Annexin V, C-type langerin (Lec2), cell-surface nucleolin (NCL) and sulfatides, the latter notably with a distinctive fate for virus production[177-181]. NCL, a major RNA-binding protein within the nucleolus, has also been shown to interact with the NP protein at early stages of infection, and hence to be involved in the temporal regulation of viral gene transcription[182]. The less abundant glycoprotein in the viral envelope, NA, has an intrinsic sialidase activity, which is needed on the one hand to facilitate virus penetration at cell entry and on the other hand to ensure the proper release of newly produced virions[127,183].

Although a serious threat to human health, Influenza virions are quite unstable outside their host, being susceptible to hot and dry surroundings or pH extreme environments[184]. Due to the presence of a lipid bilayer, organic solvents and detergents impair viral viability[158,184]. Hence, the virus must penetrate the next host organism as fast as possible.

2.3.2 The Influenza (A) replication cycle

Influenza binds to the host cell by attachment of HA trimers to its corresponding cell surface receptors and is internalised via receptor-mediated endocytosis into the endosomal compartment (Figure 2.5, lower panel)[185]. If not already processed upon exit of the previous host cell, the single-peptide HA precursor, HA(0), is cleaved by host trypsin-like or serine proteases into HA1 (globular head, the receptor binding domain) and HA2 (stalk, the fusion peptide), both linked by a disulfide bond[186-188]. Within endosomes the drop in pH induces a conformational change in the HA protein, and the HA2-fusion peptide inserts into the endosomal membrane, leading to fusion of both membranes[187,189]. The M2 protein is also activated in the acidic environment, and M2-tetramers serve as a proton-selective ion channel, resulting in the acidification of the virion[190]. Both HA and M2 contribute to the

dissociation of vRNPs from M1 and their release into the host cell cytoplasm[162,189]. Recent data suggests that IAV also exploits the host cell aggresome processing machinery for viral uncoating, via the ubiquitin-binding capacity of histone deacetylase 6 (HDAC6)[191]. The vRNP complexes are shuttled through nuclear pore complexes to the nucleus in order to initiate transcription, replication and translation processes of viral genomes[192,193]. The vRNP harbours an NLS which is crucial for nuclear entry[194]. In the nucleus, RdRP transcribes (-)ssRNA either to complementary (+)ssRNA, which is used for replication of viral genomes or translation of viral proteins, or to small viral (-)svRNA, being possibly involved in the viral transcription/replication switch[142,195]. After they have been translated from viral mRNA in the cytoplasm, viral proteins that are involved in the replication process are retransported to the nucleus. Newly synthesised vRNPs are exported presumably via interaction processes of NP and NEP with Exportin 1/chromosomal maintenance 1 (CRM1) out of the nucleus[185,196].

HA and NA initiate the budding event at the apical PM of polarised (epithelial) cells[158]. HA and NA accumulation in lipid rafts results in raft coalescence and local alterations of membrane curvature[160]. M1 does not possess a TMD and is recruited to sites of assembly by the cytoplasmic tails (CT) of HA and/or NA (and M2)[160,197]. The M1 protein serves as a docking site for vRNPs, yet it is unclear whether genomes are packed randomly or via packaging signals into virions[160,185]. The budding process is indeed not carried out only by viral proteins, but also aided (indirectly) by several host factors, such as the actin cytoskeleton, the Rab11 pathway and coat protein I (COPI) complexes[160,198-200]. The M2 protein facilitates the final, endosomal sorting complex required for transport (ESCRT)-independent scission process of viral particles via to insertion of its amphipathic helix into the edge of the viral “budozone”[163,201]. This process presumably depends on interactions with cholesterol[163,202].

2.3.3 The viral TMD proteins HA, NA and M2 harbour raft-targeting signals

Virus particles can be released from the host cell with defective or even without vRNPs, but the assembly and budding process strongly relies on the viral TM proteins HA, NA and M2, as they are the only envelope proteins[158]. The length and hydrophobicity profile of viral TMDs are presumably implicated in the raft-

associating/targeting potential of different Influenza (A) subtypes[203]. However, all three proteins harbour raft-targeting signals which might aid recruitment to sites of assembly (Figure 2.6)[160]. The HA protein is S-acylated with palmitate or stearate at cysteine residues within the TMD and the CT[204,205]. S-acylation of HA has been shown to be crucial for raft association, especially palmitoylation within the CT, yet the FA pattern can vary among cell types[206,207]. Further raft-targeting features of HA involve a CRAC or CCM (cholesterol consensus motif)[208,209]. A proposed model for HA raft association is that HA associates with raft lipids, such as cholesterol and SLs, in the Golgi and is subsequently transported to the apical membrane[210,211]. Nevertheless, other studies revealed that HA neither co-localised with SLs nor with cholesterol, and that presumable molecular interactions between HA and these "lipid raft components" might not be sufficient to trigger HA clustering at the PM[212]. Instead, clustering of HA could be mediated by cortical actin, as the actin cytoskeleton is linked to microdomains during virus infection[200,212-214].

The HA protein alone is not able to finalise the detachment of virions from the PM as it re-binds to sialic acid-containing receptors[215]. In contrast, cells expressing only NA are able to produce virus-like particles (VLPs) as a result of sialidase activity, and impairment of the latter leads to virion aggregates at the cell surface[216,217]. NA is a homotetrameric protein and localises to the same PM regions as HA[218,219]. Data strongly suggests that the TMD of NA provides signals for apical sorting and raft association[219,220]. Indeed, a putative SL-interacting interface in the TMD of NA subtype 1, facing the exoplasmic PM leaflet and hence the bulk of SLs,

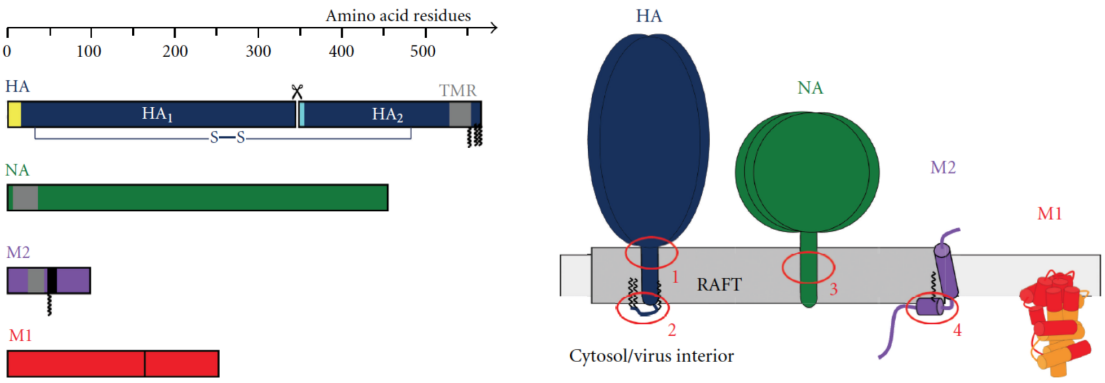

Figure 2.6: Raft-association of HA, NA and M2.

In the left panel, the amino acid sequences of HA, NA, M2 and M1 including TMDs (grey), S-acylation (black zig-zag line), as well as the signal peptide (yellow) and fusion peptide (cyan) of HA are depicted. Organisation of respective proteins in raft domains is shown in the right panel; raft-targeting features are highlighted in red. For detailed description see **section 2.3.3**. Picture modified from Veit & Thaa, 2011; Copyright © 2011 M. Veit and B. Thaa[203].

has been suggested to accelerate NA transports to sites of assembly[6,116]. However, in contrast to HA, less is known about raft-targeting of NA[219]. M2 is, similar to HA and NA, transported via the TGN to the PM; yet abundance in viral particles is very low[162,221]. The CT harbours an amphipathic helix comprising several overlapping CRAC motifs and one S-acylation site[222,223]. The CT of M2 has also been shown to interact with CAV1 via a CAV1-binding domain (CBD)[224]. M2 alone does not intrinsically localise to the L_O phase-like domains of the PM, but is rather recruited by M1[160,225]. Although not inserted into membranes, M1 harbours an amphipathic helix with CRAC motifs and hence exhibits raft-binding potential. In addition, M1 has been shown to specifically interact with PS-enriched domains at the inner leaflet of the PM, which triggers its oligomerisation[6,226]. Finally, the NP protein has been reported to be intrinsically targeted to raft domains, despite being soluble and not known to be lipid modified so far; however, this observation was not recapitulated by others[203,227].

Beside the implication of SL-enriched microdomains in the Influenza assembly and budding process, further evidence exists that points to a pro-viral function of cellular SL levels and biosynthetic pathways.

2.3.4 Roles of sphingolipids in Influenza (A) propagation

As illustrated, HA and NA are processed through the exocytic pathway and harbour apical sorting signals, finally exploiting lipid rafts as sites for assembly and budding[160]. Association with raft lipids, such as SLs (and cholesterol), might facilitate or even be crucial for directed apical transport, although the latter aspect is controversial, at least for HA[210,212]. However, it was clearly demonstrated that the velocity of cell surface arrival of both IAV glycoprotein, specifically from the Golgi to the PM, is dependent on SM *de novo* synthesis[115]. On the other hand, the presence of a putative SL-binding motif within the TMD of NA subtype 1 increased PM targeting kinetics compared to other subtypes[116].

Proof of the necessity of raft integrity for viral assembly was given by several studies. For example, the IFN-inducible anti-viral protein viperin is able to inhibit virion-release from the cell surface of HeLa cells through perturbation of lipid rafts[228]. IAV release was also impaired in nakanori-treated MDCK cells, a fungal, non-toxic protein, that binds specifically to SL and cholesterol-enriched domains[229]. IAV virions,

in comparison to the host cell, are always enriched in SM (and cholesterol), independent of the cell system and virus strain used[114,230]. GSLs, such as hexosyl-Cer (HexCer) and dihexosyl-Cer (Hex2Cer) (see Figure 3.7) are also enriched in the virus particle, whereas the amount of Cer in the viral envelope might vary. GPLs and storage lipids (DAG, TAG and CE) are mainly depleted[114,231,232]. SLs, such as SM, Cer and HexCer, have been described to be crucial for post-transcriptional & translational events, especially viral morphogenesis, and several studies report that the intracellular levels of those lipids increase upon 12 h post-infection (hpi)[114,231,233,234]. Notably, it was observed that specifically the amount of DHSLs increases during infection[231,232]. The remarkable increase of SM(d18:0/16:0) species has not only been reported to be enriched in IAV-infected MDCK cells, but also in HIV- and vesicular stomatitis virus (VSV) infected cells[113,114,235]. In accordance with the mentioned observations, a combination of lipid, proteomic and gene expression data revealed an upregulation of SM levels, enzymes of complex GSL synthesis and the CerS isoform 4, as well as increased DHSL levels and transcripts of the enzyme 3-ketodihydrosphingosine reductase (see **section 2.2**)[115,150,231]. The latter two might indicate a specific requirement for *de novo* SL synthesis; however, the contribution of *de novo* and salvage SL metabolic pathway to IAV virion formation is still obscure, since also gene expression of enzymes involved in SL degradation have been shown to be upregulated in IAV infected cells[150,231,232]. A similar controversy exists regarding the role of the SL acyl chain length in viral propagation. It has been observed that during the course of IAV infection, SMs, Cers and HexCers with an acyl chain length of 20, 22 and 26 C-atoms significantly (C18 moderately) increased in infected cells, whereas C16 species decreased. C24-containing SLs were slightly upregulated, considering all C24 species (saturated and unsaturated), but down-regulated for unsaturated C24 species only[231,232]. Synthesis of very-long chain species (C>22) is mediated by CerS3 (C26) and CerS2 (C22, C24) and depletion of the latter resulted in impaired vesicular trafficking[236-238]. Accordingly, SLs with shorter acyl chains have been postulated to be localised to the PM, longer chain SLs in intracellular vesicles. Hence IAV might exploit interaction with LC-SLs for intracellular transport[232,239]. Opposingly, especially very-long chain (VLC) SLs (C22, C24) have been shown to be enriched at apical PMs of MDCK cells, yet not in the viral envelope[114]. Interestingly, the increase in VLC SL species (C22, 24, 26) at the expense of C16 species, together with an increase

in saturation, is characteristic for epithelial-to mesenchymal transition (EMT)[240]. A distinctive gene signature correlating SL metabolic pathways to EMT, primarily identified in lung carcinomas, could also be identified in IAV infected adenocarcinomic human alveolar basal epithelial (A549) cells[241]. In this study, several SL-metabolising genes were upregulated upon EMT, such as enzymes modulating SM levels (SMS1 but also SMSase), fatty acyl chain length (CerS2, 5 and 6, but not CerS4) as well as the SL-messenger producing enzymes,e.g. CERK, SphK1 and S1PL and associated receptors (S1PR). Agonists of S1P have been shown to limit inflammatory processes and restrict lung injury via S1PR binding in IAV-infected pulmonary epithelial cells[242,243]. Another study showed that overexpression of S1PL decreased IAV protein expression and production of infectious virus particles in HEK293 T cells, and the contrary effect was achieved by overexpression of SphK1[244]. The ability of S1PL to restrict virus replication was related to its ability to initiate a type I IFN-mediated innate immune response, but importantly, independently of its S1P-degrading function[245]. It remains also elusive if SphK1 as well as SphK2 exert their pro-viral function through elevation of S1P levels[244,246].

In summary, although it is well-accepted that IAV benefits from SL metabolic pathways, it still remains elusive how SLs support viral morphogenesis or other processes during IAV infection, and which SL species might be specifically involved in any of these processes. In addition, it is not well understood if IAV directly modulates SL metabolic pathways at the gene or protein expression level, or if certain viral proteins interact with distinct SL classes and/or species to mediate viral processes, such as assembly and budding.

2.3.5 Aim of this thesis

Antiviral drugs currently on the market either target NA (Oseltamivir/Tamiflu® and Zanamivir/Relenza™) or M2 (Amantadine)[160,162,217]. However, due to the constant change of viral genomes, IAV strains acquire resistance against antiviral treatment[247]. Hence the identification of pro-viral cellular host factors, which importantly do not impair cell viability upon loss-of function, is a current key goal in combating IAV infection[142].

Bifunctional lipids depict a suitable tool to explore protein-lipid interactions in the cellular and organismal context (Figure 3.1)[247,248]. The biorthogonal labelling of cells with **p**hotoactivatable **a**nd **c**lickable (**pac**) lipid precursors already allowed the systematic proteome-wide mapping of protein-cholesterol/GPL/SL-interactions[249]. Due to the diversity of lipids and TM proteins, specific lipid-protein interactions are considered to be numerous, yet only a few specific interactions have been identified so far. The crosstalk between proteins and lipids is responsible for crucial cellular functions, such as membrane functionality, lipid distribution, cell signalling or membrane trafficking. The implication of specific SL-binding (host) proteins for viral propagation has not been assessed so far, neither if certain viral proteins might interact with distinctive SL lipid classes or species to the virus' benefit. In this study, the focus was set on the investigation of putative interactions between SLs and viral TM protein of different IAV subtypes (see **section 3.1**). Therefore, a pac-lipid precursor was used to allow biorthogonal labelling of cellular SLs (Figure 3.1)[250]. Further, a proteomic approach, specifically aimed to identify SL-binding proteins of IAV infected cells, was conducted to screen for host proteins which might be implicated in IAV infection (see **section 3.2**). Finally, it was determined if the acyl chain length of SLs is decisive for IAV propagation.

In summary, this study was supposed to shed light on the contribution of SLs to the IAV life cycle, aiming to elucidate possible SL-binding host targets and SL species which are exploited by the virus, as well as the probability that viral TM proteins might directly interact with SLs in order to initiate viral morphogenesis. The perspective was to subsequently identify SL-binding motifs in host proteins and viral proteins crucial for the IAV replication cycle, which might serve as potential antiviral drug targets in combating IAV infection.

3 Results

3.1 Validation of protein-sphingolipid interactions of Influenza A transmembrane proteins

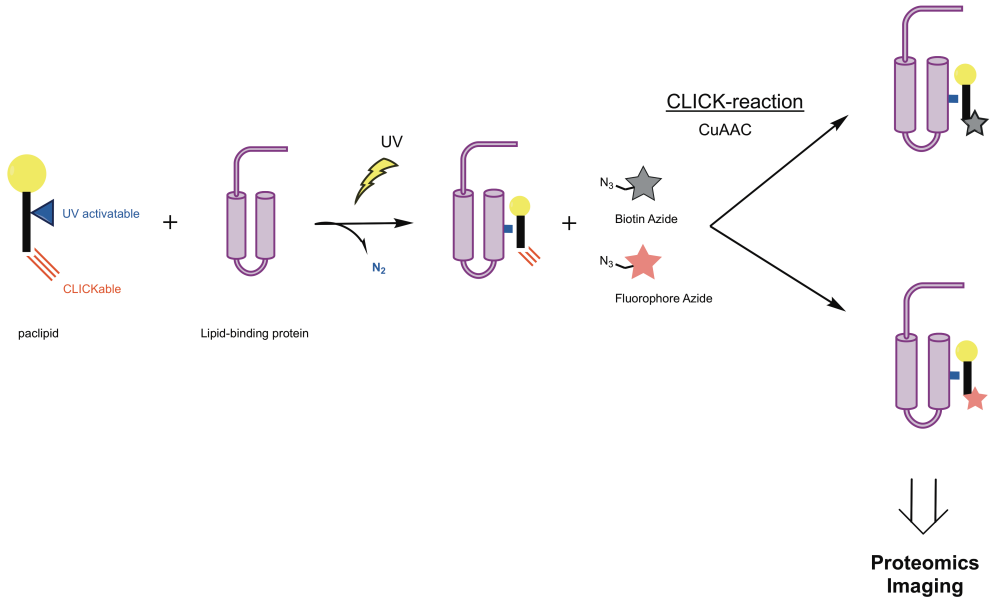

Figure 3.1: Exploring protein-lipid interactions with the use of bifunctional lipids (as reviewed in[248]).

Photoactivatable **a**nd **c**lickable lipids (**pac**lipids) consist of 1.) an UV activatable diazirine group which allows the covalent binding of the respective lipid to soluble or membrane-embedded (tagged or native) proteins in near vicinity, and 2.) of a clickable terminal alkyne residue in order to add a reporter tag. The latter is attached via "CLICK" reaction (here: copper (I)-catalysed azide alkyne cycloaddition (CuAAC)) and can be either an affinity tag (in this work: biotin-azide) or a fluorophore (in this work: Alexa647-azide for Western blot or 3-azido-7-hydroxycoumarin for TLC). Downstream applications of biorthogonal labelling include proteomics or imaging of lipid-bound protein complexes after immunoblotting. Note that the addition of Alexa647 requires tagging of proteins to enable purification of protein-lipid complexes.

The goal was to initially design FLAG-tagged versions of the Influenza A virus (IAV) transmembrane (TM) proteins HA, NA and M2 from subtype A/Hong Kong/1/1968 (H3N2) and A/Regensburg/D6/2009 (H1N1), retrieved from reverse genetics systems[251]. Tagging was conducted in order to allow identification and immunoprecipitation of IAV TM domain (TMD) proteins after transient transfection in HeLa and A549 cells, the latter serving as the closer approach to *in vivo* infection due to their resemblance to human alveolar basal epithelial cells[252].

The comparison of IAV strains H3N2 and H1N1, both subtypes mainly found in human clinical isolates[253], should be done in order to investigate if there is a subtype-dependent difference in the (extent of) interaction with sphingolipids (SLs) and if, as a consequence, this difference determines the degree of pathogenicity and potentially viral morphology. Protein-SL interaction should be monitored by

metabolic labelling of cells with **p**hotoactivatable- **a**nd **c**lickable sphingosine (**pac**Sph)[250].

Previous studies showed subtype-specific recruitment kinetics of truncated NA variants to the cell surface which was related to the presence (or absence) of a SL binding motif within the TMD[116]. Initially, experiments from the latter research finding were partly repeated and the corresponding constructs used for pacSph-labelling experiments.

3.1.1 Transient expression of NA-EGFP-FLAG fusion proteins in mammalian cells

It has been suggested that a putative SL-binding motif in the TMD consensus sequence of NA subtype 1 (NA1) might be responsible for an accelerated cell-surface localisation compared to NA subtype 2 (NA2) and subtype 8 (NA8)[116]. Cell-surface localisation of all three NA variants, only consisting of the cytoplasmic tail (CT) and TMD[116], was repeatedly investigated via cell-surface biotinylation assays in HeLa cells, with Asialoglycoprotein receptor 1 (Asgr1) as positive control for plasma membrane (PM) targeting[107].

As reported, NA2 was less efficient transported to the cell surface than NA1, while NA8 was hardly detectable at the PM (Figure 3.2A-B). In comparison to 48 h transfection, NA1 also showed a clear increase in protein abundance at the PM after 72 h transfection, in contrast to NA2 and NA8 (Figure 3.2C).

It was further investigated whether the difference in PM targeting might be due to a difference in putative SL-binding of the NA CT-TMD variants. To enable labelling with pacSph, HeLa∆S1PL cells were used. S1PL catalyses the irreversible conversion of sphingosine-1-phosphate (S1P), a metabolic product of sphingosine, to hexadecanal[55]. Thus, the photoactivatable and click functionality of pac-sphingosine are incorporated into glycerophospholipids (GPLs), such as phosphatidylcholine (PC), in wild type (WT) cells. A knock-out (KO) of *SGPL1* prevents the sphingolipid-glycerolipid metabolic link and protein interaction with (pac)sphingolipids (pacSLs) can be monitored (see **section 3.2.1**, Figure 3.7)[254]. In an initial experimental approach, pacSph-labelled cells were subjected to Alexa647-click reaction (CLICK) after UV-irradiation (see Figure 3.1) and FLAG-tagged proteins were enriched via anti-FLAG beads. The positive control for SL-binding, p24[106], showed a

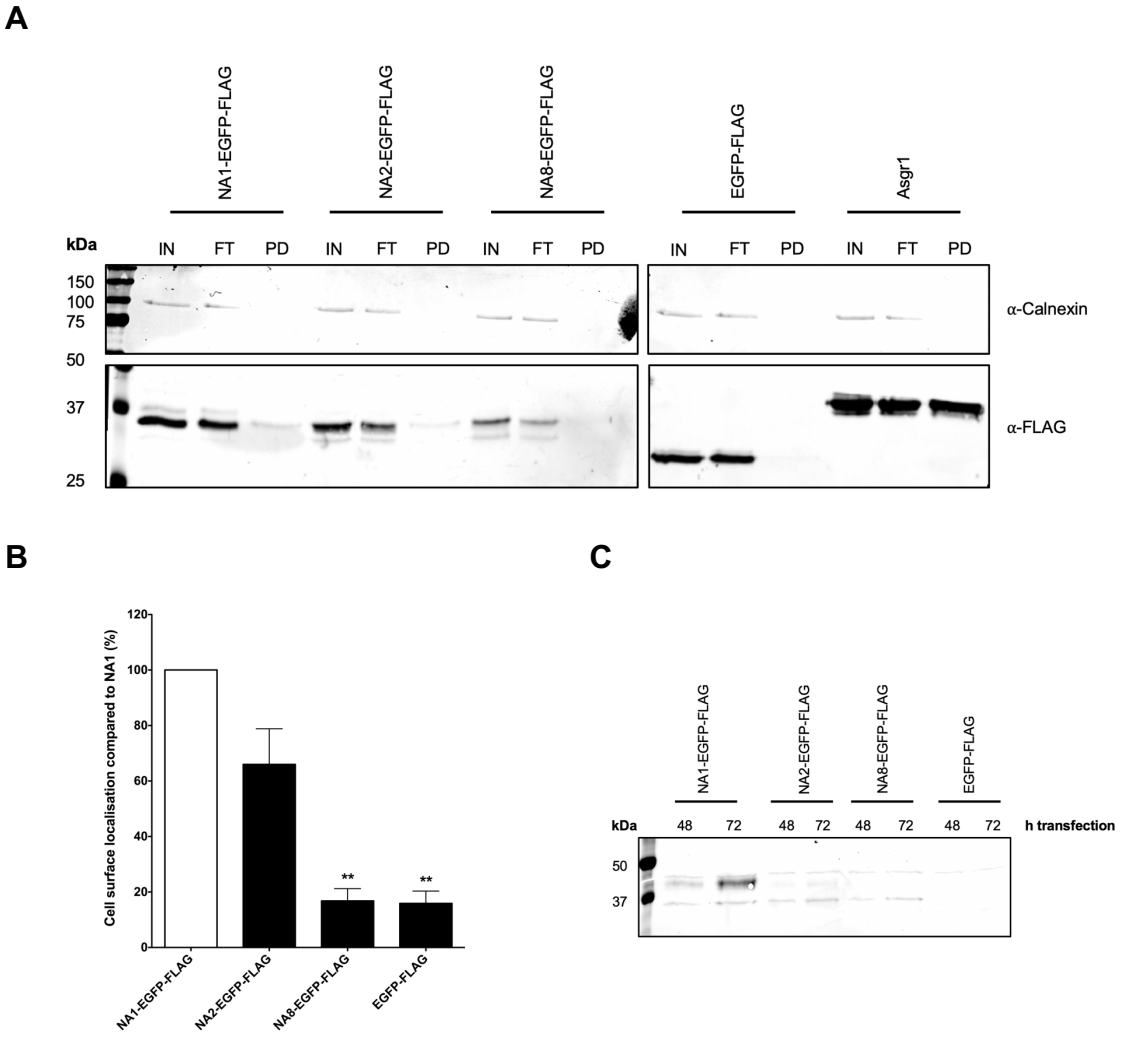

Figure 3.2: Cell-surface biotinylation assay with pEGFP-NA constructs[116].

HeLa cells were transfected with 1.1 µg of plasmid DNA (pDNA) in a 6-well plate. (A-B) Cell surface localisation of NA-EGFP-FLAG[116] variants and EGFP only was determined relative to NA1-EGFP-FLAG-transfected cells after 48 h transfection. IN, input (5%); FT, flow-through (5%); PD, Pulldown (50%). Data represents the mean ±SEM of three independent experiments; ONE-way ANOVA and Dunnett's multiple comparison test performed. (C) Cell-surface localisation was compared after 48 and 72 h transfection (PD only).

strong overlap of the FLAG signal and Alexa647-clicked pacSph metabolites in the pulldown (PD), but this overlap was also observed for the negative control Asgr1. A strong Alexa647 signal for NA1 and NA2 was detected at respective running heights; however, the FLAG signal at that height was blurred, hence it was difficult to calculate the overlap of both (Figure 3.3A). Thus, in a second experiment, the amount of pacSph was lowered to reduce unspecific labelling (see **section 4.1**) and a non-irradiated control was included. Furthermore, cells were clicked with biotin and enriched via NeutrAvidin beads (Figure 3.1) to pull down only putative paclipid-interacting proteins[250]. The PD efficiency of each protein (as a result of potential interaction with pacSph-metabolites) was defined as the ratio of protein

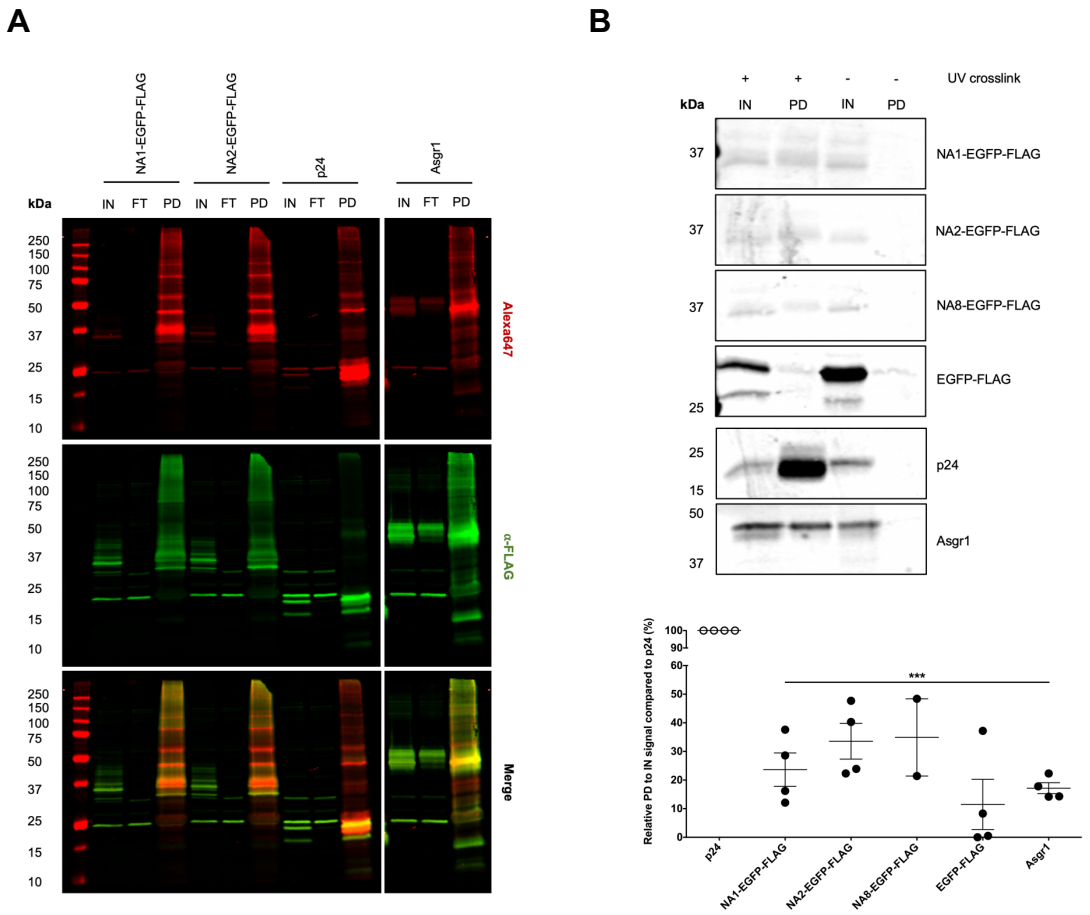

Figure 3.3: pacSph-labelling of pEGFP-NA1/NA2 transfected HeLaΔS1PL cells and subsequent Alexa647-CLICK.

(A) HeLaΔS1PL cells were transfected with 1.1 µg pDNA for 48 h. Prior UV-crosslink, cells were pulsed for 4 h with 6 µM pacSph[254] and afterwards subjected to Alexa647-CLICK and enrichment with anti-FLAG beads. 25 kDa band= unspecific background of FLAG antibody. IN, input (10%); FT, flow-through (10%); PD, Pulldown (all); n=1. (B) Cells were labelled with only 3 µM pacSph and cell lysates clicked with biotin followed by subsequent enrichment of lipid-protein complexes via NeutrAvidin beads. The PD efficiency (as a result of interaction with pacSph-metabolites) of each protein is defined as the relative ratio of PD/input signal. Positive control= p24[106], negative control= Asgr1[106]. IN, input (10%); PD, Pulldown (all). Shown: mean, ± SEM, each dot represents one experiment; ONE-way ANOVA and Dunnett's multiple comparison test performed.

signal in the PD versus input sample, instead of calculating the ratio of Alexa647/FLAG signal. No protein signal was observed in the PD of non-irradiated samples (Figure 3.3B, upper panel). PD efficiency in UV-treated samples was calculated for each construct relative to p24 (Figure 3.3B, lower panel). Strikingly, PD efficiencies were significantly lower for all overexpressed proteins compared to the positive control. Moreover, Asgr1, described as a non-SL binding protein[106,107,250], showed a PD efficiency of ≈20%.

The mean PD efficiency of NA CT-TMD constructs was between ≈25-30% and in the order NA8>NA2>NA1, while for the efficiency of cell-surface targeting a reversed order with NA1>NA2>NA8 was observed (Figure 3.2B, as also reported previously[116]).

3.1.2 Tagging of viral full-length TMD proteins

Recent findings by Tafesse *et al*. suggested that the sphingomyelin (SM) biosynthetic pathway plays a crucial role in cell surface localization of HA and NA[115]. These proteins, together with the third viral TM protein M2, are crucial for the budding process of IAV[160]. In order to elucidate the role of SLs in the life cycle of IAV, the goal was to generate full-length FLAG-tagged variants of the TM proteins HA, NA and M2 from two clinical important IAV strain subtypes[253], namely Influenza A/Hong Kong/1/68 (H3N2, HK68) and Influenza A/Regensburg/D6/2009 (H1N1, RD6), and to investigate their putative SL-binding potential as well as possible implications of SL-binding for viral propagation in HeLa and A549 cells.

First, full-length TM proteins of HK68 were cloned into the pEGFP vector to enable GFP- and FLAG-based detection[116]. FLAG- and GFP-based detection was only possible for M2, although protein expression of native HA3 could be observed (Figure 3.4, immunoblotting against NA2 not performed), suggesting that EGFP-FLAG is not accessible to immunodetection in tagged HA3 and probably also tagged NA2.

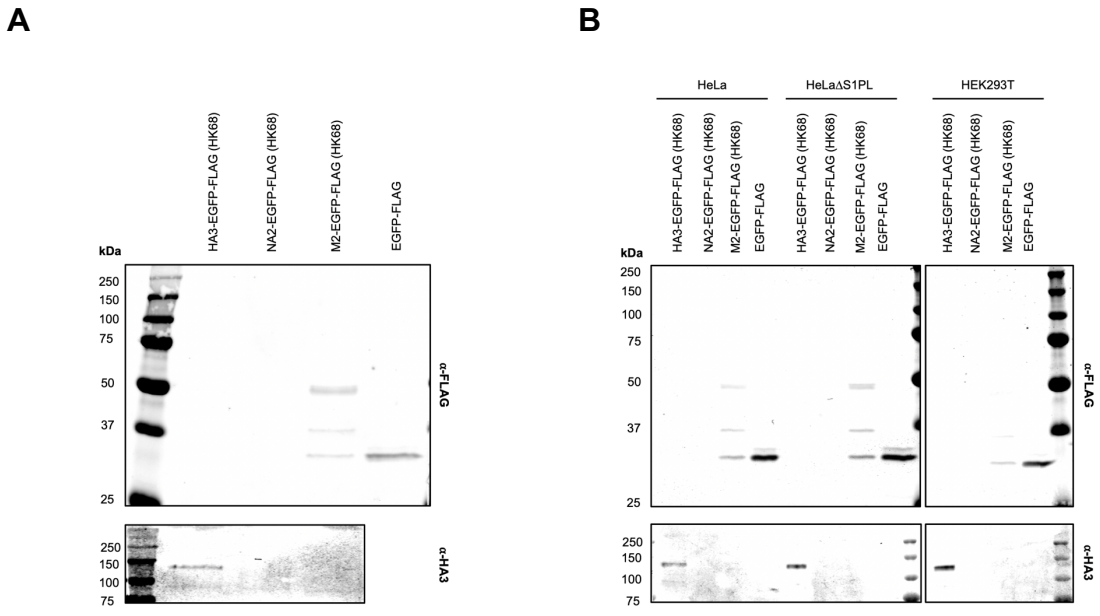

Figure 3.4: Recombinant expression of pEGFP-HA, -NA and -M2 from IAV HK68 strain in several cell lines.

(A) HeLa cells were transfected with 1.1 µg pDNA in a 6-well plate for 24 h and 18% of post-nuclear supernatant (PNS) was applied on SDS-PAGE. (B) Protein expression was compared in HeLa, HeLaΔS1PL and HEK293T cells (1.1 µg pDNA, 24 h transfection, 18% PNS loaded). Both blots were subjected to anti-FLAG/GFP immunoblotting. Anti-GFP blot not shown. Theoretical molecular weight (kDa): HA3= 94.58, NA2= 83.39, M2= 44.45 (calculated via ExPASy).

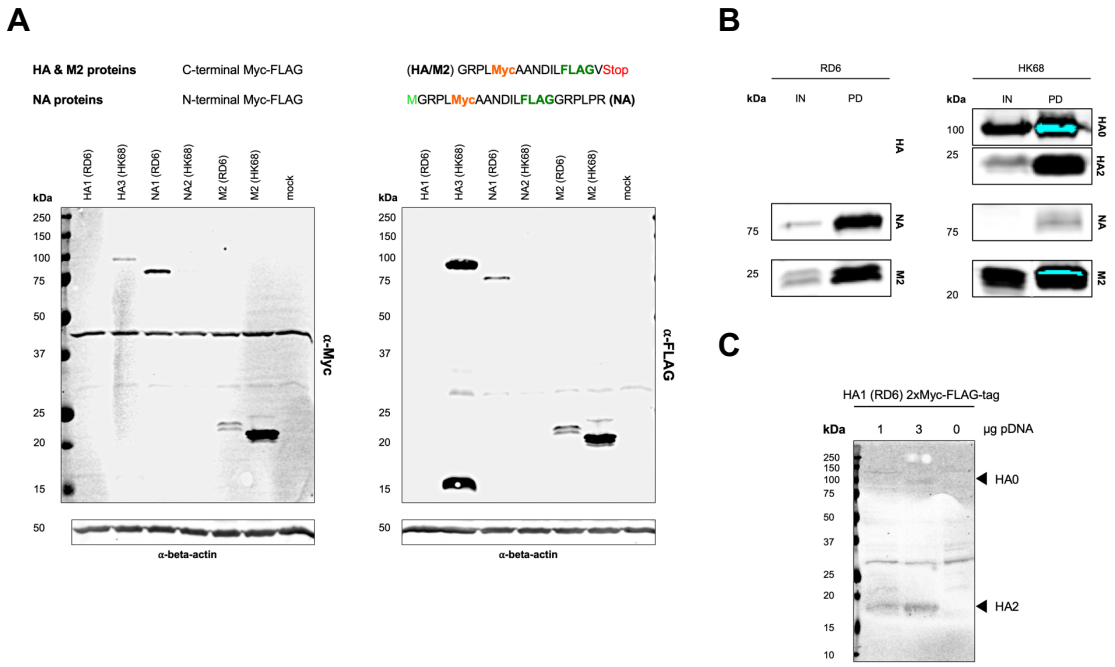

Figure 3.5: Cloning of viral transmembrane proteins HA, NA and M2 into the pCMV vector with a FLAG- and Myc tag.

(A) The expression of tagged viral proteins was tested in HeLa cells (43 h transfection, 12% of PNS loaded, collected from a 6-well plate) via anti-Myc and anti-FLAG immunoblotting. HA constructs were transfected with 1 µg pDNA, M2 encoding vectors with 0.25 µg pDNA and *NA* gene carrying plasmids with 3 µg pDNA. (B) HeLa cells were transfected under the same conditions (except for pCMV-HA1-RD6: 3 µg pDNA used for transfection) and cell lysates subjected to anti-FLAG IP. All viral proteins could be enriched with this method except for HA1 from RD6. To underline the difference in protein expression, Western blots were scanned with the same signal intensity. IN, input (10%); PD, pulldown from IP (all). (C) In order to improve FLAG-based detection of HA1, a double Myc-FLAG-tag was added to its C-terminus (48 h transfection, 12% of PNS from a 6-well plate loaded, anti-FLAG Western blot). Theoretical molecular weight (kDa): HA1 (RD6)= 66.52, HA3 (HK68)= 66.69, NA1 (RD6)= 55.6, NA2 (HK68)= 56.2, M2 (RD6)= 14.32, M2 (HK68)= 14.49, HA1 (RD6) 2xMyc-FLAG= 70.03 (calculated via ExPASy).

As an alternative approach, full-length HA, NA and M2 of HK68 and RD6 were cloned into another vector (pCMV6) without (E)GFP and designed to tag proteins with a Myc-FLAG tag at the C-terminus[254]. Viral proteins should be tagged at the cytoplasmic domain. HA and M2 were tagged at the C-terminus, as both proteins are type I TM proteins[221,255] (**protein**-Myc-FLAG; Figure 3.5A). In contrast, NA is a type II TM protein[221] and thus the Myc-FLAG tag was re-cloned to enable N-terminal tagging of NA proteins (FLAG-Myc-**protein**; Figure 3.5A). The M2 proteins could be immunodetected via the Myc and FLAG tag. HA3 (HK68) showed a stronger signal via anti-FLAG immunoblotting, NA1 (RD6) a stronger signal via anti-Myc immunoblotting, which is probably related to the length of the linker region between protein and tag (Figure 3.5A). As no protein signal could be detected for HA1 (RD6) and for NA2 (HK68), an immunoprecipitation (IP) experiment was performed to enrich viral proteins via anti-FLAG beads (Figure 3.5B). FLAG-based enrichment of overexpressed, homologous viral TM proteins was markedly

different (Figure 3.5B). As already seen in (A), M2 from IAV HK68 was stronger expressed than M2 from the RD6 strain. In contrast, NA1 from the RD6 strain showed an increased protein signal compared to NA2 from HK68. HA3 protein levels from the latter strain were abundant in cell lysates and IP fractions of transfected Hela cells, but no protein signal could be observed for HA1 (RD6), neither in the input nor after IP. Even after insertion of a second Myc-FLAG tag to the C-terminus of HA1, protein expression of tagged HA1 was very low (Figure 3.5C). Notably, two fragments could be observed for tagged HA proteins in Western blot (indicated as HA0 and HA2, Figure 3.5A-C), which corresponds to newly synthesised HA (HA0, ≈100 kDa) and the C-terminal fragment of host-protease cleaved HA0 (HA2, ≈15 kDa) (see **section 2.3.2**). In *in vivo* infections, cleavage of HA0 into HA1 and HA2 by PM-bound proteases is decisive for infectivity and dissemination of IAV[186].

In summary, tagging and expression of IAV full length proteins was hampered for different reasons, for example

- that the co-expressed EGFP-FLAG protein was apparently not accessible to FLAG- and GFP-targeted antibodies (Figure 3.4)
- the difficulty to adjust expression levels of tagged viral proteins (Figure 3.5, see text)
- it was observed that (over)expression levels of homologous proteins differed (see Figure 3.5A-B)

As a result, no more attempts were made to improve tagging of viral full-length proteins for use in pacSph-labelling experiments. Instead, the focus was set on a SILAC-based proteomic approach with the aim to identify SL-binding host proteins which might be involved in IAV infection (described in **section 3.2**).

3.2 SILAC-based proteomic screen to identify sphingolipid-binding host proteins involved in IAV infection

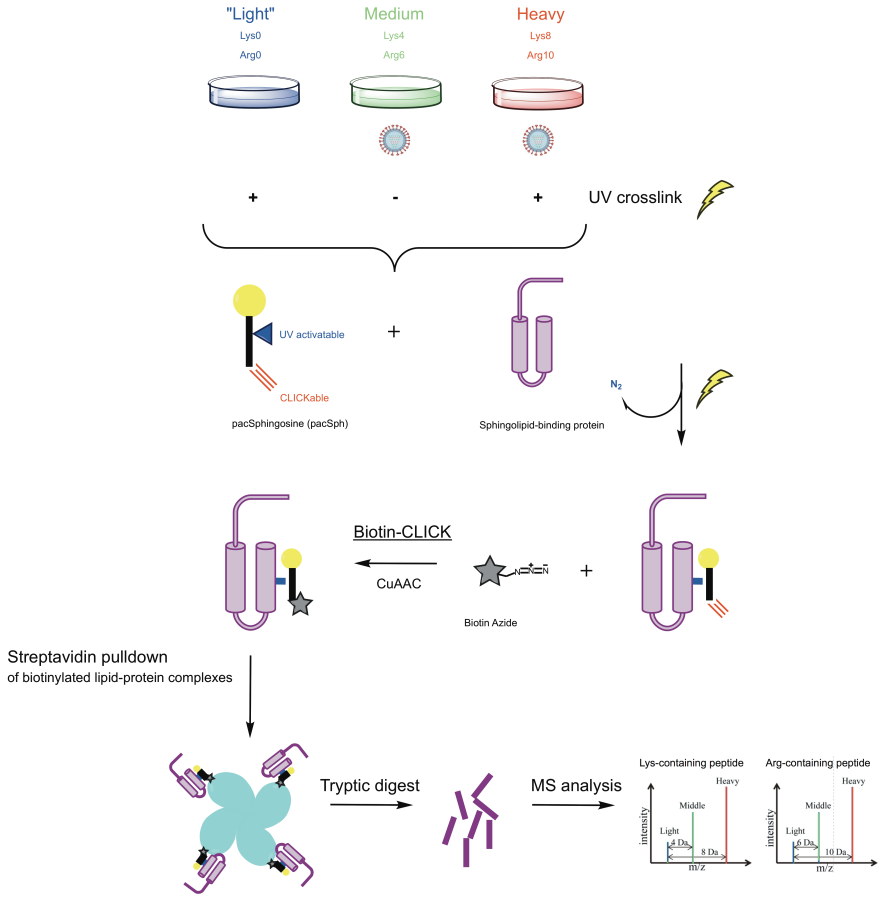

Figure 3.6: SILAC-based proteomic approach to identify putative SL-binding host proteins relevant for IAV infection.

Cells cultured in the presence of isotope labelled amino acids were subjected to 6 h labelling with 3 µM pacSph. Following infection with IAV, lysates of UV-irradiated cells were click-labelled with biotin-azide to allow for affinity enrichment of lipid-crosslinked proteins (see Figure 3.1). To determine the background of non-specific protein pulldown, one infected batch was not subjected to UV-irradiation ("Medium" SILAC, Lys4/Arg6). In addition, total RNA from infected and control cells was extracted to analyse gene transcription via microarray. Samples were collected after 1 h and 12 h post-infection (hpi). In addition, lipidomic analysis was done for PR8-screen II (see **section 3.2.3.3**).

SLs and SL-metabolising enzymes have been reported to play a pivotal role in IAV infection[115,233,245,246,256,257]. The goal of this screen was to identify SL-binding host proteins which might be implicated in IAV "entry" (1 hpi) and "assembly" (12 hpi) events[258] of different IAV subtypes by combining stable isotope labelling by amino acids in cell culture (SILAC) and pacSph-labelling (Figure 3.6). SILAC is a quantitative proteomics approach and a suitable tool to monitor host proteome changes upon virus infection[258,259]. The screen was performed in A549 cells, which resemble alveolar type II (ATII) pneumocytes and are hence a prominent cell model to study respiratory viruses[260]. Initial downstream experiments should include to

validate SL-binding of protein hits[250] and to evaluate their impact on IAV infection via transient knock-downs.

3.2.1 Characterization of the *SGPL1* KO in A549 cells

To monitor protein-SL interaction, first a CRISPR/Cas9-*SGPL1* KO (according to Gerl *et al*.[254]) had to be conducted in A549 cells. Two SG*PL1* KO clones were chosen for further characterisation: the A549ΔS1PL S2-6 clone and the A549ΔS1PL S3-10 clone. Importantly, S1PL clones were not mixed as described[254].

Sequencing results showed a length truncation of >90% of the translated S1PL protein in CRISPR-KO cells compared to the full-length WT protein (Table 3.1). Yet, no obvious impairment of cell viability was observed (see **section 7**, Figure 7.1, left panel). Metabolic fate of pacSph was analysed via thin layer chromatography (TLC) (S2-6 clone shown, Figure 3.7)[250,254]. A549ΔS1PL cells were labelled with pacSph and subjected to CLICK-reaction with coumarin-azide (Figure 3.1) after lipid extraction. In A549 WT cells, pacSph was found to be incorporated into glycerophospholipids (GPLs), illustrated by a strong labelling of PC, the bulk lipid of membranes and the most dominant GPL class[6]. In contrast, the PC band is absent in *SGPL1*-deficient S2-6 clone cells as the KO prevents the link between SL- and glycerolipid metabolism. As a result, functional pac-groups are not incorporated into PC and other glycerolipids (see **section 3.1.1**) (Figure 3.7A)[250]. The same was observed for the A549ΔS1PL S3-10 clone (data not shown). S1PL-deficiency will hence refer to the functional KO of the S1PL enzyme.

Table 3.1: Amino acid sequence of A549 SGPL1 KO clones.

Genomic DNA of A549 WT cells and *SGPL1* KO clones was isolated and processed as described in Gerl *et al*., 2016[254]. Yellow indicates amino acids (AA) which are similar to the WT, beginning from the translation start (methionine, bold). The full-length human S1PL protein is 569 AAs long (UniProt). TM= transmembrane.

	Amino acid sequence
A549ΔS1PL S2-6 clone	**M**PSTDLLMLKAFALLRDFGSILHKSQELCKWTLHQVSTOP (lumenal domain)
A549ΔS1PL S3-10 clone	**M**PSTDLLMLKAFEPYLEILEVYSTKAKNYVNGHCTKYEP-WQLIAWSVRVDPADSLGISTOP (lumenal & TM domain)

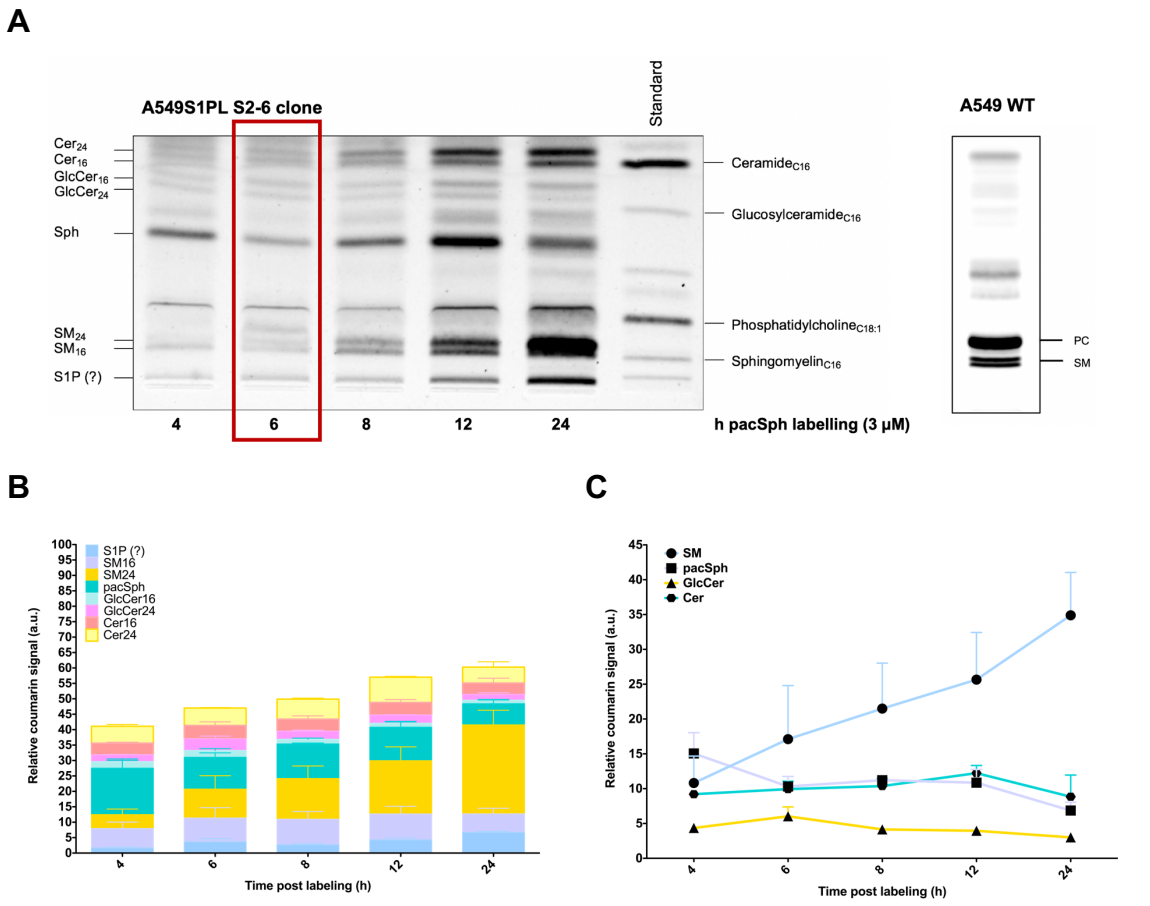

Figure 3.7: Metabolic labelling of A549ΔS1PL (S2-6 clone) cells with pacSph.

(A) A549ΔS1PL cells were labelled with 3 µM pacSph and samples collected at indicated times followed by lipid extraction. Metabolites of pacSph were clicked with coumarin-azide to allow visualization. Different SL-classes (and species) were annotated according to[250,254](upper panel, left). The red frame indicates the labelling time chosen for SILAC proteomic and downstream experiments. For comparison, A549 WT cells were labelled for 6 h with 3 µM pacSph and samples prepared accordingly (upper panel, right). (B) The relative coumarin signal of each assignable band was calculated relative to the total coumarin signal for each time point. The lowest band could be S(ph or pg)-1-P; however, this was not further verified. Shown: mean, ±SEM; n=3. Cer= ceramide, GlcCer= Glucosylceramide, Sph= sphingosine, SM= sphingomyelin, S1P= sphingosine/sphinganine-1-phosphate, PC= phosphatidylcholine. The number indicates the length of the attached fatty acyl chain (=species). Note: pacSph is mostly incorporated into GlcCer, only in trace amounts into GalCer (see **section 2.2**, personal communication D. Ostkotte, Brügger lab), both commonly referred to as hexosylceramide (HexCer, as annotated in[254]). Hence, in the following, the coumarin signal at the height of the glucosylceramide$_{C16}$ standard will be exclusively annotated as GlcCer (as in[250]).

In general, the total amounts of pacSph-incorporated SLs (pac-SLs) increased over time (Figure 3.7B). More specifically, the relative amount of pac-sphingomyelin (pac-SM) constantly increased, while the presence of pacSph-containing ceramide (Cer) and glucosylceramide (GlcCer) rather decreased at later time points (Figure 3.7C). The amount of free pacSph decreased due to its metabolisation[254], especially between 4-6 h and 12-24 h labelling. Furthermore, at later time points, the incorporation of pacSph into SL species with an acyl chain length (designated as “C”) of 24 carbon atoms (C24) was elevated compared to C16 species (illustrated by SM) (Figure 3.7B). At 6 h labelling with 3 µM pacSph, the incorporation of pacSph into both SL species was more or less similar (Figure 3.7A, red

frame, and Figure 3.7B). Hence, all SILAC proteomic and downstream experiments involving pacSph-labelling were performed under these conditions. The amount of fed pacSph (3 µM) was kept constant throughout all experiments because it was observed that varying molar concentrations of fed pacSph affect its turnover (see **section 7**, **Error! Reference source not found.**).
In addition, in order to capture protein-SL interactions within all cellular compartments, cells were kept in pacSph-containing medium over the desired labelling time since it was reported that pulse-chase experiments result in accumulation of pacSph-derivatives in specific subcellular locations[250].

Next, the lipidomes of A549 WT and both *SGPL1* KO clones were analysed. The lipid class profile of *SGPL1* KO clones showed, compared to the A549 WT, a slight

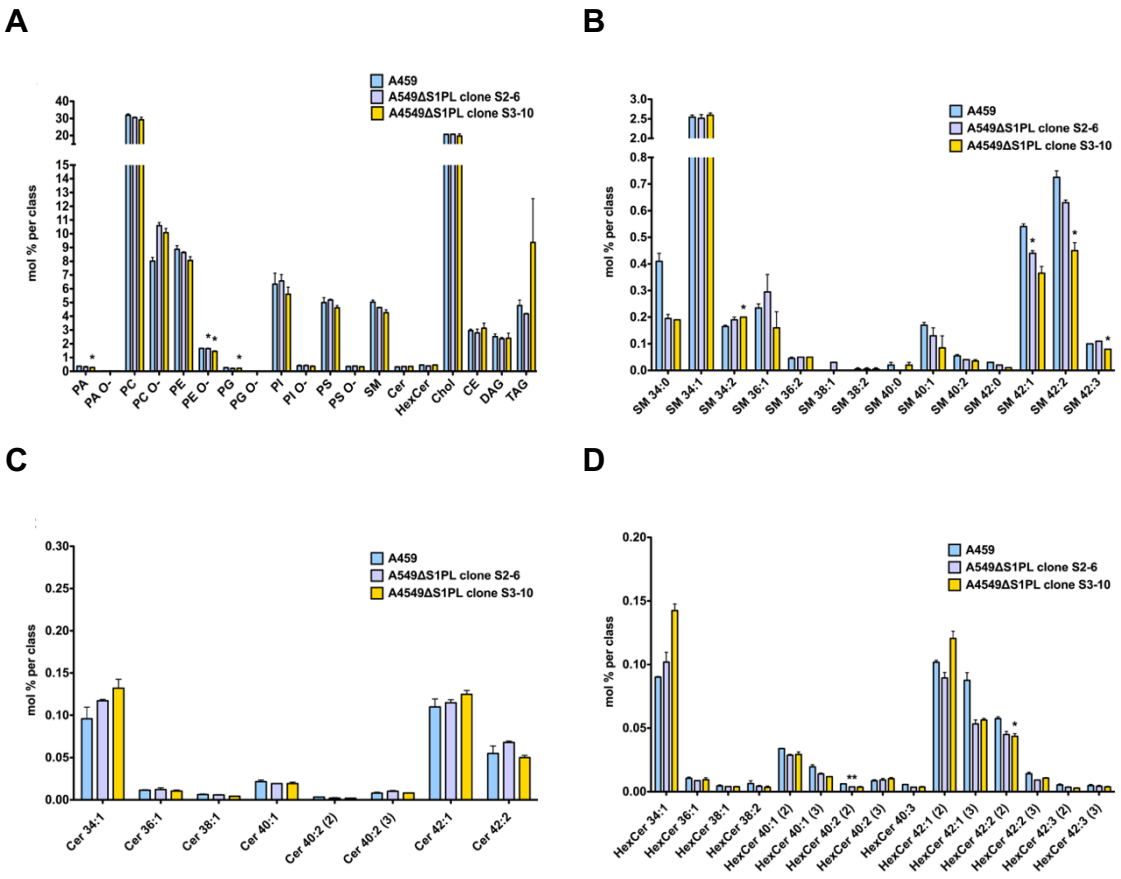

Figure 3.8: Lipidomics of A549 WT cells versus SGPL1 KO clones.

(A) Lipid composition of A549 WT and *SGPL1* KO cells. SL species are shown separately for the SL classes SM (B), Cer (C) and HexCer (D). Importantly, HexCer can be either Glc- or GalCer (see **section 2.2**). Prior the colon is the total carbon (C) number. The length of the fatty acyl chain is calculated by subtraction of 18 C atoms, which is the sphingoid backbone (either sphinganine, d18:0, or sphingosine, d18:1). The number after the colon indicates the number of double bonds, the number in brackets the amount of OH groups (hydroxylation). Data represents the mean ± SEM of three independent experiments; two-tailed, unpaired *t* test performed (A549 WT vs. *SGPL1* KO clone cells). Data can be obtained from https://lipidomicsheidelberg.shinyapps.io/id42_ghi3ohugi43/. Abbreviations: see **section 2.1.1.**, "O-"= ether. Lipidomic samples prepared and data provided by I. Leibrecht and C. Lüchtenborg, Brügger lab.

increase in ether PC (PC O-) (Figure 3.8A). TAG was almost 2-fold enriched in the S3-10 *SGPL1* KO, yet with a high SEM variation. Regarding the SL class profile in WT and KO cells, it was observed that total SM levels were not markedly lower in S1PL-deficient cells. Notably, SM C16:0 (SM 34:0) level were 50% reduced in KO compared to WT cells (Figure 3.8B). Moreover, SM C24:1 and C24:2 (SM 42:1 and 42:2) species levels were decreased in A549ΔS1PL cells. A slight decrease of certain HexCer C24 species (HexCer 42:1 (3) and HexCer 42:2 (2)) was also observed (Figure 3.8D). In addition, the cellular amounts of sphingoid bases in A549 WT and *SGPL1* KO cells was investigated[58]. In HeLa cells, the deficiency of *SGPL1* led to a significant increase in sphingosine-1-phosphate (Sph-1-P)[254]. Compared to A549 WT cells, the sphingoid base sphingosine (Sph) and Sph-1-P were enriched in *SGPL1* KO cells, while sphinganine (Spg) was less abundant and Spg-1-P only detectable in trace amounts (see **section 7**, Figure 7.4). C1P was not measured, but Cer levels were not significantly altered in A549ΔS1PL clones compared to A549 WT cells (see **section 7,** Figure 7.5).

The infection efficiency in *SGPL1* KO cells and in A549 WT cells was compared in order to determine if generated KOs were suitable to be used in SILAC proteomic experiments (see **section 3.2.2** and **3.2.3**). Cells were infected with either Influenza subtype A/Hong Kong/1/1968 (HK68) or A/Regensburg/D6/2009 (RD6) (S.

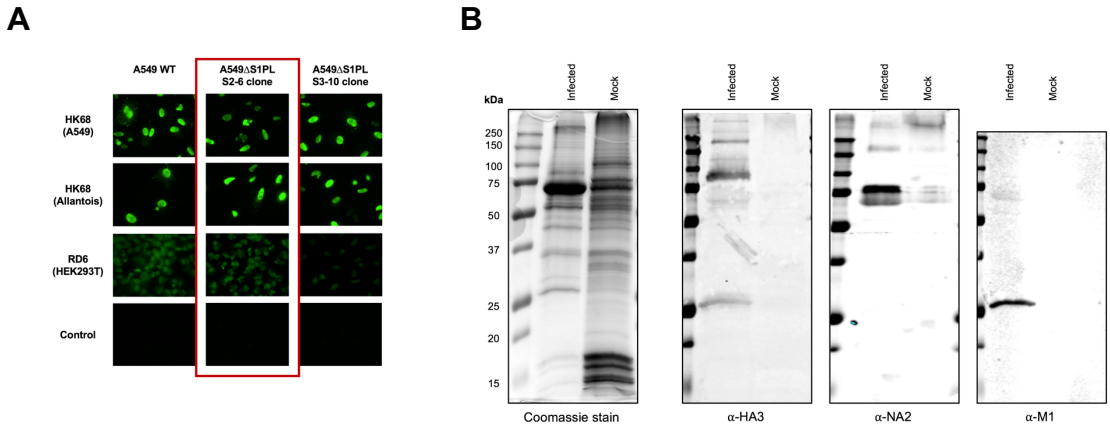

Figure 3.9: Infection of A549 WT and S1PL KO clones with two different IAV strains and virus harvest of HK68 from A549ΔS1PL S2-6 clone cells.

(A) Cells were infected with IAV strains at a MOI of 1 and visualised after 8 hours post-infection (hpi) via anti-Nucleoprotein (NP) stain (60x oil objective; image provided by S. Kummer, Kräusslich lab). The *SGPL1* KO clone chosen for the following SILAC proteomic experiments (see **section 3.2.2** and **3.2.3.1**) is highlighted in red. Brackets indicate the source of the respective virus batch. (B) A549ΔS1PL S2-6 clone cells were infected with the A549-derived HK68 strain (A) at a MOI of 1 in a T75 flask and cell culture supernatants harvested after 6 days by sucrose gradient (S. Kummer, Kräusslich lab). Resuspended pellets were applied to SDS-PAGE (25% loaded). Notably, the thick band in the "infected" sample at ≈75 kDa is BSA.

Kummer, Kräusslich lab; Figure 3.9A). As the A549ΔS1PL S2-6 clone showed an infection rate similar to the WT for the IAV strains HK68 and RD6, it was tested in virion production. To this end, A549ΔS1PL S2-6 clone cells were infected with the IAV HK68 strain (S. Kummer, Kräusslich lab) for 6 days and collected supernatants were analysed via Western blot. Indeed, virion production was observed, however the efficiency of viral particle release was not compared to A549 WT cells (Figure 3.9B).

3.2.2 SILAC-based proteome-wide mapping of protein-sphingolipid interactions in HK68-infected cells

The experiment was carried out as described in **section 3.2**. Non-infected A549ΔS1PL S2-6 clone cells were incubated in "light", infected cells in "heavy" and non-UV irradiated, background control cells in "medium" SILAC (see Figure 3.6).

Proteomic results were obtained from the Proteome Discoverer™ software (provided by S. Föhr, Krijgsveld lab), UniProt human and Influenza A/Hong Kong/1/1968 were taken as reference proteome database.

The infection efficiency of HK68-infected A549ΔS1PL cells in "medium" and "heavy" SILAC media was determined via NP-immunostaining after 12 hpi (Figure 3.10A). Cells in "heavy" SILAC medium showed higher numbers of infected cells than the background control ("medium" SILAC), and for replicate 2 the numbers of infected cells was below 1% in "medium" samples. Another HK68 virus batch was used for replicate 3, which showed the best infectivity (60-70%, Figure 3.10A). To test for incorporation and metabolism of pacSph, cell lysates were clicked with Alexa647 and analysed via in-gel fluorescence (Figure 3.10B; replicate 3 shown). Free pacSph was removed by protein precipitation performed prior the click reaction. Only UV-crosslinked protein lysates showed covalently coupled paclipid-protein conjugates, which were visualised by in-gel fluorescence. No signal was detected for the non-irradiated background control. In general, no significant change between the clicked protein band protein band patterns could be observed between the different conditions (Figure 3.10B).

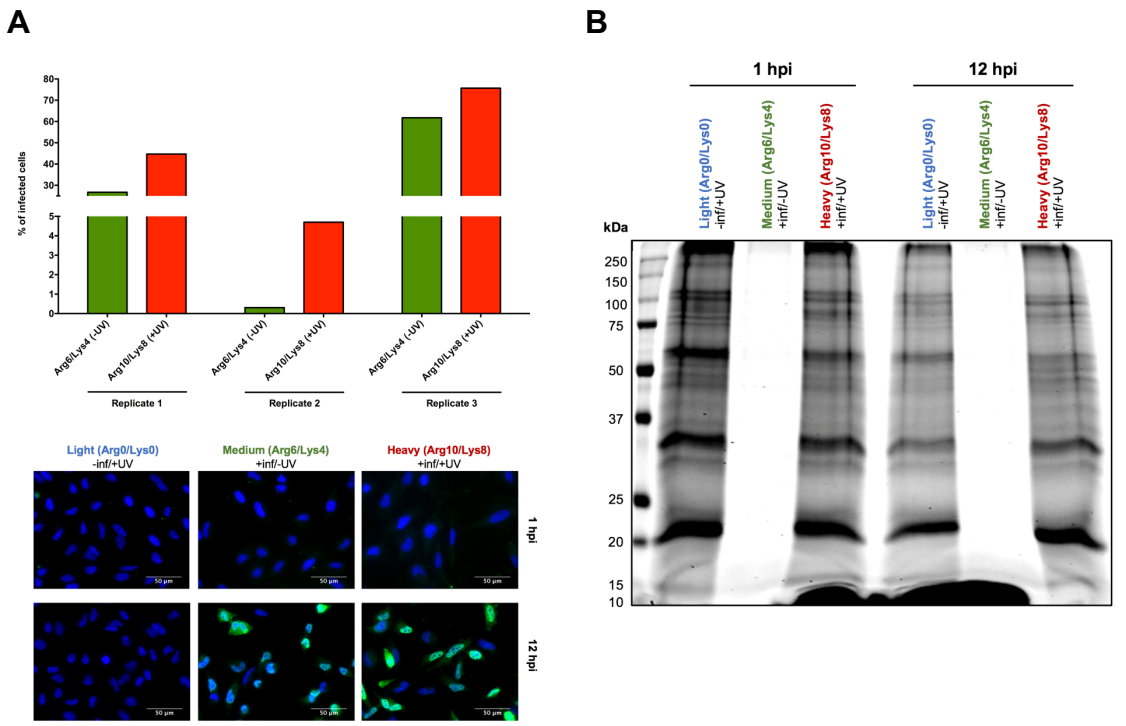

Figure 3.10: Infection and crosslink efficiency of samples subjected to the HK68-SILAC proteomic screen.

A549ΔS1PL S2-6 clone cells were infected with the HK68 strain at a MOI of 1 (S. Kummer, Kräusslich lab). Samples were collected either 1 or 12 hpi. All samples were labelled with 3 µM pacSph for 6 h. For replicate 3 another virus batch was used. (A) The percentage of infected cells was determined after 12 hpi for each replicate by counting the number of NP-positive cells (upper panel, 300 cells/sample counted). Notably, no NP-staining is possible after 1 hpi, probably related to the low abundance of viral proteins at early infection stages[259] (lower panel). A representative image of immunofluorescence staining is shown for replicate 3. NP= green channel, cell nuclei= blue channel, stained with DAPI. Scale bar= 50 µM, 40x magnification. (B) 25 µg of protein lysate was subjected to Alexa647-CLICK and clicked lysates loaded on SDS-PAGE. In-gel fluorescence was recorded with the Li-Cor device (700 nm channel). A representative image of is shown for replicate 3.

Proteomic data was first analysed according to Emmott and Goodfellow[261] in order to determine if the identified protein hits were either enriched in the mock or infected condition at the respective time point after infection. This was done by comparing the mean $\log_2$ protein abundance intensity ratio of infected over mock samples (=SILAC ratio of “heavy”/”light”) for each biological replicate after subtraction of non-specifically enriched proteins (-UV control, “medium”) (Figure 3.11). Only high confidence master and master candidate proteins were considered for analysis (see **section 5.2.6.3**). Mean SILAC ratios varied between replicates, especially within samples collected at 1 hpi (Figure 3.11, left panel). Furthermore, the overlap of all, high confidence master protein hits (mock plus infected) identified at 1 and 12 hpi was calculated (Figure 3.12, upper panel). The overlap of proteins identified in all three biological replicates at either 1 or 12 hpi was very low. Common identified proteins at 1 (=4 proteins) and 12 hpi (=6 proteins) were aligned (Figure 3.12, lower panel). From the 6 proteins used for alignment, 2 were only found in the 1 hpi

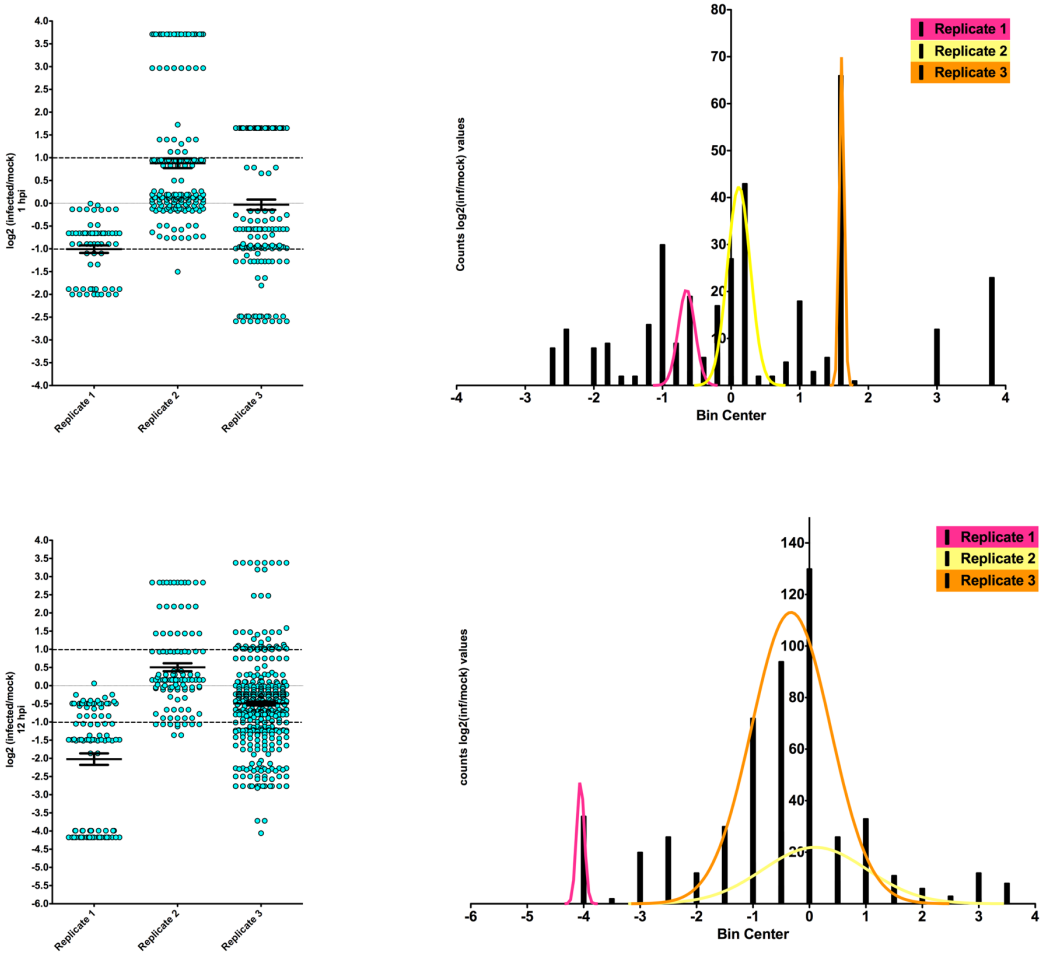

Figure 3.11: Data evaluation of protein hits obtained from the HK68-SILAC screen.

Protein hits were obtained from the Proteome Discoverer™ software (provided by S. Föhr, Krijgsveld lab). After subtraction of "background" proteins (defined as log_2(infected[+UV]/infected[-UV])<-1), the SILAC log_2(infected/mock) ratios of high confidence "master"- and "master protein candidates" were plotted (left panel) and corresponding frequency distribution histograms created (right panel) for each replicate and time point after infection (according to[261]). Shown: mean, ±SEM for protein counts of each biological replicate. Left: dotted lines indicated a SILAC ratio of 1 or -1 (≈2-fold enriched in infected or mock samples). Right: The y-achsis of frequency distribution histograms depict the count of log_2(infected/mock) ratios.

sample and 4 unique to the 12 hpi sample (Figure 3.12, lower panel and Table 3.2). However, none of the protein hits showed a clear increase or decrease of (putative) SL-binding upon infection.

As SILAC ratios for individual proteins differed significantly (Figure 3.11) and the overlap of protein hits among biological replicates was very low (Figure 3.12), no candidate validation was performed for the corresponding screen. Notably, since replicate 3 showed the highest infection efficiency (Figure 3.10A) and the highest amount of high confidence master protein annotations (Figure 3.12), a protein

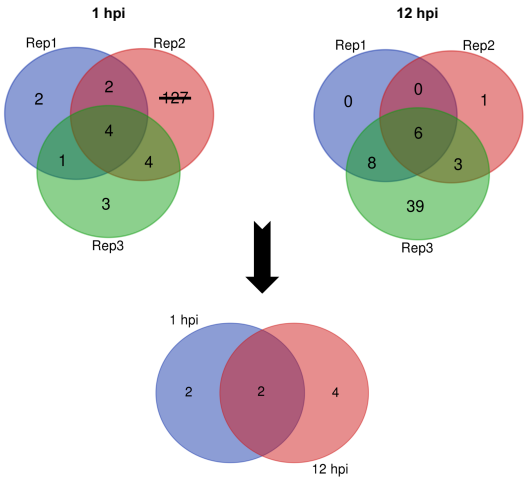

Figure 3.12: Protein alignment (Venn diagram) of protein hits from the HK68-SI-LAC screen.

Venn diagram analysis was conducted to determine the overlap of proteins identified in each biological replicate, for each time point after infection (upper panel). Afterwards, common proteins found in all three replicates/hpi were aligned (lower panel). Only proteins with a high confidence- and master protein annotation were considered (http://bioinformatics.psb.ugent.be/cgi-bin/liste/Venn/calculate_venn.htpl). Note that for Replicate 2 (Rep2)/1hpi, the annotation master- or master protein candidate was lacking.

alignment of high confidence master proteins identified 1 and 12 hpi was done (see **section 7**, Table 7.3), but will not be further discussed.

Table 3.2: Unique and common proteins identified 1 & 12hpi.

For details see text.

Sample	Nr. of proteins	Proteins
1 hpi & 12 hpi	2	Histone H4 (HIST1H4) Pyruvate carboxylase, mitochondrial (PC)
1 hpi	3	Prelamin-A/C (LMNA) Heterogeneous nuclear ribonucleoproteins A2/B1 (HNRNPA2B1) Actin, cytoplasmic 1 (ACTB)
12 hpi	4	Histone H2B (HIST2H2BF) Caveolin-1 (CAV1) Isoform 2 of Histone H2A.J (H2AFJ) Heterogeneous nuclear ribonucleoprotein A1 (HNRNPA1)

In the following, proteomic experiments were performed with the Influenza A/Puerto Rico/8/1934 (PR8) strain, as several genomic[262] and especially proteomic screens had already been conducted with this IAV strain[258,263,264]. Originally, the screen should be also performed with (H1N1) RD6-infected A549ΔS1PL cells (Figure 3.9A). However, the RD6 strain displayed a low infectivity in subsequent experiments (data not shown).

3.2.3 SILAC-based proteome-wide mapping of protein-sphingolipid interactions in PR8-infected cells

3.2.3.1 PR8 screen I

The PR8-SILAC screen I was performed analogous to the HK68-screen (see also Figure 3.6), with the exception that the “light” (-inf/+UV) and “heavy” (+inf/+UV) condition were switched in replicate 3. Proteomic results were obtained from the Proteome Discoverer™ software (provided by S. Föhr, Krijgsveld lab), UniProt human and Influenza A/Puerto Rico/8/1934 were taken as reference proteome database.

The infection rate of infected SILAC samples was determined via NP-immunostaining (Figure 3.13A). The number of infected cells varied among biological replicates (between ≈20-70%) and also between the two infected conditions (“medium” and “heavy”/”light”, Figure 3.13A). For replicate 2 and 3, the number of infected cells counted in the +UV sample was almost 2-fold higher than the number counted for the background control (“medium”). In general, replicate 2 showed the highest infection efficiency (≈50-70%). UV-induced coupling of pac-SLs to proteins was successful as monitored by in gel fluorescence (Figure 3.13B).

MS-analysis of replicate 1 and 2 was performed twice (run 1 and 2, see **section 5.2.6.3**). Proteomic data was analysed as described for the HK68-screen (see **section 3.2.2.**). After subtraction of the background control (“medium”), analysis of data quality[261] of the PR8-I screen revealed that, in contrast to the HK68-SILAC screen, the mean SILAC ratios of $\log_2$(infected/mock) samples were more similar to each other (between 0 and -1) among biological replicates for the 1 and 12 hours post-infection condition (see Figure 3.14 vs. Figure 3.11, left panels). The number of high confidence “master” proteins at 1 and 12 hpi was also markedly higher for each biological replicate in the PR8-I vs. the HK68 SILAC screen (Figure 3.14, right panel vs. Figure 3.12, upper panel), and hence the overlap of proteins of biological replicates collected at different time points after infection. Proteins commonly identified in all biological replicates at 1 or 12 hpi, independent of infection, are shown in Table 7.4 (run 1 and 2, see **section 7**). PR8-infection also had a higher, statistically significant impact on gene expression compared to HK68-infected cells at 12 hpi (see **section 7**, Figure 7.6 and Table 7.1). However, as observed for the HK68 screen, SILAC ratios of $\log_2$(infected/mock) samples varied among

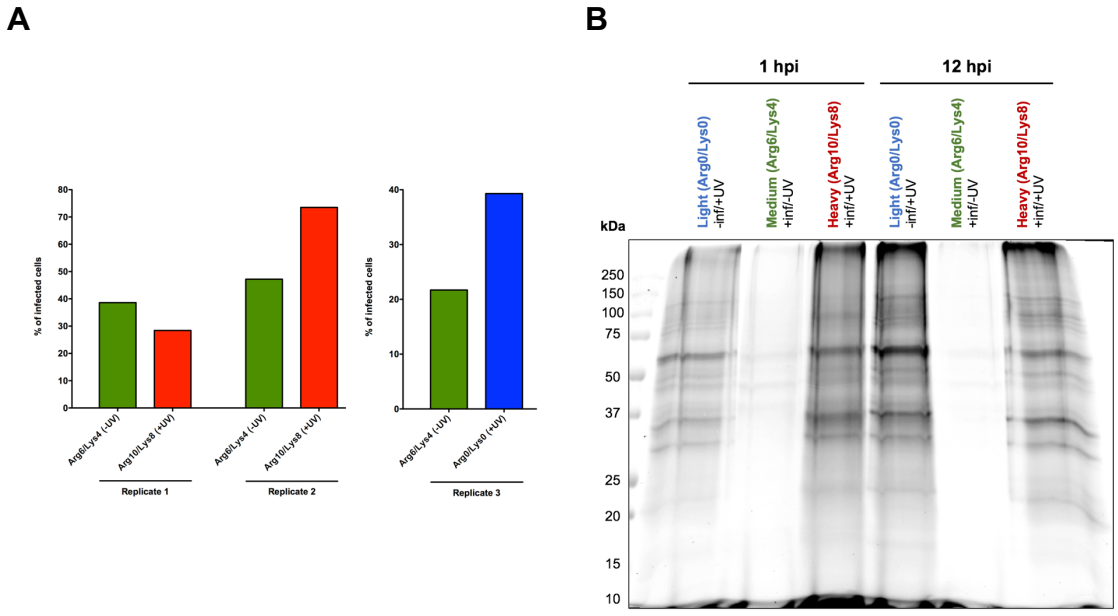

Figure 3.13: Infection and crosslink efficiency of samples subjected to the PR8-SILAC proteomic screen I.

A549ΔS1PL S2-6 clone cells were infected with the IAV PR8 strain at a MOI of 1 (S. Kummer, Kräusslich lab). Samples were collected either 1 or 12 hpi. All samples were labelled with 3 µM pacSph for 6 h. (A) The percentage of infected cells was determined after 12 hpi for each replicate by counting the number of NP-positive cells (300 cells/sample counted). Note that the "light" (mock) and "heavy" (inf) condition were switched for replicate 3. (B) 10 µg of protein lysate was subjected to Alexa647-CLICK and clicked lysates loaded on SDS-PAGE. A representative image of is shown for replicate 2. In-gel fluorescence was recorded with the Li-Cor device (700 nm channel).

replicates for the same protein, and hence statistical evaluation of the data sets was difficult. As a result, protein hits were analysed regarding their occurrence in other influenza-based or pan-viral genomic and proteomic screens. Proteins initially chosen for further validation are depicted in Table 3.3. The corresponding gene expression data is illustrated in **section 7**, Table 7.2).

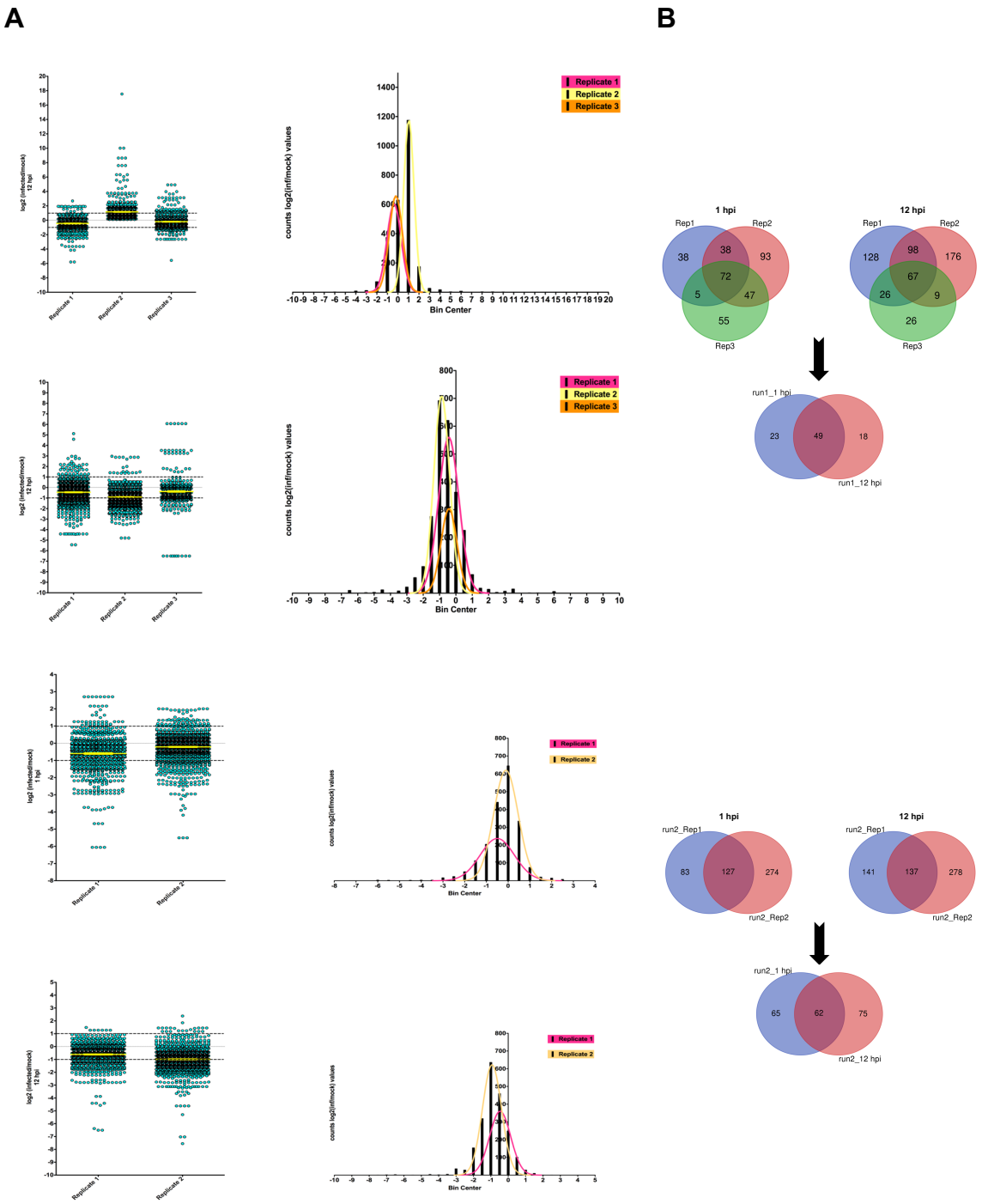

Figure 3.14: Data evaluation of protein hits obtained from the PR8-SILAC screen (run 1 and 2).

(A) Protein hits were obtained from the Proteome Discoverer™ software (provided by S. Föhr, Krijgsveld lab). After subtraction of "background" proteins (defined as $\log_2$(infected[+UV]/infected[-UV])<-1), the SILAC $\log_2$(infected/mock) ratios of high confidence "master"- and "master protein candidates" were plotted (left panel) and corresponding frequency distribution histograms created (right panel) for each replicate and time point after infection (according to[261]). Shown: mean, ±SEM for protein counts of each biological replicate. Left: dotted lines indicated a SILAC ratio of 1 or -1 (≈2-fold enriched in infected or mock samples). Right: The y-achsis of frequency distribution histograms depict the count of $\log_2$(infected/mock) ratios. Datasets of the first (upper panel) and second MS run (lower panel, only replicate 1 and 2) are depicted. (B) Venn diagram analysis was conducted to identify unique and common proteins per biological replicate and time point of harvest after infection. Afterwards, common proteins found in all three replicates/hpi were aligned (indicated by the black arrow). Venn diagrams created via http://bioinformatics.psb.ugent.be/cgi-bin/liste/Venn/calculate_venn.htpl.

.

Table 3.3: Protein candidates obtained from the PR8-I SILAC proteomic screen chosen for further validation.

For details see text. *Information about localisation and function of proteins extracted from UniProt and Human Protein Atlas. AA= Amino acid, PM= plasma membrane, ER= endoplasmic reticulum, VLCFA= very long chain fatty acid, vRNP= viral ribonucleoprotein-complexes, CerS2= ceramide synthase 2, KD= knock-down, HCV= Hepatitis C virus, MEF= mouse embryonic fibroblasts. Most findings regarding implications for IAV life cycle relate to subtype H1N1. Light grey= proteins tested in SL-binding validation assays Figure 3.15, Figure 3.16).

						PR8 screen		SILAC		HK68-screen (Table 7.3)
						Run 1 (hpi)		Run 2 (hpi)		
Accession	**Gene name**	**Localisation***	**Function***	**TMDs**	**Role in (IA) virus infection?**	**1**	**12**	**1**	**12**	
P05556	ITGB1	PM, Endosome, Focal adhesion sites (…)	Cell signalling, involved in a variety of cellular processes; always heterodimer with ITGA subunit; interacts with CD81	1	- Decreased protein abundance in infected A549 cells 16 hpi[265] - Found in viral particles[183] - Decreases gene expression 24hpi in mice lungs[266]i - Entry receptor for: cytomegalovirus/HHV-5, Epstein-Barr virus/HHV-4, mammalian reovirus (UniProt) - ITGA2:ITGB1 heterodimer entry receptor for: human echovirus 1&2, human rotavirus (UniProt) - ITGA5:ITGB1 heterodimer entry receptor for: human parvovirus (UniProt) - ITGA5:ITGB1 heterodimer binds HIV Tat protein[267]	x	x	x	x	
Q15758	SLC1A5	PM	Na^+-dependent amino acid (AA) transporter with a broad substrate specificity; preference for zwitterionic AAs	10	- Increased MHCI peptide presentation in infected HeLa cells[268] - Entry receptor for: feline endogenous virus RD114, Baboon M7 endogenous virus, type D simian retrovirus (UniProt)	x	x	x	x	Replicate 3, 12hpi

P08962	CD63	PM, Lysosome, Endosome, Extracellular/secreted	Activator of cellular signalling cascades, e.g. ITGB1 signalling; belongs to tetraspanin family	4	-	Co-localises with vRNPs in infected HeLa cells[269] - Co-localises with IAV restrictive factor IFITM3 in MDCK cells (together with LAMP1)[270]	x	x				
Q9BW60	ELOVL1	ER	Catalyses the first step in the elongation cycle of VLCFAs; important for C24 SL synthesis, regulated by CerS2[271]	7	-	Fatty acid elongases are crucial for cytomegalovirus infection[272]			x			
Q15629	TRAM1	ER	Required for translocation of secretory proteins across ER, influences glycosylation	8	-	siRNA mediated knock-down (KD) reduces IAV replication in A549 cells[273] - involved in MHCI class molecule dislocation in cytomegalovirus infection[274]	x	x	x			
P19338	NCL	Nucleus	Nucleolar phosphoprotein involved in synthesis and maturation of ribosomes	0	-	IAV binds to cell-surface nucleolin in A549 cells[180] - Interacts with NP protein at early infection stages[182]	x	x	x	x	Replicate 3, 12hpi	
Q96GC9	VMP1	PM, ER, Nucleoli	Involved in cell adhesion, cell death and autophagosome formation; interacts with autophagy protein beclin-1 (BECN1)	7	-	Autophagosome formation is blocked by interaction between BECN1 and IAV M2 or HIV accessory protein Nef[275] - M2-induced restriction of autophagosome-fusion supports filamentous budding [276]	x				Replicate 3, 12hpi	
P11279	LAMP1	PM, Endosome, Lysosome	Lysosome marker, provides selectins with carbohydrate ligands	1	-	NA of IAV subtype H5N1 (but not seasonal H1N1) induces deglycosylation of LAMPs in A549 cells, leading to lysosomal rupture[277] - LAMP1-colocalisation of autophagosome markers Atg8/LC3 is restricted in IAV-infected A549 cells[164]		x				

					- Co-localises with IAV restrictive factor IFITM3 in MDCK cells (together with CD63)[270] - Entry receptor for Lassa virus[278]					
Q14108	SCARB2	Lysosome	Receptor for glucosylceramidase (GBA) targeting	1	- Induces clathrin-mediated endocytosis of HCV[279] - Receptor for enterovirus 71[280]	x				
P60033	CD81	PM	Belongs to tetraspanin family, complexes with integrins (ITGB1) and CD63	2	- CD81 KD decreases IAV replication[273] - Involved in early steps of viral replication[281] - CD81 KD leads to defects in viral fusion/uncoating and budding in A549 cells[282] - Implicated in HIV replication in DCs[283] - Receptor for HCV entry (summarized in [284])	x	x	x		
Q03135	CAV1	PM, Golgi	Scaffolding protein, main component of caveolae (subset of lipid rafts); involved in various cellular processes	1	- Putative cellular interaction partner of IAV needed for viral progression in MDCK cells[285], might bind to M2[286] - Increased protein expression in infected A549 cells[263] - Limits (human) IAV propagation in MEFs	x	x	x	x	12 hpi, detected in all biological replicates (Table 3.2)
P0867	VIM	Cytoskeleton, Nucleus	Class-III intermediate filaments in non-epithelial cells, forms cytoskeleton together with microtubules and actin filaments	0	- IAV infection modifies VIM phosphorylation[287] - Upregulated in cytosolic proteomes upon IAV infection[288] - Plays a role in viral genome release in IAV infected MEFs[289]			x	x	
P07335	ANXA2	Extracellular or secreted	Ca2+-regulated, anionic phospholipid binding protein	0	- Might mediate activation of plasminogen which in turn leads to cleavage of HA and hence pathogenicity in mice; Incorporated into viral particles[290]	x	x	x		

					-	Primary host target during IAV infection in HeLa cells as reflected in the change of MHCI peptide presentation[268]				
P21796	VDAC1	PM, Mitochondria	Voltage-dependent anion channel in outer mitochondrial membrane	19	-	Mediates IAV PB1-F2 induced cell death in A549 cells[291]	x	x	x	Replicate 3, 12hpi

From the list of potential protein candidates, ITGB1, SLC1A5, CD63 and ELOVL1 were further characterised as they play a role in the entry of other viruses (ITGB1, SLC1A5), could indicate the requirement of very long chain SLs for viral propagation (ELOVL1) or might be involved in the transport of vRNPs (CD63) (Table 3.3). Therefore, C-terminal, 3xFLAG-tagged constructs were generated of chosen protein candidates in order to validate SL-binding using pacSph (Figure 3.1) as described[250,254]. To test expression of tagged constructs, HeLaΔS1PL cells were used; in addition, samples were subjected to biotin-CLICK[250] with subsequent enrichment via the biotin-tag.

In SLC1A5 overexpressions, two bands were visible in input and flow-through samples, presumably corresponding to different glycosylated forms[292]. Only the upper band was found enriched in the PD fraction Figure 3.15). In contrast, tagged CD63 and ELOVL1 were significantly pulled down via biotin-clicked pacSLs, comparable with p24. The "negative control" Asgr1 also showed an interaction with pacSLs. FLAG-based ITGB1 detection was not possible.

The experiment was repeated in A549ΔS1PL clone S2-6 cells (Figure 3.16), which were also used for the previous conducted SILAC proteomic experiments. Further, it was decided to investigate SL-interactions of endogenous proteins, since tag-based detection was not possible for ITGB1. The approach might be also closer to *in vivo* conditions. In addition, NCL and TRAM1 were analysed. NCL is reported to interact with NP and described as a novel entry

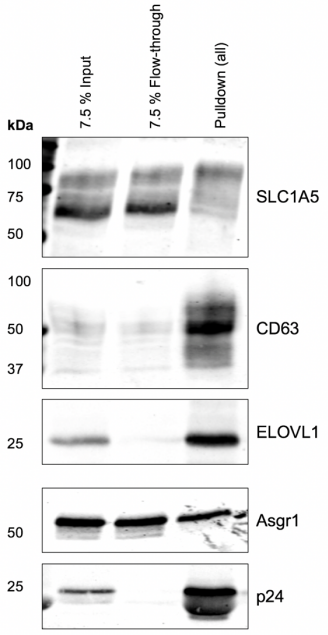

Figure 3.15: SL-binding of transiently expressed FLAG-tagged protein candidates (PR8-I) in HeLaΔS1PL cells.

HeLaΔS1PL cells were transfected with 5 µg pDNA in a 10 cm dish and labelled for 4 h with 3 µM pacSph after 44 h transfection. For biotin-CLICK, 250 µg of membrane fractions were used and clicked samples enriched via NeutrAvidin beads. Overexpressed proteins were detected by anti-FLAG antibody. Experiment was conducted once. Theoretical molecular weight (kDa): SLC1A5= 60.93, CD63= 29.95, 36.79, ELOVL1= 36.79, Asgr1= 37.5, p24= 25.23 (calculated via ExPASy). Note that the apparent molecular weight of ELOVL1 is below the theoretical molecular weight.

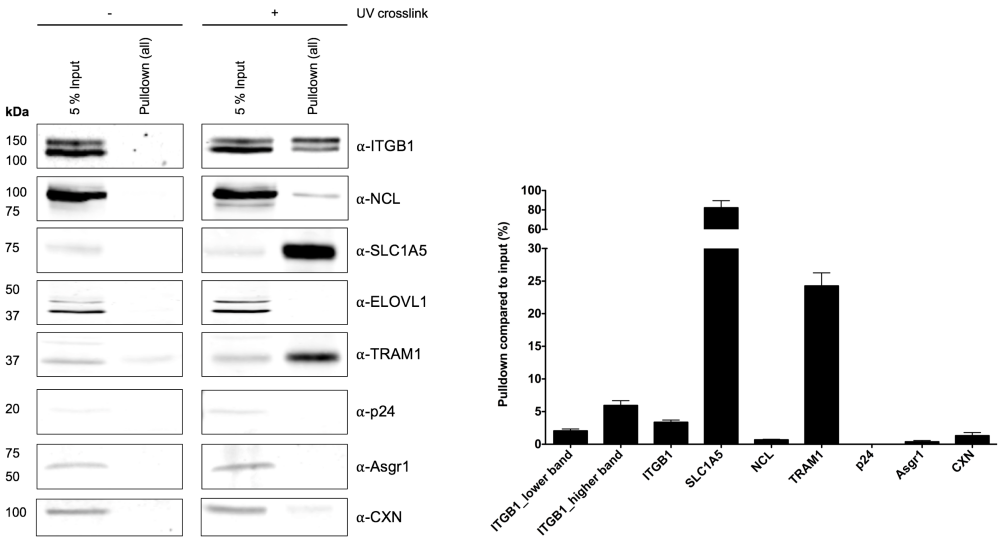

Figure 3.16: Sphingolipid-binding validation of protein candidates (PR8-I) in A549ΔS1PL (clone S2-6) cells.

Two full 10 cm dishes of A549 *SGPL1* KO cells were labelled with 3 µM pacSph for 6 h. Biotin-CLICK was performed with 200 µg protein lysate. Non-irradiated samples were also clicked to determine the background signal for each protein (unspecific PD). The pulldown efficiency was calculated relative to the input signal (%), with additional CXN immunostaining as loading control (since protein levels after CLICK reaction were not re-measured). There was no signal detectable with the antibody against endogenous CD63. Data represents the mean ± SEM of three independent experiments. Theoretical molecular weight (kDa): ITGB1= 66.62, NCL= 76.61, SLC1A5= 56.61, ELOVL1= 32.55, TRAM1= 43.07, p24= 22.76, Asgr1= 33.12, CXN= 67.57 (calculated via ExPASy).

receptor for IAV; TRAM1 might be a putative pro-viral host protein targeted to compromise antigen presentation during virus infection (see Table 3.3).

Compared to the transient expression in HeLaΔS1PL cells Figure 3.15), non-tagged, endogenous SLC1A5 showed strong interaction with pacSph derivatives in A549ΔS1PL S26-clone cells (Figure 3.16). No interaction with SLs was observed for ELOVL1, and the endogenous protein (≈32.55 kDa) was running at a higher molecular weight than the tagged protein (≈36.79 kDa). The "negative" control Asgr1 did not show SL-binding, but surprisingly neither did p24, which exhibited strong SL interaction in protein overexpression experiments conducted in HeLaΔS1PL cells (Figure 3.3 and Figure 3.15)[250,254]. However, the input signal of p24 was very weak, and p24 specifically interacts with SM C18 species[106], which are less abundant compared to C16 and C24 species in A549 and HeLa WT cells (SM36; see Figure 3.31 (A549) and Figure 3.26 (HeLa)). Thus, (pac)SL-interaction could be below detection limit. TRAM1 showed a visible PD- signal, and also the non-TMD (Table 3.3) protein NCL as well as the loading control calnexin (CXN). Immunoblotting against endogenous ITGB1 resulted in two protein signals with the higher migrating band being more pronounced in the SL-mediated PD than the lower migrating band. Except

for TRAM1, none of the investigated proteins were precipitated without UV crosslink.
Considering the huge difference in SL-PD efficiency between tagged and non-tagged proteins, which was also seen in experiments conducted with HeLa cells (data not shown), further investigations of protein-lipid interactions were exclusively performed with endogenous proteins.

To delineate specificity for SL-interaction, A549ΔS1PL cells were labelled with either pacSph or pacFA, the latter being mainly incorporated into glycerolipids and glycerophospholipids, such as PC[250,293](see **section 7,** Figure 7.10). While SLC1A5 was strongly enriched in the PD of pacSph-labelled cells, it was not detectable in the PD of pacFA -treated samples (Figure 3.17). ELOVL1 neither showed interaction with pacSph- or pacFA derivatives. TRAM1 showed more or less equal interaction with both paclipids, CXN (used as loading control in the previous experiment, see Figure 3.16) more with pacFA. PacSph interaction of the higher ITGB1 band was again stronger than of the lower band, and mainly the lower band was pulled-down via pacFA interaction. The total ITGB1 signal in the PD of pacFA-fed cells was stronger than in the PD of pacSph-treated cells (Figure 3.17). However, the lower (mainly pacFA-interacting) form of ITGB1 is also more abundant within A549 cells (see Figure 3.21C). The p24 protein only had a slight detectable band in the pacFA PD, but again, no SL interaction could be observed. Hence, as an additional control, transferrin receptor (TfR) was probed for its interaction with SL. In a mouse embryonic fibroblast (MEF)-based proteomic screen[250], TfR showed a stronger interaction in pacSph labelled cells compared to pacFA labellings. As reported[250], TfR was enriched in the PD of pacSph- and to a lesser extent in pacFA-labelled cells. Since no input signal was detectable for Asgr1 in pacSph-fed cells, no ratio could be calculated. However, Asgr1 seemed to interact more with pacFA derivatives.

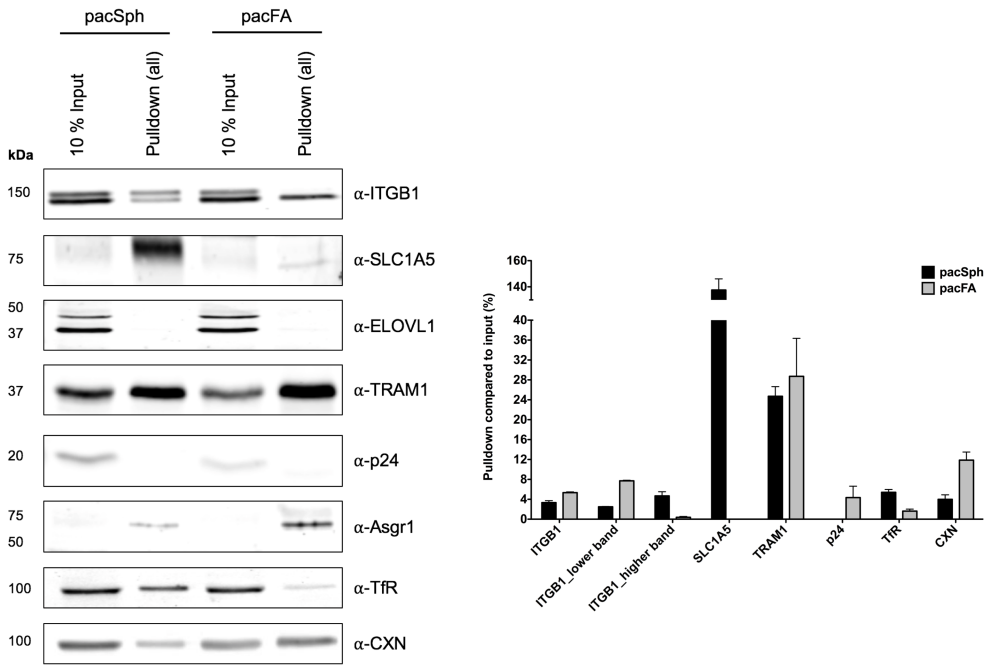

Figure 3.17: pacSph versus pacFA labelling of A549ΔS1PL (clone S2-6 cells) to specify SL-interaction of protein candidates.

Two full 10 cm dishes of A549 *SGPL1* KO cells (clone S2-6 clone) were labelled with either 3 µM pacSph or 40 µM pacFA for 6 h. For biotin-CLICK, 250 µg of protein lysate was used. Data represents the mean ± SEM of three independent experiments; two-tailed, unpaired *t* test performed (pacSph vs. pacFA labelling). Values above 100% (SLC1A5) arise from extreme differences in input and PD signal. Theoretical molecular weight (kDa): ITGB1= 66.62, NCL= 76.61, SLC1A5= 56.61, ELOVL1= 32.55, TRAM1= 43.07, p24= 22.76, Asgr1= 33.12, TfR(1)= 84.87, CXN= 67.57 (calculated via ExPASy).

Intracellular distribution of the antiviral protein interferon-induced transmembrane protein 3 (IFITM3) in infected cells was investigated in the group of collaboration partners (S. Kummer, Kräusslich lab). IFITM3 is a crucial host restriction factor and showed anti-viral activity against several IAV subtypes[270,294]. Although IFITM3 could not be identified as a protein hit in the SILAC proteomic screens, interaction of IFTM3 with pacSLs was demonstrated in HeLaΔS1PL cells (D. Ostkotte, Brügger lab) and should be validated in A549ΔS1PL cells. However, it was observed that basal IFITM3 gene and protein expression was strongly upregulated in A549ΔS1PL S2-6 clone cells compared to A549 WT cells, which correlated with a decrease in the amounts of infected cells in the KO (see **section 7**, Figure 7.12 and Figure 7.13). Although an S1PL-mediated rescue could partially restore S1PL activity, IFITM3 protein expression- and infection levels remained mainly unaffected (see **section 7**, Figure 7.12). A549ΔS1PL S3-10 clone cells also showed lower numbers of infected cells compared to A549, but a difference of IFITM3 protein expression

between WT and S3-10 KO cells was not detected (see **section 7**, Figure 7.12). Hence it is suggested that IFITM3 upregulation is probably not directly related to the KO of *SGPL1.* As a result, no further downstream experiments were conducted in A549ΔS1PL S2-6 clone cells.

3.2.3.2 PR8 screen II

The significant, infection-unrelated increase in protein expression of the viral restriction factor IFITM3[294] in A549ΔS1PL S2-6 clone cells might impact antiviral host responses. Microarray data showed that gene expression in response to infection is differentially affected in A549ΔS1PL S2-6 and S3-10 clone cells (see **section 7**, Table 7.2). Hence, the PR8-SILAC-based proteomic screen should be repeated in the A549ΔS1PL S3-10 clone in order to validate the obtained proteomic results and chosen protein candidates. Here, basal IFITM3 protein expression was comparable to A549 WT cells (see **section 7**, Figure 7.12).

Furthermore, the SILAC-based proteomic screen conducted with A549ΔS1PL S3-10 clone cells was modified regarding the purification and subsequent processing of biotinylated lipid-protein complexes (see **section 5.2.6.5**, performed by G. Sigismondo, Krijgsveld lab). In previous SILAC proteomic screens (see **section 3.2.2** and **3.2.3.1**), avidin co-eluted from NeutrAvidin beads (see **section 5.2.6.3**) was present in proteomic samples at high abundance. In addition, RAW data was processed using the MaxQuant software with subsequent Perseus analysis instead of Proteome Discoverer™ (performed by G. Sigismondo, Krijgsveld lab). The choice of SILAC media for each condition, pacSph labelling conditions, the time-point of harvest after infection and biotin-CLICK were performed as described for previous SILAC screens, without a SILAC media switch (see Figure 3.6).

The infection efficiency was between 60-70% in all three replicates and comparable between “medium” and “heavy” samples (Figure 3.18, left panel). Viral proteins (here: HA1, NS1) were only visible after 12 hpi, indicating host-mediated translation of viral proteins (Figure 3.18, right panel)[258].

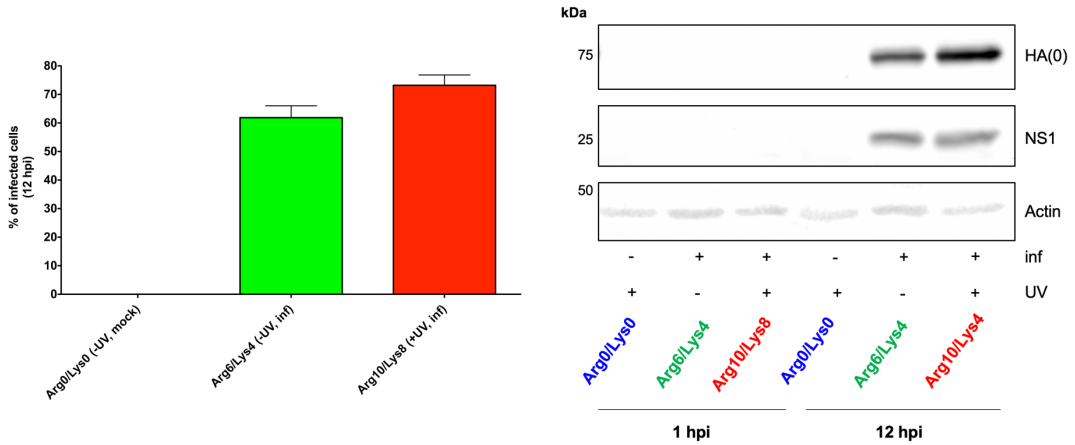

Figure 3.18: Validation of infection efficiency of the PR8-SILAC proteomic screen II.

A549ΔS1PL S3-10 clone cells were infected with the PR8 strain at a MOI of 1. The number of infected cells was determined as described (see Figure 3.10A) at 12 hpi (left panel). Data represents the mean ± SEM of three independent experiments. Further, 30 µg protein lysates were loaded on SDS-PAGE and subjected to immunoblotting (anti-HA1, anti-NS1; right panel). Beta-actin was taken as loading control. A representative blot of replicate 3 is shown.

Proteins with a 4-fold enrichment over the background control ("medium" SILAC, infected cells, non-UV irradiated) in at least 2 out of biological 3 replicates were characterised as a "valid" protein hit (indicated by a "+", see Table 3.4 and Table 7.5; G. Sigismondo, Krijgsveld lab). The number of protein hits for each condition (mock or infected at 1/12 hpi) was below 100 (see **section 7**, Table 7.5 and Figure 7.8). Notably, no significant changes in the lipidome and SL profile of infected compared to mock cells was observed, neither at 1 nor 12 hpi (see **section 7**, Figure 7.9).

The presence of a putative SL binding motif had been postulated to be present mainly in membrane proteins, specifically those located at the PM[107]. In line with this, most protein hits identified were TM proteins (84%) with a single TMD and localised to the PM, although the membrane proteome in A549 cells only represents ≈15% of the total proteome (Figure 3.19)[295]. In general, more SL-interactions were unique in mock vs. infected cells (27 vs. 4 and 31 vs. 14 at 1 and 12 hpi, respectively; see **section 7**, Figure 7.8). However, SILAC ratios for candidate proteins varied, as observed in previous SILAC proteomic screens (see **section 7**, Table 7.5). Thus, in the next step, protein hits were evaluated based on the following criteria (Table 3.4): i.) no specific increase- or decrease of (host) protein-SL-interaction upon infection (valid in all conditions), (ii) putative decrease of protein-SL-interaction upon infection (valid in only the mock conditions), (iii) protein-SL-interaction decreased at a specific infection stage

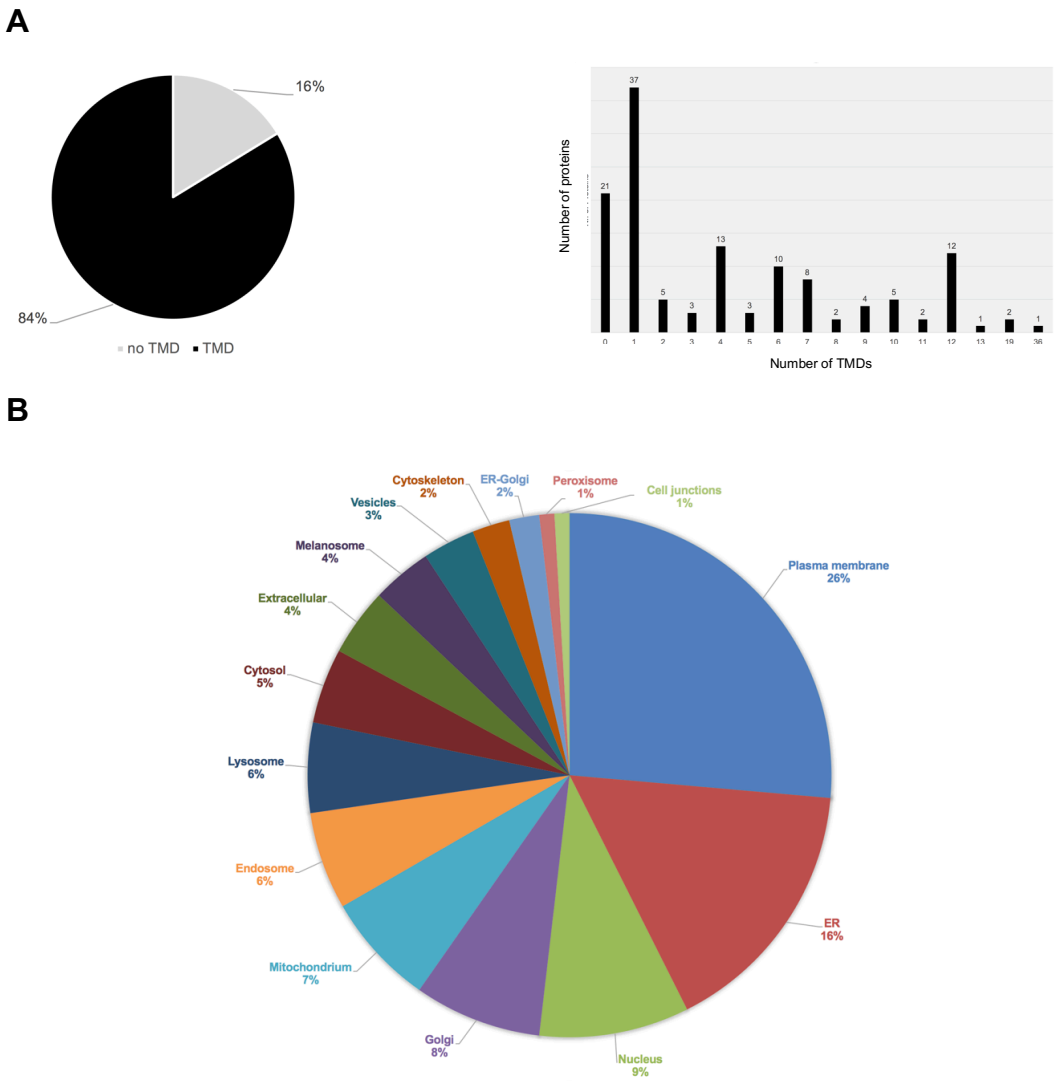

Figure 3.19: Analysis of protein hits according to the presence of transmembrane domains and their localisation.

Proteins were sorted according to the presence of (several) TMDs (A) and their localisation (B). Note that in (B) the total number of proteins exceeds the number of hits, as proteins might be located in several compartments. MS data obtained from G. Sigismond, Krijgsveld lab.

(valid in all conditions except the infected condition at either 1 or 12 hpi) and (iv) requirement of host protein-SL-interaction for viral propagation (valid in only infected conditions). Especially the latter group is of interest because those interactions might be specifically initiated in the context of viral infection.

Proteins initially selected for further downstream experiments are summarised in Table 3.5. These comprised mainly protein hits assigned to criteria (iv) (SLC46A1, TMEM41B, RAB11, TM9SF3, UGCG). Based on reports in the literature, PCYOX1, SLC25A11 and CAV1 (see Table 3.5) were also chosen for further validation, together with ITGB1 and SLC1A5, which had been already identified as promising SL-interacting protein candidates (see Table 3.3, Figure

3.17). Corresponding microarray data of selected protein hits is depicted in **section 7**, Table 7.2. Notably, all subsequent IAV infections were performed by S. Kummer (Kräusslich lab).

Table 3.4: List of protein hits from PR8-II SILAC proteomic screen.

A "+" indicates that the protein was 4-fold enriched over the background in at least 2 out of 3 replicates in the respective sample. Host proteins from Table 3.3 (identified in the previous PR8-screen) are highlighted in dark grey, those added to the target list in light orange. It is also indicated if proteins were subjected to experiments specifying SL-interaction (SL-binding validated?) and evaluated in transient KD experiments (impact of transient KD tested in infected cells?). Bckgrnd= Background; italic= likely contaminants. Data obtained from and processed by G. Sigismond, Krijgsveld lab.

Protein names	**Gene names**	**Valid mock (1hpi)**	**Valid infected (1hpi)**	**Valid mock (12hpi)**	**Valid infected (12hpi)**	**SL-binding validated?**	**Impact of transient KD tested in infected cells?**
Fatty aldehyde dehydrogenase; Aldehyde dehydrogenase	ALDH3A2	+	+	+	+		
Plasma membrane calcium-transporting ATPase 1	ATP2B1	+	+	+	+		
BRI3-binding protein	BRI3BP	+	+	+	+		
Solute carrier family 35 member F6	C2orf18; SLC35F6	+	+	+	+		
Caveolin; Caveolin-1	CAV1	+	+	+	+	yes	no
CD44 antigen	CD44	+	+	+	+		
CD97 antigen; CD97 antigen subunit alpha; CD97 antigen subunit beta	CD97	+	+	+	+		
Cytoskeleton-associated protein 4	CKAP4	+	+	+	+		
Cleft lip and palate transmembrane protein 1	CLPTM1	+	+	+	+		

Cathepsin D; Cathepsin D light chain; Cathepsin D heavy chain	CTSD	+	+	+	+
Epoxide hydrolase 1	EPHX1	+	+	+	+
Retinoic acid-induced protein 3	GPRC5A	+	+	+	+
Basigin	hEMMPRIN; BSG	+	+	+	+
Integrin alpha-3; Integrin alpha-3 heavy chain; Integrin alpha-3 light chain	ITGA3	+	+	+	+
Leucine-rich repeat-containing protein 59	LRRC59	+	+	+	+
Protein LYRIC	MTDH	+	+	+	+
Myeloid-associated differentiation marker	MYADM	+	+	+	+
Serum paraoxonase/arylesterase 2	PON2	+	+	+	+
Serum paraoxonase/lactonase 3	PON3	+	+	+	+
NADPH-cytochrome P450 reductase	POR	+	+	+	+
Presenilin-2; Presenilin-2 NTF subunit; Presenilin-2 CTF subunit	PSEN2	+	+	+	+
Very-long-chain (3R)-3-hydroxyacyl-[acyl-carrier protein] dehydratase 3	PTPLAD1	+	+	+	+
Reticulon-4	RTN4	+	+	+	+
Secretory carrier-associated membrane protein 2	SCAMP2	+	+	+	+

Solute carrier family 12 member 2	SLC12A2	+	+	+	+		
Monocarboxylate transporter 1	SLC16A1	+	+	+	+		
Monocarboxylate transporter 4	SLC16A3	+	+	+	+		
Neutral amino acid transporter B(0)	SLC1A5	+	+	+	+	yes	yes
ADP/ATP translocase 2; ADP/ATP translocase 2, N-terminally processed	SLC25A5	+	+	+	+		
Solute carrier family 2; Facilitated glucose transporter member 1	SLC2A1	+	+	+	+		
Adenosine 3-phospho 5-phosphosulfate transporter 1	SLC35B2	+	+	+	+		
4F2 cell-surface antigen heavy chain	SLC3A2	+	+	+	+		
Sodium- and chloride-dependent taurine transporter; Transporter	SLC6A6	+	+	+	+		
Large neutral amino acids transporter small subunit 1	SLC7A5	+	+	+	+		
Protein spinster homolog 1	SPNS1	+	+	+	+		
Signal recognition particle receptor subunit beta	SRPRB	+	+	+	+		
MLN64 N-terminal domain homolog	STARD3NL	+	+	+	+		
Transducin beta-like protein 2	TBL2	+	+	+	+		
Transferrin receptor protein 1; Transferrin receptor protein 1, serum form	TFRC	+	+	+	+		
Trans-Golgi network integral membrane protein 2	TGOLN2	+	+	+	+		
Transmembrane protein 199	TMEM199	+	+	+	+		
Translocating chain-associated membrane protein 1	TRAM1	+	+	+	+	no	no
Voltage-dependent anion-selective channel protein 1	VDAC1	+	+	+	+	no	no

Voltage-dependent anion-selective channel protein 2	VDAC2	+	+	+	+
Only identified in mock conditions					
Calicin	CCIN	+		+	
	CSF2RB	+		+	
Junction plakoglobin	*JUP*	+		+	
Reticulon-3	RTN3	+		+	
Ubiquitin-60S ribosomal protein L40; Ubiquitin;60S ribosomal protein L40; Ubiquitin-40S ribosomal protein S27a; Ubiquitin;40S ribosomal protein S27a; Polyubiquitin-B; Ubiquitin;Polyubiquitin-C; Ubiquitin	UBB; RPS27A; UBC; UBA52; UbC; UBBP4	+		+	
Only identified in mock conditions either 1 or 12 hpi					
G-protein coupled receptor 56; GPR56 N-terminal fragment; GPR56 C-terminal fragment	GPR56	+			
Lysosome-associated membrane glycoprotein 2	LAMP2	+			
Lipid phosphate phosphohydrolase 3	PPAP2B	+			
Suprabasin	SBSN	+			
Tetraspanin-3	TSPAN3	+			
Vesicle-associated membrane protein 8	VAMP8	+			
Skin-specific protein 32	XP32	+			
Type-1 angiotensin II receptor-associated protein	AGTRAP			+	
Platelet receptor Gi24	C10orf54			+	
CD99 antigen-like protein 2	CD99L2			+	
Battenin	CLN3			+	

Feline leukemia virus subgroup C receptor-related protein 1	FLVCR1			+			
G-protein coupled receptor 126	GPR126			+			
Integrin beta-1; Integrin beta	ITGB1			+		yes	yes
Lysosome-associated membrane glycoprotein 1	LAMP1			+		no	no
Major facilitator superfamily domain-containing protein 6	MFSD6			+			
Major facilitator superfamily domain-containing protein 8	MFSD8			+			
ORM1-like protein 1; ORM1-like protein 2	ORMDL1; ORMDL2			+			
Prenylcysteine oxidase 1	PCYOX1			+		yes	no
Mitochondrial 2-oxoglutarate/malate carrier protein	SLC25A11			+		yes	yes
Multidrug and toxin extrusion protein 1	SLC47A1			+			
Solute carrier family 52, riboflavin transporter, member 2	SLC52A2; GPCR			+			
Y+L amino acid transporter 2	SLC7A6; DKFZp686K14185			+			
Thioredoxin-related transmembrane protein 1	TMX1; TXNDC			+			
Vacuole membrane protein 1	VMP1; TMEM49			+		no	no
Identified in all conditions except in infected condition at 1 or 12 hpi							
B-cell receptor-associated protein 31	BCAP31	+	+	+			
CD151 antigen	CD151	+	+	+			
CD63 antigen	CD63	+	+	+		no	no
Sulfate transporter	SLC26A2	+	+	+			
Aspartyl/asparaginyl beta-hydroxylase	ASPH	+		+	+		
Sodium/potassium-transporting ATPase subunit alpha-1	ATP1A1	+		+	+		
Membrane cofactor protein	CD46	+		+	+		

Emerin	EMD	+	+	+		
Kinectin	KTN1	+	+	+		
Membrane-associated progesterone receptor component 2	PGRMC2	+	+	+		
Signal peptidase complex catalytic subunit SEC11A	SEC11A; SPC18	+	+	+		
Syntaxin-4	STX4; STX4A	+	+	+		
Only identified in the infected condition						
Proton-coupled folate transporter	SLC46A1	+		+	yes	yes
Transmembrane protein 41B	TMEM41B	+		+	yes	no
Apolipoprotein L2	APOL2			+		
	DLG2			+		
ER lumen protein retaining receptor 1; ER lumen protein retaining receptor 2; ER lumen protein retaining receptor	KDELR1; KDELR2			+		
	NCAM2			+		
Ras-related protein Rab-11A; Ras-related protein Rab-11B	RAB11A; RAB11B			+	yes	yes
ADP/ATP translocase 3	SLC25A6			+		
Transmembrane 9 superfamily member 3	TM9SF3; SMBP			+	yes	no
Ceramide glucosyltransferase	UGCG			+	yes	yes

Table 3.5: Protein candidates from PR8-II SILAC proteomic screen chosen for further validation.

*UniProt/Human Protein Atlas. Inf= infected, MTOC= microtubule organisation centre, VSV= vesicular stomatitis virus, vRNP= viral ribonucleoprotein, PBMC= peripheral blood mononuclear cells, SFTSV= severe fever with thrombocytopenia syndrome virus, RSV= respiratory syncytial virus subgroup B.

							1 hpi		12 hpi	
Accession	**Gene name**	**Localisation***	**Function***	**TMDs**	**Role in (IA) virus infection?**		**inf**	**mock**	**inf**	**mock**
Q96NT5	SLC46A1	PM	Intestinal H^+-coupled high-affinity folate transporter/heme transporter	12	- -	Required in HIV infection[296] Reduces VSV gene expression (might be required for viral entry and uncoating)[297]	x		x	
Q5BJD5	TMEM41B	ER	Required for motoneuron development; regulator of autophagosome biogenesis and fatty acid ß-oxidation[298]	6	-	Identified as a microRNA target in IAV infected mice[299]	x		x	
P62491	RAB11A (RAB11B)	PM, endosome, vesicles, MTOC	Rab small GTPase superfamily member; associated with constitutive and regulated secretory pathways, may be involved in protein transport; two isoforms A & B	0	-	Involved in apical trafficking, assembly and budding of vRNP's;, interaction with PB2?[198,300-302]			x	
Q9HD45	TM9SF3;SMBP	Golgi, vesicles	Binds to beta-adrenergic ligands[303]	9	-	Gene expression changed upon IAV infection in human-derived PBMCs[304]			x	
Q16739	UGCG	Golgi	Transfers activated glucose to ceramide, the first step in glycol-SL synthesis	5	- -	Genes involved in sialic acid biosynthesis crucial for IAV infection in A549 cells[305] Needed for SFTSV entry[306]			x	
Q02978	SLC25A11	Mitochondria	Transports 2-oxoglutarate across the inner membranes of mitochondria in	12	-	Binds to IAV polymerase (PA) [307]				x

			electroneutral exchange for malate or other dicarboxylic acids		- Co-IP with FLAG tagged IAV NEP in HEK293T[308] - Decreased abundance in RSV infection		
Q9UHG3	PCYOX1	Lyso-some	Involved in degradation of prenylated proteins → degrades prenylcysteines	0	- Host factor necessary for IAV infection (pro-viral)[262,309]		x

3.2.4 Validations of SL-interactions of protein candidates from the PR8-II screen

To identify proteins specifically interacting with SLs, A549ΔS1PL S3-10 clone cells were fed with either pacSph, pacFA or pacChol (see **section 7**, Figure 7.10), the latter to identify protein-cholesterol interactions[249]. Labelling with pacChol was done because SLs and cholesterol are suggested to associate in intracellular transport processes and within membranes[6], hence SL-interactors might also interact with cholesterol (see **section 2.1.2** and **2.1.3**)[310]. As an additional control, the fungal Sph-analogue Fumonisin B1 was used, which prevents incorporation of pacSph into SLs by inhibition of CerS[311] (see **section 7**, Figure 7.11). Competition experiments with Sph (as described in[250]) were not performed because the amounts of pacSph-incorporated SLs were not linearly decreasing in presence of increasing amounts of Sph (data not shown).

The strongest SL-binding was seen for SLC1A5 (as in previous experiments) and interaction with pacSph-derivatives was strongly decreased in FB1-treated cells (Figure 3.20). SLC1A5-interaction with pacFA and pacChol was very low. For ITGB1, only the upper band was enriched in the PD of pacSph-fed cells, as observed before, and this band was also mainly affected by FB1 treatment. The lower ITGB1 band showed a higher signal in the PD of pacFA-fed cells than in those fed with pacSph; and only this band could be pulled down via pacChol interaction. RAB11 lipid validation was conducted for the isoform A (RAB11A). Although isoform A and B reside in different compartments[312], a transient knock down (KD) in A549 cells of both isoforms was only slightly stronger than a single KD in RAB11A regarding the restriction of virus production[313]. Furthermore, RAB11 isoform A has been implicated in the transport of viral genomes to the PM[301]. Strongest interactions of RAB11A were observed with pacChol, followed by pacFA, while only a weak interaction with SLs was observed (Figure 3.20). SLC25A11 showed no detectable interaction with paclipids, and PCYOX1 was only pulled-down via pacFA. In contrast, CAV1, which had been identified in all replicates (like SLC1A5) showed an interaction with all paclipids, with the highest signal in the PD of pacSph-fed cells.

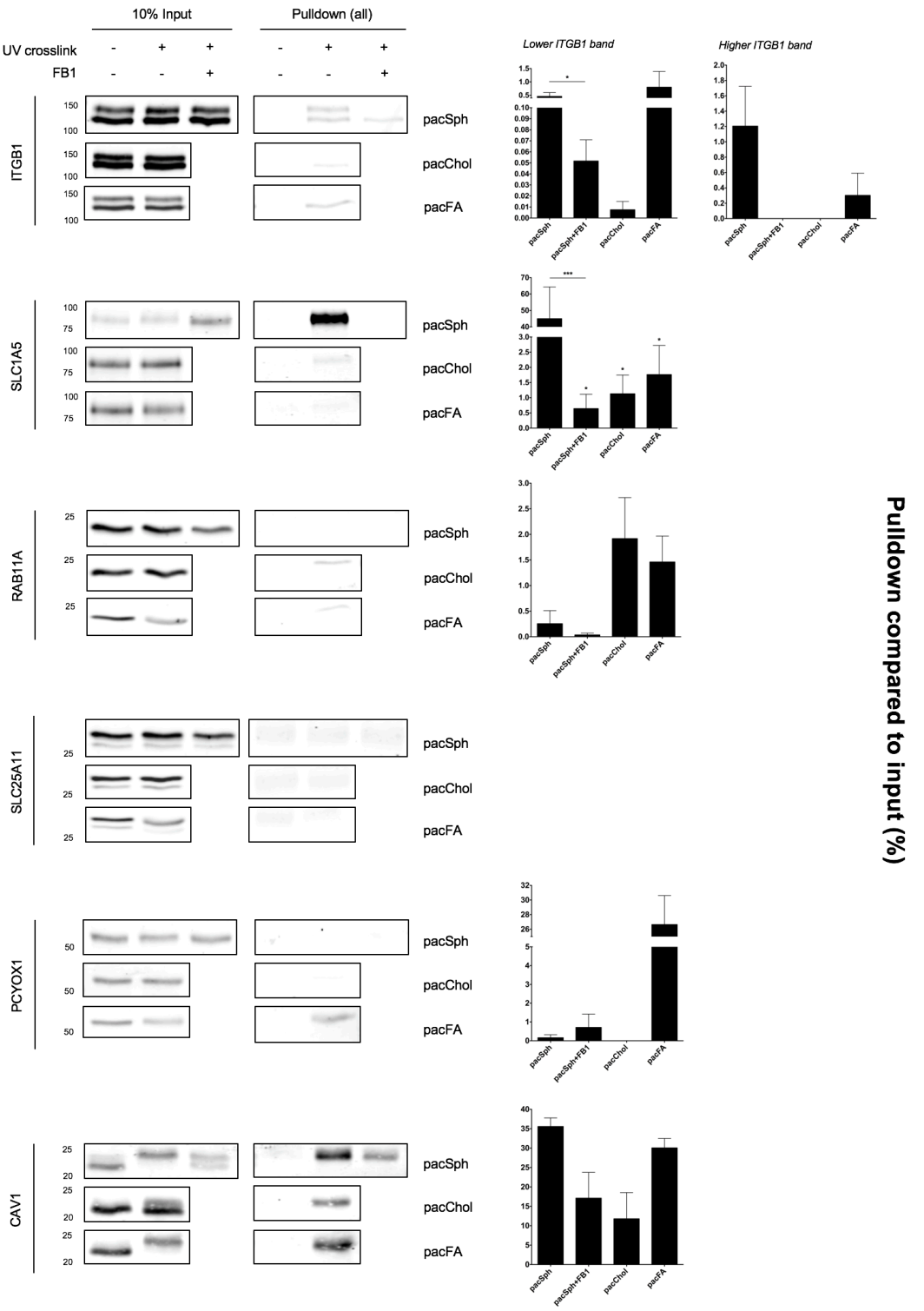

Figure 3.20: Sphingolipid-binding validation of protein candidates in A549ΔS1PL (clone S3-10) cells.

A549ΔS1PL S3-10 clone cells were labelled with either 3 µM pacSph (6 h) in presence or absence of 100 µM FB1 (1 day pre-treatment), 40 µM pacFA (6 h) or 6 µM pacChol (0.5 h) and harvested from full 2*10 cm dishes after UV-crosslink (if indicated). Lysates were subjected to biotin-CLICK (200 µg protein) and biotinylated lipid-protein complexes enriched via NeutrAvidin beads. The pulldown efficiency (protein in pulldown in %) was calculated as the ratio of input/pulldown signal. Data represents the mean ± SEM of three independent experiments; two-tailed, unpaired *t* test (pacSph vs. FB1 or pacChol or pacFA) and ONE-way ANOVA with subsequent Dunnett's multiple comparison test (pacSph-labelled cells as reference) performed. Theoretical molecular weight (kDa): ITGB1= 66.62, SLC1A5= 56.61, RAB11A= 24.39, SLC25A11= 43.07, SLC25A11= 34.06, PCYOX1= 56.64, CAV1= 20.47 (calculated via ExPASy).

The (pac)lipidation of CAV1 presumably also caused a “shift” of the protein when comparing - and +UV-treated samples. Paclipid-interaction could not be validated for SLC46A1, TMEM41B, TMSF9 and UGCG because the detection of endogenous proteins with the available antibodies was not possible.

Due to the fact that specific SL-binding was only significantly observed for SLC1A5 and (the upper band of) ITGB1, these two proteins were investigated regarding SL-interaction in infected vs. mock cells at 1 and 12 hpi. SL-interaction in infected cells was calculated relative to the interaction in non-infected cells (Figure 3.21A). Although the infection efficiency was not comparable to the SILAC-based proteomic screen (see Figure 3.21B and Figure 3.18; 15-25% vs. 60-70%), viral protein translation was clearly visible as indicated by the HA(0) (see **section 3.1.2**) and NS1 protein signal at 12 hpi (Figure 3.21A). SL-

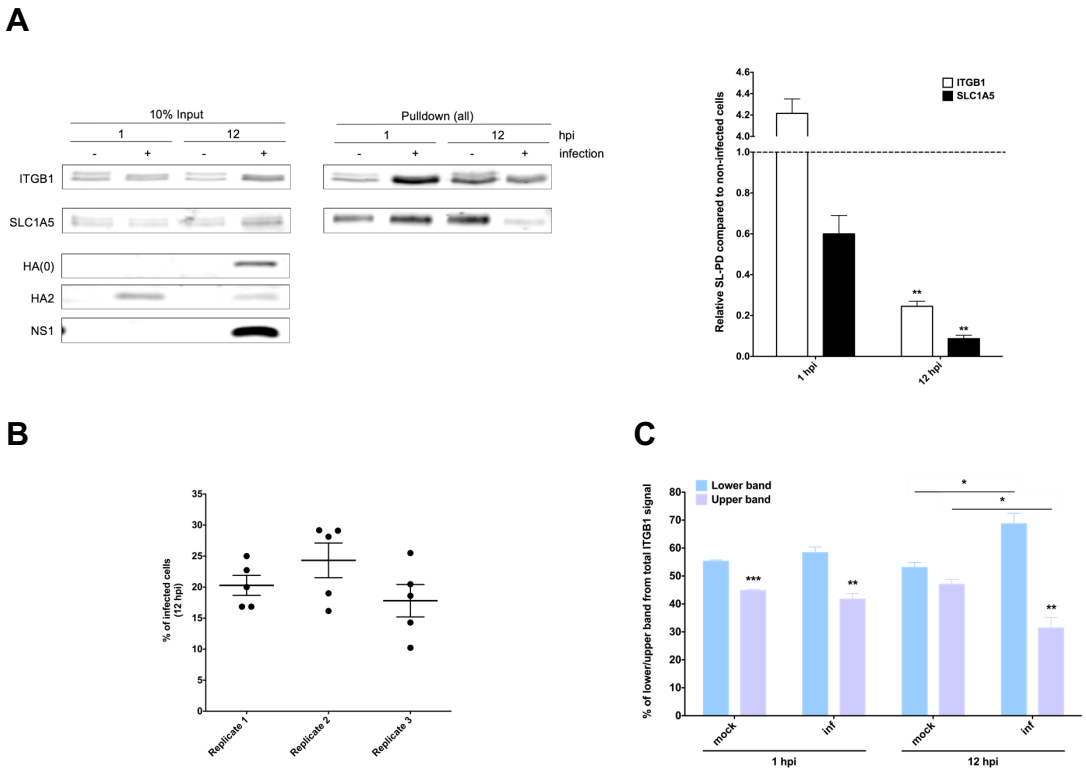

Figure 3.21: Sphingolipid-binding validation of SLC1A5 and ITGB1 in infected cells.

(A) PR8-infected and non-infected A549ΔS1PL S3-10 clone cells (MOI of 1) were harvested at 1 or 12 hpi after labelling with 3 µM pacSph for 6 h (as in the SILAC proteomic experiment) from a 10 cm dish. Biotin-CLICK was performed (300 µg protein lysate) and biotinylated protein complexes enriched via NeutrAvidin beads (left panel). The PD efficiency of ITGB1 and SLC1A5 via pacSph-derivatives in infected cells was calculated relative to the mock (dotted lines indicate a ratio of 1, right panel). (B) The number of infected cells (anti-NP stain) is depicted; each dot indicates one microscopical frame counted. Shown: mean, ± SEM. (C) The band intensity signal of the lower/upper ITGB1 band was calculated relative to the total ITGB1 signal. Data represents the mean ± SEM of three independent experiments; two-tailed, unpaired *t* test (lower vs. upper ITGB1 band) performed.

interaction of SLC1A5 was significantly decreased in infected cells after 12 hpi and already affected at 1 hpi. In contrast, at early time points of infection, ITGB1-SL-interaction seemed to be increased in infected cells, whereas after 12 hpi, interactions were strongly reduced compared to the mock condition. Note that total ITGB1 levels (signals of the upper plus lower migrating form) were taken for the calculation of SL-PD efficiencies. The protein expression of the lower and the upper ITGB1 band in infected and mock cells was also investigated (Figure 3.21C). Both after 1 and 12 hpi, the upper band of ITGB1 was less abundant than the lower band, with the effect being especially remarkable at later time points of infection.

3.2.5 Impact of transient knock-downs of protein candidates on IAV infection

In the next step, the effect of transient KDs of ITGB1 and SLC1A5 on IAV infection was investigated. Although SL-interaction of candidate proteins SLC25A11, SLC46A1 and UGCG was either not detectable or could not be quantified for technical reasons, these proteins were also included in the knockdown studies, especially since the latter two proteins were suggested to play an important role for other viruses or in GSL synthesis (see Table 3.4). RAB11A was used as a control (despite being a non-TM protein and cholesterol-binder, Figure 3.20) since its knockdown was reported to cause severe budding defects[313]. Infection-based siRNA experiments were performed in A549 WT cells as these are closer to the *in vivo* situation as the *SGPL1* KO. Impact on early IAV stages was determined via immunostaining against viral NP (8 hpi), suggesting successful entry and uncoating of viral particles and genomes. The ratio of HA0 and HA2 (the C-terminal fragment of HA, see **section 3.1.2**) at 8 hpi was calculated as a value to measure the synthesis of viral proteins. HA0 is the single-peptide precursor of the HA protein, which is not yet cleaved by PM-localised host proteases, and HA2 the C-terminal fragment of processed HA (see **section 2.3.2** and **3.1.2**)[186]. It was assumed that the HA2 protein signal is mainly related to HA from incoming particles, as HA2 was already visible at 1 hpi in cell lysates of infected A549 cells (see Figure 3.18, right panel).

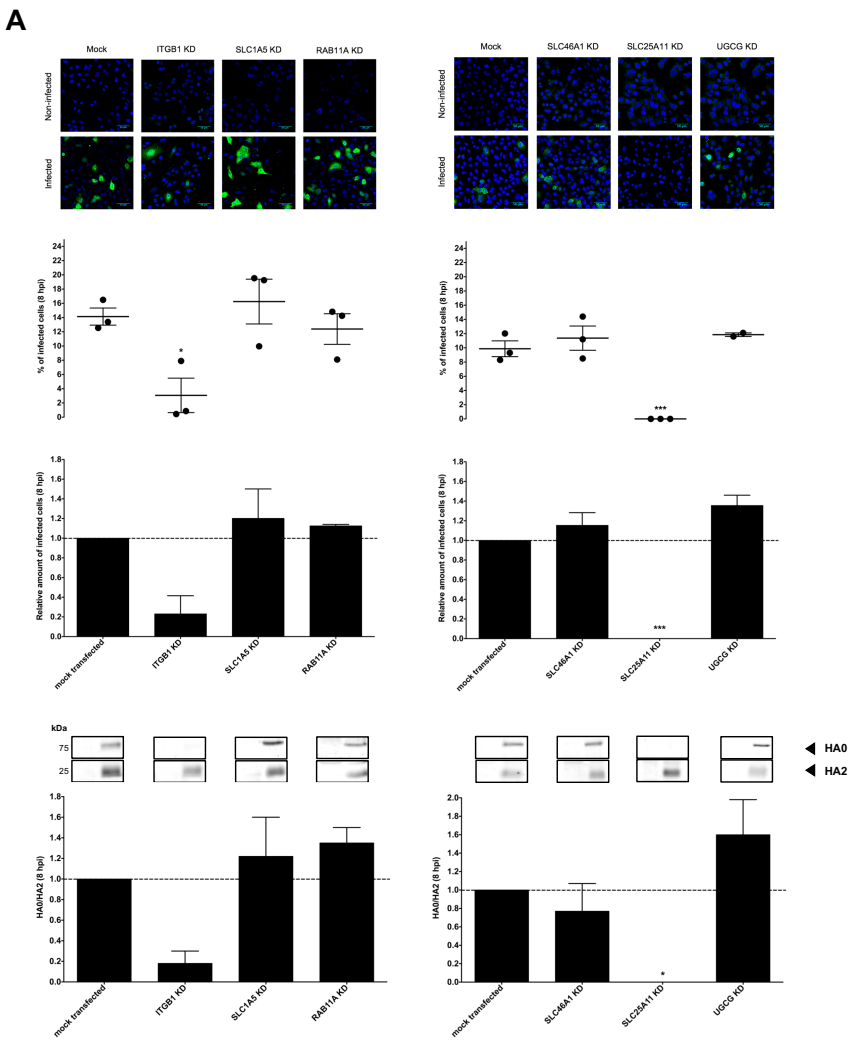

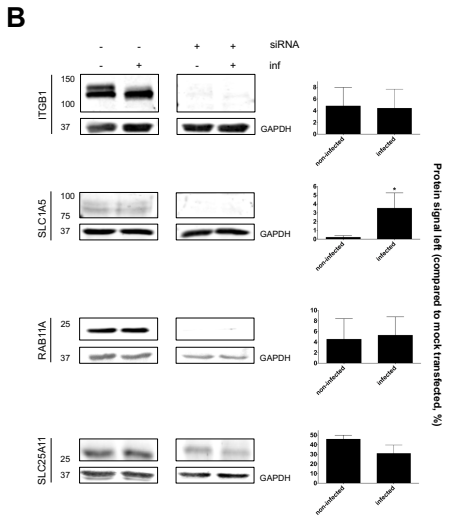

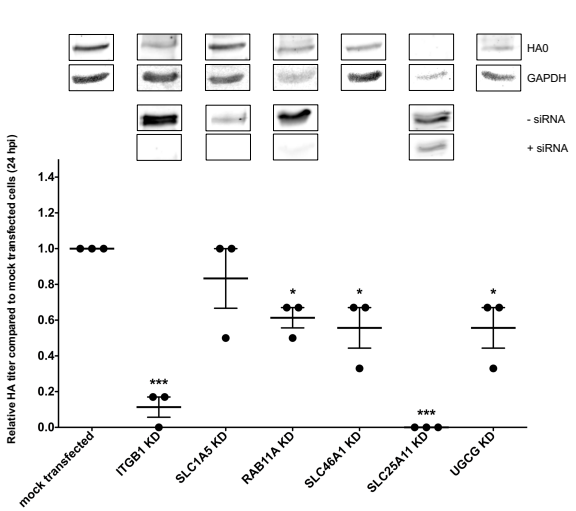

Figure 3.22: Transient KD of candidate proteins in PR8-infected A549 WT cells.

(A) Cells were infected after 48 h siRNA transfection at a MOI of 1. The amounts of infected cells were determined via anti-NP stain (green channel) at 8 hpi in mock-transfected- and siRNA-treated cells. In addition, the ratio of "newly" produced HA (HA0) and mainly incoming HA (HA2, see text) was calculated. For Western blot, 35 µg protein was loaded. Two independent siRNA experiments were conducted (left and right panel). Scale bar= 50 µM, 40x magnification. (B) The KD efficiency of siRNAs (8 hpi) was tested for infected and non-infected cells (C) The relative HA titer (compared to mock transfected cells) for different siRNAs was determined (lower panel). Protein levels for Western blot (upper panel) were not adjusted. Data represents the mean ± SEM of three independent experiments; ONE-way ANOVA and Dunnett's multiple comparison test performed.

Protein levels for ITGB1, SLC1A5 and RAB11A were reduced over 90%, SLC25A11 level approximately 50% in siRNA-treated cells collected 48 h after transfection, irrespective of infection (Figure 3.22B, see **section 5.2.6.8**). After 8 hpi, A549 cells treated with siRNAs against ITGB1 and especially SLC25A11 showed a significant reduction in the amount of infected cells which was also reflected in the impairment of viral protein translation (indicated by HA0) (Figure 3.22A)[314]. The other tested siRNAs against SLC1A5, RAB11A, SLC46A1 and UGCG showed no significant effect at 8 hpi infection.

A potential effect of candidate protein knockdown on budding and release of virions was analysed by HA titer determination at 24 hpi (see **section 5.2.4.5**). After 24 hpi, ITGB1 and SLC25A11 siRNA treated cells, as expected, displayed strongly reduced viral particle release (Figure 3.22C). All other transient KDs only showed a comparably moderate impairment in virion release compared to mock transfected cells. Due to the lack of endogenous antibodies, it cannot be excluded that the transient KD of SLC46A1 and UGCG was unsuccessful, because qRT-PCR has not been conducted in parallel. However, compared to mock transfected cells, a ≈50% reduction in GSL levels (pac-GlcCer) was detected for the UGCG KD in A549ΔS1PL S3-10 clone cells (verified by TLC), indicating a decrease of enzyme levels (data not shown).

In summary, two proteins were identified that might exert a pro-viral effect: ITGB1 and SLC25A11. The KD of SLC25A11 showed the most severe effect, even at a reduction of only ≈50% cellular protein levels (Figure 3.22B). However, a transient KD of SLC25A11 also had an impact on cell vitality, as can be seen by the low GAPDH levels at 24 hpi (Figure 3.22C). In contrast, protein levels of GAPDH were not affected in ITGB1-siRNA treated cells at 24 hpi (Figure 3.22C) and hence ITGB1 was further investigated.

Only the slower migrating form of ITGB1 was found to interact with SL (Figure 3.20). The appearance of two or more protein bands after immunoblotting might indicate different states of post-translational modification of a certain protein. In the following, the glycosylation state of ITGB1 was determined by Endo H and PNGase F treatment. EndoH is an ER-resident enzyme and only removes N-linked mannose-rich oligosaccharides, whereas PNGase F is localised to the Golgi complex and is able to remove almost all N-linked sugar residues from glycoproteins (NEB)[315]. Susceptibility of a glycoprotein to one of the enzymes

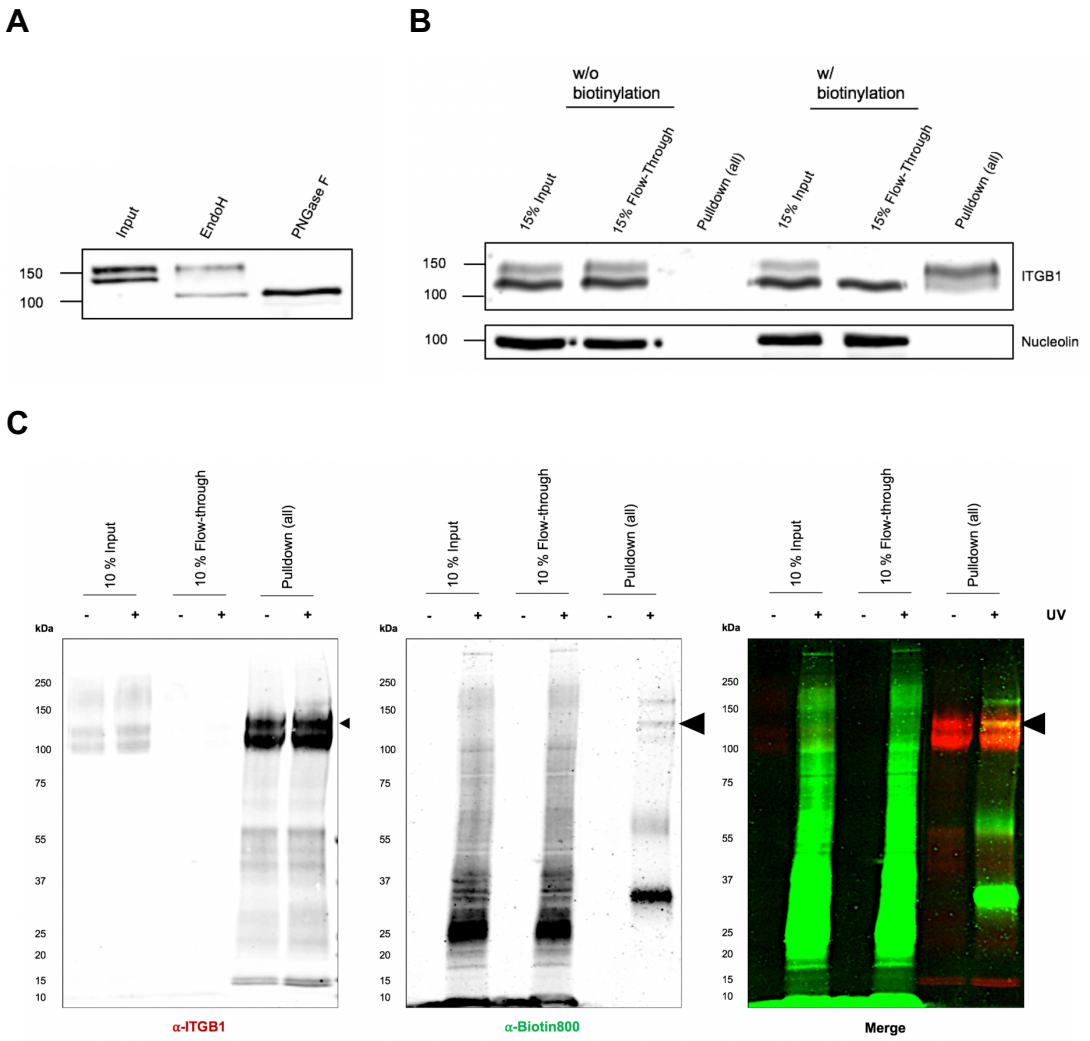

Figure 3.23: The upper ITGB1 band is the complex glycosylated, PM-localised protein form and exhibits stronger SL-interaction.

(A) Cell lysates (40 µg protein) of A549 WT cells were either treated with EndoH or PNGase F to determine the progress of (N-linked) glycosylation of ITGB1[315]. In addition, a cell-surface biotinylation assay (B) was performed in order to identify which ITGB1 form is prevalent at the PM (cells collected from 6-well plate). Nucleolin (NCL) was used as cellular control protein. (C) A549ΔS1PL S3-10 clone cells were fed 6 h with 3 µM pacSph, UV-irradiated and 400 µg protein subjected to biotin-CLICK. Protein A beads covalently coupled with anti-ITGB1 antibody were used to immunoprecipitate ITGB1 from lysates. Samples were applied on NuPAGE™ 4-12% Bis-Tris gels (MOPS buffer). ITGB1 was detected endogenously (red), biotinylated pacSph-derivatives with an anti-biotin antibody (green). The black arrow indicates the upper ITGB1 band. Experiments were performed once.

might indicate its processing stage along the secretory pathway[315]. Endo H and PNGase F treatment of A549 WT cell lysates showed that the slower migrating, upper ITGB1 band is the more complex glycosylated form, susceptible to PNGase F, but not Endo H treatment (Figure 3.23A). Furthermore, the abundance of the upper ITGB1 form was markedly higher at PMs then the lower migrating form, as demonstrated by cell-surface biotinylation assay (Figure 3.23B). It was further illustrated that biotinylated pacSph-derivatives were mainly pulled down by interaction with the upper (PM-localised) ITGB1 form in

A549ΔS1PL S3-10 clone cells (Figure 3.23C), as has been shown the other way around, e.g. by co-purification of ITGB1 via biotinylated pacSLs in previous experiments (Figure 3.20).

3.2.6 SL-interaction of native viral proteins

In the SILAC proteomic screens, some viral proteins could be identified in the pool of putative SL-interacting host proteins (Table 3.6). Except for NP (PR8-I, replicate 2), all viral proteins were found only after 12 hpi and included the structural proteins HA, NA, M1, NP as well as the non-structural protein NS1. Based on these results the interaction of pacSLs with viral proteins was investigated using the strains PR8 and HK68 for IAV infection of A459 *SGPL1* KO cells. PR8 (H1N1)- and HK68 (H3N2)-infected, pacSph-labelled A549ΔS1PL S3-10 clone cells were harvested at 8 and 12 hpi and cell lysates were subjected to biotin-CLICK. Earlier time points were not included due to the low abundance of viral proteins (Table 3.6)[258].

Except for a slight signal for HA3 (HK68) after 12 hpi, no signal was detected in the pulldown of non-UV irradiated samples (Figure 3.24). The protein amount of viral HA, NA (HK68, PR8) and M2 (HK68) clearly increased from 8 to 12 hpi, related to host-mediated viral protein expression (Figure 3.24, inputs)[258]. M2

Table 3.6: Viral proteins identified in SILAC proteomic screens.

Viral proteins are in "light" (Arg0/Lys0), as virus was produced in normal media; hence no SILAC ratio is depicted. Rep= replicate, AAs= amino acids.

	hpi	Sample	Protein ID	Protein	AAs	MW (kDa)	Unique peptides
HK68	12	Rep3	C7RWD9	HA	566	63.3	1
PR8-I (run1)	1	Rep2	P03466	NP	498	56.2	10
	12	Rep1	P03452	HA	565	60.3	8
			P03468	NA	454	50.1	3
			P03496	NS1	230	25.9	3
PR8-I (run2)	12	Rep2	P03452	HA	565	60.3	6
			P03468	NA	454	50.1	1
			P03485	M1	252	27.9	1
			P03466	NP	498	56.2	5
			P03496	NS1	230	25.9	1
PR8-II	12	Rep1	P03452	HA	565	63.3	3
		Rep2					5
		Rep3					4
		Rep1	P03466	NP	498	56.2	2
		Rep2					4
		Rep3					6
		Rep2	P03496	NS1	230	25.9	1

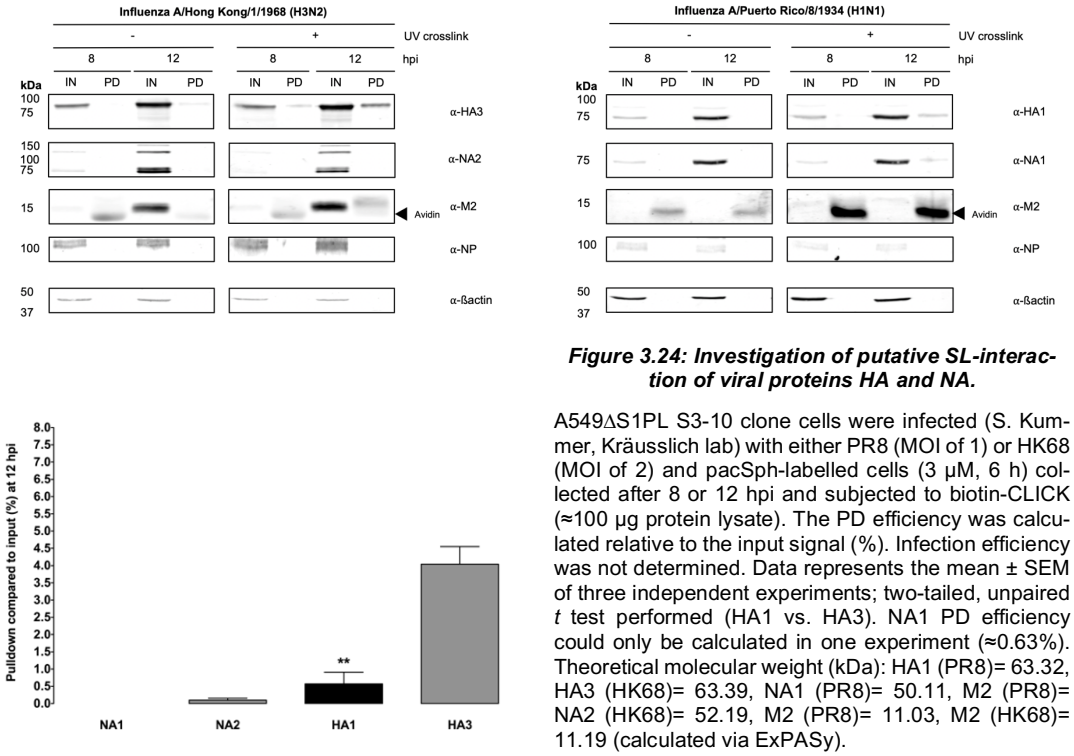

Figure 3.24: Investigation of putative SL-interaction of viral proteins HA and NA.

A549ΔS1PL S3-10 clone cells were infected (S. Kummer, Kräusslich lab) with either PR8 (MOI of 1) or HK68 (MOI of 2) and pacSph-labelled cells (3 µM, 6 h) collected after 8 or 12 hpi and subjected to biotin-CLICK (≈100 µg protein lysate). The PD efficiency was calculated relative to the input signal (%). Infection efficiency was not determined. Data represents the mean ± SEM of three independent experiments; two-tailed, unpaired *t* test performed (HA1 vs. HA3). NA1 PD efficiency could only be calculated in one experiment (≈0.63%). Theoretical molecular weight (kDa): HA1 (PR8)= 63.32, HA3 (HK68)= 63.39, NA1 (PR8)= 50.11, M2 (PR8)= NA2 (HK68)= 52.19, M2 (PR8)= 11.03, M2 (HK68)= 11.19 (calculated via ExPASy).

from PR8 was only weakly detected. In contrast to the other viral proteins studied, the amount of NP remained constant from 8 to 12 hpi, suggesting that it had already reached a plateau as observed for PR8-infected MDCK cells at 10 hpi[258]. HA and NA showed a different migration behaviour among homologous proteins, although the theoretical molecular weight is similar (Figure 3.24). HA1 from PR8 was detected at ≈75 kDa, HA3 from HK68 at ≈100 kDa; NA1 from PR8 at ≈75 kDa and NA2 from HK68 at ≈75 and 150 kDa. The overall pulldown efficiency of viral HA and NA mediated by interaction with pacSph-derivatives was below 5% and visible only at 12 hpi (except for HA3 from HK68). The HA3 protein showed highest SL-interaction (≈4%), also in comparison to HA1 (<1%). In addition, SL-interaction of HA3 was already visible at 8 hpi. NA2 showed very low interaction with pacSLs (≈0.2%) (Figure 3.24). The PD efficiency for the NA1 protein could only be validated in one experiment, but was higher (0.63%) than the PD efficiency of NA1 (data not shown).

3.3 Implications of very long-chain SLs on viral propagation

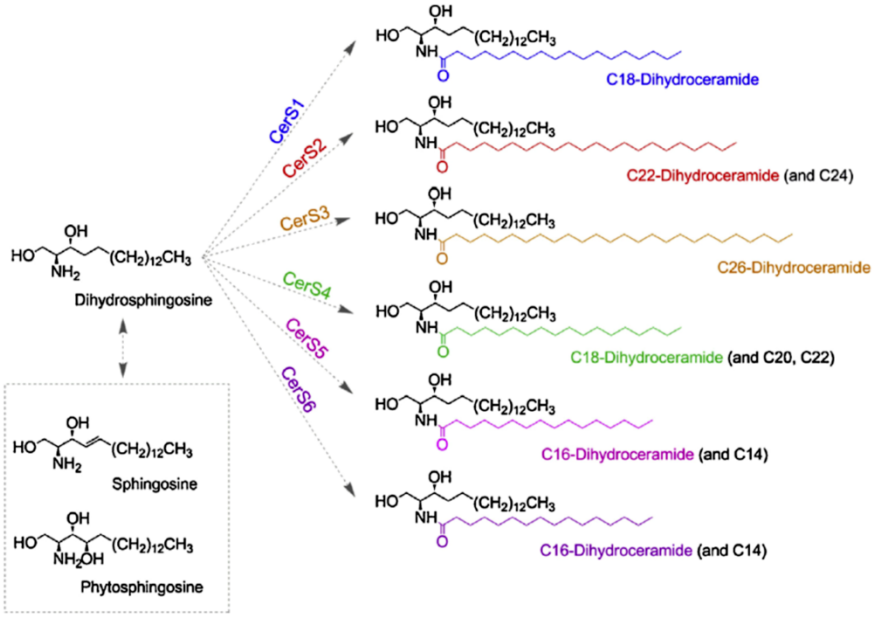

Figure 3.25: The fatty acid chain length of SLs is determined by CerS.

CerS catalyse the synthesis of ceramide either *de novo* via dihydrosphingosine (sphinganine), or from the break-down product sphingosine (recycling pathway). CerS have several isoforms (CerS1-6), each of them showing specificity towards a subset of acyl-CoAs. Phytosphingosine is mainly found in plants and fungi, but is restricted to distinctive mammalian tissues, like the skin and and bowels[316]. From: Cingolani *et al*., 2016; license number: 4463540158601[236].

Beside the *SGPL1* KO, HeLa cells with additional KOs of ceramide synthases (CerSs) were generated (this group, unpublished data). CerSs are enzymes that produce ceramides with a defined acyl chain length (Figure 3.25). CerS2 is widely distributed within the body and catalyses the synthesis of very long chain (VLC) acyl chain-containing ceramides, namely C22 and C24 species of ceramide[57,317]. CerS2-regulated ELOVL1, which is associated with C24-SL synthesis, has been identified as a proteomic hit after 1 hpi in one of the SILAC proteomic screens, although an interaction with sphingolipids could not be verified (Figure 3.16, Figure 3.17)[271]. In addition, lipidomic data of PR8-infected A549 cells showed that VLC (≥ C22) SM, Cer and HexCer species increased in the course of infection, together with C18 and species[231].

To test whether IAV propagation depends on the presence of VLC SLs in host cells, IAV infection was investigated in *CERS2* KO cells. A CRISPR/Cas9-

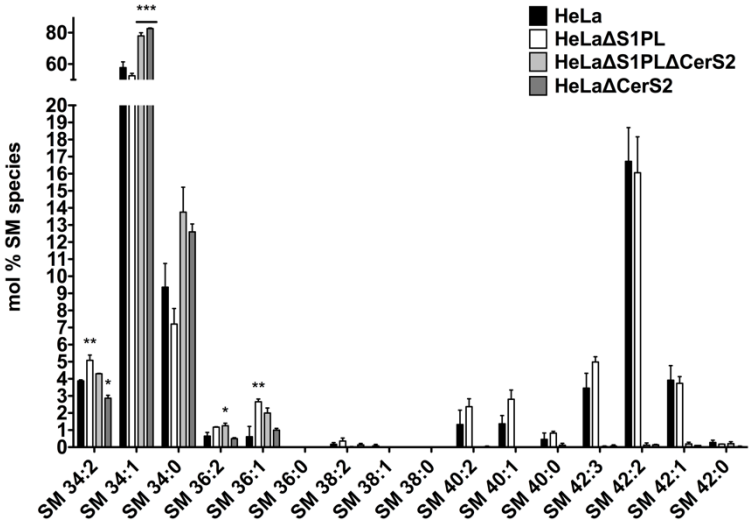

Figure 3.26: SM species profile in HeLa versus S1PL- and CerS2-KO cells.

Cells were collected from a 6-well plate and subjected to lipidomic analysis. The HeLaΔCerS2 KO was generated in the context of this work; the *SGPL1* and *SGPL1-CERS2* double KO cell lines were provided by M.Gerl/D. Ostkotte (Brügger lab). SM species are depicted as mol% of total SM levels. The first number indicates the total number of C-atoms, including the C18 sphingoid backbone; the second the number of double bonds. Data represents the mean ± SEM of three independent experiments; two-tailed, unpaired t test (WT vs. KO) and ONE-way Anova with subsequent Dunnett's multiple comparison test (WT vs. KOs) performed. Lipidomic samples prepared and data provided by I. Leibrecht and C. Lüchtenborg , Brügger lab.

based *CERS2* KO resulted, independent of an additional *SGPL1* KO, in the almost complete absence of C22 and C24 species, with a concomitant increase in C16 species, as illustrated by the SM species profile of HeLa WT and KO cells (Figure 3.26). CerS2-deficiency will hence refer to the functional KO of the the CerS2 enzyme.

Since it had been demonstrated that S1PL is suggested to be an antiviral factor in HEK293T cells[245,256], first experiments were performed with HeLa *SGPL1* and *SGPL1-CERS2* double KO cells to investigate the role of CerS2 in IAV infections. Cells deficient only in CerS2 have been generated in this study.
To determine differences in the amounts of infected cells and viral particle release, HeLa WT, HeLaΔS1PL and HeLaΔS1PLΔCerS2 cells were infected with the IAV HK68, RD6 or PR8 strain. The number of infected cells was determined 12 hpi, and viral particle release after 24 h (HA titer). Results obtained for HK68-infected cells showed a great variability, and the number of RD6-infected cells was very low (Figure 3.27). Reproducible results were only obtained for cells infected with the PR8 strain. Here, HeLaΔS1PLΔCerS2 cells exhibited increased numbers of infected cells and also viral particle release. Due to a low infectivity, the RD6 strain was not included in further studies (see also **section**

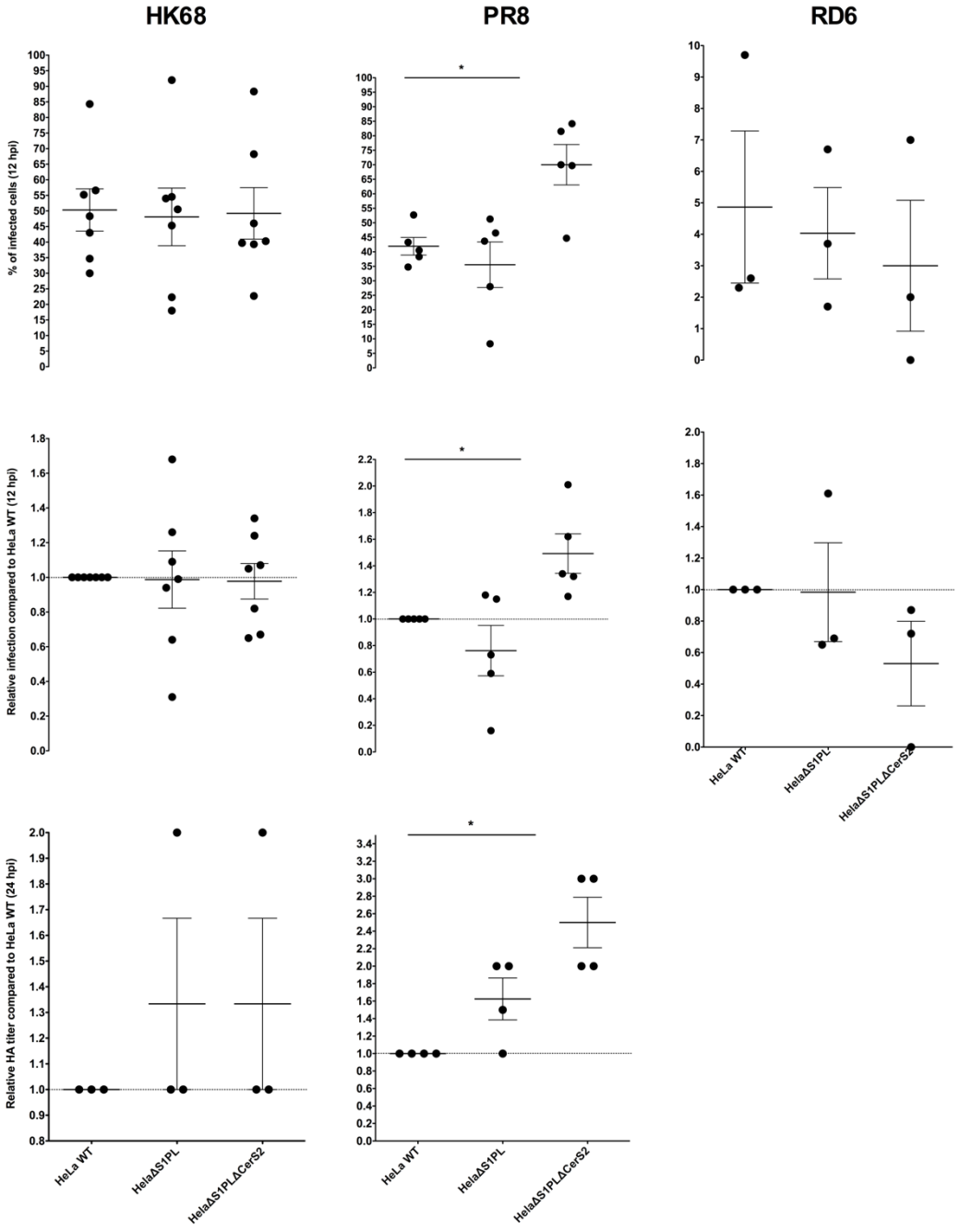

Figure 3.27: Infection efficiency and viral particle release in HeLa versus HeLa S1PL- or S1PL-CerS2-KO cells.

HeLa WT and KO cells were infected in a 6-well plate with IAV strains at a MOI of 1 (S. Kummer, Kräusslich lab) for 12 h (anti-NP stain) or 24 h (HA titer). Shown: mean, ±SEM; each dot represents one replicate; ONE-way Anova with subsequent Dunnett's multiple comparison test (WT vs. KOs) performed. Notably, all subsequent IAV infections were performed by S. Kummer, Kräusslich lab.

3.2.2). In the following experiment attachment of viral particles to the cell surface of HeLa WT, HeLaΔS1PL and HeLaΔS1PLΔCerS2 cells was investigated. The most prominent entry receptors for IAV are sialylated glycoproteins[318] and GSLs. Gangliosides are GSLs which carry terminal sialic acid residues, and the

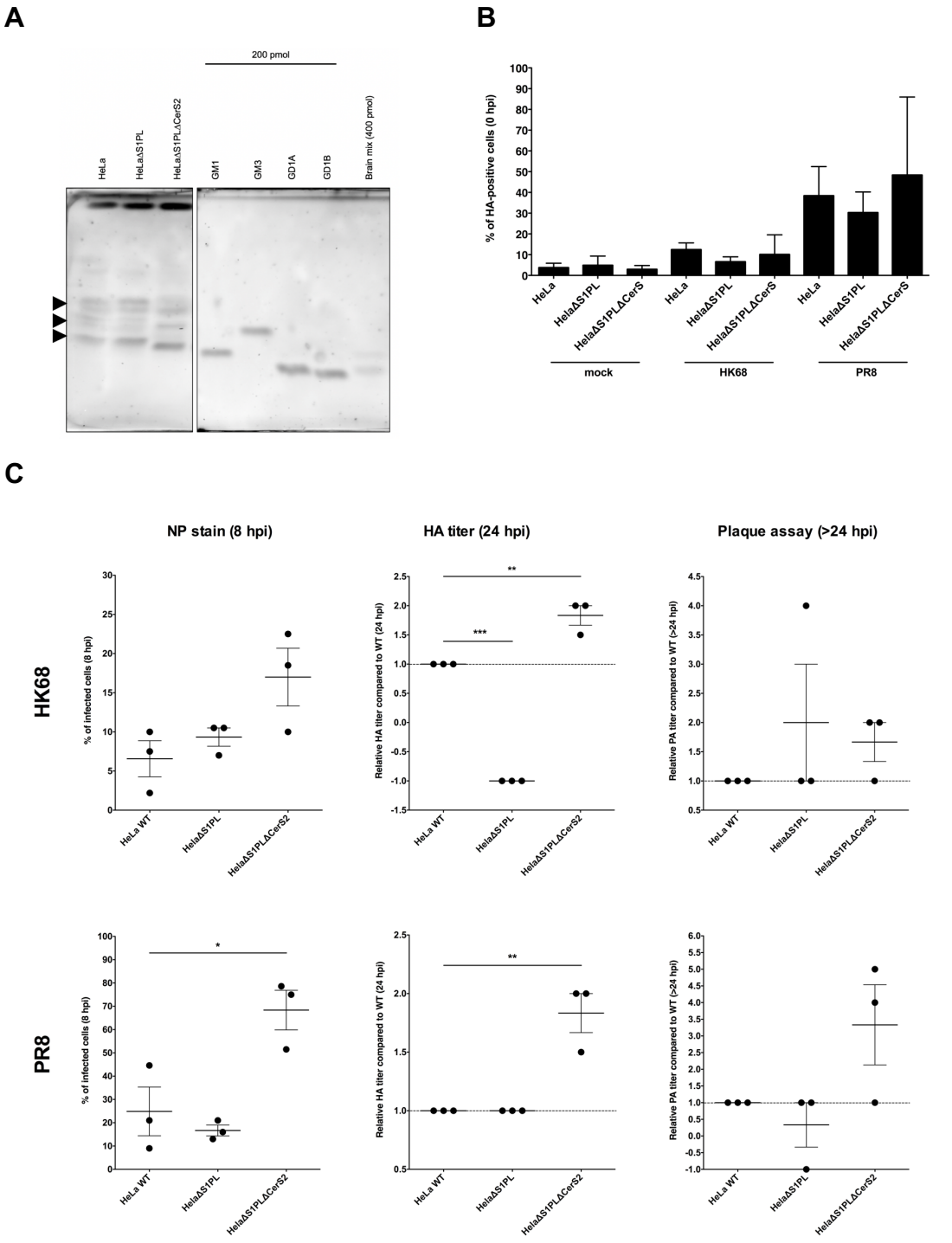

Figure 3.28: Impact of a CerS2-KO at different stages of infection in HeLa cells.

(A) To assess the GSL profile of HeLa and HeLa KO cells, a TLC was performed (10^6 cells used). Black arrows indicate bands which are aberrant in the CerS2-double KO (compared to HeLa WT and the *SGPL1* KO). (B) Cells were infected for 30 min on ice with either the PR8 or HK68 IAV strain (MOI of 1). HA-positive cells were counted via FACS. Data represents the mean ± SEM of three independent experiments; ONE-way Anova with subsequent Dunnett's multiple comparison test performed (WT vs. KOs). (C) Further, anti-NP stain, HA titer and plaque assay (the latter on MDCK cells) was performed at the indicated hpi. Data represents the mean ± SEM of three independent experiments; ONE-way Anova with subsequent Dunnett's multiple comparison test (WT vs. KOs) performed. GM1= monosialoganglioside, GM3= monosialotrihexosylganglioside, GD1A= disialoganglioside 1A, GD1B= disialoganglioside 1B.

ganglioside GM1b for example has been shown to serve as entry receptor for IAV[319,320]. Besides a role of the sphingolipid headgroup, the chain length of respective GSL might also influences IAV entry. As observed for SM (Figure 3.26), ceramide and hexosylceramide (data not shown), the CerS2-KO also had an effect on the GSL species profile (Figure 3.28A). As indicated by black arrows, the band at the height of GM1 was slightly shifted in these cells. In addition, there were two faint bands visible at the height of GM3 in WT and S1PL-KO cells, but only the lower was detected in CerS2-KO cells. The same was observed for the bands indicated by the highest arrow. Concerning the attachment of IAV, no significant difference was seen between HK68- and PR8-infected WT and KO cells; yet, the PR8-infected CerS2-KO showed the highest percentage of HA-positive cells (Figure 3.28B). Furthermore, infection efficiency (8 hpi), viral particle release (24 hpi) and infectivity (>24 hpi) was re-evaluated by anti-NP stain, HA titer and plaque assay (PA) in HeLa, HeLa∆S1PL and HeLa∆S1PL∆CerS2 cells (Figure 3.28C). In general, PR8 showed higher amounts of viral particle attachment, as well as higher numbers of infected cells. Again, CerS2-deficient HeLa cells displayed increased numbers of infected cells and higher viral particle release, compared to WT and S1PL-deficient only cells. The released virions were also able to infect MDCK cells (PA assay), yet future experiments should address whether the amounts of released virions caused a higher PA titer, or if virions are more infectious. HK68-infected HeLa∆S1PL∆CerS2 cells also showed highest virus amounts and HA titer compared to HeLa WT cells, yet the difference in the PA titer was not as drastic as for PR8-infected double KO cells. In addition, HK68-infected HeLa∆S1PL cells displayed a lower HA titer, but not PA titer compared to WT cells.

Based on the observation that the CerS2-KO might have a pro-viral effect, CerS2 rescue experiments were performed. To this end, CerS2-deficient cells were transfected with a CerS2-encoding plasmid (nontagged CerS2). Long-chain SLs could be restored by the CerS2 rescue in transfected *CERS2* KO cells, as illustrated by the presence of the SM24 band after pacSph-labelling and subsequent TLC analysis of HeLa, HeLa∆S1PL and HeLa∆S1PL∆CerS2 -/+ CerS2 cells (Figure 3.29A). The CerS2-mediated rescue decreased the

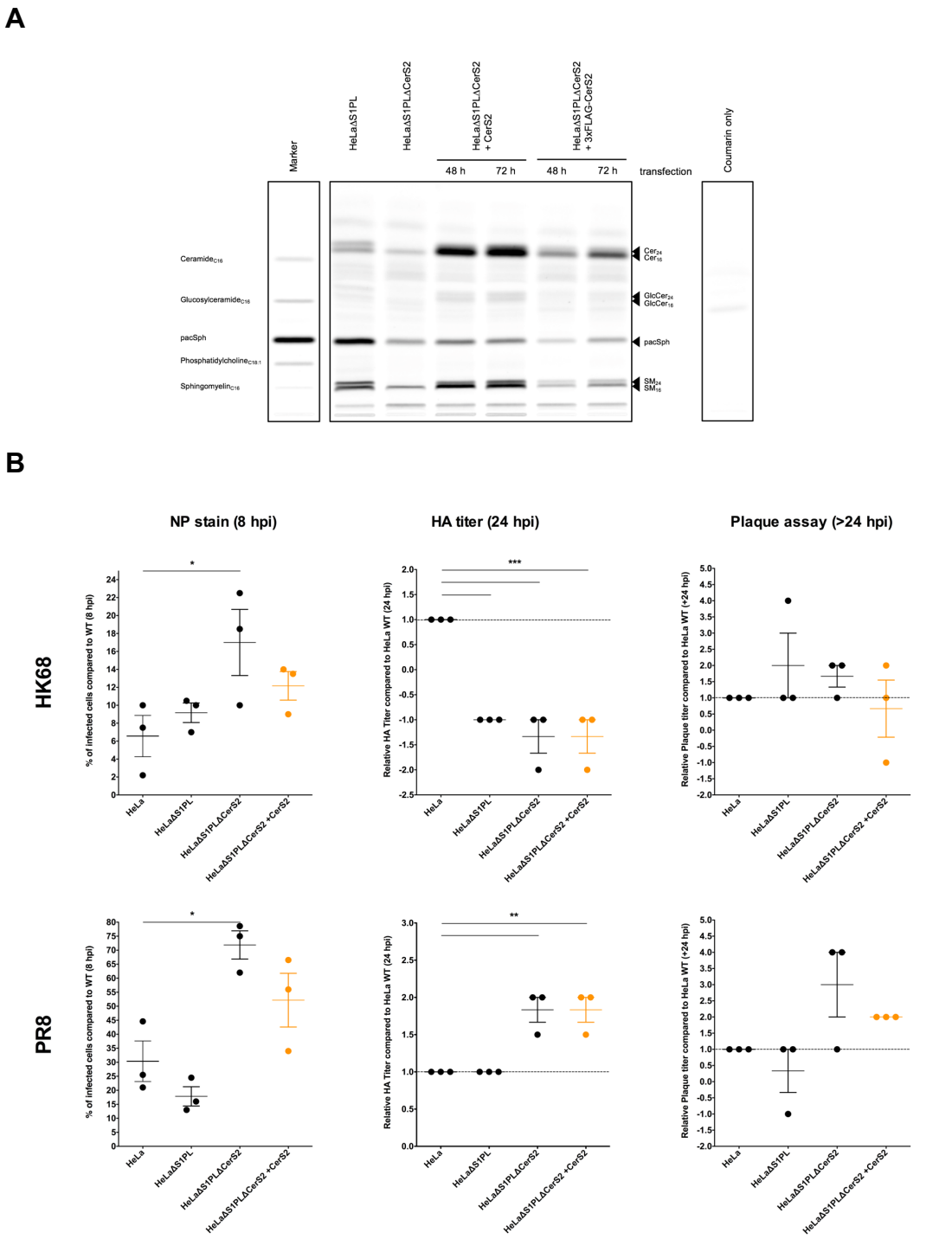

Figure 3.29: CerS2-mediated rescue experiments in IAV infected HeLa cells.

(A) HeLaΔS1PLΔCerS2 cells were transfected for either 48 or 72 h with non-tagged or tagged CerS2 and lipid extractions of pacSph-labelled cells (3 µM, 4 h) applied on TLC, together with extractions from non-transfected HeLaΔS1PL and HeLaΔS1PLΔCerS2 cells. (B) The amounts of infected cells as well as HA titer and PA assay was determined in PR8- and HK68-infected HeLa cell lines (MOI of 1 and 2, respectively). For rescue experiments, non-tagged Cers2 was used. CerS2-rescued samples were infected at 48 h transfection. Data represents the mean ± SEM of three independent experiments; ONE-way Anova with subsequent Dunnett's multiple comparison test (WT vs. KOs) performed.

amounts of infected cells compared to CerS2-deficient HeLas, in both PR8- and HK68-infected cells. The PA titer was also lowered again in the respective

rescue condition in PR8-infected cells. Since no selection of transfected cells had been performed, the impact of a CerS2 rescue might even be stronger, because the number of infected CerS2-double KO cells was still higher as in the WT. In addition, cells were infected at 48 h transfection, where restoration of VLC-SLs was not as efficient as after 72 h transfection (data not shown).

Recent findings have suggested that ablation of CerS2 leads to an accumulation of sphinganine in mouse livers[321]. Likewise, a CerS2-KO in HeLa and A549 cells resulted in an increase of sphinganine (Spg) and sphingosine (Sph) compared to WT and *SGPL1*-deficient cells (see **section 7**, Figure 7.4). In line with this, Spg-containing SM C16 species (SM C34:0), also referred to as dihydrosphingomyelin (DHSM C16 or DHSM (d18:0/16:0)), were, although not significantly, elevated in the HeLa∆CerS2-single and double KO (≈15%) compared to WT cells (≈9%) (Figure 3.26). DHSM C16 has been shown to be increased in the viral particles of HIV, VSV and SFV in comparison to (the PM of) the host cell[113,235]. DHSM C16 species also seemed to be more abundant in IAV-infected MDCK cells[114], and a constant increase in SLs with a Spg backbone (Dihydro-SLs, DHSLs) was detected in PR8-infected A549 cells up to 24 hpi[114,232]. Based on these observations, the amounts of VLC-SLs (≥C22) and the amount of DHSM C16 was compared in IAV-infected (PR8, HK68) HeLa, HeLa∆S1PL, HeLa∆S1PL∆CerS2 and CerS2-rescued cells at 0 and 24 hpi (Figure 3.30A). In general, the abundance of VLC-SM had a negative impact on DHSM C16 levels. The absence of CerS2 led to a markable increase in DHSM C16, which could be lowered again by a CerS2-mediated rescue. No significant difference of respective lipid levels was detected after 0 hpi and 24 hpi in infected versus mock WT and KO cells, however, an infection-unrelated, clear increase of DHSM C16 levels was observed in HeLa WT cells from 0 to 24 hpi. This effect was not seen in HeLa∆S1PL and CerS2-KO as well as CerS2-rescued cells (the latter exhibited a high standard deviation). In another experiment, the molar amount of DHSM C16 in PR8-infected HeLa WT and KO cells was determined and correlated to the number of infected cells (Figure 3.30B). The more abundant DHSM C16 was, the higher was the infection efficiency. Supplementation of CerS2-KO HeLa cells with a CerS2-encoding plasmid lowered the amounts of DHSM C16 and also the number of infected cells.

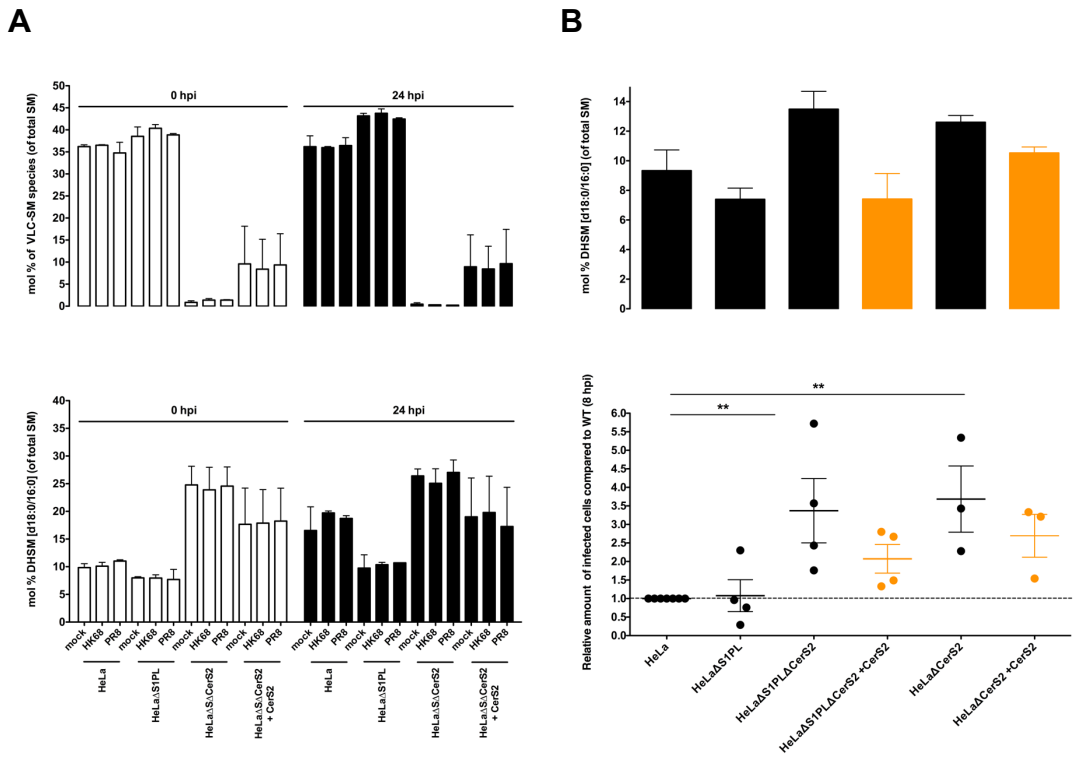

Figure 3.30: Comparison of VLC-SLs and DHSM C16 levels in infected and non-infected cells.

(A) The amounts of VLC-SMs (≥C22) were calculated relative to total SM levels; in addition, the levels of DHSM C16 were determined in infected and non-infected HeLa cells at 0 and 24 hpi (MOI of 1). Lipidomic samples were collected from the experiment shown in Figure 3.29C (24 hpi-samples, 0 hpi-samples not shown). Data represents the mean ± SD of two replicates. (B) DHSM C16 levels and the infection efficiency were determined in PR8-infected HeLa cells (MOI of 1) at 8 hpi. Data represents the mean ± SEM of three (upper panel) or more (lower panel, indicated by dots) independent experiments; ONE-way Anova with subsequent Dunnett's multiple comparison test (WT vs. KOs) performed. CerS2-rescued samples were infected at 48 h transfection. Lipidomic samples prepared and data provided by I. Leibrecht and C. Lüchtenborg, Brügger lab.

Conclusively, as DHSM C16 levels (and other DH-SLs) might affect (directly or indirectly) viral infection and the CerS-KO increases the abundance of DHSLs, it was difficult to independently study the role for VLC sphingolipid species in IAV infection in HeLa cells at this point. To test for a role of DHSL species in infection of HeLa WT cells, the drug 4-HPR/fenretinide was used. Fenretinide is an inhibitor of desaturase 1 (Des1), the enzyme that reduces *de novo* generated dihydroceramide to ceramide, hence leading to elevated DHSL levels[322].

Inhibitor treatment led to a significant increase in DHSM C16 levels, yet, a striking difference of infection efficiency in treated vs. non-treated cells was not observed (data not shown). Complementing on this, effect of CerS2 overexpression in HeLa WT cells (assumingly leading to a decrease in infected cells) remains to be investigated in future experiments.

A CerS2-KO was also generated in A549 cells to investigate whether the KO increases the IAV numbers of infected cells, as observed for HeLa *CERS2* KO cells. As in CerS2-deficient HeLa cells (Figure 3.26), VLC-SL species (≥C22) were almost absent in A549 KO cells, with a concomitant increase in C34:1 and C36:1 species and a decrease in C34:2 species (illustrated by the SM species profile, Figure 3.31A). The amount of DHSM C16 (SM C34:0) was slightly increased (≈11%) compared to WT cells (≈9%) (Figure 3.31A). The CerS2-KO

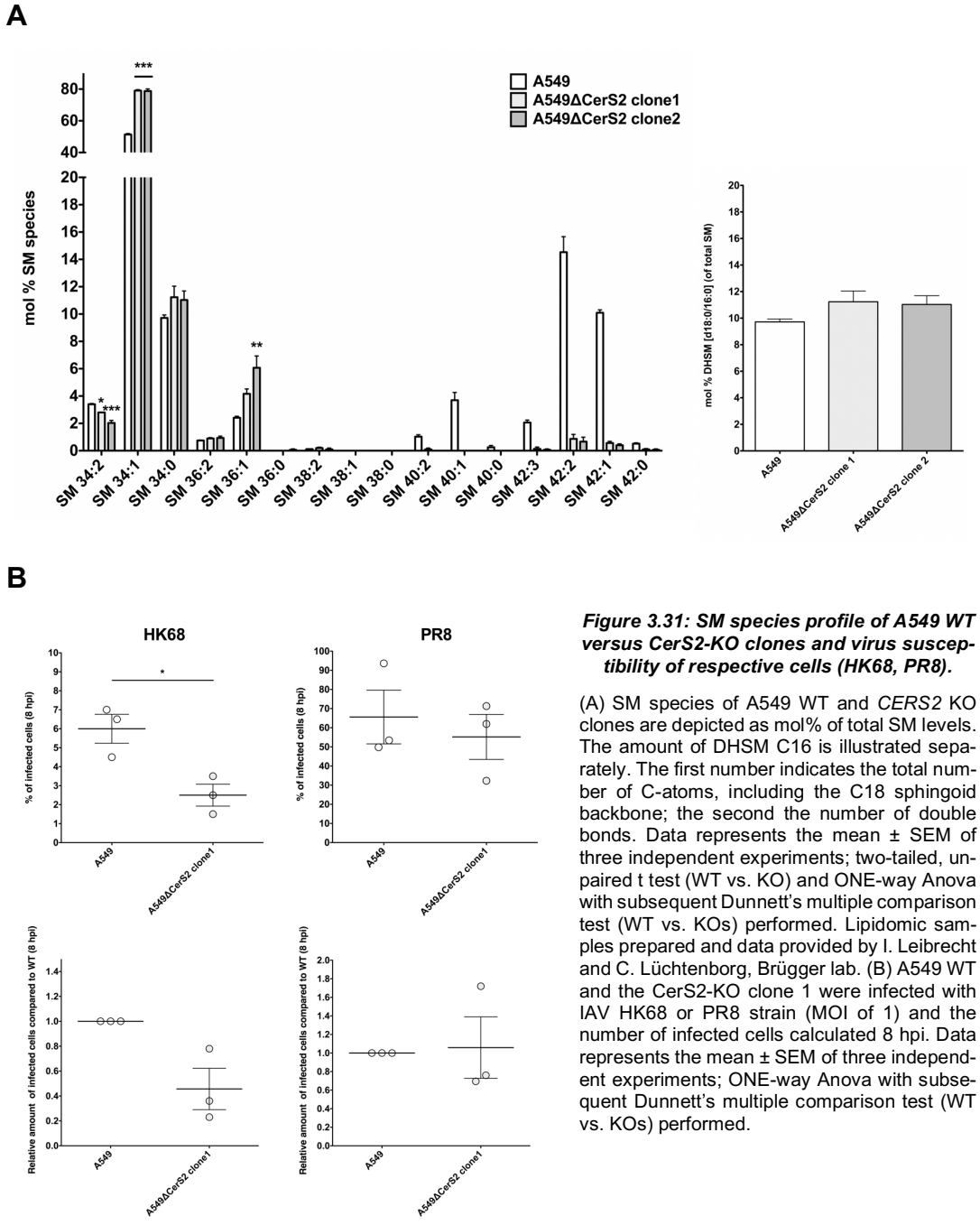

Figure 3.31: SM species profile of A549 WT versus CerS2-KO clones and virus susceptibility of respective cells (HK68, PR8).

(A) SM species of A549 WT and *CERS2* KO clones are depicted as mol% of total SM levels. The amount of DHSM C16 is illustrated separately. The first number indicates the total number of C-atoms, including the C18 sphingoid backbone; the second the number of double bonds. Data represents the mean ± SEM of three independent experiments; two-tailed, unpaired t test (WT vs. KO) and ONE-way Anova with subsequent Dunnett's multiple comparison test (WT vs. KOs) performed. Lipidomic samples prepared and data provided by I. Leibrecht and C. Lüchtenborg, Brügger lab. (B) A549 WT and the CerS2-KO clone 1 were infected with IAV HK68 or PR8 strain (MOI of 1) and the number of infected cells calculated 8 hpi. Data represents the mean ± SEM of three independent experiments; ONE-way Anova with subsequent Dunnett's multiple comparison test (WT vs. KOs) performed.

clone 1 was chosen for a subsequent infection experiment with the IAV strains HK68 and PR8. Surprisingly, the CerS2-KO displayed lower numbers of PR8- and HK68-infected cells (Figure 3.31B), opposite to the observation made in HeLa cells. The experiment was repeated (PR8 strain only) with two CerS2-KO clones (clone 1 and 2), including also a CerS2 rescue (Figure 3.32A). In this

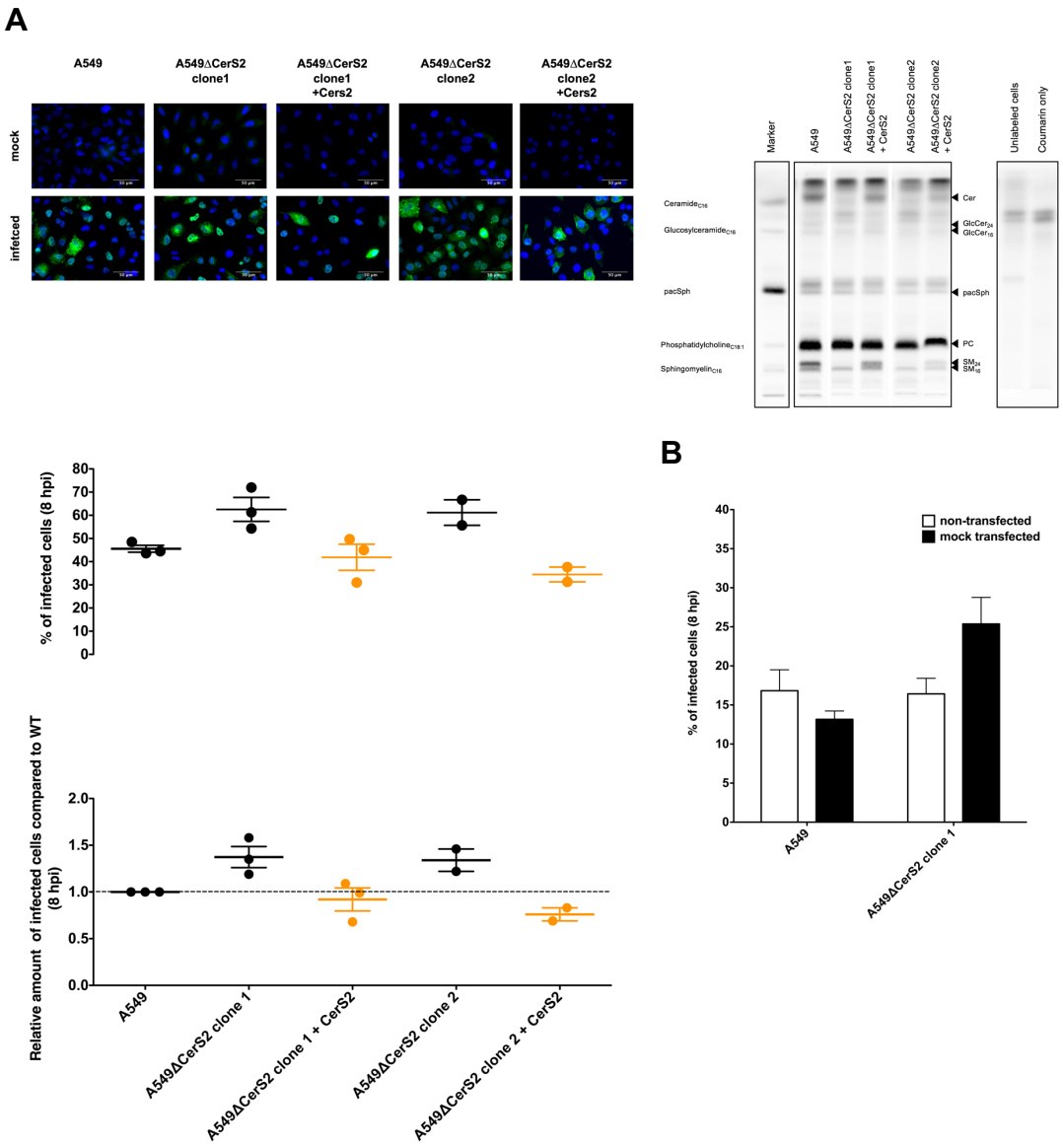

Figure 3.32: Infection of A549 WT and CerS2-KO plus Cers2-rescued cells with the IAV PR8 strain.

(A) A549 WT and CerS2-KO clones were infected with PR8 (MOI of 1) in a 6-well plate and the (relative) number of infected cells calculated 8 hpi (left panel). A CerS2 rescue was also conducted via electroporation of CerS2-KO clones with non-tagged CerS2; cells were infected at 48 h transfection. Scale bar= 50 µM, 40x magnification. Data represents the mean ± SEM of three independent experiments; ONE-way Anova with subsequent Dunnett's multiple comparison test (WT vs. KOs) performed. To qualitatively verify the CerS2-mediated rescue, non-infected cells were labelled with pacSph (3 µM, 6 h) after 48 h transfection and subjected to lipid extraction with subsequent coumarin-CLICK and TLC analysis (right panel). As *CERS2* KO cells have functional S1PL, pacSph is also incorporated into PC species[254]. (B) The infection efficiencies of A549 WT and CerS2-deficient clone 1 cells were analysed under normal and mock-transfected conditions (PR8, MOI of 1; analysis 48 h post-electroporation). Shown: mean, ±SD (n=2), 4 different frames counted per replicate.

set of experiments, both CerS2-KO clones showed an increase of PR8-infected cells compared to the WT, which was reduced again by transfection with a CerS2-encoding plasmid. In the previous experiment, CerS2-deficient A549 cells showed lower numbers of infected cells (Figure 3.31B). Notably, two different PR8 virus batches were used in the first (Figure 3.31) and second (Figure 3.32) experiment. Further, the quantitative rescue was not analysed by lipidomics, but CerS2-transfected CerS2-KO cells, although not as strong as the WT, produced SM C24 (Figure 3.32A, right panel). Since A549 WT cells were not mock-transfected (Figure 3.32A), it was investigated whether transfection in general affects infection efficiency (Figure 3.32B). According to the results, A549 wild type cells showed slightly less numbers of infected cells upon electroporation, whereas the number of infected cells was visibly increased in the A549 CerS2-KO cells. The latter observation might explain the CerS2-nonspecific increase in virus-loaded cells in the previous experiment; yet, a CerS2-rescue could reduce the amounts of infected cells (Figure 3.32A). It remains to be investigated if the CerS2-KO in A549 cells leads to an increase of IAV-infected cells, as seen for HeLa *CERS2* KO cells, and if DHSM C16 level are also correlated with the absence of VLC-SLs by supplementing A549ΔCerS2 cells with a CerS2-encoding plasmid.

In conclusion, a CerS2-KO-dependent increase in viral replication, as seen in HeLa cells, was not reproduced in A549 cells. Additional experiments regarding the putative role of CerS2 for IAV infection are required and discussed in **section 4.3.**

4 Discussion

In this thesis, roles of sphingolipids in IAV replication were investigated via three different approaches, namely i) the analysis of putative interactions of viral (transmembrane) proteins with SLs, (ii) the proteome-wide mapping of SL-host protein interactions, and (iii) the analysis of the role of very long chain SLs for viral propagation.
In the following, the results obtained will be discussed separately for each approach.

4.1 Putative interactions of viral transmembrane proteins with SLs

The idea that Influenza proteins might interact with SLs in the context of viral assembly and budding processes aroused from several findings (see **section 2.3.3** and **2.3.4**). Although crucial raft-targeting features of HA have been identified, recruitment of NA to sites of IAV assembly is less explored (see **section 2.3.3**). The N-terminal region of NA includes the cytoplasmic domain (CT), followed by the TMD, the stalk and the extracellular globular/enzymatically active head domain[221]. The aa residues 1-6 are highly conserved among all IAV NA subtypes; however, diversity occurs from aa position 12 on, and only NA1-6 share the same aa until position 11[116]. Motifs for apical transport have been postulated to be situated within the TMD of NA proteins, specifically within the part facing the exoplasmic membrane leaflet upon insertion into PMs[220,323,324]. A consensus sequence (aa 1-40) construct of NA subtype 1, only possessing the CT and TMD domain, has been shown to comprise a SL-binding signature similar to the one identified in the SM-interacting p24 protein[106], which was not present in the NA2 and NA8 consensus sequences[116]. It was hypothesised that differential SL-binding potentials of viral NA proteins from different IAV subtypes might lead to distinctive replication and spreading abilities [116]. Specifically, compared to the NA2 and NA8 subtype, the putative SL-interacting motif found in NA1 might contribute to a more efficient apical sorting in infected host cells. NA2 also possesses features for SL-binding within the TMD, yet it lacks the characteristic SL-binding signature found in p24[116].

First, consensus sequence constructs of NA subtype 1, 2 and 8, were re-evaluated with respect to cell surface transport kinetics in HeLa cells (see Figure 3.2). In agreement with Ernst *et al*.[116], NA1 was more abundant at the plasma membrane (PM) after 48 and 72 h transfection compared to NA2 and NA8 (see Figure 3.2). SL-interaction of FLAG-tagged NA-EGFP constructs was validated by metabolic labelling of transfected HeLaΔS1PL cells with pacSph, and subsequent enrichment of these proteins via FLAG-IP after Alexa647-CLICK (see **section 3.1.1**)[250,254]. However, the analysis of SL interactions of viral proteins turned out to be technically challenging. For example, high background signals remained in all pulldown fractions, most probably due to non-specifically labelled proteins (see Figure 3.3A). To decrease these background signals, NA variants were specifically enriched via interaction with biotin-clicked pacSph derivatives and subsequently subjected to anti-FLAG immunoblotting in a second experiment (see Figure 3.3B). This method did prevent the appearance of additional signals originating from the eluted, bead-coupled anti-FLAG antibody (corresponding to the light and heavy chain) that partially interfered with the signal of overexpressed proteins (specifically p24). A further limitation of the Alexa647-CLICK approach that was overcome with the biotin-CLICK method is that the Alexa647 dye confers an additional negative charge, and hence clicked proteins run slightly faster than their non-clicked counterparts in SDS-PAGE. Therefore, the overlap of protein signals recorded in the 700 (here: Alexa647) and 800 (here: anti-FLAG) channel might not be 100% accurate.

To reduce unspecific protein-sphingolipid interactions, the pacSph labelling concentration was reduced from 6[254] to 3 µM, resulting in a lower intracellular amount of total pacSLs. Unfortunately, despite the change in the experimental approach, PD efficiencies of NA1, NA2 and NA8 were still highly variable (see Figure 3.3B). Compared to EGFP, p24 and Asgr1, the expression of NA-EGFP-FLAG variants was quite low, and faint protein signals in the input and PD might have led to inaccurate calculations of PD ratios, especially in case of NA8. Here, only two biological replicates could be used for analysis. Indeed, according to mean values of PD efficiencies of NA1, NA2 and NA8, the latter exhibited highest SL binding potential and NA1 lowest. This result is in contrast to the data reported[116]. Due to these technical challenges, NA consensus sequence variants were not further studied.

The next goal was to investigate SL-binding of viral full-length membrane proteins (HA, NA and M2 from the IAV strain RD6 and HK68; see **section 3.1.2**) in order to determine if SL-binding might confer advantages, for example in terms of more efficient cell-surface delivery of a specific subtype, as has been shown for the consensus CT-TMD sequence of NA subtype 1[115,116]. Tagging of viral full-length proteins should be done in order to 1.) simplify immuno-based detection and adapt protein expression levels and 2.) to enable affinity purification of viral proteins.

Tag-based detection of HA3 and M2 from the HK68 as well as NA1 and M2 from the RD6 strain after overexpression in HeLa cells was possible, but very low for NA2 (HK68) and not possible for HA1 (RD6), even after enrichment via FLAG-IP (see Figure 3.5A-B). Protein tagging can become challenging if N- or C-terminal epitopes impair protein folding and function (such as post-translational modifications or trafficking), or affect protein-protein interactions[325]. Hence, no further experiments were conducted in order to optimise tag-based detection of IAV TMD proteins, and SL-interaction of viral proteins has been eventually investigated based on detection of native proteins (see **section** Error! Reference source not found.).

Among other viral proteins, HA and NA could be identified via MS-analysis in the SL-binding protein pool of IAV-infected A549ΔS1PL cells (see Table 3.6). Consequently, PR8- and HK68-derived HA and NA were investigated for SL-interaction after 8 and 12 hours post-infection (hpi) in A549ΔS1PL cells (S3-10 clone, see Figure 3.24), as literature also suggests the requirement of the SM biosynthetic pathway for cell-surface transport of these proteins[115]. At 12 hpi, the HA3 protein from IAV HK68 showed a stronger SL-interaction as HA1 from PR8. The PD efficiency of NA1 (PR8) via pacSLs was so far only assessed in a preliminary experiment, but showed an increased interaction over NA2 (HK68). The latter observation might strengthen the hypothesis that NA1 possesses a SL-binding motif within the TMD similar to p24, which is lacking in NA2, resulting in accelerated cell-surface targeting[116]. It could be further speculated that SL-binding efficiency is distinctive for homologous glycoproteins (here: HA3>HA1 and NA1>NA2) of different IAV subtypes, with a yet unknown function[115]. Interestingly, the apparent molecular weight observed after immunoblotting of homologous TMD proteins derived from different IAV subtypes

varied (see Figure 3.24; HA1 vs. HA3 and NA1 vs. NA2). This might be related to different glycosylation patterns of viral proteins[166,326], as well as oligomer formation[327], both affecting the electrophoretic mobility of proteins and hence the apparent molecular weight in SDS-PAGE.
The M2 protein from the HK68 strain also showed a slight signal in the PD of UV-irradiated, pacSph-fed cells after 12 hpi (see Figure 3.24). M2 comprises a well-defined cholesterol-binding motif that enables the scission event in the viral budding process (see **section 2.3.3** and **2.3.4**), but studies addressing a potential interaction of M2 with SLs are lacking so far. SL-interaction of the NP protein, although identified in the proteomic experiment, could not be detected at that time point. Raft-targeting of NP has been reported[227], yet NP does not possess a TMD. The NS1 protein, also present in the proteomic hitlist (Table 3.6), was not investigated for SL-interaction.

In summary, although this study re-capitulated that truncation variants of NA subtypes, only possessing the CT and the TMD, exhibited different PM targeting kinetics[116], increased cell surface transport velocity of NA1 could not be related to enhanced SL binding. Nevertheless, metabolic labelling of IAV-infected, S1PL-deficient A549 cells with pacSph suggested that HA and NA interact with SLs, which might become relevant at later stages of infection (see Figure 3.24), and contribute to IAV assembly processes[115]. However, further studies are needed to (i) validate and re-capitulate these observations, (ii) to determine if an enhanced SL-interaction might promote cell-surface targeting of these proteins (as suggested for NA subtype 1 and 2)[116], which could contribute to increased spreading abilities *in vivo*, and (iii) to determine whether SL-interaction of viral proteins triggers their recruitment not only to the PM, but also to sites of viral assembly. Recruitment to budding platforms and SL-interaction could be non-overlapping functions, and the latter might solely serve to increase the rate of anterograde transport towards the cell surface[115,116].
Thus, if SL-interaction of viral proteins can be significantly re-capitulated, a future perspective might include to identify the minimal motifs required for SL-binding, and to investigate the outcome of the loss of SL-binding on PM targeting and eventually on viral propagation. SL-species specificity can be determined by targeting individual CerS proteins and is discussed in **section 4.3**.

The elucidation of the requirement of distinct SL classes and species for viral replication would be of particular interest in the context of therapeutical treatment of IAV infections.

4.2 Exploring the role of SL-binding host proteins in IAV infection

An unbiased proteomic SILAC screen was performed to identify SL-binding host proteins which might be implicated in early and late stages of IAV infection (see **section 3.2**). Certain aspects of this screen will be discussed in the following.

4.2.1 CRISPR-mediated *SGPL1* KO

First, a CRISPR-based *SGPL1* KO was conducted in A549 cells according to Gerl *et al*.[254]. An active S1PL enzyme would otherwise mediate the irreversible degradation of pacSph-derivatives (pac-Sph-1-P) into ethanolamine-1-phosphate and (pac)hexadecanal (see Figure 2.3)[55,254,328]. (Pac)hexadecanal is further metabolised to (pac)palmitoyl-CoA and can hence be incorporated into G(P)Ls[328]. The KO of *SGPL1* disrupts the SL-glycerolipid hub, and thus allows to specifically monitor only protein-sphingolipid interactions.

Two *SGPL1* KO clones (S2-6 and S3-10) were chosen for further characterisation. Sequence analysis showed that S1PL was strongly truncated in both A549 *SGPL1* KO clones. The loss of enzymatic function was further validated via TLC. Labelling of A549 *SGPL1* KO clones with pacSph showed that the paclipid is exclusively incorporated into SLs, hence indicating a successful functional KO of the respective enzyme in both CRISPR clones.

In addition, the impact of the *SGPL1* KO on lipids and sphingoid bases was characterised (see Figure 3.8 and Figure 7.4). Notably, the S1PL-KO is associated with a significant increase in sphingosine-1-phosphate (S(ph)-1-P) (see Figure 7.4), an observation also made in HeLa[254] and MEF[329] *SGPL1*-KO cells, most likely because S1P is not degraded by the enzyme (see **section 2.2**).

SL classes were more or less unchanged in HeLaΔS1PL compared to WT cells[254], but in MEF *SGPL1*$^{-/-}$ cells, the lipid levels of Cer were significantly decreased with a concomitant, significant increase in HexCer[250]. No significant alterations in SM, Cer and HexCer could be detected in A549 *SGPL1* KO cells,

and only a few SL species, mainly C24, were slightly changed in KO cells compared to the A549 WT (see Figure 3.8B-D). Here, the respective SL species were mostly decreased in *SGPL1* KO cells. In livers of *SGPL1* KO mice, an increase in C14-C18 Cer species was observed with a simultaneous decrease in C20-24 species, which was suggested to be related to an increase in S1P and a corresponding inhibition of CerS2 function[330]. In contrast, HeLaΔS1PL cells exhibited in general lower levels of C14-C18 SL species, and C20-C22 SL species were elevated compared to the WT[254]. Conclusively, the impact of the *SGPL1* KO on the SL class profile is distinctive for different cell lines for reasons (still) elusive.

A deficiency of functional S1PL has also been reported to increase the intracellular cholesterol content in MEF cells compared to WT cells[329]. However, cholesterol levels were neither affected in A549S1PL cells (see Figure 3.8A) nor in HeLaΔS1PL cells[254].

The comparison of whole cell proteomes of A549 WT versus A549ΔS1PL cells has not been performed in the context of this study. Comparison of whole cell proteomes would be useful to validate if proteins of interest show an increased or decreased protein expression compared to WT cells. Protein expression of ITGB1, SLC1A5, RAB11A and SLC25A11 was investigated in S1PL-deficient A549 compared to WT cells via immunoblotting. However, no significant difference could be observed (data not shown). The comparison of HeLa vs. HeLaΔS1PL whole cell proteomes revealed that only ≈1% of the total proteome was changed in S1PL-deficient cells, including false-positives[254].

In summary, the loss of functional S1PL of the A549 cell clones investigated did not markedly impact the cellular lipid class composition, except for the elevation of bioactive Sph-1-P. Yet, another noteworthy observation was that the A549ΔS1PL S2-6 clone exhibited a remarkable enhanced basal gene and protein expression of the antiviral protein IFITM3 (see Figure 7.12 and Figure 7.13). IFITM3 contributes significantly to basal resistance against IAV and other viruses, and is induced by IFN type I and II-mediated responses early in infection[294,331]. Since IFITM3 protein levels in the S3-10 clone were more or less unchanged compared to A549 WT cells, IFITM3 upregulation in clone S2-6 is hence probably an unspecific result of the CRISPR/Cas9-mediated knockout.

4.2.2 pacSph metabolism during IAV infection

SL-protein interactions have been suggested to contribute to regulation of membrane protein activities[22,106,107]. To identify protein-SL interactions, the metabolic labelling of cells with pacSph has been shown to be a suitable approach[250,254]. As a prerequisite, the photoactivatable group (here: diazirine) and the clickable group (here: alkyne) were designed to be as small and hydrophobic as possible to imitate their natural equivalent[250,293]. Importantly, the pac-containing sphingoid backbone (pacSph) is maintained in SL anabolic and catabolic processes[250,254]. Interaction can be monitored for both membrane and soluble proteins. The disturbance of protein-lipid interaction is minimised due to the fact that clickable lipids are covalently linked to a purification or reporter tag after UV-induced crosslink[248].

The observation that pacSph is metabolised into various SL classes (see Figure 3.7) implies that it is readily taken up and transported to the ER, where it is used as substrate for CerS[250]. In HeLa cells, pacSph has been shown to be strongly incorporated into SM, and after 4 h labelling, pac-SM levels already reached their equilibrium[254]. In contrast, Cer and HexCer (GlcCer and GalCer) species only slightly increased between 4-12 h labelling, and total pac-Cer as well as HexCer levels were significantly below pac-SM contents[254]. Predominant incorporation into SM can be explained by the fact that SM is the major cellular SL class (see **section 2.2**). In A549ΔS1PL cells, pacSph also seemed to be predominantly incorporated into SM (as shown for the S2-6 clone in Figure 3.7B-C). There was a steady increase in pac-SM content up to 24 h; pac-Cer level slightly increased from 4-6 h, then slowly decreased, and HexCer species remained more or less unchanged (see Figure 3.7C). The amount of free pacSph continuously decreased up to 24 h labelling due to its metabolisation to complex SLs[254]. Interestingly, it was observed that the amount of pac-long chain SLs (pac-SM C24) markedly increased over time compared to the pac-short chain (pac-SM C16) species (see Figure 3.7B). However, the lipidome of A549 and A549ΔS1PL cells is more abundant in C16 SM species than in SM C24 (see Figure 3.8, determined via ShinyLipids). It has been shown that an increased cell density induces gene expression of several SL-metabolising

enzymes, such as CerS2 and CerS4 (see Figure 3.25), and is thus associated with elevated levels of long-chain SL classes[332]. This might explain why pacSph is preferentially incorporated into in (SM)C24 species up to 24 h labelling. Incubation of cells in high glucose DMEM also resulted in a preferential incorporation of pacSph into C24 species (see Figure 7.2). Higher levels of glucose might trigger metabolic downstream processes (such as glycolysis), stimulating cell growth and hence cell density, further resulting in elevated expression of CerS2[3,332]. Notably, glycolysis is interconnected with serine biosynthesis, the precursor for *de novo* generated SLs (see **section 2.2**)[333].

In summary, the SILAC-based proteomic screen might preferentially lead to the identification of SM-interacting proteins, as pacSph is mainly incorporated into SM, followed by Cer and GlcCer (see Figure 3.7A). For the SILAC-based proteome-wide mapping of protein-SL interactions, a labelling condition was chosen where pacSph-incorporation into C16 and C24 SL species has been observed to be more or less equal (6 h, see Figure 3.7A, red frame, and B). Nevertheless, the impact of cell density and SILAC cultivation media on pacSph metabolisation was not experimentally verified for the proteomic experiments and e.g. could, referring to the aforementioned observations, shift pacSph incorporation into long-chain SL species (see Figure 7.2). Importantly, the infection of cells with IAV might also influence pacSph incorporation compared to non-infected conditions at different hpi. This is currently investigated, as it could affect e.g. the pacSL-mediated enrichment of a specific protein in the mock vs. infected condition, depending on its specificity for a specific SL class or species.

4.2.3 Data quality of the proteomic screen

As illustrated in Figure 3.6, non-infected cells were incubated in “light” (Arg0/Lys0), infected cells in “heavy” (Arg10/Lys8) and the background control in “medium” (Arg6/Lys4) SILAC media. To determine the background of non-specifically enriched proteins, the (infected) background sample was not subjected to UV crosslink, hence preventing the covalent crosslinking of pacSLs to proteins (see Figure 3.6). Proteins identified in the background control were not

considered for the calculation of SILAC ratios of infected/mock samples. Notably, the "light" (Arg0/Lys0) condition is conventionally used as background control, since all contaminants (such as keratin) derive from "light".

Due to the S1PL KO-unrelated, but significantly elevated expression of IFITM3 in the A549ΔS1PL S2-6 clone compared to A549 WT cells (see Figure 7.12 and Figure 7.13), mainly the results of the PR8-screen conducted in A549ΔS1PL S3-10 clone cells will be addressed. Here, the enrichment, recovery and subsequent preparation for MS analysis of putative SL-interacting proteins was modified compared to the SILAC screens performed with A549ΔS1PL S2-6 clone cells (see **section 3.2.2** and **3.2.3.1**). In the latter screens, proteomic samples were enriched via NeutAvidin beads (see **section 5.2.6.3**), which resulted in considerable avidin contaminations within eluted protein fractions. SL-binding proteins are quite low in abundancy compared to whole cell proteomes (≈1-2%)[250,334], hence highly abundant contaminations might aggravate identification of these proteins. For the PR8 screen conducted in A549ΔS1PL S3-10 clone cells, lipid-binding proteins were enriched and digested on trypsin-resistant avidin beads (G. Sigismondo, Krijgsveld lab, in preparation; see **section 5.2.6.5**). Only proteins with a 4-fold enrichment over background were considered as "valid", putative SL-binding proteins (see **section 3.2.3.2**). The number of identified proteins within mock or infected samples at 1 or 12 hpi was below 100 (see Table 7.5). In comparison, 186 SL-binding proteins were found to be significantly enriched over non-UV treated samples in S1PL-deficient MEF cells[250]. Notably, the amount of putative SL-binding proteins might vary dependent on species origin, cell line and cell type used.
Unfortunately, SILAC proteomic screens conducted in both A549ΔS1PL S2-6 (see **section 3.2.2** and **3.2.3.1**) and S3-10 clone cells (see **section 3.2.3.2**) showed strongly variable SILAC ratios among replicates. Technical limitations, that can derive from the quality of MS analysis and data evaluation, generally play a minor role in the variation of SILAC ratios within a given experiment[259]. SILAC ratios can be affected by an unequal ratio of the mixed conditions, which is a prerequisite for the accuracy of SILAC experiments[259]. Furthermore, virus infection might modulate the expression levels of host proteins, as reported for IAV[258,335], resulting in distinctive quantitative amounts within the mock and

infected condition[259]. Notably, endogenous protein levels of protein candidates (ITGB1, SLC1A5, RAB11A and SLC25A11) validated for SL-binding and tested in transient KD experiments (see **section 3.2.4.** and **section 3.2.5**) were determined at 12 hpi in infected and non-infected A549 cells. No significant changes could be observed under the conditions tested (PR8 strain, MOI of 1, ≈22% infected cells; data not shown). Host-proteome changes could be correlated with the infection efficiency, since IAV infection induces a global shutdown of host protein translation[335]. However, with regard to SILAC ratios of the proteomic screens, the number of infected cells varied among biological replicates in HK68- and PR8-infected A549ΔS1PL S2-6 clone cells (see Figure 3.10 and Figure 3.13), but not in replicates of PR8-infected A549ΔS1PL S3-10 clone cells (see Figure 3.18). Still, statistical analysis of SILAC ratios was not possible for all screens.

Nevertheless, although conducted with different S1PL-deficient A549 KO clones, protein hits identified in the SILAC proteomic screens of PR8-infected cells partially overlapped (see Table 3.3 and Table 3.4 as well as Table 7.4 and Table 7.5). Certain proteins of that list could also be pulled down via pacSLs in murine cells (MEF cells)[250], such as ITGB1 and SLC1A5.

Hence, certain SL-binding proteins were validated regarding their SL-binding potential and functional implication in viral replication.

4.2.4 Protein hits identified in the SILAC proteomic screen

A study dedicated to identify SL-binding motifs in mammalian TMD proteins revealed that proteins harbouring a SL-binding motif are mainly located at the PM, which is characterised by a high concentration of SLs[6,107].

According to the results obtained from the A549ΔS1PL S3-10 clone SILAC screen, most protein candidates are TMD proteins with a single TMD (like p24)[107], and also mainly localised to PMs (see Figure 3.19)[107]. The enrichment of primarily membrane proteins speaks for the reliability of the screen, because the whole cell proteome of A549 cells contains only ≈15% TMD proteins[295]. Yet, this screen also proposes the presence of soluble SL-binding proteins, e.g. cytosolic proteins or those secreted into the extracellular matrix (ECM)[107]. Cytosolic, non-TMD proteins, such as nucleolin (NCL), vimentin (VIM) or annexin

A2 (ANXA2) (see Table 3.3) might interact with soluble, bioactive SLs, like Sph/Spg and S1P (see **section 2.2**). Protein-S1P interactions might be increased under certain physiological conditions, such as infection. However, since Sph and S1P levels are elevated in *SGPL1* KO compared to WT cells, protein interactions with these lipids might not be a specific result of infection and will have to be evaluated in future experiments (see **section 2.3.4**).

Several proteins, which were already described in the context of viral and specifically IAV infection, were probed for SL-interaction (see Figure 3.15, Figure 3.16, Figure 3.17 and Figure 3.20; Table 3.3 and Table 3.5). In the following, only those proteins will be discussed which were also tested in siRNA-mediated transient knock down (KD) experiments in IAV-infected A549 cells (see **section 3.2.5**).

RAB11(A) RAB11 is an organelle marker for recycling endosomes (REs), and mediates, together with other proteins, the (re)distribution of endocytosed cholesterol (and SLs) from early endosomes (EEs), late endosomes (LE) and lysosomes to cholesterol-enriched endocytic recycling compartments (ERCs), and finally back to the PM via the TGN[310,336,337]. The interaction of RAB11 with Rab11-FIP2 proteins is important for the organisation of lipid and cargo trafficking through REs [338]. RAB11 exists in two isoforms, and mainly RAB11A has been studied in the context of IAV infection (see **section 3.2.4**). Specifically, RAB11A has been implicated in apical trafficking of vRNPs, IAV assembly and budding processes and might be a host interactor of PB2 (see Table 3.5). It has also been demonstrated that IAV induces the formation of ERCs to support budozone formation[339]. RAB11 has been identified as a "valid" SL-interactor only at 12 hpi in infected cells (see Table 3.5). Since RAB11-positive REs are also crucial for intracellular SL transport[310], RAB11A might contribute to viral morphogenesis by redistribution of SLs to PMs[115]. However, SL-interactions were not observed in infected cells at 12 hpi (data not shown), and only pacChol-interaction, but not pacSph-RAB11A interactions were found in non-infected cells (see Figure 3.20). RAB11-positive organelles have been shown to traffic only certain SLs[310] and it is possible that the interaction with certain

pacSLs is below detection limit. Nevertheless, a transient KD of RAB11A did not result in a significant impairment of IAV replication (see Figure 3.22).

UGCG UGCG catalyses the transfer of glucose to ceramide, the first step in complex GSL synthesis (see **section 2.2**). UGCG was identified as a "valid" SL binder only in infected cells at 12 hpi (see Table 3.5). It has been reported that IAV-infected cells exhibit increased GSL-levels, and that GSLs are further enriched in viral envelopes (see **section 2.3.4**)[114,231], which might indicate a necessity for functional UGCG in viral assembly. However, SL-interactions of UGCG could not be validated (see **section 3.2.4**). In addition, transient KD experiments neither revealed an impairment of infection efficiency at 8 hpi nor decreased viral particle release at 24 hpi (see Figure 3.22). Virion formation also strongly depends on SM, and intact SM biosynthesis might more important for virion formation (see **section 2.3.4**). Indeed, the SM content has been reported to be increased in virions compared to cellular SM levels[231]. Surprisingly, interaction of the SM-synthesising enzyme sphingomyelin synthase 1 (SMS1) with pacSLs could only be observed in non-infected cells at 1 and 12 hpi (see Table 7.6).

SLC46A1, SLC25A11 and SLC1A5 A variety of members of the solute carrier (SLC) family was identified in the pool of SL-binding proteins (see Table 7.5). SLCs are divided into 65 families comprising more than 400 members, mostly located at PMs, but also other intracellular compartments[340,341]. They are involved in a variety of cellular processes, such as molecule transport across lipid bilayers, and are indispensable for cellular homeostasis, which makes them promising drug targets[341]. Some SLCs have been also identified as essential host factors for HIV (SLC46A1 and SLC35B2)[296,342] or IAV infection (SLC35A1)[305]. The mitochondrial ADP/ATP transporter SLC25A5 has been further reported to interact with the IAV-NEP protein[308].
No significant effect on IAV replication was observed after transient transfection of A549 cells with siRNA targeting SLC46A1 (see Figure 3.22). Notably, the detection of the native protein was not possible (see **section 3.2.4**), hence it cannot be ruled out that the transient KD was not successful. However, the mitochondrial 2-oxoglutarate/malate carrier protein (SLC25A11) markedly

restricted IAV replication (see Figure 3.22). The latter protein, like SLC25A5 (see above), was also identified as a putative interactor of NEP[309]. Interestingly, specifically mitochondrial proteins have been shown to interact with the vRdRP complex[307,308]. However, inactive mutations within the *SLC25A11* gene lead to severe disease, as it plays a key role in several metabolic processes, and SLC25A11 might thus be not suitable for drug target design[343]. Moreover, no (pac)lipid-binding could be verified for SLC25A11.

Among the investigated SLCs, a clear SL-interacting property could only be assigned to SLC1A5 (see Figure 3.22). Specificity of SL-interaction was further verified by FB1 treatment, which restricts pacSph metabolism by inhibition of CerS (see **section 3.2.4**). SLC1A5 did not show an interaction with pacFA, indicating that it is not located in a glycerophospholipid-enriched "lipid shell", as suggested e.g. for the integral membrane protein p24[106,293]. The p24 protein has been shown to interact with both pacSph- and pacFA-derivatives in overexpression experiments in HeLaΔS1PL cells[250]. Further, SLC1A5 showed only a slight interaction with pacChol, hence SLC1A5 could be localised to PM domains with a low cholesterol content (see **section 2.1.3**). Conclusively, SLC1A5 seems to have a specific affinity for SL-interactions only.
Endogenous SLC1A5 is mainly detected at ≈75 kDa in A549 cells (see Figure 3.22). In overexpression experiments conducted in HeLaΔS1PL cells, several bands were detected in immunoblot analyses (see Figure 3.15), likely corresponding to different glycosylation states during protein maturation as SLC1A5 is N-glycosylated along the secretory pathway, which is crucial for its PM targeting[344]. The ≈75 kDa band has been shown to be localised exclusively at PMs of A549 cells (data not shown), and only this form showed an interaction with pacSLs in transfected HeLaΔS1PL cells (see Figure 3.15). Thus, SL interaction of SLC1A5 likely occurs at PMs. However, although SL-binding of SLC1A5 was decreased at 12 hpi in A549-infected cells (see Figure 3.21), transient KD of SLC1A5 had no effect on viral replication (see Figure 3.22).

ITGB1 Integrins comprise a huge family of glycosylated, single-TM spanners[345]. Non-covalently associated heterodimers of alpha- and beta subunits are receptors for various ligands, including pathogens, and different

heterodimer assemblies are implied in distinctive cellular functions[345,346]. It was suggested that ITGB1 is localised to membrane rafts[347]. ITGB1-clustering has been reported to occur in (G)SLs-enriched microdomains, thus triggering the initiation of ITGB1-mediated downstream signalling[348].

For ITGB1, two bands can be detected in immunoblot analysis (see Figure 3.20, ≈100 and 150 kDa). It could be verified that the upper form is the PM-localised variant of ITGB1, which shows preferable interaction with pacSLs in comparison to the lower band (see Figure 3.20 and Figure 3.23). A previously performed bioinformatic screen published a list of putative SL-interacting proteins based on the presence of a putative SL-binding motif generated *in silico*[107]. The corresponding screen suggested that SL-interacting proteins are mostly localised to PMs. However, ITGB1 (and also SLC1A5) were not listed as putative SL-interacting proteins, which could indicate the presence of additional SL-binding motifs *in vivo*.

The role of ITGB1 in IAV infection has not been deciphered so far (see Table 3.3). A transient KD of ITGB1 resulted in a significant decrease of IAV-infected A549 cells at 8 hpi (see Figure 3.22). Furthermore, ITGB1 exhibited stronger SL-binding in infected cells at 1 hpi compared to 12 hpi (see Figure 3.21). Notably, a significant decrease of the upper, PM localised ITGB1 protein band was observed in infected compared to mock cells at 12 hpi (see Figure 3.21C). However, this is likely related to the global impact of IAV infection on cellular processes, which might impair trafficking of ITGB1 to the PM[258].

ITGB1 has been e.g. demonstrated to play an important role in HCV entry[284] and might also be relevant in early IAV replication stages. Further studies will be performed to address the role of the SL-interacting potential of ITGB1 for IAV propagation. Here, a CRISPR-based stable KO in A549 (and HeLa) cells will help to elucidate the impact of ITGB1 deficiency on IAV replication.

In summary, ITGB1 could be identified as a SL-binding protein with a putative pro-viral role for IAV propagation. However, only a few potential SL-binding proteins were validated (see Table 3.4 and Table 3.5) regarding their role in infection. Furthermore, certain proteins were only pulled down via interaction with pacSph-derivatives in the mock or infected condition (see Table 7.6) and might contain additional putative SL-interacting, anti- or pro-viral effectors.

Notably, since lipidome analysis did not reveal significant changes in infected vs. mock cells at 1 and 12 hpi (see Figure 7.9) and most changes in the lipidome[114,231] or implications of SL metabolism[75] were investigated and observed at 24 hpi, it might be considerable to also screen for SL-interacting proteins at that time point after infection.

An overview of the current and future experimental setup of the proteome-wide mapping of putative SL-binding proteins and the elucidation of their role in IAV replication is shown in Figure 4.1. (S1PL-deficient) A549 cells will be used for ongoing candidate validation (step 1-5). Yet, A549 cells possess an aberrant repertoire of cellular functions compared to primary respiratory cells[349]. Conclusively, SL-binding protein candidates should be further tested in cell systems closer to the *in vivo* situation, such as primary human bronchial epithelial cells (HBE) (step 6 in Figure 4.1)[264].

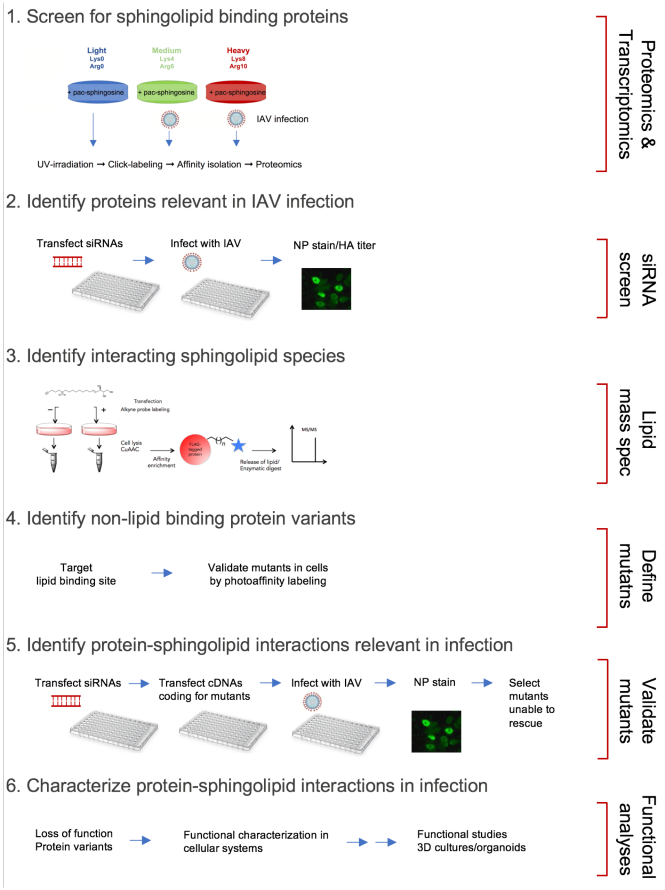

Figure 4.1: Experimental pipeline to further validate protein candidates.

The screen for putative SL-interactors (step 1) has been conducted in this study, as well as step 2 for some candidates. Steps 4-6 will be future perspectives, starting with ITGB1 (see text). Picture provided by B. Brügger.

4.3 The role of very long chain sphingolipids for IAV replication

In order to study roles of the lipid environment in the IAV replication, CRISPR-based, CerS-specific KOs were generated in HeLa cells. Each CerS is specific for the production of SLs with a certain acyl chain length (see Figure 3.25). Based on the observation that cellular long-chain (LC)-SLs increase during IAV infection (specifically, C20, 22 and 26 species)[231,232], the impact of CerS2 depletion for viral propagation was investigated in an unbiased approach, first in HeLa, then in A549 cells. CerS2 is responsible for the synthesis of C22 and C24 SLs, referred to as very long chain (VLC)-SL species (see **section 3.3**)[317].

CerS2-deficient HeLa cells displayed a higher number of infected cells than S1PL-deficient or WT cells, independent of the viral strain used (see Figure 3.28, NP stain). A CerS2-mediated rescue lowered the number of infected cells again (see Figure 3.29). Consequently, it should be further investigated at which stage CerS2-deficiency seems to support viral infection. The importance of acyl-chain length of lipid IAV entry receptors (such as the GSLs GM3 and GD1A, see **section 2.3.1**) has not been addressed yet, and HA has been only described to show specificity for the glycosidic linkage of sialoglycans (see **section 2.3.1**). The amounts of HA-positive cells were not significantly different between PR8- and HK68-infected WT and CerS2-deficient HeLa cells, although the GSL class profiles of these cells differed (see Figure 3.28A-B). Importantly, only the number of HA-positive cells can be counted via the FACS method; however, it is not possible to determine the amount of virus particles per cell. Furthermore, the number of attached virus particles might not correlate with the efficiency of virus entry. The latter should be determined in future experiments, e.g. by applying the beta-lactamase assay[305,350].

CerS2-deficient HeLa cells showed an increased virus load already at 8 hpi, suggesting that the effect of the KO targets early infection stages. Higher infection rates presumably also resulted in an increase in released virions, as demonstrated by the HA titer. Virus infectivity was measured using a plaque assay (PA); however high variations in the PA titer observed for the HK68 strain between experiments did not allow to draw conclusive results (see Figure 3.28 and Figure 3.29). For the PR8 strain, the PA titer was elevated in CerS2-

deficient cells and could be lowered again by a CerS2-mediated rescue, yet differences were not significant (see Figure 3.29).
An increased release of viral particles might indeed result in an elevated uptake of the IAV in the first infection round, as the lack of functional CerS2 was reported to elevate fusion and budding processes, related to changes in lipid packing[237]. Nevertheless, CerS2-depletion has severe impacts on the physical property of membranes, such as increased membrane fluidity and decreased membrane order, both a consequence of acyl chain length reduction and an increase in saturated FA moieties (see **section 2.1.3** and **2.2**)[237], which could affect viral envelope integrity. Therefore, in order to estimate a long-term pro-viral effect on CerS2-depletion, IAV virus derived from CerS2-KO cells have to be subjected to several rounds of infection in future experiments.

Notably, CerS2-depletion lead to a shift towards saturated SLs (SLs with a sphinganine backbone, see **section 2.2**). In A549 cells, the amount of free sphinganine (Spg) and Spg-1-P bioactive second messengers significantly increased in CerS2-KO compared to WT cells (see Figure 7.4).
DHSLs have been shown to increase in the context of IAV-infected A549[231,232] and MDCK[114] cells, and also in HIV infection[113], indicating a pro-viral function for the respective SL species. In particular, the increase of SM(d18:0/16:0) or DHSM C16 species was observed in the respective host cell systems[113,114].
In HeLa cells, a correlation between a lack of CerS2 (abundance of VLC SL(SM)-species), elevated DHSM C16 levels and higher numbers of infected cells was observed (see Figure 3.30). Specifically, a reduction of VLC-SM (as a consequence of CerS2-depletion) was associated with an increase in DHSM C16 (see Figure 3.30A), and higher viral titers (see Figure 3.30B). A CerS2-mediated rescue lowered the levels of DHSM C16, with a concomitant increase in VLC-SLs, and reduced the number of infected, transfected Hela *CERS2* KO compared to non-rescued HelaΔCerS2 cells (see Figure 3.30). Notably, DHSM C16 levels were almost 2-fold higher in HeLa WT cells after 24 hpi compared to 0 hpi (see Figure 3.30A). However, DHSM C16 levels were not significantly different in infected and mock WT cells and also not between infected and non-infected ΔS1PL, ΔS1PLΔCerS2 and ΔS1PLΔCerS2+CerS2 cells (see Figure

3.30A), indicating that the increase of the respective lipid species might not be related to IAV infection.

Taken together, these observations suggest that the abundance of (CerS2-generated) VLC-SLs might restrict the level of DHSM C16 and presumably DHSLs in general in HeLa cells (see Figure 3.30A). Interestingly, HeLa cells deficient of CerS5 or/and CerS6, the enzymes which produce short-chain SLs, have decreased DHSM C16 levels compared to WT cells (unpublished data, M. Gerl/D. Ostkotte, Brügger lab). It remains to be investigated if the CerS2- and CerS5/6 KO could have an impact on desaturase (Des) activity, the enzyme which concerts dihydroceramide (DH-Cer) to Cer and is hence implied in the cellular SL/DHSL homeostasis (see **section 2.2**). Furthermore, it is possible that the basal DHSL level (here: DHSM C16) in HeLa WT and KO cells could influence the outcome of infection, and that DHSM C16 might support viral replication in HeLa cells (see Figure 3.30B). The length of the SL acyl chain has been reported to contribute to selectivity of protein-sphingolipid interaction [351]; however, unsaturation of SLs might have a greater impact on membrane physiology, such as the formation of rigidified domains[352,353]. Interestingly, the DHSL-mediated rigidification of membrane (micro)domains has been proposed to attenuate HIV entry due to an impairment in entry-receptor clustering[94]. In contrast, HIV virus envelopes have been shown to be specifically enriched in DHSM C16 species, which might contribute to virion stability[113]. Thus, the SL/DHSL rheostat could have distinctive effects on single replication stages of certain viruses, as cell penetration of IAV was likely not affected in CerS2-deficient, DHSM C16-enriched HeLa cells (see Figure 3.28 and Figure 3.29).

As lung epithelial-derived A549 cells represent a more suitable model for IAV infection[354] than HeLa cells, a CRISPR-based single CerS2-KO was also generated in A549 cells. CerS2-depleted HeLa and A549 cells had a similar SM species profile, with 80% monounsaturated SM C16 species (C16:1/34:1) and ≈15% saturated SM C16 species (=DHSM C16/34:0); and only low amounts (≈<2%) of SM (C≥22) species (see Figure 3.26 and Figure 3.31)[317]. The latter might be explained by the activity of other CerS, like CerS4[56].

CerS2-depleted A549 cells had also slightly higher DHSM C16 levels as WT cells (see Figure 3.31). Yet it could not experimentally re-capitulated that CerS2-depleted A549 cells show increased viral titers compared to WT cells, as seen for HeLa cells (see Figure 3.31 and Figure 3.32). Notably, a different PR8 virus stock was used in the two experiments. Here, experiments have to be re-validated. To improve the analysis of CerS2-rescued cells, a CerS2-mCherry expressing vector with a T2A-splicing site[355] is currently cloned, to (i) allow for independent expression of both proteins in order to ensure proper folding and hence function of CerS2, and (ii) to enable sorting of CerS2 transfected cells only. Furthermore, it should be determined if experimental observations are similar for different virus batches of the same IAV strain, as well as similar for different subtypes used.

5 Materials and Methods

5.1 Materials

5.1.1 Chemicals, solvents and reagents

All chemicals are in p.a. quality.

Reagent	Company
Acetic acid (AcOH)	Merck
Acetylacetate	Zentralbereich, Im Neuenheimer Feld
Acetonitrile	Sigma-Aldrich
Acrylamide-bisacrylamide stock (37.5:1), 30% (v/v)	Carl Roth
Acyl-Coenzyme A (CoA) 24:0 and 24:1 (870724 and 870725)	Avanti Polar Lipids
Agarose	Carl Roth
Albumin fraction V	Carl Roth
Alkaline phosphatase, calf intestinal (CIP)	NEB
Aluminium sulfate hydrate	Sigma-Aldrich
Amido Black 10B	Sigma-Aldrich
Ammoniumperoxodisulfat (APS)	Carl Roth
Ammonium bicarbonate	Honeywell Fluka™
Ampicillin sodium salt	Sigma-Aldrich
Bacto™ Agar	BD Biosciences
Bacto™ Tryptone	BD Biosciences
Bacto™ Yeast extract	BD Biosciences
Benzonase® Endonuclease, 250 U/µL (70764)	Merck
Benzonase® Nuclease, 250 U/µL (E1014)	Sigma-Aldrich
Bovine serum albumine (BSA)	Carl Roth
Bovine serum albumine (BSA), fatty acid free	Sigma-Aldrich
Bromphenol blue	Waldeck
Calciumchloride ($CaCl_2$) dihydrate	Sigma-Aldrich
Chloramphenicol	Sigma-Aldrich
Chloroform ($CHCl_3$)	VWR
Copper(II) sulfate pentahydrate ($CuSO_4$)	Sigma-Aldrich
Coomassie brilliant blue G-250	ThermoFisher Scientific
Crystal violet	Sigma-Aldrich
DAPI	ThermoFisher Scientific

Deoxynucleotide (dNTP) mix, long range, peqGOLD	Peqlab (VWR brand), Germany
Dimethyl pimelimidate (DMP)	ThermoFisher Scientific
Dimethyl sulfoxide (DMSO)	Sigma-Aldrich
Dithiothreitol (DTT)	Bio-Rad
DMEM (1 mg/mL glucose)	Sigma-Aldrich
DMEM (1 mg/mL glucose), pyruvate, no glutamine, no phenol red	Gibco
DMEM (4.5 mg/mL glucose)	Sigma-Aldrich
DMEM (4.5 mg/mL glucose) (SILAC)	Silantes
6x DNA loading dye (B7024S)	New England BioLabs® (NEB)
DNase I (RNase-free), 2 U/µL (M0303S)	New England BioLabs® (NEB)
Ethanol (EtOH), 100% (v/v)	VWR
Ethanol (EtOH), 96% (v/v)	Zentralbereich, Im Neuenheimer Feld
Ethanolamine	Sigma-Aldrich
EZ-Link™ Sulfo-NHS-Biotin solution	ThermoFisher Scientific
EZview™ Red ANTI-FLAG® M2 Affinity Gel	Sigma-Aldrich
Endoglycosidase H (EndoH) (P0702S)	New England BioLabs® (NEB)
Ethylenediaminetetraacetic acid (EDTA)	Carl Roth
Fetal bovine serum (FBS) (SILAC)	Silantes
Fetal bovine serum (FBS) Superior	Merck
Formaldehyd	Sigma-Aldrich
Formic acid	Merck
FuGENE® HD	Promega
Fumonisin B1 (FB1)	Cayman Chemical
Glacial acetic acid	Sigma-Aldrich
Glycerol	Sigma-Aldrich
Glycine	LaboChem international
Hydrochloric acid (HCl)	Honeywell
Hexane	Sigma-Aldrich
HPTLC silica gel 60 plate (1.05641.0001)	Merck
4-(2-hydroxyethyl)-1-piperazineethanesulfonic acid (HEPES)	Carl Roth
Hybri-Max™ Dimethyl sulfoxide (DMSO)	Sigma-Aldrich
Iodacetamide	Bio-Rad
Isopropanol	Sigma-Aldrich
Kanamycin-sulfate	Sigma-Aldrich
L-Arginine	Sigma-Aldrich
L-Arginine:HCl ^{13}C-labeled	Silantes
L-Arginine:HCl $^{13}C^{15}N$-labeled	Silantes

Water HPLC grade	Merck
L-glutamine	Sigma-Aldrich
L-Lysine	Sigma-Aldrich
L-Lysine:2*HCl 4,4,5,5,-^{2}H-labeled	Silantes
Lipofectamine® 2000	ThermoFisher Scientific
Lipofectamine™ RNAiMAX	ThermoFisher Scientific
L-Lysine:HCl $^{13}C^{15}N$-labeled	Silantes
2-Log DNA ladder (N3200S)	New England BioLabs® (NEB)
L-stable glutamine (SILAC)	Silantes
Magnesium chloride ($MgCl_2$) hexahydrate	Labochem
Methanol (MeOH)	VWR
Mobicols, 35 µM pore size	MoBi Tec
Microcrystalline cellulose (MCC)	FMC
Milk powder, low fat	Carl Roth
N',N'-diisopropylethylamine	Sigma-Aldrich
Nervonic acid (C24)	Sigma-Aldrich
NeutrAvidin™ Agarose beads (29202)	ThermoFisher Scientific
Nonidet P40 (NP40) Substitute	Roche
N, N, N', N'-Tetramethylethylendiamine (TEMED)	Carl Roth
NuPAGE™ 4-12% Bis-Tris Protein Gels, 1.5 mm, 10 well	ThermoFisher Scientific
NuPAGE™ MOPS SDS Running buffer	ThermoFisher Scientific
Opti-MEM®	Gibco
Ortho-phosphoric acid	Sigma-Aldrich
Paraformaldehyd (PFA)	Sigma-Aldrich
Penicillin-Streptomycin	Sigma-Aldrich
Phosphate Buffered Saline (PBS)	Sigma-Aldrich
PNGase F (P0704S)	New England BioLabs® (NEB)
Potassium chloride	Roth
Precision Plus Protein™ All Blue Prestained Protein Standards (#1610373)	Bio-Rad
ProLong™ Gold Diamond Antifade Mountant	ThermoFisher Scientific
Protease Inhibitor Cocktail (PIC), EDTA-free	Roche
ProteinA Sepharose™ 4 Fast Flow	GE Healthcare
Q5® High-Fidelity DNA Polymerase	NEB
Resorcinol	Sigma-Aldrich
Retinoic acid p-hydroxyanilide (4-HPR, fen-retinide)	Sigma-Aldrich

Sera-Mag Carboxylate-Modified Magnetic Beads (SP3) 4515-2105-050250 and 6515-2105-050250	GE Healthcare
Sodium azide	Sigma-Aldrich
Sodium chloride (NaCl)	Carl Roth
Sodium dodecyl sulfate (SDS)	Serva
Sodium deoxycholate	Carl Roth
Sodium hydroxide (NaOH)	Sigma-Aldrich
Sodium tetraborate	Sigma-Aldrich
Sucrose	Sigma-Aldrich
SYBR™ Select Master Mix	ThermoFisher Scientific
Taq-polymerase	Axon
Tetrakis(acetonitrile)copper(I) tetrafluoroborate ($CuBF_4$)	Sigma-Aldrich
TPCK Trypsin	Sigma-Aldrich
Triethylamine (TEA)	Sigma-Aldrich
Trifluoroacetic acid (TFA)	Sigma-Aldrich
Tris[(1-benzyl-1*H*-1,2,3-triazol-4-yl)methyl]amine (TBTA)	Sigma-Aldrich
Tris(2carboxyethyl)phosphine hydrochloride (TCEP)	Sigma-Aldrich
Tris(hydroxymethyl)aminomethane (Tris)	Carl Roth
Triton X-100 (TX-100)	Merck
Trypan blue	Sigma-Aldrich
Trypsin	Sigma-Aldrich
Trypsin/LysC (V5071)	Promega
TurboFect™	ThermoFisher Scientific
Tween® 20	Carl Roth

All restriction enzymes were purchased from NEB. If not mentioned otherwise, buffers were prepared with double-distilled water (ddH_2O).

5.1.2 Kits

Kit	**Company**
Cell Line Nucleofector® Kit T	Lonza
CellTiter-Blue® Cell Viability Assay	Promega
DNeasy® Blood & Tissue Kit	Qiagen
Pierce™ BCA protein assay kit	ThermoFisher Scientific
Plasmid Midi and Maxi Kit	Qiagen

QIAprep® Spin Miniprep Kit	Qiagen
QIAquick® Gel Extraction Kit	Qiagen
QIAquick® PCR Purification Kit	Qiagen
Quick Ligation™ Kit	NEB
RNeasy® Mini Kit	Qiagen
TA Cloning™ Kit, with pCR™2.1 vector	ThermoFisher Scientific
Transcriptor First Strand cDNA Synthesis Kit	Roche
Titanium® Taq PCR Kit	Takara
Venor®GeM Classic Mycoplasm Detection Kit	Minerva biolabs®

Expendable items

Consumable	**Company**
Cell counting slides (Luna™)	Logos biosystems
Cell culture dishes (Cellstar®, 96-well, 24-well, 6-well, 6 cm, 10 cm)	Greiner bio-one
Cell culture dishes (12-well)	Corning® Costar®
Cell culture dishes (3.5 cm)	Sarstedt
Cell culture dishes (15 cm, Thermo Scientific™ Nunc™ cell culture dish)	ThermoFisher Scientific
Cell scraper	TPP®
Cover slips	Carl Zeiss™
Cryovials (Cryo.S™)	Greiner bio-one
DCS-C8 columns	Supelco
Deactivated glass vial	Agilent
Erlenmeyer flasks	VWR
Filter unit (0.22 µM, Millex®-GS and 0.45 µm, Millex® Durapore® PVDF)	Merck
Glass pasteur pipettes (disposable, 230 mm)	VWR
Glass ware	VWR/Simax
Gloves (TouchNTuff®)	Ansell
MicroAmp™ Clear Adhesive Film	ThermoFisher Scientific
Microfuge tube polypropylene, 1.5 mL	Beckman Coulter
Microscope slides	Carl Roth
Open-top polyclear tubes (9/16x3-1/2 inch 7030)	Seton Scientific
PCR plate (96-well), white, DNase-, RNase free	Biozym

Pipet tips	Sarstedt
Pipet tips, with filter	Greiner bio-one
Plastic Concentric Luer-Lock Syringe (BD Plastipak™)	BD
PVDF membrane (Immobilon®-FL)	Merck
Pyrex® glass tube	Pyrex®
RNase-free 1.5 mL tubes	Ambion
Schott flasks	VWR
Serological plastic pipettes (5, 10, 25 mL)	Greiner bio-one
Serological plastic pipettes (50 mL)	Corning® Costar®
Stericup-GP (0.22 µM), polyethersulfone, 500 mL volume, gamma-sterilised	Merck
T25/75/175 flasks	Greiner
0.2 mL tubes	Kisker Biotech GmbH & Co. KG
0.5 mL tubes	Sarstedt
1.5 and 2 mL tubes	Sarstedt and Eppendorf
5 mL tubes	Eppendorf
15 and 50 mL tubes	Falcon™
Whatman® blotting paper	GE Whatman®

5.1.3 Equipment

Device	**Company**
Agarose gel chambers (Class II)	Peqlab
Bacteria incubator	Memmert (agar plates), Edmund Bühler (liquid culture)
Cell culture hood (Herasafe™ KS, class II biological safety cabinet)	ThermoFisher Scientific
Cell incubator (Forma™ Steri-Cycle™ CO_2 incubator)	Thermo Scientific
Centrifuges for 1.5 and 2 mL tubes (5424, 5427R)	Eppendorf
Centrifuges for 15 and 50 mL tubes (Mega Star 1.6R and Megafuge 16R)	VWR
Heating chamber (Function line)	Heraeus
Li-Cor (Odyssey CLx)	Li-Cor®
Luna™ automated cell counter	Logos biosystems
Magnetic PCR rack	Manufactured at EMBL
Magnetic stirrer (with heating)	Starlab, Heidolph

Mass spectrometers (Lipidomics)	See section 5.2.8.9
Mass spectrometers (Proteomics)	See section 5.2.6.3 and 5.2.6.5
Microplate reader (EZ read 2000)	Biochrom
Microscale (ABT 120-5DNM)	Kern
Microscope (cell culture, ELWD 0.3, T1-SNCP)	Nikon
Fluorescence microscope (Axiovert 200)	Zeiss
Fluorescence microscope (LSM 800)	Zeiss
Nanodrop (NanoDrop™ 2000c)	Peqlab
PCR Thermocycler (peqSTAR)	Peqlab
pH meter	Mettler Toledo
Photometer (GENESYS™ 10S UV-Vis)	Thermo Scientific
Power supply (agarose gels, Consort™ EV261)	Thermo Scientific
Power supply (SDS-PAGE, WB, PowerPac™ Basic)	Bio-Rad
Real-Time PCR instrument (Applied Biosystems™ 7500)	ThermoFisher Scientific
Rotating mixer (RM 5-30 V)	NeoLab®
Rotor wheel	NeoLab®
Scale (PCB)	Kern
Scanner (Perfection V850 Pro)	Epson
SDS & Western blot chamber (Mini-PROTEAN® Tetra System)	Bio-Rad
Shaking platform (ST 5)	NeoLab®
Sonic water bath (Sonorex)	Bandelin
Rotational vacuum concentrator (RVC 2-18)	Christ
Table centrifuge (0.2, 0.5, 1.5 and 2 mL tubes)	Starlab
Table vortexer	Starlab
Thermoblocks (ThermoMixer C)	Eppendorf
TLC automated applicator (Linomat 5) using WINCATS software	CAMAG
TLC automatic development chamber 2 (ADC2)	CAMAG
TLC imaging (Amersham Imager 600)	GE Healthcare
Ultrapure water system	Veolia
Ultrazentrifuge (Optima™ MAX-XP)	Beckman Coulter
UV lamp (UVP Blak-Ray®, B-100AP, 100W)	Blak-Ray®
Vacuum manifold (ganglioside TLC)	Ashcroft®

Water bath (LSB Aqua Pro)	Grant
Water bath, cell culture (AQUAline AL 12)	Lauda
XCell SureLock™ Mini-Cell electrophoresis system	ThermoFisher Scientific

5.1.4 Antibodies

Primary antibodies used for Western blot (WB) were diluted in 5% (w/v) BSA, 0.1% (v/v) Tween20 and 0.01% (w/v) SDS and stored at either -20°C or 4°C (as suggested by the supplier). Secondary WB antibodies were diluted in 2.5% (w/v) BSA, 0.1% (v/v) Tween20, 0.01% (w/v) SDS and 0.02% (w/v) natrium-azide and kept at 4°C. For immunofluorescence (IF) staining, antibodies were diluted in 2.5% BSA (w/v) in PBS prior use.

Table 5.1: Antibodies used in this study.

Protein names as listed in UniProt (gene name). Poly= polyclonal, mono= monoclonal, WB= Western blot, IF= immunofluorescence.

Anti-	Species	Company	Dilution
Primary antibodies			
Asgr1 (ASGPR1) (WB)	Rabbit, poly	GeneTex (GTX122674)	1:500
Beta-actin (ACTB) (WB)	Mouse, mono	Sigma-Aldrich (A5441)	1:5000
Calnexin (CXN) (WB)	Rabbit, poly	Enzo (ADI-SPA-860)	1:1000
Caveolin-1 (CAV1)	Rabbit, poly	ThermoFisher Scientific (PA1-064)	2 µg/mL
CD63	Mouse, mono	Invitrogen (10628D)	1:1000
DDDDK (FLAG) (WB, IF)	Rabbit, poly	Sigma (#F1804)	1:1000
DDK (FLAG) (WB)	Mouse, mono	OriGene (TA50011-5)	1:2000
ELOVL1 (WB)	Rabbit, poly	ThermoFisher Scientific (PA5-75396)	1:500
GAPDH (WB)	Mouse, mono	Abcam (ab8245)	1:5000
GFP (WB)	Mouse, mono	Santa Cruz (#sc-9996)	1:1000
HA1 (WB)	Rabbit, poly	GeneTex (GTX127357)	1:1000
HA3 (IAV) (WB, IF)	Goat, polyclonal	BEI Resources (NR-3118)	1:1000
ITGA5 (WB)	Rabbit poly	Cell signalling (4711S)	1:1000
ITGB1	Rabbit, poly	Abcam	1:5000

(WB)		(ab179471)	
NA1 (IAV) (WB)	Guinea pig, poly	Pineda (custom designed against NA1 from IAV RD6 strain)	1:100
NA2 (IAV) (WB)	Guinea pig, poly	Pineda (custom designed against NA2 from IAV HK68 strain)	1:100
NP (IAV) (WB, IF)	Mouse, mono	Merck Millipore (MAB8257)	1:100
NS1 (IAV) (WB)	Mouse, mono	Santa Cruz (sc130568)	1:500
NCL (WB)	Rabbit, poly	Abcam (ab22758)	1:1000
M1 (IAV) (WB)	Mouse, mono	Abcam (ab22396)	1:500
M2 (IAV) (WB)	Mouse, mono	Abcam (ab5416)	1:1000
M2 (IAV) (WB)	Rat, poly	Pineda (custom designed against M2 from IAV RD6 strain)	1:100
Myc (WB)	Rabbit, poly	Acris (NB600-336)	1:1000
p24 (TMED2) (WB)	Rabbit, poly	ThermoFisher Scientific (PA5-51304)	1:500
PCYOX1 (WB)	Mouse, mono	Santa Cruz (sc-136391)	1:200
RAB11A (WB)	Rabbit, poly	ThermoFisher Scientific (#71-5300)	2 µg/mL
SLC1A5 (WB)	Rabbit, poly	Atlas Antibodies (ab155196)	1:200
SLC25A11 (WB)	Rabbit, poly	Abcam (ab155196)	1:1000
SLC64A1 (WB)	Rabbit, poly	Sigma-Aldrich (SAB2108339)	1 µg/mL
SGPL1 (WB)	Rabbit, poly	Santa Cruz (sc-67368)	1:200
TM9SF3 (WB)	Rabbit, poly	ThermoFisher Scientific (PA5-69605)	1 µg/mL
TMEM41B (WB)	Rabbit, poly	ThermoFisher Scientific (PA5-53259)	0.4 µg/mL
TRAM1 (WB)	Rabbit, poly	Proteintech (12705-1-AP)	1:500
TfR (WB)	Mouse, mono	ThermoFisher Scientific (13-6800)	1:500
UGCG (WB)	Mouse, mono	Santa Cruz (sc-293235)	1:200
Secondary antibodies			
Anti-rabbit IgG (H+L) antibody, Alexa Fluor® 680 Conjugate	Goat	ThermoFisher Scientific (A-210676)	1:10000

(WB)			
Anti-rabbit IgG (H+L) antibody IRDye® 800 CW (WB)	Goat	Rockland (611-131-002)	1:10000
Anti-mouse IgG (H+L) antibody, Alexa Fluor® 680 Conjugate (WB)	Goat	ThermoFisher Scientific (A-21057)	1:10000
Anti-mouse IgG (H+L) antibody, IRDye® 800CW Conjugate (WB)	Donkey	Rockland (600-145-098)	1:10000
Anti-guinea pig IgG (H+L) antibody, IRDye® 680RD Conjugate (WB)	Donkey	Li-Cor (925-68077)	1:10000
Anti-goat IgG (H+L), Alexa Fluor® 680 Conjugate (WB)	Donkey	ThermoFisher Scientific (A-21084)	1:10000
Anti-Biotin, DyLight™ 800 Conjugated (WB)	Goat	Rockland (600-145-098)	1:10000
Anti-rabbit IgG (H+L), Alexa Fluor® 488 Conjugate (IF)	Goat	ThermoFisher Scientific (A-11008)	1:10000
Anti-mouse IgG (H+L), Alexa Fluor® 488 Conjugate (IF)	Goat	ThermoFisher Scientific (A-11029)	1:10000
Anti-goat IgG (H+L), Alexa Fluor® 680 Conjugate (IF)	Donkey	ThermoFisher Scientific (A-21084)	1:10000

5.1.5 Bifunctional lipids

Table 5.2: Bifunctional lipids used in this study.

Lipids were dissolved as described and stored at -20°C.

Pac-lipid	**Company**
pacSph (20 mM in EtOH)	Synthesised in-house (T. Sachsenheimer)[250]
pacFA (50 mM in EtOH)	Fa. Avanti 900401P
Trans-pacChol (6.25 mM in DMSO)	Fa. Sigma Aldrich 804657

5.1.6 Azide reporter molecules

Table 5.3: Azide reporters used in this study.

All reagents were stored at -20°C in DMSO.

Reagents	Company
Alexa647™-azide	Fa. ThermoFisher Scientific (A10277)
PEG4 carboxamide-6-azidohexanyl biotin (Biotin-azide)	Fa. ThermoFisher Scientific (B10184)
3-azido-hydroxycoumarin (Coumarin-azide)	Fa. Jena Biosciences CLK-FA047-1

5.2 Methods

5.2.1 Bacteria

5.2.1.1 Cultivation of bacteria

Bacteria (*E. coli* DH5a) were cultivated in liquid or on solid LB media (10 g Tryptone, 5 g NaCl, 5 g yeast extract, -/+ 15 g Agar per 1000 mL) at 37°C, liquid cultures additionally shaken at 180 rpm. All media were autoclaved prior use. If needed, LB was supplemented with antibiotics (Table 5.4).

Table 5.4: Antibiotics used in this study.

Antibiotic	Concentration
Kanamycin (Kan)	30 µg/mL
Ampicillin (Amp)	100 µg/mL
Chloramphenicol (Chl)	25 µg/mL

5.2.1.2 Preparation of chemically competent *E. coli*

All steps were performed under sterile conditions. Briefly, 200 mL sterile LB media were inoculated 1:50 with an *E. coli* DH5a liquid overnight (ON) culture and grown until an OD_{600} of 0.5-0.7 in a 500 mL Erlenmeyer flask. Bacteria were placed on ice for 20 min and centrifuged for 5 min, 5000 rpm at 4°C in sterile 50 mL falcons. Bacterial pellets were carefully resuspended in 100 mL ice-cold, sterile $MgCl_2$ (0.1 M) and left on ice for 45 min prior gentle mixing of 100 mL ice-cold, sterile $CaCl_2$ (0.1 M). After centrifugation (5 min, 3000 rpm at 4°C), pellets were resuspended in 6 mL ice-cold, sterile 0.1 M $CaCl_2$ containing 18% (v/v) glycerol. Resuspended bacteria were aliquoted in 1.5 mL tubes, incubated on ice for 2 h and frozen at -80°C.

5.2.1.3 Heat-transformation of chemically competent *E. coli*

Chemically competent bacteria were thawed on ice and 5 µL plasmid added to 50 µL *E. coli* DH5a. After incubation for 30 min on ice, cells were put in a thermomixer (42 s at 42°C) and shortly re-placed on ice before addition of 950 µL pre-warmed LB media. Bacteria were incubated for 1 h, spread out on LB Agar plates supplemented with the respective antibiotic and incubated ON at 37°C.

5.2.1.4 Freezing and thawing of bacterial cells

Selected bacterial strains were incubated in 5 mL LB supplemented with the respective antibiotic (if needed) ON, pelleted (5 min, 3000 at 4°C) and resuspended in 1 mL ice-cold LB containing 20% (v/v) glycerol. After incubation for 20 min on ice, bacteria were stored at -80°C. For re-cultivation, frozen material was picked with a sterile tooth pick and spread on appropriate agar plates.

5.2.2 Cloning

Primers and plasmids used in this study are listed in Table 5.5 and Table 5.6. Synthetic gene fragments were obtained from GeneArt (ThermoFisher Scientific). PCR reaction settings were used as suggested by the corresponding suppliers. Prior loading on agarose gels, DNA fragments were mixed with 6x DNA loading dye purple at 1x end-concentration (2-log DNA ladder).

5.2.2.1 Agarose gels

Agarose gels were prepared freshly prior electrophoresis of nucleic acids with the desired percentage (w/v) of agarose dissolved in 1x TAE buffer (40 mM Tris, 20 mM glacial acetic acid, 1 mM EDTA, pH 8) by heating.

5.2.2.2 Amplification of gene fragments

Gene fragments were amplified from the respective vectors (1 ng vector template) using Q5® High-Fidelity DNA Polymerase according to the manufacturer's instructions. PCR products were purified (QIAquick® PCR Purification Kit), eluted in 51 µL elution buffer and DNA yields measured at the nanodrop.

5.2.2.3 Restriction digest

DNA fragments and vectors were digested with restriction enzymes from NEB in 1x CutSmart® Buffer as suggested (NEBcloner®). Blunt-end-digested vectors were additionally treated with alkaline phosphatase (calf intestinal, CIP). After separation on agarose gel, DNA fragments were purified via gel extraction (QIAquick® Gel Extraction Kit) and eluted in 36 µL ddH_2O prior DNA measurement.

5.2.2.4 Ligation

Ligation was performed with Quick T4 DNA ligase (Quick Ligation™ Kit) according to the manufacturer's instructions. Ligations were either stored at -20°C or 5 µL directly used for heat transformation of *E. coli* DH5a (see 5.2.1.3).

5.2.2.5 Colony PCR

Insert-positive colonies grown after heat-transformation of chemically competent *E. coli* with the respective ligation reactions were determined via Colony PCR. Therefore, a small amount of bacterial material was resuspended in the Taq-Polymerase PCR reaction mix (Axon) containing the respective sequencing primers. PCR reactions were analysed on agarose gels. Positive clones derived from an ON culture were sent for sequencing (Eurofins) after plasmid isolation (QIAprep® Spin Miniprep Kit).

5.2.2.6 Plasmid isolation

Plasmids were isolated either with the QIAprep® Spin Miniprep Kit, QIAGEN® Plasmid Midi or Maxi Kit according to the manufacturer's instructions. Plasmids were stored in elution buffer at -20°C.

5.2.2.7 Primers

Table 5.5: List of primers used in this study.

The pHW2000 reverse genetics systems[356] and indicated pCAGGS plasmids[357,358] containing viral proteins were kindly provided by S. Kummer (Kräusslich lab). Primers were synthesised by ThermoFisher Scientific.

Name	Sequence	T_A (°C)	Purpose
HA68-pEGFP_FW	5'-ctg tct cat cat cgt ggc ata gaa ttc atg aag acc-3'	57	Cloning of HA3 from IAV HK68 out of pCAGGS[357] vector into pEGFP[116] via 5' EcoRI, 3' AgeI → no expression
HA68-pEGFP_RV	5'-gag ctc gcg acc ggt aag atg caa-3'	57	
NA-pEGFP_FW	5'-ctc tct cat cat cgt ggc ata gaa ttc atg aat cc-3'	57	Cloning of NA2 IAV HK68 out of pCAGGS[357] vector into pEGFP[116] via 5' EcoRI, 3' AgeI → no expression
NA-pEGFP_RV	5'-gct cgc gac cgg taa tat agg cat-3'	57	
M2-pEGFP_FW	5'-gct cga att cat gag cct tct aac cg-3'	57	Cloning of M2 from IAV HK68 out of GeneArt Carrierplasmid into pEGFP[116] via 5' EcoRI, 3' AgeI
M2-pEGFP_RV	5'-cca ggt acc aac cgg taa ctc cag-3'	57	
pCMV-HA68_FW	5'-gct acc gga tcc aga tct cga gcg ccg ccg cga tcg cca tga aga cca tca tt-3'	63	Cloning of HA3 from IAV HK68 out of pEGFP_GGG_FLAG vector (not shown) into pCMV-Cterm Myc-FLAG[254] via 5' BamHI, 3' NotI
pCMV-HA68_RV	5'-gct tac tta tcg tcg tca tcc ttg taa tgc ggc cgc cca atg caa atg ttg cac cta-3'	63	
pCMV-NA68_FW	5'-gct acc gga tcc aga tct cga gcg ccg ccg cga tcg cca tga cca tga atc caa atc-3'	63	Cloning of NA2 from IAV HK68 out of pEGFP_GGG_FLAG vector (not shown) into pCMV-Cterm Myc-FLAG[254] via 5' BamHI, 3' NotI
pCMV-NA68_RV	5'-gct tac tta tcg tcg tca tcc ttg taa tgc ggc cgc cct ata ggc atg aaa ttg atg ttc gcc-3'	63	
pCMV-M268_FW	5'-acc gga tcc aga tct cga gcg ccg ccg cga tcg cca tga gcc tt-3'	63	Cloning of M2 from IAV HK68 out of pEGFP_GGG_FLAG vector (not shown) into pCMV-Cterm Myc-FLAG[254] via 5' BamHI, 3' NotI
pCMV-M268_RV	5'-gct tac tta tcg tcg tca tcc ttg taa tgc ggc cgc ccc tcc agc tct atg ctg ac-3'	63	
M268-EcoRI_FW	5'-gga ctc aga tct cga gct caa gct tcg aat tca tga tga gcc ttc taa ccg agg tcg aa-3'	60-65	Cloning of M2 from IAV HK68 out of pEGFP_M2 into pCAGGS[357] via 5' EcoRI and 3'NotI
M268-EcoRI_RV	5'-cca tgg cgg ccg ccg gtt act cca gct cta tgc tga caa aat gac tat cg-3'	60-65	
RD6-HA1_FW	5'-agc aga att cat gaa ggc aat act agt agt tct gc-3'	54	Cloning of HA1 from IAV RD6 out of reverse genetics

RD6-HA1_RV	5'-cta tgc ggc cgc tta aat aca tat tct aca ctg tag aga-3'	54	system (pHW2000)[356] into pCAGGS vector[357] via 5'EcoRI/3'NotI
RD6-NA1_FW	5'-cga tga att cat gaa tcc aaa cca aaa gat aat aac cat tgg ttc g-3'	54	Cloning of NA1 from IAV RD6 out of reverse genetics system (pHW2000)[356] into pCAGGS vector[357] via 5'EcoRI/3'NotI
RD6-NA1_RV	5'-ata tgc ggc cgc tta ctt gtc aat ggt aaa tgg-3'	54	
pCMV-NA1RD6_FW	5'-ggc aaa ccg cgg atg aat cca aac caa aag ata ata ac-3'	55	N-terminal Myc-FLAG tagging of NA1 out of pCAGGS construct from IAV RD6 via SacII
pCMV-NA2RD6_RV	5'-gct cgc ccg cgg tta ctt gtc aat ggt aa-3'	55	
pCMV-NA2HK68_FW	5'-ggc aaa ccg cgg atg aat cca aat caa-3'	55	N-terminal Myc-FLAG tagging of NA2 out of pCAGGS construct from IAV HK68 via SacII
pCMV_NA2HK68_RV	5'-gct cgc ccg cgg tta tat agg cat gaa-3'	55	
pCMV-HA1RD6_FW	5'-caa cgt gct gga tcc tgt gct gtc tca tca tgc cgc cgc gat cgc cat gaa ggc aat ac-3'	62	For cloning of HA1 from IAV RD6 out of pCAGGS construct into pCMV vector with C-terminal Myc/FLAG via 5'BamHI/3'NotI
pCMV-HA1RD6_RV	5'-gat ctg cta gct aat taa gag ctc ggc ggc cgc cca ata cat att cta cac tgt aga gac c-3'	62	
pCMV-M2RD6_FW	5'-caa cgt gct gga tcc tgt gct gtc tca tca tgc cgc cgc gat cgc cat gag tct t-3'	62	For cloning of M2 from IAV RD6 out of pCAGGS construct into pCMV vector with C-terminal Myc/FLAG via 5'BamHI/3'NotI → M2 generated via GeneArt for cloning into pCAGGS[357] via 5' EcoRI/3' NotI
pCMV-M2RD6_FRV	5'-gat ctg cta gct aat taa gag ctc ggc ggc cgc ccc tcc agc tct atg ttg aca a-3'	62	
HA1RD6-dbtag_FW	5'-gtc tct aca gtg tag aat atg tat tgg gcg gcc gct cga g-3'	62	For adding 2nd Myc/FLAG tag to HA1 from IAV RD6 within pCMV vector via 5'/3' NotI
HA1RD6-dbtag_RV	5'-acc gcg cgg ccg cg tata aac ctt atc gtc gtc gtc at-3'	62	
CerS2-Nterm_3FLAG-FW	5'-cgg gct gca gcc gcg gct cca gac ctt gta tg-3'	60	For N-terminal 3xFLAG tag of CerS2 (plasmid kindly provided by D. Höglinger)
CerS2-Nterm_3FLAG-FW	5'-ctc gag gtc gac ggt atc gat ccg cgg tca gtc att ctt acg-3'	60	
FW-CerS2_nontagged	5'-gat aag agc ccg ggc ctc gag gcc gcc gcg atc gcc atg ctc cag acc ttg tat g-3'	60	For cloning of non-tagged CerS2 into pCMV vector (plasmid kindly provided by D. Höglinger) via 5'XhoI & 3'SacII
RV-CerS2_nontagged	5'-gta ccg ggc ccc ccc tcg agg tcg acg gta tcg atc cgc ggt cag tca ttc tta cg-3'	60	
ELOVL1_FW	5'-gag gag atc tgc cga att cgc cac cat gga ggc tgt tgt gaa ctt gta c-3'	60	For cloning of PR8 SILAC screen candidates (A549ΔS1PL S2-6 clone) into pCMV_Cterm3xFLAG via 5'EcoRI & 3'NotI
ELOVL1_RV	5'-ctg ctc gag ctg ctg cgc ggc cgc gtt ggc ctt gacctt gac ctt ggc aat a-3'	60	

SLC1A5_FW	5'-gaa acc ccg gaa ttc gcc acc atg gtg gcc gat cct cct cga-3'	62	
SLC1A5_RV	5'-gaa ggt ccc tcc cgc ggc cgc cat gac tga ttc ctt ctc a-3'	62	
ITGB1_FW	5'-aga agc atg acg gcg aat tcg cca cca tga att tac aac-3'	60	
ITGB1_RV	5'-cgg cga tcc tct ggc ggc cgc ttt tcc ctc ata ctt cg-3'	60	
Asgr1_FW	5'-ccg gta ccg ag gaga tct gcc gaa ttc gcc acc atg acc aag gag tat c-3'	66	
Asgr1_RV	5'-ttc tgc tcg agc tgc tgc gcg gcc gca ag gaga ggt ggc tc-3'	66	
p24_FW	5'-gag atc tcg agc tga att cgc cac cat gta ttt cgt tag cat cga cgc c-3'	60	
p24_RV	5'-tgc tcg agc ggg cgg ccg caa caa ctc tcc gg-3'	60	
CD63_FW	5'-tac cga gga gat ctg ccg aat tcg cca cca tgg cgg tgg aag gag ga-3'	62	
CD63_RV	5'-tgc tcg agc tgt cgc gcg gcc gcc atc acct cg tag-3'	62	
pEGFP_FW (pCMV_FW)	5'-cgc aaa tgg gcg gta ggc gtg-3'	59	Sequencing primer for constructs in pEGFP vector and pCMV vector
pEGFP_RV	5'-gtc agc ttg ccg tag gtg gca tcg-3'	59	Sequencing primer for constructs in pEGFP vector
pCMV_RV	5'-gtg ggc act gga gtg gca act t-3'	59	Sequencing primer for constructs in pCMV vector
pCMV_RVII	5'-ctccataccacccccctccacccca-taatattatag-3'		Sequencing primer for constructs in pCMV vector
pCAGGS_FW	5'-ggt tcg gct tct ggc gtg tga-3'	57	Sequencing primer for pCAGGS constructs
pCAGGS_RV	5'ctc cca tat gtc ctt ccg agt gag aga cac-3'	57	
GAPDH_FW	5'-cgc tct ctg ctc ctc ctg tt-3'	61	qRT PCR primer Housekeeping gene Kindly provided by C. Amaya-Ramirez (Bethune lab)
GAPDH_RV	5'-cca tgg tgt ctg agc gat gt-3'	61	
50S ribosomal L9_FW	5'-acc cca atg aga cca atg aaa t-3'	?	qRT PCR primer Housekeeping gene Kindly provided by S. Kummer (Kräusslich lab)
50S ribosomal L9_RV	5'-cag ccc atc ttt gat gag ctt-3'	?	

5.2.2.8 Plasmids

All isolated plasmids were sequenced by Eurofins.

M2 proteins were synthesised by GeneArt, other viral gene fragments were cloned out of the reverse genetics system pHW2000[356] or pCAGGS plasmids[357] (kindly provided by S. Kummer, Kräusslich lab).

Table 5.6: List of plasmids used in this study.

Cterm= C-terminal, Nterm= N-terminal, Kan= Kanamycin, Amp= Ampicillin.

Plasmid	Characteristic	Resistance	Promoter	Source
pEGFP	GFP	Kan	CMV	[116]
pEGFP-NA1	consensus 5' 40aa of NA1 & GFP	Kan	CMV	[116]
pEGFP-NA2	consensus 5' 40aa of NA2 & GFP	Kan	CMV	[116]
pEGFP-NA8	consensus 5' 40aa of NA8 & GFP	Kan	CMV	[116]
pCMV6-p24	TMD of p24 with Cterm FLAG	Kan	CMV	[254]
pCMV6-Asgr1	Asgr1 with Cterm FLAG+Myc	Kan	CMV	M. Gerl
pCAGGS-HA3 (HK68)	HA3 from IAV HK68 strain	Amp	CAG	[358]
pCAGGS-M2 (HK68)	M2 from IAV HK68 strain	Amp	CAG	This study
pCAGGS-HA1 (RD6)	HA1 from IAV RD6 strain	Amp	CAG	This study
pCAGGS		Amp	CAG	This study
pEGFP-HA3 (HK68)	HA3 from IAV HK68 strain, Cterm 1xFLAG+GFP	Kan	CMV	This study
pEGFP-NA2 (HK68)	NA2 from IAV HK68 strain, Cterm 1xFLAG+GFP	Kan	CMV	This study
pEGFP-M2 (HK68)	M2 from IAV HK68 strain, Cterm 1xFLAG+GFP	Kan	CMV	This study
pCMV6-HA3 (HK68)	HA3 from IAV HK68 strain, Cterm 1xFLAG+Myc	Kan	CMV	This study
pCMV6-NA2 (HK68)	NA2 from IAV HK68 strain, Nterm 1xMyc+FLAG	Kan	CMV	This study
pCMV6-M2 (HK68)	M2 from IAV HK68 strain, Cterm 1xFLAG+Myc	Kan	CMV	This study
pCMV6-HA1 (RD6)	HA1 from IAV RD6 strain, Cterm 1xFLAG+Myc	Kan	CMV	This study
pCMV6-NA1 (RD6)	NA1 from IAV RD6 strain, Nterm 1xMyc+FLAG	Kan	CMV	This study
pCMV6-M2 (RD6)	M2 from IAV RD6 strain, Cterm 1xFLAG+Myc	Kan	CMV	This study
pCMV6-CerS2 Nterm-3xFLAG	CerS2 with Nterm 3xFLAG	Kan	CMV	This study
pCMV6-CerS2	CerS2 only	Kan	CMV	This study
pCMV6-Cterm-3xFLAG-p24	TMD of p24 with Cterm 3xFLAG	Kan	CMV	This study
pCMV6-Cterm-3xFLAG-Asgr1	Asgr1 with Cterm 3xFLAG	Kan	CMV	This study
pCMV6-Cterm-3xFLAG-ITGB1	ITGB1 with Cterm 3xFLAG (cDNA from Fa. Sino Biological)	Kan	CMV	This study

pCMV6-Cterm-3xFLAG-SLC1A5	SLC1A5 with Cterm 3xFLAG (cDNA from Fa. BioCat)	Kan	CMV	This study
pCMV6-Cterm-3xFLAG-CD63	CD63 with Cterm 3xFLAG (cDNA from Fa. OriGene)	Kan	CMV	This study
pCMV6-Cterm-3xFLAG-ELOVL1	ELOVL1 with Cterm 3xFLAG (cDNA from Fa. OriGene)	Kan	CMV	This study
pSpCas9(BB)-2A-GFP (PX458)	CRISPR plasmid	Amp	CMV	Feng Zhang Fa. Addgene #48138

Table 5.7: cDNA used in this study.

cDNA	Company
ITGB1	Fa. Sino Biological (HG10587-M)
SLC1A5	Fa. BioCat (BC000062-seq-TCHS1003-GVO-TRI)
CD63	Fa. OriGene (SC126650)
ELOVL1	Fa. Origene (RC200027)

5.2.3 Cell culture

Table 5.8: Cell lines used in this study.

WT= wild type. A549 cells were kindly provided by S. Kummer (Kräusslich lab).

Cell line	Origin	Source	Features
A549	Human lung carcinoma	ATCC	WT
A549ΔS1PL		This study	Loss of S1PL function
A549ΔCerS2		This study	Loss of Cers2 function
HeLa	Human cervical carcinoma	DSMZ	WT
HeLaΔS1PL		Gerl *et al.*[254]	Loss of S1PL function
HeLaΔS1PLΔCerS2		This group (unpublished)	Loss of S1PL and CerS2 function
HeLaΔCerS2		This study	Loss of Cers2 function

5.2.3.1 Cultivation of A549 and HeLa cells

HeLa wild type (WT) and CRISPR/Cas9 knock-out (KO) cells were cultured at 37°C and 5% CO_2 in Dulbecco's Modified Eagle Medium (DMEM, 4.5 g/l glucose) supplemented with 10% (v/v) fetal bovine serum superior (FBS) and 1%

(w/v) penicillin/streptomycin (P/S). A549 WT and KO cells were cultivated at 37°C and 5% CO_2 in DMEM (1 g/l glucose) supplemented with 10% (v/v) fetal bovine serum superior (FBS) and 1% (w/v) penicillin/streptomycin (P/S). If indicated, cells were incubated in high glucose DMEM (4.5 g/L).
Cells were kept in monolayers and splitted 1:5/1:10 (HeLa) or 1:10/1:15 (A549) after 3 to 4 days. Therefore, plates were washed 2x with PBS and trypsinized for 5 min at 37°C, 5% CO_2. Trypsin was quenched at a 1:10 ratio with pre-warmed (37°C) DMEM and cells transferred to a new cell culture dish or plate in the respective splitting ratio.

5.2.3.2 Determination of cell numbers

Cell numbers were determined automatically via the Luna™ Automated cell counter. Therefore, 10 µL of trypsinized cells were pipetted onto Luna™ cell counting slides.

5.2.3.3 Freezing and thawing of cells

Cells were grown to 70-80% confluency on a 15 cm dish, washed 2x with PBS and detached with 3 mL trypsin. Cells were quenched 1:10 with DMEM, transferred into a sterile 50 mL falcon and pelleted (5 min, 300 xg at 4°C). Cell pellets were resuspended in 1.5 mL ice-cold FBS, distributed to three cryovials and incubated on ice for 20 min. Afterwards, per vial 500 µL ice-cold 20% DMSO in DMEM was added to cells and the cryovial inverted a few times until components were homogenously mixed. Cells were stored at -80°C or in liquid N_2.
To thaw cells, cryovials were put into a 37°C water bath until only a small ice-clump remained. Cells were transferred into a 15 mL falcon with 10 mL cold DMEM, centrifuged (5 min, 300 xg at 4°C) and cell pellets resuspended in 1 mL pre-warmed DMEM prior transfer to a 6 cm dish filled with 4 mL warm DMEM.

5.2.3.4 Mycoplasma PCR

Cells were tested for mycoplasmas using the Venor®GeM Classic Mycoplasm Detection Kit for conventional PCR according to the manufacturer's instructions.

5.2.3.5 Transfection

HeLa WT and KO cells were transfected with FuGene® HD at a ratio 1:3 of plasmid DNA to transfection reagent. A549 WT and KO cells were transfected either with FuGene® HD, TurboFect™ at a ratio 1:2 or electroporated with the Cell Line Nucleofector® Kit T. Transfection reaction set up was prepared as suggested by the supplier.

5.2.3.6 CRISPR/Cas9-mediated KO of the *SGPL1* and *CERS2*

Engineering of HeLaΔS1PL knockout cell lines is described in Gerl *et al*.[254]. HeLaΔS1PLΔCerS2 cells in were produced by M. Gerl. HeLaΔCerS2, A549ΔS1PL and A549ΔCerS2 cells in this study. The sgRNAs used for the corresponding CRISPR KO are listed in Table 5.9. Respective sgRNA-containing pSpCas9(BB)-2A-GFP plasmids were transfected into cells and GFP-positive clones sorted out 48 h after transfection via FACS (ZMBH FACS core facility (FFCF), Heidelberg). Single expanded cell clones were metabolically labelled with pacSph to verify KO-positive clones via thin layer chromatography (TLC) (see 5.2.8.7)[254].

Table 5.9: sgRNA sequences used for CRISPR/Cas9-mediated KO cell lines.

sgRNA	Sequence (5'-3')	Cell clones	Source
S2 forward	CACCGAATCTCTAAGTAGGGCTCAA	A549ΔS1PL S2-6 clone	Gerl *et al*.[254]
S2 reverse	AAACTTGAGCCCTACTTAGAGATTC		
S3 forward	CACCGTAATTGCATGGAGTGTCGTG	A549ΔS1PL S3-10 clone	
S3 reverse	AAACCACGACACTCCATGCAATTAC		
e22 forward	CACCGCAAAGAAGTATCGAACGATG	HeLaΔCerS2 clone	Unpublished (M. Gerl)
e22 reverse	AAACCATCGTTCGATACTTCTTTGC	A549ΔCerS2 clone 2	
e31 forward	CACCGGAAATGTTCCAAGGTGGCGT	A549ΔCerS2 clone 1	
e31 reverse	AAACACGCCACCTTGGAACATTTCC		

5.2.3.7 Sequencing of CRISPR/Cas9-generated clones

Genomic PCR was isolated (DNeasy® Blood & Tissue Kit) and the target sequence amplified using the Titanium® Taq PCR Kit. The forward and reverse

primer sequences used for the *SGPL1* and *CERS2* KO are listed in Table 5.10. DNA fragments were sub-cloned into pCR™2.1 Vector (TA Cloning™ Kit) and single clones chosen for sequencing with the M13-FP primer (Eurofins, see Table 5.10).

Table 5.10: FW and RV primer sequences used for the SGPL1 and CERS2 KO.

The *SGPL1* PCR product has a size of ≈600 bp, the *CERS2* PCR product a size of ≈800 bp.

SGPL1	Sequence	Source
Forward (5'-3')	AAGAAGGGCAAGATCCG-GAA	Gerl *et al.*[254]
Reverse (5'-3')	GTGGATCACGAGGTCAA-GAGA	
CERS2		
Forward (5'-3')	TAGCTACTCCCTCTT-GATGCCCTCCCCT	Unpublished (M. Gerl)
Reverse (5'-3')	TCCCCAGCCTCTCCCAG-TAACAACCTCA	
M13-FP (5'-3')	TGTAAAACGACGGCCAGT	

5.2.4 Influenza A virus infection (S. Kummer, Kräusslich lab)

The following experiments were performed in the Kräusslich laboratory by S. Kummer.

5.2.4.1 Virus strains

Table 5.11: IAV virus strains.

Detailed strain information can be obtained from https://www.fludb.org/.

Strain	**Harvested from**
Influenza A/Hong Kong/1/68 (H3N2)	MDCK cells
Influenza A/Regensburg/D6/2009 (H1N1)	
Influenza A/Puerto Rico/8/34 (H1N1)	

5.2.4.2 Virus harvest

Virus stocks were produced in HEK293T-MDCK-co-culture using the plasmid reverse genetics system as described[359]. The viral titer was determined by plaque assay (PA) according to[360] as plaque forming units/mL (PFU/mL) (see 5.2.4.6).

5.2.4.3 Virus infection

Cells were infected with the indicated multiplicity of infection (MOI) for 1 h at 37°C in sterile-filtered (Millex®-GS filter unit, 0.22 µM, 33 mm) DMEM

containing 1 % (w/v) glutamine, 0.3 % (w/v) BSA, 20 mM HEPES, 1% (w/v) P/S and TPCK-trypsin (2 µg/mL, ThermoFisher Scientific). Afterwards, medium was removed and cells incubated in fresh DMEM until harvest.

5.2.4.4 Anti-nucleoprotein (NP) stain

After 8 hours post-infection (hpi), cells were prepared for immunofluorescence microscopy (see 5.2.8.6) using anti-nucleoprotein antibody as primary antibody (see Table 5.1).

5.2.4.5 Hemagglutinin (HA) titer

Human blood was derived from the University Clinic in Heidelberg and prepared freshly at the day of the experiment (S. Kummer, Kräusslich lab).
A549 cells were seeded in 6-well plates at $3*10^5$ cells/well and infected the next day. After 24 hpi, supernatants were collected and used for HA. To this end, per well 50 µL PBS were pipetted in a 96-well plate except for the first well in each row. 100 µL of supernatant was pipetted to the first well in each row and from this, 50 µL were transferred to the following well and so forth, resulting in a two-fold-dilution series per row. Then, 50 µL of freshly prepared human blood erythrocytes (1 % (v/v) in in PBS) were added to each well. DMEM only was used as blank. After 45 min incubation at RT, the HA titer was determined (the last dilution step with a homogenous, red-coloured appearance).

5.2.4.6 Plaque assay

The PFU/mL (plaque titer) was performed as described[360] with minor changes. MDCK cells were seeded in 6-well plates and grown to monolayers overnight. 500 µl of a10-fold dilution of the respective virus stock (in sterile-filtered infection medium, see 5.2.4.3) was added over the cells for 1 h at 37°C and 5% CO_2 while gently shaking. Virus was removed and cells overlaid with 2 mL 2.4% (w/v) microcrystalline cellulose (MCC, Avicel® Stabilizer, FMC) dissolved in ddH_2O and 2x DMEM (1:1 ratio) plus TPCK-trypsin at a concentration of 2 µg/mL. The overlay was removed after 5 days incubation at 37°C, 5% CO_2. Cells were fixed with 1 mL 70% (v/v) ethanol per well for 30 min at RT, followed

by staining with 1 mL of 0.3% (w/v) crystal violet (Sigma-Aldrich) in 20 % (v/v) methanol for 10 min at RT.

5.2.5 Specific methods from section 3.1

5.2.5.1 Alexa647-CLICK

HeLaΔS1PL cells were seeded in a 6-well plate at $3*10^5$ cells in 3 mL DMEM and transfected the next day for 48 h. Prior harvest, cells were labelled for 4 h with the indicated amounts of pacSph in 1 mL DMEM. Cells were washed twice on ice with 1 mL ice-cold PBS and UV-irradiated (365 nm) in 1 ml ice-cold PBS for 5 min on ice at ≈10 cm distance to the light cone, lid open. PBS was removed, cells scraped off in 1 mL ice-cold PBS and transferred to a 1.5 mL tube. Cell pellets (3 min, 3000 rpm at 4°C) were resuspended in 100 µL HEPES-lysis buffer (50 mM HEPES-NaOH, pH 7.4, 100 mM NaCl, 1% (v/v) TX-100, 0.5% (w/v) sodium-deoxycholate, 2x protease-inhibitor cocktail (PIC)) and incubated for 1 h at 4°C on a rotor wheel. A post-nuclear supernatant (PNS) was created at 8 min, 16000 xg at 4°C centrifugation. PNS lysates was further used for CLICK reaction (in 1.5 mL tubes):

Table 5.12: Alexa647-CLICK master mix.

$CuSO_4$ and TBTA were freshly prepared.

Substance	Solvent	Stock (mM)	End-concentration (µM)	µL/reaction (3.5 µL)
$CuSO_4$	H_2O	40	500	1.36
Alexa647-azide	DMSO	10	50	0.54
TCEP, pH 7.5	H_2O	50	500	1.08
TBTA	DMSO	10	50	0.54

Components were mixed and 3.25 µL CLICK-mix added to lysates. The reaction was allowed to proceed for 4 h, 800 rpm at RT. An input sample was taken and lysates applied to 25 µL EZ view™ Red ANTI-FLAG™ M2 Affinity Gel (anti-FLAG beads), which were pre-washed (1 min, 800 g, RT) 2x with 1 mL HEPES-lysis buffer. The protein lysate was incubated with the beads for 1 h at RT on a rotor wheel. Afterwards, beads were spun down, a flow-through sample taken, and beads washed 4x with 1 mL HEPES-lysis buffer. Proteins were eluted with 2x SDS loading buffer (see 5.2.8.2) in HEPES-lysis buffer for 5 min, 95°C. Input, flow-through and pulldown samples were shortly centrifuged (1 min, 13000 rpm) and applied to SDS-PAGE.

5.2.6 Specific methods from section 3.2

5.2.6.1 Harvest of viral particles from A549ΔS1PL cells

A549ΔS1PL S2-6 cells were seeded in a T75 flask ($2.1*10^6$ cells) in 20 mL DMEM and infected the next day with IAV HK68 at a MOI of 1 (S. Kummer, Kräusslich lab). After 6 days, supernatants were collected via sucrose gradient (S. Kummer, Kräusslich lab). Pellets were resuspended in 50 µL HEPES lysisbuffer (see 5.2.5.1) for 10 min, 1200 rpm at 37°C, mixed with 5x SDS-loading buffer (to 1x) and subsequently subjected to SDS-PAGE analysis.

5.2.6.2 Incubation in SILAC media

SILAC media ingredients were purchased from Silantes. DMEM (without glutamine, without arginine, without lysine; 4.5 mg/L glucose) containing 2 mM L-stable glutamine and 10% (v/v) FBS was supplemented either with L-arginine:HCl ^{13}C-labeled and L-lysine:2*HCl 4,4,5,5,-^{2}H-labeled ("Medium") or L-arginine:HCl $^{13}C^{15}N$-labeled and L-lysine:HCl $^{13}C^{15}N$-labeled ("Heavy"); the "Light" medium was mixed with L-arginine:HCl and L-lysine:HCl, both from Sigma-Aldrich. (Isotopic) amino acids were added in a final concentration of 0.398 mM (arginine) and 0.798 mM (lysine). Medium was sterile-filtered (Steri-cup-GP, 0.22 µM, 500 mL volume) after addition of all components. A549ΔS1PL cells were passaged in SILAC media at least 7 times in presence of 1% P/S (w/v) at 37°C with 5% CO_2.

5.2.6.3 Proteomic screens performed with A549ΔS1PL S2-6 clone cells (HK68, PR8-I)

A549ΔS1PL cells were seeded at $2*10^6$ cells in one 10 cm dish/condition. Cells were (mock) infected (see 5.2.4.3) the next day for 1 and 12 hpi at indicated MOI's. Six hours prior harvest, cells were labelled with 3 µM pacSph. Cells were washed on ice 2x with ice-cold PBS and UV-irradiated (365 nm) in 5 ml ice-cold PBS for 5 min on ice at ≈10 cm distance to the light cone, lid open. PBS was removed and cells scraped off in PBS on ice. Cells were pelleted at 3 min, 3000 g at 4°C and resuspended in 300 µL PBS. Protein precipitation was performed by addition of 600 µL MeOH and 150 µL $CHCl_3$, followed by vigorous vortexing and centrifugation for 5 min, 14000 rpm at RT. The

supernatant was removed and the remaining pellet (proteins and cell debris) air-dried, resuspended in 4% (w/v) SDS in PBS and diluted to 1% SDS with PBS (to 200 µL end-volume) and a final concentration of 4x PIC. After addition of 100 µL HEPES buffer (50 mM HEPES, pH 8.5), cell lysates were incubated 5 min at 95 °C, cooled down on ice and incubated with 2 µL benzonase (Merck) for 30 min at 25°C. Samples were snap-frozen in liquid N_2 and stored at -80°C until further use.

Samples were thawed at RT and first incubated with 100 µL DTT (200 mM in 200 mM HEPES, pH 8.5) for 30 min at 45°C, prior disulphide bond alkylation with 20 µL 400 mM iodacetamide (in 200 mM HEPES, pH 8.5) for 30 min, 600 rpm at 24°C in the dark. The reaction was quenched with 20 µL 200 mM DTT (in 200 mM HEPES, pH 8.5). Proteins were MeOH/$CHCl_3$-precipitated as described above and protein pellets resuspended in 200 µL 1% (w/v) SDS in PBS and 2x PIC by sonic water bath and incubation at 1400 rpm (RT) until pellets were completely dissolved. Lysates were centrifuged for 3 min at 3000 g to remove insoluble material, transferred to a new 1.5 mL tube and the protein concentration measured in triplicates (1 µL) via BCA assay (see 5.2.8.1).

To verify successful pacSph-labelling, 25 µg of protein/condition was subjected to Alexa647-CLICK (see 5.2.5.1) and precipitated via MeOH/ $CHCl_3$ precipitation (see above). Precipitated protein was resolubilised in 1x SDS loading buffer (see 5.2.8.2) and loaded onto SDS-PAGE. In-gel fluorescence was measured at 700 nm with the Li-Cor device.

Then, “Light”, “medium” and “heavy” samples mixed in a ration 1:1:1 (200 µg total protein). For Biotin-CLICK, 200 µg of protein were adjusted to 187 µL volume (1% SDS in PBS/2xPIC) in a 2 mL tube prior addition of 13 µL CLICK mix (see Table 5.13):

Table 5.13: Biotin-CLICK mastermix.

$CuSO_4$, TCEP and TBTA were freshly prepared

Substance	**Solvent**	**Stock (mM)**	**End-concentration (µM)**	**µL/reaction (13 µL)**
$CuSO_4$	H_2O	40	500	5
Biotin-azide	DMSO	10	50	2
TCEP	H_2O	50	500	4
TBTA	DMSO	10	50	2

The reaction was allowed to proceed for 4 h at 800 rpm and 37°C. Clicked samples were topped up with ice-cold MeOH, stored at -80°C ON and centrifuged for 20 min, 15000 g, 4°C the next day. Protein precipitates were washed 3x with 2 ml ice-cold MeOH and the protein pellet left to air-dry for 2 min. Pellets were resuspended in 30 µL 4% (w/v) SDS in PBS and adjusted to 0.4 % SDS with PBS/2x PIC end-concentration. Protein lysates were centrifuged for 3 min at 3000 xg to remove insoluble material and supernatants applied to 25 µL Pierce™ NeutrAvidin™ beads, pre-washed 3x with 0.2% (w/v) SDS in PBS (1000 g, 1 min at RT). After 1.5 h incubation at RT on a rotor wheel, the supernatant was removed and beads washed 20x with 1% (w/v) SDS in PBS. Proteins were eluted with 50 µL elution buffer (4% (w/v) SDS, 4% (v/v) ß-mercaptoethanol, 100 mM Tris/HCl, pH 6.8) for 1 h at RT and 30 min at 95°C, then separated from avidin beads by centrifugation (1 min, 13000 rpm, RT) using Mobicols (35 µM pore size). The protein concentration was determined via Amido Black assay (see 5.2.6.4). Samples were topped up to 100 µL with 50 mM HEPES pH 8.0 and subjected to Protein clean-up was performed with 5 µg protein in a total volume of 100 µL (50 mM HEPES pH 8), using SP3 beads (according to Hughes *et al*., 2014)[361]. Therefore, 30 µL of hydrophilic and hydrophobic Sera-Mag Carboxylate-Modified Magnetic (SP3) Beads were mixed with 140 µL ddH_2O in 0.2 mL PCR-tubes, placed on a magnetic rack (manufactured by EMBL) and left to settle for 5 min. The supernatant was removed and beads washed 3x with 200 µL ddH_2O. Beads were resuspended in 10 µL ddH_2O and 2 µL mixed carefully with 100 µL (=10 µg) of protein lysate in a 0.2 mL PCR tube prior addition of 5 µL 5% (v/v) formic acid and acetonitrile (50% end-concentration). Samples were incubated for 8 min off and 2 min on the magnetic rack at RT. The supernatant was removed, SP3 beads washed 2x with 70% (v/v) ethanol and 1x with acetonitrile and the beads left to air-dry off the rack for 1 min at RT. Beads were carefully resuspended in 5 µL trypsin/LysC-solution (0.4 µL in 50 mM HEPES, pH 8) to avoid air-bubbles, sonicated for 1 min and the tryptic digest performed ON in a PCR thermocycler at 37°C. The next day, beads were shortly spun down and resuspended, prior addition of 200 µL acetonitrile and incubation for 8 min off and 2 min on rack at RT. The supernatant was removed, beads washed 2x with 180 µL acetonitrile and reconstituted in 9 µL 2% (v/v) DMSO, followed by sonification for 5 min.

Beads were shortly spun down, tubes placed on the magnetic rack and supernatants transferred 3x into a new PCR tube, letting the beads settle for 1 min in between, in order to remove beads from samples. These were then mixed with formic acid (1% (v/v) end-concentration) in a deactivated glass vial and stored at 4°C. MS-analysis was done with 5 µL sample (performed by S. Föhr, Krijgsveld lab) on Orbitrap Fusion mass spectrometers (ThermoFisher Scientific) coupled to Easy-n-LC 1200 liquid chromatograph (ThermoFisher Scientific). Samples were loaded onto trap column (Acclaim™ PepMap™ 100 100 µm x 2 cm, nanoViper) and separated via analytical column (Acclaim™ PepMap™ RSLC 75 µm x 50 cm, nanoViper); total runtime 120 min (gradient: 105 min, A: 0.1% (v/v) formic acid B: 80% (v/v) acetonitrile, 0.1% (v/v) formic acid, gradient from 4% B to 8% in 3 min, to 21% in 53 min, to 34% in 26 min and to 50% in 4 min, with washing at 100% B; max. pressure of 800 bar). RAW data was processed with Proteome Discoverer™ and tandem MS (MS/MS) spectra were searched against the UniProt *Homo sapiens* and the corresponding Influenza A database. Only high confidence (=False Discovery Rate (FDR) <1%) master protein (candidates) (=leading protein X of a protein group, in which proteins were ranked according to the probability that identified peptides belong to protein X) were considered for further analysis.

5.2.6.4 Amido Black assay

Protein concentration was measured in triplicates (1 µL). Therefore, samples were topped up with 100 µL ddH_2O and mixed with 400 µL Amido Black solution (0.02% (w/v) amido black, 40% (v/v) methanol, 10% (v/v) glacial acetic acid, 50% (v/v) ddH_2O), vortexed, incubated for 5 min at RT and centrifuged for 5 min, 14000 rpm at RT. The supernatant was removed and washed 2x with 500 µL MeOH/acetic acid (10/1) prior dissolving protein pellets in 300 µL 0.1 M NaOH. The absorbance of 150 µL solution was measured at 550 nm in a 96-well plate. Serial dilutions of BSA in 100 µL ddH_2O were used as reference.

5.2.6.5 Proteomic screen performed with A549ΔS1PL S3-10 clone cells (PR-II)

Labelling, infection, UV crosslink, cell lysis and biotin-CLICK were performed as described in 5.2.6.3 with the exception that protein samples were not alkylated after cell lysis. Approximately 10% of PBS-solubilised cells was subjected to lipidome analysis (see 5.2.8.9). Biotinylated protein-lipid complexes were enriched via trypsin-resistant magnetic streptavidin beads (under patenting, G. Sigismondo, Krijgsveld lab). Briefly, 600 µL of trypsin-resistant beads were washed 3x with 1 mL 0.2% (w/v) SDS in PBS (1.5 mL tubes) on a magnetic rack prior addition of lysates. After incubation ON at RT on a rotor wheel, beads were washed 3x with SDS washing buffer (10 mM Tris-HCl pH 7.5, 1 mM EDTA, 1% (w/v) SDS, 200 mM NaCl), 1x with NaCl washing buffer (10 mM Tris-HCl pH 7.5, 1 mM EDTA, 0.1% (v/v) TX-100, 2 M NaCl, 2x with 10% (v/v) isopropanol and twice with 20% (v/v) acetonitrile. Beads were transferred to a PCR tube and resuspended in 50 mM ammonium bicarbonate (AmBic). DTT was added to a final concentration of 7 mM and samples reduced by heating at 95°C for 30 min, followed by alkylation with 12 mM iodoacetamide for 40 min at RT in the dark. The reaction was quenched with DTT (12 mM end-concentration) and proteins were trypsin-digested (trypsin/LysC) on beads at 37°C ON. Peptides were cleaned up by the SP3 protocol (see 5.2.6.3) as previously described (Hughes *et al*., 2014)[361] with minor modifications. Briefly, 2 µL of SP3 beads (1:1 mixture) were added to each sample and acetonitrile was added to reach at least 90–95% (v/v) of organic solvent. Beads were incubated for 10 min and washed twice with 100 % (v/v) acetonitrile on the magnetic rack. Peptides were eluted off the rack with 0.1% (v/v) trifluoroacetic acid (TFA) by sonification for 5 min in the water bath. Supernatants were recovered on the magnetic rack and transferred 2x to a new PCR tube. Afterwards, peptides were eluted from SP3 beads in 0.1% (v/v) TFA in water through sonication for 5 min in a water bath. Samples were injected and analysed on an Orbitrap Fusion mass spectrometer coupled to an EASY LC 1200 UPLC system (ThermoFisher Scientific). Samples were loaded onto the trap column (Acclaim PepMap100 C18 Nano-Trap 2 cm x 100 µm x 5 µm) with Buffer A (0.1% (v/v) formic acid in water) and separated over a 50 cm analytical column (Acclaim PepMap RSLC, 75 µm x 2 µm) using a 105 min linear gradient from 3% to 40% Buffer B (0.1%

(v/v) formic acid, 80% (v/v) acetonitrile). MS2 fragmentation was set to HCD and MSMS scans were acquired in the ion trap. RAW data were processed with MaxQuant (1.5.2.8)[362] using default settings. MSMS spectra were searched against the *Homo sapiens* Uniprot database linked to a database containing protein sequences of contaminants and of Influenza A/Puerto Rico/8/34 (H1N1) virus. Enzyme specificity was set to trypsin/P, allowing a maximum of two missed cleavages. Cysteine carbamidomethylation was set as fixed modification, while methionine oxidation and protein N-terminal acetylation were used as variable modifications. Global false discovery rate for both protein and peptides was set to 1%. The match-between-runs and re-quantify options were enabled. Intensity-based quantification options (iBAQ and LFQ) were calculated. Data analysis was performed with Perseus software (1.5.3.0)[363]. Per each SILAC ratio, only proteins quantified with a minimum $\log_2$ ratio of 2 (=4-fold enrichment) over the mock control in at least two out of the three biological replicates were considered as enriched in the respective experiment.

5.2.6.6 Microarray

A549ΔS1PL cells were seeded in a 6-well plate at $3*10^5$ cells/well and infected the next day as described (see 5.2.4.3). RNA was harvested after 1 and 12 hpi according to the RNeasy® Mini Kit protocol. After treatment of RNA samples with DNase I (2 U/µL) for 15 min at 37°C, RT-PCR was performed with the Transcriptor First Strand cDNA Synthesis Kit using anchored oligo(dT)18 primers as described in the manufacturer's instruction. Obtained cDNA samples were sent to Genomics Core facility at EMBL and analysed via Affymetrix Human Gene Chip 2.0 array (Ambion protocol, ThermoFisher Scientific).

5.2.6.7 Metabolic labelling of cells with bifunctional lipids

A549ΔS1PL S3-10 clone cells from two full 10 cm dishes were labelled with 3 µM pacSph or 40 µM pacFA for 6 h or with 6 µM pacChol for 30 min (see Table 5.2). Cells treated with Fumonisin B1 (100 µM, freshly dissolved in PBS) were pre-incubated one day prior labelling experiments. Cell harvest, UV-irradiation, protein precipitation and biotin-CLICK was performed as described for

the proteomic experiments (see 5.2.6.3). Protein pellets were resuspended in 4% (w/v) SDS in PBS and diluted to 1% SDS with PBS/2x PIC prior BCA assay (see 5.2.8.1), followed by biotin-CLICK and protein precipitation with ice-cold MeOH at -80°C ON. An input sample was taken from resuspended (0.4% (w/v) SDS in PBS/2xPIC) proteins. To enrich biotinylated lipid-protein complexes, Pierce™ High Capacity NeutrAvidin™ Agarose beads were washed 3 times with 1 mL 0.2% (w/v) SDS in PBS (1 min, 1000 g, RT), incubated with biotin-clicked protein lysates for 90 min on a rotor wheel at RT and washed 10x with 1% (w/v) SDS in PBS. To elute proteins, 2x SDS loading buffer (see 5.2.8.2) in 4% (w/v) SDS was added to avidin agarose beads and samples were cooked 2x for 15 min at 95°C. Beads were spun down and supernatant taken for SDS-PAGE separation and Western blot analysis.

5.2.6.8 siRNA treatment

All siRNAs (endo-ribonuclease prepared siRNA, esiRNA), except *UGCG* siRNA, were purchased from Sigma-Aldrich (see Table 5.14). Per knock-down, 10^6 A549 cells were seeded in a 6-well plate and transfected in solution with 30 pmol siRNA against human gene targets using Lipofectamine™ RNAiMAX (ThermoFisher Scientific) according to the manufacturer's instruction. Cells were splitted the next day at $3*10^5$ cells/6-well plate and infected 24 h later (=at 48 h transfection). Anti-NP stain or HA titer were used as read out at 8 and 24 hpi, respectively (see 5.2.4.4 and 5.2.4.5).

Table 5.14: siRNAs used in transient knock-down experiments.

MISSION® esiRNA's (except UGCG= Ambion®) were diluted with RNAse-free water to 10 µM.

Gene-specific siRNA	Order number
ITGB1	EHU065071
SLC1A5	Custom designed
RAB11A	EHU018981
SLC25A11	EHU024351
SLC46A1	EHU079701
UGCG	#AM51334

5.2.6.9 Deglycosylation assay

N-linked deglycosylation was performed with EndoH and PNGaseF purchased from NEB according to the manufacturer's instruction, using 40 µg A549 cell lysate.

5.2.6.10 Covalent coupling of anti-ITGB1 antibody to Protein A beads

ProteinA beads were diluted 1:1 with PBS and washed 3x (3000 g, 2.5 min) with 500 µL conjugation buffer (50 mM Tris pH 7.6, 150 mM NaCl, 2% (w/v) BSA) and adjusted to 1 mL volume in a 2 mL tube. Antibody (anti-Integrin beta 1, see Table 5.1) was added and incubated ON at 4°C on a rotor wheel. Afterwards, beads were spun down (5 min, 3000 g, RT), transferred to a 15 mL falcon with Na-borate buffer (pH 9) and washed 2x (3500 rpm, 4 min, RT) prior covalent coupling of antibody to beads with dimethyl pimelimidate (DMP) in Na-borate buffer (10 mg in 2 mL) for 30 min at RT at pH > 8.3. Antibody-coupled beads were spun down and the reaction was stopped by addition of 2 mL 0.2 M ethanolamine, pH 8.0, followed by a wash step and incubation for 2 h at RT in the according buffer. Finally, beads were pelleted, washed 2x in 5 mL PBS, resuspended in 1 bed volume PBS and stored in 0.02% (w/v) sodium azide, pH 7-8, at 4°C.

5.2.6.11 ITGB1-immunoprecipitation after biotin-CLICK

A549ΔS1PL S3-10 clone cells were labelled with pacSph (3 µM, 6 h), UV irradiated and cell pellets harvested as described (see 5.2.6.3). Cell were lysed in NP-40 lysis buffer[364] (50 mM TEA, pH 7.4, 150 mM NaCl, 1% (v/v) NP-40, 2x PIC) for 90 min, 4°C on a rotor wheel and protein concentration measured of PNS. For Biotin-CLICK, 300 µg protein was diluted to 187 µL with NP-40 lysis buffer and 13 µL CLICK-Mix (see Table 5.13) was added. The reaction was allowed to proceed for 1 h, 800 rpm at RT[364]. After CLICK, lysates were spun down (3000 g, 5 min, RT) and the supernatant applied to Protein A-coupled anti-ITGB1 beads which were washed 3x (3000 g, 2.5 min, RT) with NP-40 lysis buffer. Immunoprecipitation was performed at 4°C ON on a rotor wheel. Afterwards, beads were washed 3x with 1 mL ice-cold NP-40 lysis buffer and proteins eluted in 2x SDS loading buffer (see 5.2.8.2) in 4% (w/v) SDS at 95°C

for 15 min. Input, flow-through und elution fractions were loaded on NuPAGE™ 4-12% Bis-Tris gels, electrophoresis performed with NuPAGE™ MOPS running buffer for 50 min, 200 V, and protein lysates subsequently analysed via Western Blot using anti-ITGB1 and anti-biotin antibody.

5.2.6.12 Membrane fractionation

Cells were washed twice with ice-cold PBS on ice, scraped off in an appropriate volume of PBS and transferred to a pre-weighed, 1.5 mL ultracentrifugation tube. Cells were pelleted (3 min, 3000 rpm at 4°C), weighed after aspiration of the supernatant and the wet weight determined. Per 25 mg cell pellet, 500 µL homogenisation buffer (PBS, 2xPIC and 1 µL/mL benzonase, Sigma-Aldrich) was added. After resuspension, cells were sonicated (5 s with cooling on ice in between) until the solution became clear. Complete cell rupture was verified using trypan blue (1:1 ratio of cell suspension:trypan blue). Membrane fractions were created by centrifugation (1 h, 100000 g at 4°C, Opti™ MAX-XP ultracentrifuge, rotor TLA55). Membrane pellets were resuspended in an appropriate volume of lysis buffer (1% (v/v) TX-100, 0.1% (v/v) SDS in PBS, 2x PIC, 0.5 µL/mL benzonase, Sigma-Aldrich) and solubilised by sonication and incubation for 1 h at 4°C on a rotor wheel. Lysates were centrifuged (8 min, 16000 g, 4°C), supernatants transferred to a new 1.5 mL tube, snap frozen in liquid N_2 and stored at -80°C until further use.

5.2.6.13 Real-time quantitative (qRT) PCR

RNA extraction and cDNA synthesis were conducted as described in 5.2.6.6. The obtained cDNA template (1 ng/µL in RNase-free water) was taken for qRT-PCR using SYBR™ Select Master Mix and the respective forward- and reverse primer for amplification of housekeeping genes (GAPDH, 50S ribosomal protein L9, or beta-actin, see Table 5.5) or IFITM3 (see Table 5.5, provided by S. Kummer, Kräusslich lab) in concentrations as suggested. Samples were pipetted in a DNase- and RNase-free 96-well PCR plate, covered with adhesive film and qRT-PCR performed in the Applied Biosystems™ 7500 Real Time PCR machine with SYBR green as setting, standard cycling mode. Data was analysed with the corresponding software.

5.2.7 Specific methods from section 3.3

5.2.7.1 Ganglioside TLC

10^6 cells were collected in PBS and pelleted (5 min, 3000 rpm, 4°C). Pellets were snap-frozen in liquid N_2 and stored at -20°C until further use. Pellets were thawed at RT, 50 µL MS-pure water added and samples sonicated in a water bath for 3 min. Cell lysates were transferred to a Pyrex® glass tube and mixed with 1.3 mL $CHCl_3$:MeOH:ddH_2O (30:60:8) by vortexing for 30 sec, and centrifuged afterwards (15 min, 4500 rpm at RT). The supernatant was transferred to a new Pyrex® tube, evaporated under N_2 stream and stored at -20°C. The next day, 1 mL of 60% (v/v) MeOH (in LC-MS water) was given to lipid extracts, samples sonicated for 3 min in a water bath and centrifuged for 5 min at 14000 rpm at RT in 1.5 mL tubes. Standards (400 pmol bovine GM1, GDA1+B and brain mix in MeOH:CHCl3:H_2O, 1:1:1, 10 µM stock, Avanti Polar Lipids) were also pipetted to 1 mL 60% MeOH and treated likewise. Glycosphingolipids (GSLs) were purified with DCS-C8 columns in a vacuum minifold. Therefore, columns were washed 3x with 1 mL MeOH and pre-conditioned with 2 mL 60% (v/v) MeOH. To bind GSLs, samples were applied twice and collected in a Pyrex® tube. Columns were washed 3x with 1 mL MeOH and collected in a new Pyrex® tube by elution with 4 mL MeOH. The solvent was evaporated under N_2 stream and stored at -20°C. Ganglioside TLC was performed according to[365]. Samples and markers were dissolved in 300 µL MeOH and transferred to a 1.5 mL tube, evaporated in a rotational vacuum concentrator and re-solubilised in 30 µL MeOH. Samples were applied on a HPTLC silica gel 60 plate with a CAMAG Linomat 5 applicator and developed to 100% in 103 mL $CHCl_3$: MeOH:H_2O (60:35:8) supplemented with 0.25% potassium chloride after equilibration of the glass chamber for 30 min. TLC plates were dried for 1 h at RT under the fume hood and developed in Resorcinol solution (freshly prepared, see Table 5.15):

Table 5.15: Resorcinol solution to visualise gangliosides.

According to[365]. LC= liquid chromatographie.

For 100 ml	Ingredient	
20 ml	Aqueous Resorcinol 1.5 % (w/v)	300 mg in LC-MS water
0.3 ml	$CuSO_4$-5x H_2O 1 % (w/v)	10 mg in 1 ml LC-MS water

30 ml	Conc. HCl (37 % fuming hydrochlorid acid)
50 ml	LC-MS water

TLC plates were sprayed with a glass vaporiser, covered with a glass plate and incubated 20 min at 135°C. After cooling down, GSL bands were recorded in the red fluorescence channel in the Amersham Imager 600.

5.2.7.2 Fenretinide (4-HPR) labelling

Cells were seeded in a 6-well plate at $3*10^5$ cells/well in 3 mL DMEM the day prior labelling. Cells were treated with 10 µg/mL of the inhibitor (from 25 mg/mL stock in DMSO) for 1 h in infection medium (see 5.2.4.3). Afterwards, medium was removed and replaced by 3 mL DMEM. After 7 h, cells were harvested and used for the respective downstream experiment.

5.2.8 General methods

5.2.8.1 BCA assay

Protein concentration of cell lysates was measured via the Pierce™ BCA protein assay kit in triplicates (topped up to 25 µL with ddH_2O) according to the manufacturer's instructions (96-well format). A BSA calibration curve of 0, 0.5, 1, 1.5, 2, 3, 4 and 5 µg BSA in 25 µL volume was used.

5.2.8.2 SDS-PAGE

Protein separation was performed by one-dimensional discontinuous SDS-PAGE as described by Laemmli[366]. The composition of separation (10%, 12%) and stacking gel (4%) is depicted in Table 5.16:

Table 5.16: SDS-gel composition.

Volume sufficient for 2x 0.75 mm gels or 1x 1.5 mm gel.

Separating gel	**volume (10%-SDS gel)**	**volume (12% SDS-gel)**
ddH_2O	4,05 mL	3,35 mL
Tris (1,5 M), pH 8,8	2,5 mL	2,5 mL
Acryl amide 30% (v/v)	3,3 mL	4,0 mL
SDS 10% (w/v)	100 µL	100 µL
TEMED	10 µL	10 µL
APS 10%	100 µL	100 µL
Stacking gel	**volume (4% stacking gel)**	
ddH_2O	3,05 mL	
Tris (1,5 M) pH 6,8	1,25 mL	
Acryl amide 30% (v/v)	0,65 mL	
SDS 10% (w/v)	50 µL	

TEMED	10 µL
APS 10% (w/v)	50 µL

If not mentioned otherwise, protein samples were mixed with 5x SDS loading buffer (100 mM Tris pH 6.8, 5 mM EDTA pH 8, 4% SDS, 0.04% bromphenolblue, 10% glycerol, 0.2 mM DTT) to 1x concentration and cooked for 5 min at 95°C. Gels were run in 1x SDS gel electrophoresis buffer (25 mM (w/v) Tris, 192 mM (w/v) glycine, 0.1% (w/v) SDS) at 30 mA/gel (Mini-PROTEAN® Tetra System). Indicated experiments were performed with NuPAGE™ 4-12% Bis-Tris gels using NuPAGE™ MOPS running buffer, run time 50 min, 200 V. Proteins were either detected by colloidal Coomassie stain or by Western blot.

5.2.8.3 Colloidal Coomassie stain

SDS gels were stained according to[367]. Briefly, SDS gels were washed 3x for 10 min in ddH_2O after protein separation on a horizontal shaker. Gels were stained ON at RT with colloidal Coomassie solution (0.02% (w/v) Coomassie brilliant blue G-250, 5% (w/v) aluminium-sulfate-(14-18)-hydrate, 10% (v/v) ethanol (96%), 2% (v/v) orthophosphoric acid (85%)). Afterwards, the solution was removed and gels washed twice with ddH_2O to remove dye particles. Gels were destained with 10% (v/v) ethanol (96%), 2% (v/v) orthophosphoric acid (85%), washed twice with ddH_2O and scanned.

5.2.8.4 Western blot

SDS-gel separated proteins were transferred to PVDF membranes by the wet or tank electrotransfer protocol. PVDF membranes were pre-wetted for 10 s in methanol, the blot assembled as a “sandwich” (2x blotting paper-SDS gel-PVDF membrane-2x blotting paper) and protein transfer performed for 1.5 h, 100 V at 4°C or ON at 30 V, 4°C (Mini-PROTEAN® Tetra System) in transfer buffer (25 mM (w/v) Tris, 192 mM (w/v) glycine,10% (v/v) methanol). Prior decoration with antibodies, the membrane was blocked for 20-60 min at RT or ON at 4°C in 5% (w/v) low fat milk diluted in PBS. Incubation of the membrane with the primary antibody was performed for 1 h at RT or ON at 4°C, incubation with the second antibody for 30-60 min at RT or ON at 4°C (list of antibodies see Table 5.1). Before, after as well as in between incubation with antibodies, the membrane was washed 3x with PBS and 0.1% (v/v) Tween20 (PBS-T).

Scanning and analysis of Western blots was done with the Li-Cor system and software recording signals in the respective channels.

5.2.8.5 Cell-surface biotinylation

Cell surface biotinylation was performed as described in Ernst *et al*.[116]. Briefly, cells were seeded in a 6-well plate at $3*10^5$ cells in 3 mL DMEM and transfected the next day for 48-72 h. Non-transfected cells were seeded at 10^6 cells/well the day prior the experiment. Cells were incubated for 30 min gently shaking on ice in 500 µL/well EZ-Link™ Sulfo-NHS-Biotin solution (dissolved in 150 mM NaCl, 10 mM triethanolamine (TAE) pH 9.0, 2 mM $CaCl_2$) after media removal and 2x wash with 1 mL ice-cold PBS Ca^{2+}/Mg^{2+} (1 mM $MgCl_2$, 0.1 mM $CaCl_2$ in PBS). Afterwards, cells were washed with 1 mL ice-cold quenching buffer (PBS Ca^{2+}/Mg^{2+}, 100 mM glycine) prior incubation in the respective buffer for 20 min on ice. The quenching solution was removed, cells washed 2x with 1 mL ice-cold PBS, scraped off in 1 mL ice-cold PBS, transferred into 1.5 mL tubes, pelleted (3 min, 3000 rpm at 4°C) and resuspended in 300 µL lysis buffer (1% (v/v) TX-100, 0.1% (w/v) SDS, 2x PIC, 1 µL/mL benzonase, Sigma-Aldrich, in PBS). Cell lysates were sonicated for 3 min in a sonic water bath, incubated for 15 min, 1200 rpm at 25°C and insoluble material removed by centrifugation (10 min, 13000 rpm at 4°C). An input sample was taken from the supernatant, and lysates incubated with 50 µL Pierce™ High NeutrAvidin™ beads, which were washed 2x with 500 µL lysis buffer (1 min, 3000 g at 4°C) beforehand, for 1.5 h at RT on a rotor wheel. Beads were spun down, a flow-through sample taken and further washed with 1 mL ice-cold wash buffer I (lysis buffer and 0.5 M NaCl) and 1 mL wash buffer II (lysis buffer, 0.5 M NaCl and 0.1% (v/v) NP-40). Proteins bound to beads were eluted with 2x SDS loading buffer (see 5.2.8.2) in lysis buffer for 5 min, 95°C. Input, flow-through and pulldown samples were shortly centrifuged (1 min, 13000 rpm) and applied to SDS-PAGE.

5.2.8.6 Microscopy

After removal of cell culture media, cells were washed 3x with PBS and fixed with 4% (w/v) paraformaldehyde (PFA) for 10 min at RT. Cells were rinsed 3x with PBS to remove PFA prior lysis for 10 min with 0.1% (v/v) TX-100 at RT

and blocking overnight (2.5% (w/v) BSA in PBS). Incubation with primary (1:100 in 2.5% (w/v) BSA in PBS) and secondary (1:1000 in 2.5% (w/v) BSA in PBS) antibodies was performed at RT for 1 h. Cell nuclei were stained with DAPI (300 nM in PBS) for 10 min at RT and coverslips were mounted in ProLong™ Gold Diamond Antifade Mountant. The relative amounts of NP-positive cells were either determined directly (Axiovert 200, 300 cells counted) or from 4 different frames (LSM 800).

5.2.8.7 Metabolic labelling of pacSph with subsequent lipid extraction for thin layer chromatography (TLC)

Cells were seeded at $3*10^5$ cells/well in 6-well plates and labelled with 3 µM pacSph the following day for 6 h. Afterwards, cells were washed twice with PBS, detached with 250 µl trypsin and resuspended in 1 mL DMEM. Cells were pelleted at 3000 rpm, 3 min at 4°C and washed twice in 1 mL ice-cold DMEM w/o supplements and 1x with 1 mL ice-cold PBS. The cell pellet was resuspended in 300 µL PBS and subjected to lipid extraction (according to Thiele *et al*., 2012)[368]: 600 µL MeOH and 150 µL $CHCl_3$ were added and samples mixed by vortexing. After centrifugation (14000 rpm, 5 min at RT), the supernatant was transferred into a 2 ml tube and mixed with 300 µL $CHCl_3$ and 600 µL 0.1% (v/v) acetic acid in H_2O and centrifuged (14000 rpm, 5 min at RT). Lipids dissolved in the lower organic phase were transferred into a fresh 1.5 mL tube and dried in a rotational vacuum concentrator for 20 min at 30 °C. Lipid extracts were resuspended in 7 µL $CHCl_3$ and 30 µL of a freshly prepared Coumarin-CLICK mix was added (see Table 5.17):

Table 5.17: Coumarin-azide-CLICK master mix.

The $CuBF_4$ stock was freshly prepared.

Substance	Solvent	Stock (mM)	Volume (µL)	End-concentration (µM)
$CuBF_4$	acetonitrile	10	250	2000
Coumarin-azide	DMSO	44.5	1	35.6
Ethanol		50	1000	80% (v/v)

The Click reaction was allowed to proceed for 20 min at 45 °C in a rotational vacuum concentrator. The clicked lipids were resuspended in 20 µL of mobile

phase I ($CHCl_3$:MeOH:H_2O:AcOH at 65:25:4:1), applied to a HPTLC silica gel 60 plate with the CAMAG Linomat 5 applicator and developed to 70% in mobile phase I in a CAMAG ADC2 system followed by development to 100% in mobile phase II (hexane:ethyl actetate at 1:1). For increased fluorescence intensity, plates were treated with 4% (v/v) N,N-diisopropylethylamine in hexane. Coumarin-clicked lipids were visualized with the Amersham Imager 600 at 460 nm. Charring of lipids was performed by spraying the TLC plate with 20% (v/v) sulfuric acid in ddH_2O using a glass evaporator, incubation for 10 min at 125°C and subsequent scanning of charred lipid bands.

5.2.8.8 Cell viability assay

Cell viability was tested with the CellTiter-Blue® Cell Viability Assay. Briefly, $0.25*10^4$ cells were seeded in a 96-well plate in quadruplicates in DMEM low glucose w/o phenolred and glutamine, supplied with 10% FBS, 1% L-glutamine and 1% P/S. Cell viability was determined at day 0, 1, 2 and 3 according to the manufacturer's instructions.

5.2.8.9 Lipidome analysis

Lipid extraction was done by I. Leibrecht, C. Lüchtenborg and T. Sachsenheimer. Lipidome data was analysed and provided by C. Lüchtenborg and T. Sachsenheimer (Brügger lab).

Cells were placed on ice and washed 2x with ice-cold 150 mM (w/v) ammonium-bicarbonate buffer. Cells were scraped off in 1 mL buffer, pelleted (3 min, 3000 rpm at 4°C) and resuspended in 50 µL buffer. Approximately 10% were subjected to pre-analysis. Therefore, lipids were extracted via the Bligh & Dyer method[369] with slight modifications. Briefly, PC (13:0/13:0, 14:0/14:0, 20:0/20:0, 21:0/21:0, Avanti Polar Lipids) and SM (d18:1, with N-acylated 13:0/17:0/25:0, semi-synthesised by T. Sachsenheimer, according to Özbalci *et al*., 2013[370]) lipid standards were pipetted into a Pyrex® glass tube (I). Then, 1.9 mL SBD solution ($CHCl_3$:MeOH:37% (v/v) HCl at a ratio of 5:10:0.15 (v/v/v)) plus 5 µL of the sample was added. The volume was adjusted to 500 µL with MS-grade water, samples were vortexed, and mixed thoroughly with additional 500 µL

$CHCl_3$ and MS-grade water. Pyrex® tubes were centrifuged (2 min, 2000 rpm at 4°C) and the lower (organic) phase transferred to a new tube (II). Subsequently, 500 µL $CHCl_3$ and MS-grade water were added to the second tube and 500 µL $CHCl_3$ to the first one. After vortexing and centrifugation, the lower phase of tube II was transferred to the final one (III), and the organic phase of tube I transferred to tube II and re-extracted (vortexed and centrifuged, see above). The lower phase of tube II was transferred to tube III, the organic phase was evaporated under N_2 stream and dried lipids stored at -20°C until further analysis. Lipid content of samples was analysed on a Quattro II instrument (Waters) after re-solubilisation of lipids in 10 mM (w/v) ammonium acetate in methanol. Quantitative lipid analysis of full lipidomes was performed as described[370]. Samples were extracted according to the Bligh & Dyer method (see above) and spiked with the following internal lipid standards in a mastermix containing PC (13:0/13:0, 14:0/14:0, 20:0/20:0, 21:0/21:0), PI (16:0/16:0, 17:0/20:4), PA (17:0/20:4, 21:0/22:6), LPC (17:1) and TAG (TAG, D5-Mix, LM-6000/D5-17:0/17:1/17:1) (all purchased from Avanti Polar Lipids), DAG (17:0/17:0, Larodan), D6-cholesterol (Cambridge Isotope Laboratory), CE (9:0/19:0/24:1, Sigma-Aldrich) as well as SM (d18:1 with N-acylated 15:0, 17:0, 25:0), Cer and GlcCer (both d18:1 with N-acylated 15:0, 17:0, 25:0), LacCer (d18:1 with N-acylated 12:0), PE and PS (both 14:1/14:1, 20:1/20:1, 22:1/22:1) and PG (14:1/14:1, 20:1/ 20:1, 22:1/22:1), all semi-synthesised by T. Sachsenheimer (Brügger lab) according to[370]. To measure plasmalogens, lipids were extracted under neutral conditions[370] and supplemented with a PE-plasmalogen (PE P-)-containing standard mix: PE P-Mix 1 (16:0p/15:0, 16:0p/19:0, 16:0p/ 25:0), PE P- Mix 2 (18:0p/15:0, 18:0p/19:0, 18:0p/25:0) and PE P-Mix 3 (18:1p/15:0, 18:1p/19:0, 18:1p/25:0). After evaporation, samples were resuspended in 60 µL 10 mM (w/v) ammonium acetate in methanol and 10% pipetted to 96-well plates (Eppendorf Twintec 96, colourless, Sigma-Aldrich). Lipid extracts were analysed by direct injection into the AB SCIEX QTRAP 6500+ mass spectrometer (Sciex), the latter equipped with chip-based (HD-D ESI Chip, Advion Biosciences) electrospray infusion, and ionisation via Triversa Nanomate (Advion Biosciences) as described previously[370]. The distinction of various lipid classes was achieved by measurement in the positive polarity and precursor or neutral loss scanning mode (see Özbalci *et al.*, 2013)[370]. Data was analysed

with the LipidView software (ABSciex) and the in-house developed software ShinyLipids.

5.2.8.10 Analysis of sphingoid bases

Derivatisation and analysis of sphingoid bases was performed by T.Sachsenheimer (Brügger lab).

To quantify sphingoid backbones (Sph, Sph-1-P, Spg and Spg-1-P), cells were collected from a confluent 10 cm dish. Cells were washed twice on ice with 5 mL 150 mM (w/v) ammonium-bicarbonate buffer, the supernatant aspirated and cells scraped off without buffer. Cells pellets were transferred to a 2 mL tube containing 25 pmol of a SL-standard mixture (LM-6002, containing various sphingoid C17:1 bases, Avanti Polar Lipids) in 990 µL $CHCl_3$/MeOH (17:1 (v/v)) after resuspension in 200 µL buffer. Samples were incubated for 2 h at 4°C in a thermomixer, centrifuged (5 min, 9000 g, 4°C) and the lower organic phase transferred to a new 1.5 mL tube, evaporated under N_2 stream (neutral extraction). The upper, aqueous phase was mixed first with 10 µL HCl (2 M), then with 375 µL $CHCl_3$/MeOH/37% (v/v) HCl (40:80:1, (v/v/v)) and 125 µL $CHCl_3$. Samples were incubated and centrifuged as above. The lower phase was transferred to a new 1.5 mL tube and evaporated under N_2 stream (acidic extraction). Lipid extracts from the neutral and the acidic extraction were resuspended in 110 µL methanol and 10 µL used to determine the phosphate content[370]. Then, both extractions were derivatised with Trimethylsilyl (TMS)-diazomethane[371]. Therefore, the solvents were mixed with 2 mL of TMS-diazomethane (2 M) in hexane and incubated for 20 min, 750 rpm/min at RT. Lipids were dried under N_2 stream after stopping the reaction with 1 µL acetic acid and subsequently taken up in 100 µL isopropanol:water:acetonitrile (2:1:1, (v/v/v)) containing 10 mM ammonium formiate and 0.1% (v/v) formic acid. A sample volume of 5 µL was analysed on a Dionex UHPLC coupled to a QExactive™ high resolution mass spectrometer (ThermoFisher Scientific) as described[254].

5.2.8.11 Data analysis and software

Western blots were scanned with the Li-Cor device and analysed either with the corresponding software (Image Studio™ Lite) or with Fiji. Microscope

images were processed with Fiji. Statistical analysis of datasets was carried out using Microsoft Excel and GraphPad Prism. Statistical significance of parametrically datasets was analysed by GraphPad Prism using either unpaired, two-tailed *t* test (two samples compared) or ONE-way ANOVA with subsequent Dunnett's multiple comparison test (comparison of ≥3 samples against a reference sample); *, *p* 0.05; **, *p* 0.01; ***, *p* 0.001. Microarray data was analysed using R (Bioconductor package), script provided by S. Bender. Lipidomics data was processed in Microsoft Excel (C. Lüchtenborg, T. Sachsenheimer) and the in-house developed ShinyLipids software. A protein abundance (SILAC) ratio of (X/Y)>2 (=$\log_2$(X/Y)>1) was used as a cut-off for enrichment in condition X, a protein abundance ratio of (X/Y)<0.5 (=$\log_2$(X/Y)<-1) as a cut-off for enrichment in condition Y (if not mentioned otherwise).

6 References

1 Fahy, E., Cotter, D., Sud, M. & Subramaniam, S. Lipid classification, structures and tools. *Biochim Biophys Acta* **1811**, 637-647, doi:10.1016/j.bbalip.2011.06.009 (2011).

2 Wenk, M. R. The emerging field of lipidomics. *Nat Rev Drug Discov* **4**, 594-610, doi:10.1038/nrd1776 (2005).

3 Berg, J. M., Tymoczko, J. L., Gatto, G. J. & Stryer, L. *Biochemistry*. Eighth edition. edn, (W.H. Freeman & Company, a Macmillan Education Imprint, 2015).

4 http://www.lipidmaps.org/data/structure/index.php, 2018).

5 Muro, E., Atilla-Gokcumen, G. E. & Eggert, U. S. Lipids in cell biology: how can we understand them better? *Mol Biol Cell* **25**, 1819-1823, doi:10.1091/mbc.E13-09-0516 (2014).

6 van Meer, G., Voelker, D. R. & Feigenson, G. W. Membrane lipids: where they are and how they behave. *Nat Rev Mol Cell Biol* **9**, 112-124, doi:10.1038/nrm2330 (2008).

7 Saliba, A. E., Vonkova, I. & Gavin, A. C. The systematic analysis of protein-lipid interactions comes of age. *Nat Rev Mol Cell Biol* **16**, 753-761, doi:10.1038/nrm4080 (2015).

8 Resh, M. D. Fatty acylation of proteins: The long and the short of it. *Prog Lipid Res* **63**, 120-131, doi:10.1016/j.plipres.2016.05.002 (2016).

9 van Meer, G. Cellular lipidomics. *EMBO J* **24**, 3159-3165, doi:10.1038/sj.emboj.7600798 (2005).

10 Harayama, T. & Riezman, H. Understanding the diversity of membrane lipid composition. *Nat Rev Mol Cell Biol* **19**, 281-296, doi:10.1038/nrm.2017.138 (2018).

11 van Meer, G. Caveolin, cholesterol, and lipid droplets? *J Cell Biol* **152**, F29-34 (2001).

12 McMahon, H. T. & Boucrot, E. Membrane curvature at a glance. *J Cell Sci* **128**, 1065-1070, doi:10.1242/jcs.114454 (2015).

13 Futerman, A. H. & Riezman, H. The ins and outs of sphingolipid synthesis. *Trends in cell biology* **15**, 312-318, doi:10.1016/j.tcb.2005.04.006 (2005).

14 Huang, J. & Feigenson, G. W. A microscopic interaction model of maximum solubility of cholesterol in lipid bilayers. *Biophys J* **76**, 2142-2157, doi:10.1016/S0006-3495(99)77369-8 (1999).

15 Dai, J., Alwarawrah, M. & Huang, J. Instability of cholesterol clusters in lipid bilayers and the cholesterol's Umbrella effect. *J Phys Chem B* **114**, 840-848, doi:10.1021/jp909061h (2010).

16 Fantini, J., Garmy, N., Mahfoud, R. & Yahi, N. Lipid rafts: structure, function and role in HIV, Alzheimer's and prion diseases. *Expert Rev Mol Med* **4**, 1-22, doi:doi:10.1017/S1462399402005392 (2002).

17 Farhan, H. & Rabouille, C. Signalling to and from the secretory pathway. *J Cell Sci* **124**, 171-180, doi:10.1242/jcs.076455 (2011).

18 Fagone, P. & Jackowski, S. Membrane phospholipid synthesis and endoplasmic reticulum function. *J Lipid Res* **50 Suppl**, S311-316, doi:10.1194/jlr.R800049-JLR200 (2009).

19 Bell, R. M., Ballas, L. M. & Coleman, R. A. Lipid topogenesis. *J Lipid Res* **22**, 391-403 (1981).
20 Sprong, H. *et al.* UDP-galactose:ceramide galactosyltransferase is a class I integral membrane protein of the endoplasmic reticulum. *J Biol Chem* **273**, 25880-25888 (1998).
21 Fullekrug, J. & Nilsson, T. Protein sorting in the Golgi complex. *Biochim Biophys Acta* **1404**, 77-84 (1998).
22 Contreras, G. A. *et al.* Single genotypes underestimate the prevalence of antiretroviral resistance in patients with perinatally acquired HIV. *J Infect* **64**, 125-126, doi:10.1016/j.jinf.2011.10.013
S0163-4453(11)00532-9 [pii] (2012).
23 Holthuis, J. C., Pomorski, T., Raggers, R. J., Sprong, H. & Van Meer, G. The organizing potential of sphingolipids in intracellular membrane transport. *Physiol Rev* **81**, 1689-1723, doi:10.1152/physrev.2001.81.4.1689 (2001).
24 van der Wouden, J. M., Maier, O., van, I. S. C. & Hoekstra, D. Membrane dynamics and the regulation of epithelial cell polarity. *Int Rev Cytol* **226**, 127-164 (2003).
25 Nyasae, L. K., Hubbard, A. L. & Tuma, P. L. Transcytotic efflux from early endosomes is dependent on cholesterol and glycosphingolipids in polarized hepatic cells. *Mol Biol Cell* **14**, 2689-2705, doi:10.1091/mbc.e02-12-0816 (2003).
26 Di Paolo, G. & De Camilli, P. Phosphoinositides in cell regulation and membrane dynamics. *Nature* **443**, 651-657, doi:10.1038/nature05185 (2006).
27 Alberts, B. *Molecular biology of the cell*. Sixth edition. edn, (Garland Science, Taylor and Francis Group, 2015).
28 Liu, D. *et al.* Enzymatic removal of alphaGal antigen in pig kidneys by ex vivo and in vivo administration of endo-beta-galactosidase C. *Xenotransplantation* **9**, 228-236 (2002).
29 Rusinol, A. E., Cui, Z., Chen, M. H. & Vance, J. E. A unique mitochondria-associated membrane fraction from rat liver has a high capacity for lipid synthesis and contains pre-Golgi secretory proteins including nascent lipoproteins. *J Biol Chem* **269**, 27494-27502 (1994).
30 van Meer, G. & Simons, K. Lipid polarity and sorting in epithelial cells. *J Cell Biochem* **36**, 51-58, doi:10.1002/jcb.240360106 (1988).
31 van Meer, G. & Lisman, Q. Sphingolipid transport: rafts and translocators. *J Biol Chem* **277**, 25855-25858, doi:10.1074/jbc.R200010200 (2002).
32 Devaux, P. F. & Morris, R. Transmembrane asymmetry and lateral domains in biological membranes. *Traffic* **5**, 241-246, doi:10.1111/j.1600-0854.2004.0170.x (2004).
33 Daleke, D. L. Phospholipid flippases. *J Biol Chem* **282**, 821-825, doi:10.1074/jbc.R600035200 (2007).
34 Ohvo-Rekila, H., Ramstedt, B., Leppimaki, P. & Slotte, J. P. Cholesterol interactions with phospholipids in membranes. *Prog Lipid Res* **41**, 66-97 (2002).
35 Baumann, N. A. *et al.* Transport of newly synthesized sterol to the sterol-enriched plasma membrane occurs via nonvesicular equilibration. *Biochemistry* **44**, 5816-5826, doi:10.1021/bi048296z (2005).

36 Sandhu, J. *et al.* Aster Proteins Facilitate Nonvesicular Plasma Membrane to ER Cholesterol Transport in Mammalian Cells. *Cell* **175**, 514-529 e520, doi:10.1016/j.cell.2018.08.033 (2018).
37 Pralle, A., Keller, P., Florin, E. L., Simons, K. & Horber, J. K. Sphingolipid-cholesterol rafts diffuse as small entities in the plasma membrane of mammalian cells. *J Cell Biol* **148**, 997-1008 (2000).
38 Simons, K. & Vaz, W. L. Model systems, lipid rafts, and cell membranes. *Annu Rev Biophys Biomol Struct* **33**, 269-295, doi:10.1146/annurev.biophys.32.110601.141803 (2004).
39 Ipsen, J. H., Karlstrom, G., Mouritsen, O. G., Wennerstrom, H. & Zuckermann, M. J. Phase equilibria in the phosphatidylcholine-cholesterol system. *Biochim Biophys Acta* **905**, 162-172 (1987).
40 Veatch, S. L. & Keller, S. L. Separation of liquid phases in giant vesicles of ternary mixtures of phospholipids and cholesterol. *Biophys J* **85**, 3074-3083, doi:10.1016/S0006-3495(03)74726-2 (2003).
41 Kaiser, H. J. *et al.* Order of lipid phases in model and plasma membranes. *Proc Natl Acad Sci U S A* **106**, 16645-16650, doi:10.1073/pnas.0908987106 (2009).
42 Sezgin, E., Levental, I., Mayor, S. & Eggeling, C. The mystery of membrane organization: composition, regulation and roles of lipid rafts. *Nat Rev Mol Cell Biol* **18**, 361-374, doi:10.1038/nrm.2017.16 (2017).
43 Pike, L. J. Rafts defined: a report on the Keystone Symposium on Lipid Rafts and Cell Function. *J Lipid Res* **47**, 1597-1598, doi:10.1194/jlr.E600002-JLR200 (2006).
44 Raghupathy, R. *et al.* Transbilayer lipid interactions mediate nanoclustering of lipid-anchored proteins. *Cell* **161**, 581-594, doi:10.1016/j.cell.2015.03.048 (2015).
45 Lingwood, D. & Simons, K. Lipid rafts as a membrane-organizing principle. *Science* **327**, 46-50, doi:10.1126/science.1174621
327/5961/46 [pii] (2010).
46 Sodt, A. J., Pastor, R. W. & Lyman, E. Hexagonal Substructure and Hydrogen Bonding in Liquid-Ordered Phases Containing Palmitoyl Sphingomyelin. *Biophys J* **109**, 948-955, doi:10.1016/j.bpj.2015.07.036 (2015).
47 Ramstedt, B. & Slotte, J. P. Interaction of cholesterol with sphingomyelins and acyl-chain-matched phosphatidylcholines: a comparative study of the effect of the chain length. *Biophys J* **76**, 908-915, doi:10.1016/S0006-3495(99)77254-1 (1999).
48 Simons, K. & Ikonen, E. Functional rafts in cell membranes. *Nature* **387**, 569-572, doi:10.1038/42408 (1997).
49 Cremesti, A. E., Goni, F. M. & Kolesnick, R. Role of sphingomyelinase and ceramide in modulating rafts: do biophysical properties determine biologic outcome? *FEBS Lett* **531**, 47-53 (2002).
50 Bollinger, C. R., Teichgraber, V. & Gulbins, E. Ceramide-enriched membrane domains. *Biochim Biophys Acta* **1746**, 284-294, doi:10.1016/j.bbamcr.2005.09.001 (2005).
51 Bieberich, E. Sphingolipids and lipid rafts: Novel concepts and methods of analysis. *Chemistry and physics of lipids* **216**, 114-131, doi:10.1016/j.chemphyslip.2018.08.003 (2018).

52 Stancevic, B. & Kolesnick, R. Ceramide-rich platforms in transmembrane signaling. *FEBS Lett* **584**, 1728-1740, doi:10.1016/j.febslet.2010.02.026 (2010).
53 El-Haddad, H. *et al.* Characterization of TtALV2, an essential charged repeat motif protein of the Tetrahymena thermophila membrane skeleton. *Eukaryot Cell* **12**, 932-940, doi:10.1128/EC.00050-13
EC.00050-13 [pii] (2013).
54 Kraft, M. L. Sphingolipid Organization in the Plasma Membrane and the Mechanisms That Influence It. *Front Cell Dev Biol* **4**, 154, doi:10.3389/fcell.2016.00154 (2016).
55 Gault, C. R., Obeid, L. M. & Hannun, Y. A. An overview of sphingolipid metabolism: from synthesis to breakdown. *Adv Exp Med Biol* **688**, 1-23 (2010).
56 Pewzner-Jung, Y. *et al.* A critical role for ceramide synthase 2 in liver homeostasis: II. insights into molecular changes leading to hepatopathy. *J Biol Chem* **285**, 10911-10923, doi:10.1074/jbc.M109.077610 (2010).
57 Mullen, T. D. & Obeid, L. M. Ceramide and apoptosis: exploring the enigmatic connections between sphingolipid metabolism and programmed cell death. *Anticancer Agents Med Chem* **12**, 340-363 (2012).
58 Bartke, N. & Hannun, Y. A. Bioactive sphingolipids: metabolism and function. *J Lipid Res* **50 Suppl**, S91-96, doi:10.1194/jlr.R800080-JLR200 (2009).
59 Siddique, M. M., Li, Y., Chaurasia, B., Kaddai, V. A. & Summers, S. A. Dihydroceramides: From Bit Players to Lead Actors. *J Biol Chem* **290**, 15371-15379, doi:10.1074/jbc.R115.653204 (2015).
60 Abdel Hadi, L. *et al.* Sphingosine Kinase 2 and Ceramide Transport as Key Targets of the Natural Flavonoid Luteolin to Induce Apoptosis in Colon Cancer Cells. *PLoS One* **10**, e0143384, doi:10.1371/journal.pone.0143384 (2015).
61 Kumagai, K., Kawano, M., Shinkai-Ouchi, F., Nishijima, M. & Hanada, K. Interorganelle trafficking of ceramide is regulated by phosphorylation-dependent cooperativity between the PH and START domains of CERT. *J Biol Chem* **282**, 17758-17766, doi:10.1074/jbc.M702291200 (2007).
62 Kudo, N. *et al.* Structural basis for specific lipid recognition by CERT responsible for nonvesicular trafficking of ceramide. *Proc Natl Acad Sci U S A* **105**, 488-493, doi:10.1073/pnas.0709191105 (2008).
63 Yamaji, T., Kumagai, K., Tomishige, N. & Hanada, K. Two sphingolipid transfer proteins, CERT and FAPP2: their roles in sphingolipid metabolism. *IUBMB Life* **60**, 511-518, doi:10.1002/iub.83 (2008).
64 Hanada, K. *et al.* Molecular machinery for non-vesicular trafficking of ceramide. *Nature* **426**, 803-809, doi:10.1038/nature02188 (2003).
65 Merrill, A. H., Jr. Sphingolipid and glycosphingolipid metabolic pathways in the era of sphingolipidomics. *Chem Rev* **111**, 6387-6422, doi:10.1021/cr2002917 (2011).
66 Ichikawa, S., Sakiyama, H., Suzuki, G., Hidari, K. I. & Hirabayashi, Y. Expression cloning of a cDNA for human ceramide glucosyltransferase that catalyzes the first glycosylation step of glycosphingolipid synthesis. *Proc Natl Acad Sci U S A* **93**, 4638-4643 (1996).

67 Yamashita, T. *et al.* A vital role for glycosphingolipid synthesis during development and differentiation. *Proc Natl Acad Sci U S A* **96**, 9142-9147 (1999).

68 Jeckel, D., Karrenbauer, A., Burger, K. N., van Meer, G. & Wieland, F. Glucosylceramide is synthesized at the cytosolic surface of various Golgi subfractions. *J Cell Biol* **117**, 259-267 (1992).

69 D'Angelo, G. *et al.* Glycosphingolipid synthesis requires FAPP2 transfer of glucosylceramide. *Nature* **449**, 62-67, doi:10.1038/nature06097 (2007).

70 Buton, X. *et al.* Transbilayer movement of monohexosylsphingolipids in endoplasmic reticulum and Golgi membranes. *Biochemistry* **41**, 13106-13115 (2002).

71 D'Angelo, G., Capasso, S., Sticco, L. & Russo, D. Glycosphingolipids: synthesis and functions. *FEBS J* **280**, 6338-6353, doi:10.1111/febs.12559 (2013).

72 Aureli, M., Loberto, N., Chigorno, V., Prinetti, A. & Sonnino, S. Remodeling of sphingolipids by plasma membrane associated enzymes. *Neurochem Res* **36**, 1636-1644, doi:10.1007/s11064-010-0360-7 (2011).

73 Schulze, H. & Sandhoff, K. Lysosomal lipid storage diseases. *Cold Spring Harb Perspect Biol* **3**, doi:10.1101/cshperspect.a004804 (2011).

74 Kitatani, K., Idkowiak-Baldys, J. & Hannun, Y. A. The sphingolipid salvage pathway in ceramide metabolism and signaling. *Cell Signal* **20**, 1010-1018, doi:10.1016/j.cellsig.2007.12.006 (2008).

75 Tafesse, F. G. *et al.* Both sphingomyelin synthases SMS1 and SMS2 are required for sphingomyelin homeostasis and growth in human HeLa cells. *J Biol Chem* **282**, 17537-17547, doi:10.1074/jbc.M702423200 (2007).

76 Gillard, B. K., Clement, R. G. & Marcus, D. M. Variations among cell lines in the synthesis of sphingolipids in de novo and recycling pathways. *Glycobiology* **8**, 885-890 (1998).

77 Taha, T. A., Hannun, Y. A. & Obeid, L. M. Sphingosine kinase: biochemical and cellular regulation and role in disease. *J Biochem Mol Biol* **39**, 113-131 (2006).

78 Riboni, L., Prinetti, A., Bassi, R. & Tettamanti, G. Formation of bioactive sphingoid molecules from exogenous sphingomyelin in primary cultures of neurons and astrocytes. *FEBS Lett* **352**, 323-326 (1994).

79 Riboni, L. *et al.* Metabolic fate of exogenous sphingosine in neuroblastoma neuro2A cells. Dose-dependence and biological effects. *Ann N Y Acad Sci* **845**, 46-56 (1998).

80 Chatelut, M. *et al.* Natural ceramide is unable to escape the lysosome, in contrast to a fluorescent analogue. *FEBS Lett* **426**, 102-106 (1998).

81 Wijesinghe, D. S. *et al.* Substrate specificity of human ceramide kinase. *J Lipid Res* **46**, 2706-2716, doi:10.1194/jlr.M500313-JLR200 (2005).

82 Cuvillier, O. Sphingosine kinase-1--a potential therapeutic target in cancer. *Anticancer Drugs* **18**, 105-110, doi:10.1097/CAD.0b013e328011334d (2007).

83 Maceyka, M. *et al.* SphK1 and SphK2, sphingosine kinase isoenzymes with opposing functions in sphingolipid metabolism. *J Biol Chem* **280**, 37118-37129, doi:10.1074/jbc.M502207200 (2005).

84 Pyne, S., Long, J. S., Ktistakis, N. T. & Pyne, N. J. Lipid phosphate phosphatases and lipid phosphate signalling. *Biochem Soc Trans* **33**, 1370-1374, doi:10.1042/BST20051370 (2005).

85 Delon, C. *et al.* Sphingosine kinase 1 is an intracellular effector of phosphatidic acid. *J Biol Chem* **279**, 44763-44774, doi:10.1074/jbc.M405771200 (2004).

86 Johnson, K. R. *et al.* Role of human sphingosine-1-phosphate phosphatase 1 in the regulation of intra- and extracellular sphingosine-1-phosphate levels and cell viability. *J Biol Chem* **278**, 34541-34547, doi:10.1074/jbc.M301741200 (2003).

87 Le Stunff, H. *et al.* Recycling of sphingosine is regulated by the concerted actions of sphingosine-1-phosphate phosphohydrolase 1 and sphingosine kinase 2. *J Biol Chem* **282**, 34372-34380, doi:10.1074/jbc.M703329200 (2007).

88 Le Stunff, H., Galve-Roperh, I., Peterson, C., Milstien, S. & Spiegel, S. Sphingosine-1-phosphate phosphohydrolase in regulation of sphingolipid metabolism and apoptosis. *J Cell Biol* **158**, 1039-1049, doi:10.1083/jcb.200203123 (2002).

89 Ikeda, M., Kihara, A. & Igarashi, Y. Sphingosine-1-phosphate lyase SPL is an endoplasmic reticulum-resident, integral membrane protein with the pyridoxal 5'-phosphate binding domain exposed to the cytosol. *Biochem Biophys Res Commun* **325**, 338-343, doi:10.1016/j.bbrc.2004.10.036 (2004).

90 Stoffel, W., LeKim, D. & Sticht, G. Distribution and properties of dihydrosphingosine-1-phosphate aldolase (sphinganine-1-phosphate alkanal-lyase). *Hoppe Seylers Z Physiol Chem* **350**, 1233-1241 (1969).

91 Chalfant, C. E. & Spiegel, S. Sphingosine 1-phosphate and ceramide 1-phosphate: expanding roles in cell signaling. *J Cell Sci* **118**, 4605-4612, doi:10.1242/jcs.02637 (2005).

92 Brockman, H. L. *et al.* The 4,5-double bond of ceramide regulates its dipole potential, elastic properties, and packing behavior. *Biophys J* **87**, 1722-1731, doi:10.1529/biophysj.104.044529 (2004).

93 Nousiainen, T. *et al.* Anthracycline-induced cardiomyopathy: long-term effects on myocardial cell integrity, cardiac adrenergic innervation and fatty acid uptake. *Clin Physiol* **21**, 123-128 (2001).

94 Vieira, C. R. *et al.* Dihydrosphingomyelin impairs HIV-1 infection by rigidifying liquid-ordered membrane domains. *Chem Biol* **17**, 766-775, doi:10.1016/j.chembiol.2010.05.023 (2010).

95 Koster, D. V. *et al.* Actomyosin dynamics drive local membrane component organization in an in vitro active composite layer. *Proc Natl Acad Sci U S A* **113**, E1645-1654, doi:10.1073/pnas.1514030113 (2016).

96 Ray, A., Jatana, N. & Thukral, L. Lipidated proteins: Spotlight on protein-membrane binding interfaces. *Prog Biophys Mol Biol* **128**, 74-84, doi:10.1016/j.pbiomolbio.2017.01.002 (2017).

97 Lucero, H. A. & Robbins, P. W. Lipid rafts-protein association and the regulation of protein activity. *Arch Biochem Biophys* **426**, 208-224, doi:10.1016/j.abb.2004.03.020 (2004).

98 Levental, I., Grzybek, M. & Simons, K. Greasing their way: lipid modifications determine protein association with membrane rafts. *Biochemistry* **49**, 6305-6316, doi:10.1021/bi100882y (2010).
99 Rietveld, A., Neutz, S., Simons, K. & Eaton, S. Association of sterol- and glycosylphosphatidylinositol-linked proteins with Drosophila raft lipid microdomains. *J Biol Chem* **274**, 12049-12054 (1999).
100 Shi, D. *et al.* Smoothened oligomerization/higher order clustering in lipid rafts is essential for high Hedgehog activity transduction. *J Biol Chem* **288**, 12605-12614, doi:10.1074/jbc.M112.399477 (2013).
101 Diaz-Rohrer, B. B., Levental, K. R., Simons, K. & Levental, I. Membrane raft association is a determinant of plasma membrane localization. *Proc Natl Acad Sci U S A* **111**, 8500-8505, doi:10.1073/pnas.1404582111 (2014).
102 Heberle, F. A. *et al.* Bilayer thickness mismatch controls domain size in model membranes. *J Am Chem Soc* **135**, 6853-6859, doi:10.1021/ja3113615 (2013).
103 Jensen, M. O. & Mouritsen, O. G. Lipids do influence protein function-the hydrophobic matching hypothesis revisited. *Biochim Biophys Acta* **1666**, 205-226, doi:10.1016/j.bbamem.2004.06.009 (2004).
104 Fantini, J. & Barrantes, F. J. How cholesterol interacts with membrane proteins: an exploration of cholesterol-binding sites including CRAC, CARC, and tilted domains. *Front Physiol* **4**, 31, doi:10.3389/fphys.2013.00031 (2013).
105 Coskun, U., Grzybek, M., Drechsel, D. & Simons, K. Regulation of human EGF receptor by lipids. *Proc Natl Acad Sci U S A* **108**, 9044-9048, doi:10.1073/pnas.1105666108 (2011).
106 Contreras, F. X. *et al.* Molecular recognition of a single sphingolipid species by a protein's transmembrane domain. *Nature* **481**, 525-529, doi:10.1038/nature10742
nature10742 [pii] (2012).
107 Bjorkholm, P. *et al.* Identification of novel sphingolipid-binding motifs in mammalian membrane proteins. *Biochim Biophys Acta* **1838**, 2066-2070, doi:10.1016/j.bbamem.2014.04.026 (2014).
108 Levental, I., Lingwood, D., Grzybek, M., Coskun, U. & Simons, K. Palmitoylation regulates raft affinity for the majority of integral raft proteins. *Proc Natl Acad Sci U S A* **107**, 22050-22054, doi:10.1073/pnas.1016184107
1016184107 [pii] (2010).
109 van der Meer-Janssen, Y. P., van Galen, J., Batenburg, J. J. & Helms, J. B. Lipids in host-pathogen interactions: pathogens exploit the complexity of the host cell lipidome. *Prog Lipid Res* **49**, 1-26, doi:10.1016/j.plipres.2009.07.003 (2010).
110 Zaas, D. W., Duncan, M., Rae Wright, J. & Abraham, S. N. The role of lipid rafts in the pathogenesis of bacterial infections. *Biochim Biophys Acta* **1746**, 305-313, doi:10.1016/j.bbamcr.2005.10.003 (2005).
111 Bastiani, M. & Parton, R. G. Caveolae at a glance. *J Cell Sci* **123**, 3831-3836, doi:10.1242/jcs.070102 (2010).
112 Suzuki, T. & Suzuki, Y. Virus infection and lipid rafts. *Biological & pharmaceutical bulletin* **29**, 1538-1541 (2006).

113 Brugger, B. *et al.* The HIV lipidome: a raft with an unusual composition. *Proc Natl Acad Sci U S A* **103**, 2641-2646, doi:10.1073/pnas.0511136103 (2006).
114 Gerl, M. J. *et al.* Quantitative analysis of the lipidomes of the influenza virus envelope and MDCK cell apical membrane. *J Cell Biol* **196**, 213-221, doi:10.1083/jcb.201108175
jcb.201108175 [pii] (2012).
115 Tafesse, F. G. *et al.* Intact sphingomyelin biosynthetic pathway is essential for intracellular transport of influenza virus glycoproteins. *Proc Natl Acad Sci U S A* **110**, 6406-6411, doi:10.1073/pnas.1219909110
1219909110 [pii] (2013).
116 Ernst, A. M. *et al.* Differential transport of Influenza A neuraminidase signal anchor peptides to the plasma membrane. *FEBS Lett* **587**, 1411-1417, doi:10.1016/j.febslet.2013.03.019
S0014-5793(13)00230-5 [pii] (2013).
117 Stohr, K. Influenza--WHO cares. *The Lancet. Infectious diseases* **2**, 517 (2002).
118 Russell, C. A. *et al.* Improving pandemic influenza risk assessment. *Elife* **3**, e03883, doi:10.7554/eLife.03883 (2014).
119 Taubenberger, J. K. & Morens, D. M. Pandemic influenza--including a risk assessment of H5N1. *Rev Sci Tech* **28**, 187-202 (2009).
120 Zambon, M. C. Epidemiology and pathogenesis of influenza. *J Antimicrob Chemother* **44 Suppl B**, 3-9 (1999).
121 Tong, S. *et al.* New world bats harbor diverse influenza A viruses. *PLoS Pathog* **9**, e1003657, doi:10.1371/journal.ppat.1003657 (2013).
122 Szewczyk, B., Bienkowska-Szewczyk, K. & Krol, E. Introduction to molecular biology of influenza a viruses. *Acta Biochim Pol* **61**, 397-401 (2014).
123 Medina, R. A. & Garcia-Sastre, A. Influenza A viruses: new research developments. *Nature reviews. Microbiology* **9**, 590-603, doi:10.1038/nrmicro2613 (2011).
124 Webster, R. G., Bean, W. J., Gorman, O. T., Chambers, T. M. & Kawaoka, Y. Evolution and ecology of influenza A viruses. *Microbiol Rev* **56**, 152-179 (1992).
125 Petrova, V. N. & Russell, C. A. The evolution of seasonal influenza viruses. *Nature reviews. Microbiology* **16**, 47-60, doi:10.1038/nrmicro.2017.118 (2018).
126 Watanabe, T. *et al.* Circulating avian influenza viruses closely related to the 1918 virus have pandemic potential. *Cell Host Microbe* **15**, 692-705, doi:10.1016/j.chom.2014.05.006 (2014).
127 Taubenberger, J. K. & Kash, J. C. Influenza virus evolution, host adaptation, and pandemic formation. *Cell Host Microbe* **7**, 440-451, doi:10.1016/j.chom.2010.05.009 (2010).
128 Domingo, E. Quasispecies and the implications for virus persistence and escape. *Clin Diagn Virol* **10**, 97-101 (1998).
129 Bizebard, T. *et al.* Structure of influenza virus haemagglutinin complexed with a neutralizing antibody. *Nature* **376**, 92-94, doi:10.1038/376092a0 (1995).

130 Cohen, M. *et al.* Influenza A penetrates host mucus by cleaving sialic acids with neuraminidase. *Virol J* **10**, 321, doi:10.1186/1743-422X-10-321 (2013).
131 Nicholson, K. G. *et al.* Immunogenicity and safety of a two-dose schedule of whole-virion and AS03A-adjuvanted 2009 influenza A (H1N1) vaccines: a randomised, multicentre, age-stratified, head-to-head trial. *The Lancet. Infectious diseases* **11**, 91-101, doi:10.1016/S1473-3099(10)70296-6 (2011).
132 Yamayoshi, S., Watanabe, M., Goto, H. & Kawaoka, Y. Identification of a Novel Viral Protein Expressed from the PB2 Segment of Influenza A Virus. *J Virol* **90**, 444-456, doi:10.1128/JVI.02175-15 (2016).
133 Kobayashi, M., Toyoda, T. & Ishihama, A. Influenza virus PB1 protein is the minimal and essential subunit of RNA polymerase. *Arch Virol* **141**, 525-539 (1996).
134 Fechter, P. *et al.* Two aromatic residues in the PB2 subunit of influenza A RNA polymerase are crucial for cap binding. *J Biol Chem* **278**, 20381-20388, doi:10.1074/jbc.M300130200 (2003).
135 Dias, A. *et al.* The cap-snatching endonuclease of influenza virus polymerase resides in the PA subunit. *Nature* **458**, 914-918, doi:10.1038/nature07745 (2009).
136 Plotch, S. J., Bouloy, M., Ulmanen, I. & Krug, R. M. A unique cap(m7GpppXm)-dependent influenza virion endonuclease cleaves capped RNAs to generate the primers that initiate viral RNA transcription. *Cell* **23**, 847-858 (1981).
137 Zheng, W. & Tao, Y. J. Structure and assembly of the influenza A virus ribonucleoprotein complex. *FEBS Lett* **587**, 1206-1214, doi:10.1016/j.febslet.2013.02.048 (2013).
138 Chen, W. *et al.* A novel influenza A virus mitochondrial protein that induces cell death. *Nat Med* **7**, 1306-1312, doi:10.1038/nm1201-1306 (2001).
139 Wise, H. M. *et al.* A complicated message: Identification of a novel PB1-related protein translated from influenza A virus segment 2 mRNA. *J Virol* **83**, 8021-8031, doi:10.1128/JVI.00826-09 (2009).
140 Varga, Z. T., Grant, A., Manicassamy, B. & Palese, P. Influenza virus protein PB1-F2 inhibits the induction of type I interferon by binding to MAVS and decreasing mitochondrial membrane potential. *J Virol* **86**, 8359-8366, doi:10.1128/JVI.01122-12 (2012).
141 Yoshizumi, T. *et al.* Influenza A virus protein PB1-F2 translocates into mitochondria via Tom40 channels and impairs innate immunity. *Nat Commun* **5**, 4713, doi:10.1038/ncomms5713 (2014).
142 Valladares-Ayerbes, M. *et al.* Prognostic impact of disseminated tumor cells and microRNA-17-92 cluster deregulation in gastrointestinal cancer. *International journal of oncology* **39**, 1253-1264, doi:10.3892/ijo.2011.1112 (2011).
143 Muramoto, Y., Noda, T., Kawakami, E., Akkina, R. & Kawaoka, Y. Identification of novel influenza A virus proteins translated from PA mRNA. *J Virol* **87**, 2455-2462, doi:10.1128/JVI.02656-12 (2013).
144 Jagger, B. W. *et al.* An overlapping protein-coding region in influenza A virus segment 3 modulates the host response. *Science* **337**, 199-204, doi:10.1126/science.1222213 (2012).

145 Desmet, E. A., Bussey, K. A., Stone, R. & Takimoto, T. Identification of the N-terminal domain of the influenza virus PA responsible for the suppression of host protein synthesis. *J Virol* **87**, 3108-3118, doi:10.1128/JVI.02826-12 (2013).
146 Dubois, J., Terrier, O. & Rosa-Calatrava, M. Influenza viruses and mRNA splicing: doing more with less. *MBio* **5**, e00070-00014, doi:10.1128/mBio.00070-14 (2014).
147 Hale, B. G., Randall, R. E., Ortin, J. & Jackson, D. The multifunctional NS1 protein of influenza A viruses. *J Gen Virol* **89**, 2359-2376, doi:10.1099/vir.0.2008/004606-0 (2008).
148 Nemeroff, M. E., Barabino, S. M., Li, Y., Keller, W. & Krug, R. M. Influenza virus NS1 protein interacts with the cellular 30 kDa subunit of CPSF and inhibits 3'end formation of cellular pre-mRNAs. *Mol Cell* **1**, 991-1000 (1998).
149 Engelhardt, O. G. & Fodor, E. Functional association between viral and cellular transcription during influenza virus infection. *Rev Med Virol* **16**, 329-345, doi:10.1002/rmv.512 (2006).
150 Billharz, R. *et al.* The NS1 protein of the 1918 pandemic influenza virus blocks host interferon and lipid metabolism pathways. *J Virol* **83**, 10557-10570, doi:10.1128/JVI.00330-09 (2009).
151 Fernandez-Sesma, A. *et al.* Influenza virus evades innate and adaptive immunity via the NS1 protein. *J Virol* **80**, 6295-6304, doi:10.1128/JVI.02381-05 (2006).
152 Gack, M. U. *et al.* Influenza A virus NS1 targets the ubiquitin ligase TRIM25 to evade recognition by the host viral RNA sensor RIG-I. *Cell Host Microbe* **5**, 439-449, doi:10.1016/j.chom.2009.04.006 (2009).
153 Li, S., Min, J. Y., Krug, R. M. & Sen, G. C. Binding of the influenza A virus NS1 protein to PKR mediates the inhibition of its activation by either PACT or double-stranded RNA. *Virology* **349**, 13-21, doi:10.1016/j.virol.2006.01.005 (2006).
154 Nogales, A., Rodriguez, L., DeDiego, M. L., Topham, D. J. & Martinez-Sobrido, L. Interplay of PA-X and NS1 Proteins in Replication and Pathogenesis of a Temperature-Sensitive 2009 Pandemic H1N1 Influenza A Virus. *J Virol* **91**, doi:10.1128/JVI.00720-17 (2017).
155 O'Neill, R. E., Talon, J. & Palese, P. The influenza virus NEP (NS2 protein) mediates the nuclear export of viral ribonucleoproteins. *EMBO J* **17**, 288-296, doi:10.1093/emboj/17.1.288 (1998).
156 Reuther, P. *et al.* Adaptive mutations in the nuclear export protein of human-derived H5N1 strains facilitate a polymerase activity-enhancing conformation. *J Virol* **88**, 263-271, doi:10.1128/JVI.01495-13 (2014).
157 Selman, M., Dankar, S. K., Forbes, N. E., Jia, J. J. & Brown, E. G. Adaptive mutation in influenza A virus non-structural gene is linked to host switching and induces a novel protein by alternative splicing. *Emerg Microbes Infect* **1**, e42, doi:10.1038/emi.2012.38 (2012).
158 Nayak, D. P., Balogun, R. A., Yamada, H., Zhou, Z. H. & Barman, S. Influenza virus morphogenesis and budding. *Virus Res* **143**, 147-161, doi:10.1016/j.virusres.2009.05.010
S0168-1702(09)00209-3 [pii] (2009).

159 Ruigrok, R. W., Calder, L. J. & Wharton, S. A. Electron microscopy of the influenza virus submembranal structure. *Virology* **173**, 311-316 (1989).
160 Rossman, J. S. & Lamb, R. A. Influenza virus assembly and budding. *Virology* **411**, 229-236, doi:10.1016/j.virol.2010.12.003
S0042-6822(10)00747-6 [pii] (2011).
161 Elleman, C. J. & Barclay, W. S. The M1 matrix protein controls the filamentous phenotype of influenza A virus. *Virology* **321**, 144-153, doi:10.1016/j.virol.2003.12.009 (2004).
162 Pinto, L. H. & Lamb, R. A. The M2 proton channels of influenza A and B viruses. *J Biol Chem* **281**, 8997-9000, doi:R500020200 [pii]
10.1074/jbc.R500020200 (2006).
163 Liu, J. J. *et al.* Pyrazolobenzodiazepines: part I. Synthesis and SAR of a potent class of kinase inhibitors. *Bioorg Med Chem Lett* **20**, 5984-5987, doi:10.1016/j.bmcl.2010.08.079
S0960-894X(10)01215-1 [pii] (2010).
164 Gannage, M. *et al.* Matrix protein 2 of influenza A virus blocks autophagosome fusion with lysosomes. *Cell Host Microbe* **6**, 367-380, doi:10.1016/j.chom.2009.09.005 (2009).
165 Wise, H. M. *et al.* Identification of a novel splice variant form of the influenza A virus M2 ion channel with an antigenically distinct ectodomain. *PLoS Pathog* **8**, e1002998, doi:10.1371/journal.ppat.1002998 (2012).
166 Kim, P. *et al.* Glycosylation of Hemagglutinin and Neuraminidase of Influenza A Virus as Signature for Ecological Spillover and Adaptation among Influenza Reservoirs. *Viruses* **10**, doi:10.3390/v10040183 (2018).
167 Ma, K., Roy, A. M. & Whittaker, G. R. Nuclear export of influenza virus ribonucleoproteins: identification of an export intermediate at the nuclear periphery. *Virology* **282**, 215-220, doi:10.1006/viro.2001.0833
S0042-6822(01)90833-5 [pii] (2001).
168 Hidari, K. I. *et al.* Influenza virus utilizes N-linked sialoglycans as receptors in A549 cells. *Biochem Biophys Res Commun* **436**, 394-399, doi:10.1016/j.bbrc.2013.05.112 (2013).
169 Baigent, S. J. & McCauley, J. W. Influenza type A in humans, mammals and birds: determinants of virus virulence, host-range and interspecies transmission. *Bioessays* **25**, 657-671, doi:10.1002/bies.10303 (2003).
170 Matrosovich, M. N., Matrosovich, T. Y., Gray, T., Roberts, N. A. & Klenk, H. D. Human and avian influenza viruses target different cell types in cultures of human airway epithelium. *Proc Natl Acad Sci U S A* **101**, 4620-4624, doi:10.1073/pnas.0308001101
0308001101 [pii] (2004).
171 Shinya, K. *et al.* Avian flu: influenza virus receptors in the human airway. *Nature* **440**, 435-436, doi:10.1038/440435a (2006).
172 Ito, T. *et al.* Molecular basis for the generation in pigs of influenza A viruses with pandemic potential. *J Virol* **72**, 7367-7373 (1998).
173 Shan, S. *et al.* Strategies for improving the efficacy of a H6 subtype avian influenza DNA vaccine in chickens. *J Virol Methods* **173**, 220-226, doi:10.1016/j.jviromet.2011.02.008
S0166-0934(11)00062-0 [pii] (2011).

174 Suzuki, Y. Sialobiology of influenza: molecular mechanism of host range variation of influenza viruses. *Biological & pharmaceutical bulletin* **28**, 399-408 (2005).

175 Sato, T., Serizawa, T. & Okahata, Y. Binding of influenza A virus to monosialoganglioside (GM3) reconstituted in glucosylceramide and sphingomyelin membranes. *Biochim Biophys Acta* **1285**, 14-20 (1996).

176 Lee, D. W., Hsu, H. L., Bacon, K. B. & Daniel, S. Image Restoration and Analysis of Influenza Virions Binding to Membrane Receptors Reveal Adhesion-Strengthening Kinetics. *PLoS One* **11**, e0163437, doi:10.1371/journal.pone.0163437 (2016).

177 Huang, R. T., Lichtenberg, B. & Rick, O. Involvement of annexin V in the entry of influenza viruses and role of phospholipids in infection. *FEBS Lett* **392**, 59-62 (1996).

178 Ng, W. C. *et al.* The C-type Lectin Langerin Functions as a Receptor for Attachment and Infectious Entry of Influenza A Virus. *J Virol* **90**, 206-221, doi:10.1128/JVI.01447-15 (2016).

179 Yang, M. L. *et al.* Galectin-1 binds to influenza virus and ameliorates influenza virus pathogenesis. *J Virol* **85**, 10010-10020, doi:10.1128/JVI.00301-11 (2011).

180 Chan, C. M. *et al.* Hemagglutinin of influenza A virus binds specifically to cell surface nucleolin and plays a role in virus internalization. *Virology* **494**, 78-88, doi:10.1016/j.virol.2016.04.008 (2016).

181 Takahashi, T. & Suzuki, T. Role of sulfatide in influenza A virus replication. *Biological & pharmaceutical bulletin* **38**, 809-816, doi:10.1248/bpb.b15-00119 (2015).

182 Kumar, D., Broor, S. & Rajala, M. S. Interaction of Host Nucleolin with Influenza A Virus Nucleoprotein in the Early Phase of Infection Limits the Late Viral Gene Expression. *PLoS One* **11**, e0164146, doi:10.1371/journal.pone.0164146 (2016).

183 Shaw, M. L., Stone, K. L., Colangelo, C. M., Gulcicek, E. E. & Palese, P. Cellular proteins in influenza virus particles. *PLoS Pathog* **4**, e1000085, doi:10.1371/journal.ppat.1000085 (2008).

184 Fields, B. N., Knipe, D. M. & Howley, P. M. *Fields virology*. 5th edn, (Wolters Kluwer Health/Lippincott Williams & Wilkins, 2007).

185 Samji, T. Influenza A: understanding the viral life cycle. *Yale J Biol Med* **82**, 153-159 (2009).

186 Bottcher-Friebertshauser, E. *et al.* Cleavage of influenza virus hemagglutinin by airway proteases TMPRSS2 and HAT differs in subcellular localization and susceptibility to protease inhibitors. *J Virol* **84**, 5605-5614, doi:10.1128/JVI.00140-10 (2010).

187 Huang, Q. *et al.* Early steps of the conformational change of influenza virus hemagglutinin to a fusion active state: stability and energetics of the hemagglutinin. *Biochim Biophys Acta* **1614**, 3-13 (2003).

188 Chen, J. *et al.* Structure of the hemagglutinin precursor cleavage site, a determinant of influenza pathogenicity and the origin of the labile conformation. *Cell* **95**, 409-417 (1998).

189 Wiley, D. C. & Skehel, J. J. The structure and function of the hemagglutinin membrane glycoprotein of influenza virus. *Annu Rev Biochem* **56**, 365-394, doi:10.1146/annurev.bi.56.070187.002053 (1987).

190 Pinto, L. H., Holsinger, L. J. & Lamb, R. A. Influenza virus M2 protein has ion channel activity. *Cell* **69**, 517-528 (1992).
191 Banerjee, I. *et al.* Influenza A virus uses the aggresome processing machinery for host cell entry. *Science* **346**, 473-477, doi:10.1126/science.1257037 (2014).
192 Banerjee, I., Yamauchi, Y., Helenius, A. & Horvath, P. High-content analysis of sequential events during the early phase of influenza A virus infection. *PLoS One* **8**, e68450, doi:10.1371/journal.pone.0068450 (2013).
193 O'Neill, R. E., Jaskunas, R., Blobel, G., Palese, P. & Moroianu, J. Nuclear import of influenza virus RNA can be mediated by viral nucleoprotein and transport factors required for protein import. *J Biol Chem* **270**, 22701-22704 (1995).
194 Wu, W. W., Sun, Y. H. & Pante, N. Nuclear import of influenza A viral ribonucleoprotein complexes is mediated by two nuclear localization sequences on viral nucleoprotein. *Virol J* **4**, 49, doi:10.1186/1743-422X-4-49 (2007).
195 Perez, J. T. *et al.* Influenza A virus-generated small RNAs regulate the switch from transcription to replication. *Proc Natl Acad Sci U S A* **107**, 11525-11530, doi:10.1073/pnas.1001984107 (2010).
196 Boulo, S., Akarsu, H., Ruigrok, R. W. & Baudin, F. Nuclear traffic of influenza virus proteins and ribonucleoprotein complexes. *Virus Res* **124**, 12-21, doi:10.1016/j.virusres.2006.09.013 (2007).
197 Jin, H., Leser, G. P., Zhang, J. & Lamb, R. A. Influenza virus hemagglutinin and neuraminidase cytoplasmic tails control particle shape. *EMBO J* **16**, 1236-1247, doi:10.1093/emboj/16.6.1236 (1997).
198 Bruce, E. A., Stuart, A., McCaffrey, M. W. & Digard, P. Role of the Rab11 pathway in negative-strand virus assembly. *Biochem Soc Trans* **40**, 1409-1415, doi:10.1042/BST20120166 (2012).
199 Sun, E., He, J. & Zhuang, X. Dissecting the role of COPI complexes in influenza virus infection. *J Virol* **87**, 2673-2685, doi:10.1128/JVI.02277-12 (2013).
200 Simpson-Holley, M. *et al.* A functional link between the actin cytoskeleton and lipid rafts during budding of filamentous influenza virions. *Virology* **301**, 212-225, doi:S0042682202915953 [pii] (2002).
201 Hughey, P. G., Compans, R. W., Zebedee, S. L. & Lamb, R. A. Expression of the influenza A virus M2 protein is restricted to apical surfaces of polarized epithelial cells. *J Virol* **66**, 5542-5552 (1992).
202 Veglia, G., Nelson, S. E. & Gopinath, T. Allosteric Regulation of the M2 Protein from Influenza A by Cholesterol. *Biophys J* **110**, 1207-1208, doi:10.1016/j.bpj.2016.01.034 (2016).
203 Thaa, B., Levental, I., Herrmann, A. & Veit, M. Intrinsic membrane association of the cytoplasmic tail of influenza virus M2 protein and lateral membrane sorting regulated by cholesterol binding and palmitoylation. *Biochem J* **437**, 389-397, doi:10.1042/BJ20110706 BJ20110706 [pii] (2011).
204 Veit, M. & Schmidt, M. F. Palmitoylation of influenza virus proteins. *Berl Munch Tierarztl Wochenschr* **119**, 112-122 (2006).
205 Kordyukova, L. V., Serebryakova, M. V., Baratova, L. A. & Veit, M. S acylation of the hemagglutinin of influenza viruses: mass spectrometry

reveals site-specific attachment of stearic acid to a transmembrane cysteine. *J Virol* **82**, 9288-9292, doi:10.1128/JVI.00704-08 JVI.00704-08 [pii] (2008).

206 Brett, K. *et al.* Site-specific S-Acylation of Influenza Virus Hemagglutinin: THE LOCATION OF THE ACYLATION SITE RELATIVE TO THE MEMBRANE BORDER IS THE DECISIVE FACTOR FOR ATTACHMENT OF STEARATE. *J Biol Chem* **289**, 34978-34989, doi:10.1074/jbc.M114.586180 (2014).

207 Veit, M. & Siche, S. S-acylation of influenza virus proteins: Are enzymes for fatty acid attachment promising drug targets? *Vaccine* **33**, 7002-7007, doi:10.1016/j.vaccine.2015.08.095 (2015).

208 Roussel, A. M. *et al.* Beneficial effects of hormonal replacement therapy on chromium status and glucose and lipid metabolism in postmenopausal women. *Maturitas* **42**, 63-69, doi:S0378512202000038 [pii] (2002).

209 Papadopoulos, V. *et al.* In vivo studies on the role of the peripheral benzodiazepine receptor (PBR) in steroidogenesis. *Endocr Res* **24**, 479-487 (1998).

210 Skibbens, J. E., Roth, M. G. & Matlin, K. S. Differential extractability of influenza virus hemagglutinin during intracellular transport in polarized epithelial cells and nonpolar fibroblasts. *J Cell Biol* **108**, 821-832 (1989).

211 Keller, P. & Simons, K. Cholesterol is required for surface transport of influenza virus hemagglutinin. *J Cell Biol* **140**, 1357-1367 (1998).

212 Wilson, R. L. *et al.* Hemagglutinin clusters in the plasma membrane are not enriched with cholesterol and sphingolipids. *Biophys J* **108**, 1652-1659, doi:10.1016/j.bpj.2015.02.026 (2015).

213 Scolari, S. *et al.* Lateral distribution of the transmembrane domain of influenza virus hemagglutinin revealed by time-resolved fluorescence imaging. *J Biol Chem* **284**, 15708-15716, doi:10.1074/jbc.M900437200 M900437200 [pii] (2009).

214 Gudheti, M. V. *et al.* Actin mediates the nanoscale membrane organization of the clustered membrane protein influenza hemagglutinin. *Biophys J* **104**, 2182-2192, doi:10.1016/j.bpj.2013.03.054 (2013).

215 Chen, B. J., Leser, G. P., Morita, E. & Lamb, R. A. Influenza virus hemagglutinin and neuraminidase, but not the matrix protein, are required for assembly and budding of plasmid-derived virus-like particles. *J Virol* **81**, 7111-7123, doi:JVI.00361-07 [pii] 10.1128/JVI.00361-07 (2007).

216 Ooi, P. L. *et al.* Clinical and molecular evidence for transmission of novel influenza A(H1N1/2009) on a commercial airplane. *Arch Intern Med* **170**, 913-915, doi:10.1001/archinternmed.2010.127 170/10/913 [pii] (2010).

217 Air, G. M. Influenza neuraminidase. *Influenza Other Respir Viruses* **6**, 245-256, doi:10.1111/j.1750-2659.2011.00304.x (2012).

218 da Silva, D. V., Nordholm, J., Madjo, U., Pfeiffer, A. & Daniels, R. Assembly of subtype 1 influenza neuraminidase is driven by both the transmembrane and head domains. *J Biol Chem* **288**, 644-653, doi:10.1074/jbc.M112.424150 M112.424150 [pii] (2013).

219 Leser, G. P. & Lamb, R. A. Influenza virus assembly and budding in raft-derived microdomains: a quantitative analysis of the surface distribution of HA, NA and M2 proteins. *Virology* **342**, 215-227, doi:S0042-6822(05)00603-3 [pii]
10.1016/j.virol.2005.09.049 (2005).
220 Kundu, A., Avalos, R. T., Sanderson, C. M. & Nayak, D. P. Transmembrane domain of influenza virus neuraminidase, a type II protein, possesses an apical sorting signal in polarized MDCK cells. *J Virol* **70**, 6508-6515 (1996).
221 Ohkura, T., Momose, F., Ichikawa, R., Takeuchi, K. & Morikawa, Y. Influenza A virus hemagglutinin and neuraminidase mutually accelerate their apical targeting through clustering of lipid rafts. *J Virol* **88**, 10039-10055, doi:10.1128/JVI.00586-14
JVI.00586-14 [pii] (2014).
222 Veit, M. *et al.* Site-specific mutagenesis identifies three cysteine residues in the cytoplasmic tail as acylation sites of influenza virus hemagglutinin. *J Virol* **65**, 2491-2500 (1991).
223 Schroeder, C., Heider, H., Moncke-Buchner, E. & Lin, T. I. The influenza virus ion channel and maturation cofactor M2 is a cholesterol-binding protein. *Eur Biophys J* **34**, 52-66, doi:10.1007/s00249-004-0424-1 (2005).
224 Sun, W. & Hu, K. Role for SUR2A in coupling cardiac K(ATP) channels to caveolin-3. *Cell Physiol Biochem* **25**, 409-418, doi:10.1159/000303045
000303045 [pii] (2010).
225 Chen, C. & Zhuang, X. Epsin 1 is a cargo-specific adaptor for the clathrin-mediated endocytosis of the influenza virus. *Proc Natl Acad Sci U S A* **105**, 11790-11795, doi:10.1073/pnas.0803711105
0803711105 [pii] (2008).
226 Tsfasman, T. *et al.* Amphipathic alpha-helices and putative cholesterol binding domains of the influenza virus matrix M1 protein are crucial for virion structure organisation. *Virus Res* **210**, 114-118, doi:10.1016/j.virusres.2015.07.017 (2015).
227 Carrasco, M., Amorim, M. J. & Digard, P. Lipid raft-dependent targeting of the influenza A virus nucleoprotein to the apical plasma membrane. *Traffic* **5**, 979-992, doi:10.1111/j.1600-0854.2004.00237.x (2004).
228 Wang, X., Hinson, E. R. & Cresswell, P. The interferon-inducible protein viperin inhibits influenza virus release by perturbing lipid rafts. *Cell Host Microbe* **2**, 96-105, doi:S1931-3128(07)00135-7 [pii]
10.1016/j.chom.2007.06.009 (2007).
229 Takada, T., Watanabe, K., Makino, H. & Kushiro, A. Reclassification of Eubacterium desmolans as Butyricicoccus desmolans comb. nov., and Butyricicoccus faecihominis sp. nov., a novel butyrate-producing bacterium from human faeces. *Int J Syst Evol Microbiol*, doi:10.1099/ijsem.0.001323 (2016).
230 Ivanova, P. T. *et al.* Lipid composition of viral envelope of three strains of influenza virus - not all viruses are created equal. *ACS Infect Dis* **1**, 399-452, doi:10.1021/acsinfecdis.5b00040 (2015).

231 Tanner, L. B. *et al.* Lipidomics identifies a requirement for peroxisomal function during influenza virus replication. *J Lipid Res* **55**, 1357-1365, doi:10.1194/jlr.M049148 (2014).
232 Tanner, L. B. *LIPIDOMICS OF INFLUENZA VIRUS: IMPLICATIONS OF HOST CELL CHOLINE- AND SPHINGOLIPID METABOLISM*, National University of Singapore (NUS), (2012).
233 Hidari, K. I., Suzuki, Y. & Suzuki, T. Suppression of the biosynthesis of cellular sphingolipids results in the inhibition of the maturation of influenza virus particles in MDCK cells. *Biological & pharmaceutical bulletin* **29**, 1575-1579 (2006).
234 Woods, P. S. *et al.* Lethal H1N1 influenza A virus infection alters the murine alveolar type II cell surfactant lipidome. *American journal of physiology. Lung cellular and molecular physiology* **311**, L1160-L1169, doi:10.1152/ajplung.00339.2016 (2016).
235 Kalvodova, L. *et al.* The lipidomes of vesicular stomatitis virus, semliki forest virus, and the host plasma membrane analyzed by quantitative shotgun mass spectrometry. *J Virol* **83**, 7996-8003, doi:10.1128/JVI.00635-09 (2009).
236 Cingolani, F., Futerman, A. H. & Casas, J. Ceramide synthases in biomedical research. *Chemistry and physics of lipids* **197**, 25-32, doi:10.1016/j.chemphyslip.2015.07.026 (2016).
237 Silva, L. C. *et al.* Ablation of ceramide synthase 2 strongly affects biophysical properties of membranes. *J Lipid Res* **53**, 430-436, doi:10.1194/jlr.M022715 (2012).
238 Markham, J. E. *et al.* Sphingolipids containing very-long-chain fatty acids define a secretory pathway for specific polar plasma membrane protein targeting in Arabidopsis. *Plant Cell* **23**, 2362-2378, doi:10.1105/tpc.110.080473 (2011).
239 Koivusalo, M., Jansen, M., Somerharju, P. & Ikonen, E. Endocytic trafficking of sphingomyelin depends on its acyl chain length. *Mol Biol Cell* **18**, 5113-5123, doi:10.1091/mbc.e07-04-0330 (2007).
240 Sampaio, J. L. *et al.* Membrane lipidome of an epithelial cell line. *Proc Natl Acad Sci U S A* **108**, 1903-1907, doi:10.1073/pnas.1019267108 1019267108 [pii] (2011).
241 Meshcheryakova, A. *et al.* Exploring the role of sphingolipid machinery during the epithelial to mesenchymal transition program using an integrative approach. *Oncotarget* **7**, 22295-22323, doi:10.18632/oncotarget.7947 (2016).
242 McMahon, R., Zaborowska, I. & Walsh, D. Noncytotoxic inhibition of viral infection through eIF4F-independent suppression of translation by 4EGi-1. *J Virol* **85**, 853-864, doi:10.1128/JVI.01873-10 (2011).
243 Walsh, K. B., Teijaro, J. R., Rosen, H. & Oldstone, M. B. Quelling the storm: utilization of sphingosine-1-phosphate receptor signaling to ameliorate influenza virus-induced cytokine storm. *Immunol Res* **51**, 15-25, doi:10.1007/s12026-011-8240-z (2011).
244 Nguyen, H. H. *et al.* Prophylactic and therapeutic efficacy of avian antibodies against influenza virus H5N1 and H1N1 in mice. *PLoS One* **5**, e10152, doi:10.1371/journal.pone.0010152 (2010).
245 Vijayan, M. *et al.* Sphingosine 1-Phosphate Lyase Enhances the Activation of IKKepsilon To Promote Type I IFN-Mediated Innate

Immune Responses to Influenza A Virus Infection. *J Immunol* **199**, 677-687, doi:10.4049/jimmunol.1601959 (2017).

246 Xia, C. *et al.* Transient inhibition of sphingosine kinases confers protection to influenza A virus infected mice. *Antiviral Res* **158**, 171-177, doi:10.1016/j.antiviral.2018.08.010 (2018).

247 Poland, G. A., Jacobson, R. M. & Ovsyannikova, I. G. Influenza virus resistance to antiviral agents: a plea for rational use. *Clin Infect Dis* **48**, 1254-1256, doi:10.1086/598989 (2009).

248 Haberkant, P. & Holthuis, J. C. Fat & fabulous: bifunctional lipids in the spotlight. *Biochim Biophys Acta* **1841**, 1022-1030, doi:10.1016/j.bbalip.2014.01.003 (2014).

249 Hulce, J. J., Cognetta, A. B., Niphakis, M. J., Tully, S. E. & Cravatt, B. F. Proteome-wide mapping of cholesterol-interacting proteins in mammalian cells. *Nat Methods* **10**, 259-264, doi:10.1038/nmeth.2368 (2013).

250 Haberkant, P. *et al.* Bifunctional Sphingosine for Cell-Based Analysis of Protein-Sphingolipid Interactions. *ACS chemical biology* **11**, 222-230, doi:10.1021/acschembio.5b00810 (2016).

251 Stech, J. *et al.* Rapid and reliable universal cloning of influenza A virus genes by target-primed plasmid amplification. *Nucleic Acids Res* **36**, e139, doi:10.1093/nar/gkn646 (2008).

252 Fiege, J. K. & Langlois, R. A. Investigating influenza A virus infection: tools to track infection and limit tropism. *J Virol* **89**, 6167-6170, doi:10.1128/JVI.00462-15 (2015).

253 (CDC), C. f. D. C. a. P.

254 Gerl, M. J. *et al.* Sphingosine-1-Phosphate Lyase Deficient Cells as a Tool to Study Protein Lipid Interactions. *PLoS One* **11**, e0153009, doi:10.1371/journal.pone.0153009 (2016).

255 Rossman, J. S., Jing, X., Leser, G. P. & Lamb, R. A. Influenza virus M2 protein mediates ESCRT-independent membrane scission. *Cell* **142**, 902-913, doi:10.1016/j.cell.2010.08.029
S0092-8674(10)00960-8 [pii] (2010).

256 Seo, Y. J., Blake, C., Alexander, S. & Hahm, B. Sphingosine 1-phosphate-metabolizing enzymes control influenza virus propagation and viral cytopathogenicity. *J Virol* **84**, 8124-8131, doi:10.1128/JVI.00510-10 (2010).

257 Vijayan, M. & Hahm, B. Influenza viral manipulation of sphingolipid metabolism and signaling to modulate host defense system. *Scientifica (Cairo)* **2014**, 793815, doi:10.1155/2014/793815 (2014).

258 Kummer, S. *et al.* Alteration of protein levels during influenza virus H1N1 infection in host cells: a proteomic survey of host and virus reveals differential dynamics. *PLoS One* **9**, e94257, doi:10.1371/journal.pone.0094257 (2014).

259 Munday, D. C. *et al.* Using SILAC and quantitative proteomics to investigate the interactions between viral and host proteomes. *Proteomics* **12**, 666-672, doi:10.1002/pmic.201100488 (2012).

260 England, P. H. Cell line profile A549. *European Collection of Authenticated Cell Cultures (ECACC)*.

261 Emmott, E. & Goodfellow, I. Identification of protein interaction partners in mammalian cells using SILAC-immunoprecipitation quantitative

proteomics. *Journal of visualized experiments : JoVE*, doi:10.3791/51656 (2014).

262 Shapira, S. D. *et al.* A physical and regulatory map of host-influenza interactions reveals pathways in H1N1 infection. *Cell* **139**, 1255-1267, doi:10.1016/j.cell.2009.12.018 (2009).

263 Coombs, K. M. *et al.* Quantitative proteomic analyses of influenza virus-infected cultured human lung cells. *J Virol* **84**, 10888-10906, doi:10.1128/JVI.00431-10 (2010).

264 Kroeker, A. L., Ezzati, P., Halayko, A. J. & Coombs, K. M. Response of primary human airway epithelial cells to influenza infection: a quantitative proteomic study. *J Proteome Res* **11**, 4132-4146, doi:10.1021/pr300239r (2012).

265 Dove, B. K. *et al.* A quantitative proteomic analysis of lung epithelial (A549) cells infected with 2009 pandemic influenza A virus using stable isotope labelling with amino acids in cell culture. *Proteomics* **12**, 1431-1436, doi:10.1002/pmic.201100470 (2012).

266 Kash, J. C. *et al.* Global host immune response: pathogenesis and transcriptional profiling of type A influenza viruses expressing the hemagglutinin and neuraminidase genes from the 1918 pandemic virus. *J Virol* **78**, 9499-9511, doi:10.1128/JVI.78.17.9499-9511.2004 (2004).

267 Barillari, G. *et al.* The Tat protein of human immunodeficiency virus type-1 promotes vascular cell growth and locomotion by engaging the alpha5beta1 and alphavbeta3 integrins and by mobilizing sequestered basic fibroblast growth factor. *Blood* **94**, 663-672 (1999).

268 Wahl, A., Schafer, F., Bardet, W. & Hildebrand, W. H. HLA class I molecules reflect an altered host proteome after influenza virus infection. *Hum Immunol* **71**, 14-22, doi:10.1016/j.humimm.2009.08.012 (2010).

269 Sieczkarski, S. B., Brown, H. A. & Whittaker, G. R. Role of protein kinase C betaII in influenza virus entry via late endosomes. *J Virol* **77**, 460-469 (2003).

270 Feeley, E. M. *et al.* IFITM3 inhibits influenza A virus infection by preventing cytosolic entry. *PLoS Pathog* **7**, e1002337, doi:10.1371/journal.ppat.1002337 (2011).

271 Ohno, Y. *et al.* ELOVL1 production of C24 acyl-CoAs is linked to C24 sphingolipid synthesis. *Proc Natl Acad Sci U S A* **107**, 18439-18444, doi:10.1073/pnas.1005572107 (2010).

272 Koyuncu, E., Purdy, J. G., Rabinowitz, J. D. & Shenk, T. Saturated very long chain fatty acids are required for the production of infectious human cytomegalovirus progeny. *PLoS Pathog* **9**, e1003333, doi:10.1371/journal.ppat.1003333 (2013).

273 Karlas, A. *et al.* Genome-wide RNAi screen identifies human host factors crucial for influenza virus replication. *Nature* **463**, 818-822, doi:10.1038/nature08760 (2010).

274 Oresic, K., Ng, C. L. & Tortorella, D. TRAM1 participates in human cytomegalovirus US2- and US11-mediated dislocation of an endoplasmic reticulum membrane glycoprotein. *J Biol Chem* **284**, 5905-5914, doi:10.1074/jbc.M807568200 (2009).

275 Levine, B., Mizushima, N. & Virgin, H. W. Autophagy in immunity and inflammation. *Nature* **469**, 323-335, doi:10.1038/nature09782 (2011).

276 Beale, R. *et al.* A LC3-interacting motif in the influenza A virus M2 protein is required to subvert autophagy and maintain virion stability. *Cell Host Microbe* **15**, 239-247, doi:10.1016/j.chom.2014.01.006 (2014).
277 Ju, X. *et al.* Neuraminidase of Influenza A Virus Binds Lysosome-Associated Membrane Proteins Directly and Induces Lysosome Rupture. *J Virol* **89**, 10347-10358, doi:10.1128/JVI.01411-15 (2015).
278 Jae, L. T. *et al.* Virus entry. Lassa virus entry requires a trigger-induced receptor switch. *Science* **344**, 1506-1510, doi:10.1126/science.1252480 (2014).
279 Grove, J. *et al.* Scavenger receptor BI and BII expression levels modulate hepatitis C virus infectivity. *J Virol* **81**, 3162-3169, doi:10.1128/JVI.02356-06 (2007).
280 Yamayoshi, S. *et al.* Scavenger receptor B2 is a cellular receptor for enterovirus 71. *Nat Med* **15**, 798-801, doi:10.1038/nm.1992 (2009).
281 Konig, R. *et al.* Human host factors required for influenza virus replication. *Nature* **463**, 813-817, doi:10.1038/nature08699 (2010).
282 He, J. *et al.* Dual function of CD81 in influenza virus uncoating and budding. *PLoS Pathog* **9**, e1003701, doi:10.1371/journal.ppat.1003701 (2013).
283 Garcia, E., Nikolic, D. S. & Piguet, V. HIV-1 replication in dendritic cells occurs through a tetraspanin-containing compartment enriched in AP-3. *Traffic* **9**, 200-214, doi:10.1111/j.1600-0854.2007.00678.x (2008).
284 Zona, L. *et al.* CD81-receptor associations--impact for hepatitis C virus entry and antiviral therapies. *Viruses* **6**, 875-892, doi:10.3390/v6020875 (2014).
285 Bohm, K., Sun, L., Thakor, D. & Wirth, M. Caveolin-1 limits human influenza A virus (H1N1) propagation in mouse embryo-derived fibroblasts. *Virology* **462-463**, 241-253, doi:10.1016/j.virol.2014.05.028 (2014).
286 Sun, L., Hemgard, G. V., Susanto, S. A. & Wirth, M. Caveolin-1 influences human influenza A virus (H1N1) multiplication in cell culture. *Virol J* **7**, 108, doi:10.1186/1743-422X-7-108
1743-422X-7-108 [pii] (2010).
287 Wheeler, J. G., Winkler, L. S., Seeds, M., Bass, D. & Abramson, J. S. Influenza A virus alters structural and biochemical functions of the neutrophil cytoskeleton. *Journal of leukocyte biology* **47**, 332-343 (1990).
288 Ohman, T., Rintahaka, J., Kalkkinen, N., Matikainen, S. & Nyman, T. A. Actin and RIG-I/MAVS signaling components translocate to mitochondria upon influenza A virus infection of human primary macrophages. *J Immunol* **182**, 5682-5692, doi:10.4049/jimmunol.0803093 (2009).
289 Wu, W. & Pante, N. Vimentin plays a role in the release of the influenza A viral genome from endosomes. *Virology* **497**, 41-52, doi:10.1016/j.virol.2016.06.021 (2016).
290 LeBouder, F. *et al.* Annexin II incorporated into influenza virus particles supports virus replication by converting plasminogen into plasmin. *J Virol* **82**, 6820-6828, doi:10.1128/JVI.00246-08 (2008).
291 Zamarin, D., Garcia-Sastre, A., Xiao, X., Wang, R. & Palese, P. Influenza virus PB1-F2 protein induces cell death through mitochondrial

ANT3 and VDAC1. *PLoS Pathog* **1**, e4, doi:10.1371/journal.ppat.0010004 (2005).

292 Wollscheid, B. *et al.* Mass-spectrometric identification and relative quantification of N-linked cell surface glycoproteins. *Nat Biotechnol* **27**, 378-386, doi:10.1038/nbt.1532 (2009).

293 Haberkant, P. *et al.* In vivo profiling and visualization of cellular protein-lipid interactions using bifunctional fatty acids. *Angew Chem Int Ed Engl* **52**, 4033-4038, doi:10.1002/anie.201210178 (2013).

294 Brass, A. L. *et al.* The IFITM proteins mediate cellular resistance to influenza A H1N1 virus, West Nile virus, and dengue virus. *Cell* **139**, 1243-1254, doi:10.1016/j.cell.2009.12.017 (2009).

295 Lehner, I., Niehof, M. & Borlak, J. An optimized method for the isolation and identification of membrane proteins. *Electrophoresis* **24**, 1795-1808, doi:10.1002/elps.200305387 (2003).

296 Brass, A. L. *et al.* Identification of host proteins required for HIV infection through a functional genomic screen. *Science* **319**, 921-926, doi:10.1126/science.1152725 (2008).

297 Panda, D. *et al.* RNAi screening reveals requirement for host cell secretory pathway in infection by diverse families of negative-strand RNA viruses. *Proc Natl Acad Sci U S A* **108**, 19036-19041, doi:10.1073/pnas.1113643108 (2011).

298 Moretti, F. *et al.* TMEM41B is a novel regulator of autophagy and lipid mobilization. *EMBO Rep* **19**, doi:10.15252/embr.201845889 (2018).

299 Wu, Z. *et al.* MicroRNA expression profile of mouse lung infected with 2009 pandemic H1N1 influenza virus. *PLoS One* **8**, e74190, doi:10.1371/journal.pone.0074190 (2013).

300 Momose, F. *et al.* Apical transport of influenza A virus ribonucleoprotein requires Rab11-positive recycling endosome. *PLoS One* **6**, e21123, doi:10.1371/journal.pone.0021123 (2011).

301 Eisfeld, A. J., Kawakami, E., Watanabe, T., Neumann, G. & Kawaoka, Y. RAB11A is essential for transport of the influenza virus genome to the plasma membrane. *J Virol* **85**, 6117-6126, doi:10.1128/JVI.00378-11 (2011).

302 Avilov, S. V., Moisy, D., Naffakh, N. & Cusack, S. Influenza A virus progeny vRNP trafficking in live infected cells studied with the virus-encoded fluorescently tagged PB2 protein. *Vaccine* **30**, 7411-7417, doi:10.1016/j.vaccine.2012.09.077 (2012).

303 Sugasawa, T. *et al.* The iodocyanopindolol and SM-11044 binding protein belongs to the TM9SF multispanning membrane protein superfamily. *Gene* **273**, 227-237 (2001).

304 Ovsyannikova, I. G. *et al.* Gene signatures related to HAI response following influenza A/H1N1 vaccine in older individuals. *Heliyon* **2**, e00098, doi:10.1016/j.heliyon.2016.e00098 (2016).

305 Han, J. *et al.* Genome-wide CRISPR/Cas9 Screen Identifies Host Factors Essential for Influenza Virus Replication. *Cell Rep* **23**, 596-607, doi:10.1016/j.celrep.2018.03.045 (2018).

306 Drake, M. J. *et al.* A role for glycolipid biosynthesis in severe fever with thrombocytopenia syndrome virus entry. *PLoS Pathog* **13**, e1006316, doi:10.1371/journal.ppat.1006316 (2017).

307 Bradel-Tretheway, B. G. *et al.* Comprehensive proteomic analysis of influenza virus polymerase complex reveals a novel association with mitochondrial proteins and RNA polymerase accessory factors. *J Virol* **85**, 8569-8581, doi:10.1128/JVI.00496-11 (2011).
308 Poshusta, G. R. & Aitchison, J. 1 online resource (viii, 156 pages) (University of Washington Libraries ,, Seattle, 2015).
309 Bushman, F. D. *et al.* Host cell factors in HIV replication: meta-analysis of genome-wide studies. *PLoS Pathog* **5**, e1000437, doi:10.1371/journal.ppat.1000437 (2009).
310 Holtta-Vuori, M., Tanhuanpaa, K., Mobius, W., Somerharju, P. & Ikonen, E. Modulation of cellular cholesterol transport and homeostasis by Rab11. *Mol Biol Cell* **13**, 3107-3122, doi:10.1091/mbc.e02-01-0025 (2002).
311 Merrill, A. H., Jr., van Echten, G., Wang, E. & Sandhoff, K. Fumonisin B1 inhibits sphingosine (sphinganine) N-acyltransferase and de novo sphingolipid biosynthesis in cultured neurons in situ. *J Biol Chem* **268**, 27299-27306 (1993).
312 Lapierre, L. A. *et al.* Rab11b resides in a vesicular compartment distinct from Rab11a in parietal cells and other epithelial cells. *Exp Cell Res* **290**, 322-331 (2003).
313 Bruce, E. A., Digard, P. & Stuart, A. D. The Rab11 pathway is required for influenza A virus budding and filament formation. *J Virol* **84**, 5848-5859, doi:10.1128/JVI.00307-10
JVI.00307-10 [pii] (2010).
314 Skehel, J. J. & Wiley, D. C. Receptor binding and membrane fusion in virus entry: the influenza hemagglutinin. *Annu Rev Biochem* **69**, 531-569, doi:69/1/531 [pii]
10.1146/annurev.biochem.69.1.531 (2000).
315 Roth, J. Protein N-glycosylation along the secretory pathway: relationship to organelle topography and function, protein quality control, and cell interactions. *Chem Rev* **102**, 285-303 (2002).
316 Kondo, N. *et al.* Identification of the phytosphingosine metabolic pathway leading to odd-numbered fatty acids. *Nat Commun* **5**, 5338, doi:10.1038/ncomms6338 (2014).
317 Imgrund, S. *et al.* Adult ceramide synthase 2 (CERS2)-deficient mice exhibit myelin sheath defects, cerebellar degeneration, and hepatocarcinomas. *J Biol Chem* **284**, 33549-33560, doi:10.1074/jbc.M109.031971 (2009).
318 Ge, S. & Wang, Z. An overview of influenza A virus receptors. *Crit Rev Microbiol* **37**, 157-165, doi:10.3109/1040841X.2010.536523 (2011).
319 Ravindran, M. S., Tanner, L. B. & Wenk, M. R. Sialic acid linkage in glycosphingolipids is a molecular correlate for trafficking and delivery of extracellular cargo. *Traffic* **14**, 1182-1191, doi:10.1111/tra.12100 (2013).
320 Suzuki, Y. *et al.* Ganglioside GM1b as an influenza virus receptor. *Vaccine* **3**, 201-203 (1985).
321 Zigdon, H. *et al.* Ablation of ceramide synthase 2 causes chronic oxidative stress due to disruption of the mitochondrial respiratory chain. *J Biol Chem* **288**, 4947-4956, doi:10.1074/jbc.M112.402719 (2013).

322 Rahmaniyan, M., Curley, R. W., Jr., Obeid, L. M., Hannun, Y. A. & Kraveka, J. M. Identification of dihydroceramide desaturase as a direct in vitro target for fenretinide. *J Biol Chem* **286**, 24754-24764, doi:10.1074/jbc.M111.250779 (2011).

323 Barman, S. *et al.* Role of transmembrane domain and cytoplasmic tail amino acid sequences of influenza a virus neuraminidase in raft association and virus budding. *J Virol* **78**, 5258-5269 (2004).

324 Barman, S. & Nayak, D. P. Analysis of the transmembrane domain of influenza virus neuraminidase, a type II transmembrane glycoprotein, for apical sorting and raft association. *J Virol* **74**, 6538-6545 (2000).

325 Zordan, R. E., Beliveau, B. J., Trow, J. A., Craig, N. L. & Cormack, B. P. Avoiding the ends: internal epitope tagging of proteins using transposon Tn7. *Genetics* **200**, 47-58, doi:10.1534/genetics.114.169482 (2015).

326 Unal, E. S., Zhao, R., Qiu, A. & Goldman, I. D. N-linked glycosylation and its impact on the electrophoretic mobility and function of the human proton-coupled folate transporter (HsPCFT). *Biochim Biophys Acta* **1778**, 1407-1414, doi:10.1016/j.bbamem.2008.03.009 (2008).

327 Saito, T., Taylor, G. & Webster, R. G. Steps in maturation of influenza A virus neuraminidase. *J Virol* **69**, 5011-5017 (1995).

328 Aguilar, A. & Saba, J. D. Truth and consequences of sphingosine-1-phosphate lyase. *Adv Biol Regul* **52**, 17-30, doi:10.1016/j.advenzreg.2011.09.015 (2012).

329 Vienken, H. *et al.* Characterization of cholesterol homeostasis in sphingosine-1-phosphate lyase-deficient fibroblasts reveals a Niemann-Pick disease type C-like phenotype with enhanced lysosomal Ca2+ storage. *Scientific reports* **7**, 43575, doi:10.1038/srep43575 (2017).

330 Koeberlein, B. *et al.* Hepatitis B virus overexpresses suppressor of cytokine signaling-3 (SOCS3) thereby contributing to severity of inflammation in the liver. *Virus Res* **148**, 51-59, doi:10.1016/j.virusres.2009.12.003 (2010).

331 Smith, S., Weston, S., Kellam, P. & Marsh, M. IFITM proteins-cellular inhibitors of viral entry. *Curr Opin Virol* **4**, 71-77, doi:10.1016/j.coviro.2013.11.004 (2014).

332 Lee, A. J. *et al.* CERT depletion predicts chemotherapy benefit and mediates cytotoxic and polyploid-specific cancer cell death through autophagy induction. *J Pathol* **226**, 482-494, doi:10.1002/path.2998 (2012).

333 Gao, X. *et al.* Serine Availability Influences Mitochondrial Dynamics and Function through Lipid Metabolism. *Cell Rep* **22**, 3507-3520, doi:10.1016/j.celrep.2018.03.017 (2018).

334 Geiger, T., Wehner, A., Schaab, C., Cox, J. & Mann, M. Comparative proteomic analysis of eleven common cell lines reveals ubiquitous but varying expression of most proteins. *Mol Cell Proteomics* **11**, M111 014050, doi:10.1074/mcp.M111.014050 (2012).

335 Beloso, A., Martinez, C., Valcarcel, J., Santaren, J. F. & Ortin, J. Degradation of cellular mRNA during influenza virus infection: its possible role in protein synthesis shutoff. *J Gen Virol* **73 (Pt 3)**, 575-581, doi:10.1099/0022-1317-73-3-575 (1992).

336 Chen, W., Feng, Y., Chen, D. & Wandinger-Ness, A. Rab11 is required for trans-golgi network-to-plasma membrane transport and a preferential target for GDP dissociation inhibitor. *Mol Biol Cell* **9**, 3241-3257 (1998).

337 Sobajima, T. *et al.* The Rab11-binding protein RELCH/KIAA1468 controls intracellular cholesterol distribution. *J Cell Biol* **217**, 1777-1796, doi:10.1083/jcb.201709123 (2018).

338 Naslavsky, N., Rahajeng, J., Sharma, M., Jovic, M. & Caplan, S. Interactions between EHD proteins and Rab11-FIP2: a role for EHD3 in early endosomal transport. *Mol Biol Cell* **17**, 163-177, doi:10.1091/mbc.e05-05-0466 (2006).

339 Kawaguchi, A., Hirohama, M., Harada, Y., Osari, S. & Nagata, K. Influenza Virus Induces Cholesterol-Enriched Endocytic Recycling Compartments for Budozone Formation via Cell Cycle-Independent Centrosome Maturation. *PLoS Pathog* **11**, e1005284, doi:10.1371/journal.ppat.1005284 (2015).

340 Hediger, M. A. *et al.* The ABCs of solute carriers: physiological, pathological and therapeutic implications of human membrane transport proteinsIntroduction. *Pflugers Arch* **447**, 465-468, doi:10.1007/s00424-003-1192-y (2004).

341 Perland, E. & Fredriksson, R. Classification Systems of Secondary Active Transporters. *Trends Pharmacol Sci* **38**, 305-315, doi:10.1016/j.tips.2016.11.008 (2017).

342 Schott, K. & Konig, R. Picking the Survivor! CRISPR Reveals HIV Dependency Factors. *Trends Microbiol* **25**, 243-245, doi:10.1016/j.tim.2017.02.004 (2017).

343 Buffet, A. *et al.* Germline Mutations in the Mitochondrial 2-Oxoglutarate/Malate Carrier SLC25A11 Gene Confer a Predisposition to Metastatic Paragangliomas. *Cancer Res* **78**, 1914-1922, doi:10.1158/0008-5472.CAN-17-2463 (2018).

344 Console, L., Scalise, M., Tarmakova, Z., Coe, I. R. & Indiveri, C. N-linked glycosylation of human SLC1A5 (ASCT2) transporter is critical for trafficking to membrane. *Biochim Biophys Acta* **1853**, 1636-1645, doi:10.1016/j.bbamcr.2015.03.017 (2015).

345 Hynes, R. O. Integrins: bidirectional, allosteric signaling machines. *Cell* **110**, 673-687 (2002).

346 Perdih, A. & Dolenc, M. S. Small molecule antagonists of integrin receptors. *Curr Med Chem* **17**, 2371-2392 (2010).

347 Leitinger, B. & Hogg, N. The involvement of lipid rafts in the regulation of integrin function. *J Cell Sci* **115**, 963-972 (2002).

348 Sharma, D. K. *et al.* The glycosphingolipid, lactosylceramide, regulates beta1-integrin clustering and endocytosis. *Cancer Res* **65**, 8233-8241, doi:10.1158/0008-5472.CAN-05-0803 (2005).

349 Forbes, B. & Ehrhardt, C. Human respiratory epithelial cell culture for drug delivery applications. *Eur J Pharm Biopharm* **60**, 193-205, doi:10.1016/j.ejpb.2005.02.010 (2005).

350 Tscherne, D. M., Manicassamy, B. & Garcia-Sastre, A. An enzymatic virus-like particle assay for sensitive detection of virus entry. *J Virol Methods* **163**, 336-343, doi:10.1016/j.jviromet.2009.10.020 (2010).

351 Contreras, F. X., Ernst, A. M., Wieland, F. & Brugger, B. Specificity of intramembrane protein-lipid interactions. *Cold Spring Harb Perspect Biol* **3**, doi:10.1101/cshperspect.a004705
a004705 [pii]
cshperspect.a004705 [pii] (2011).
352 Kuikka, M., Ramstedt, B., Ohvo-Rekila, H., Tuuf, J. & Slotte, J. P. Membrane properties of D-erythro-N-acyl sphingomyelins and their corresponding dihydro species. *Biophys J* **80**, 2327-2337, doi:10.1016/S0006-3495(01)76203-0 (2001).
353 Maula, T., Al Sazzad, M. A. & Slotte, J. P. Influence of Hydroxylation, Chain Length, and Chain Unsaturation on Bilayer Properties of Ceramides. *Biophys J* **109**, 1639-1651, doi:10.1016/j.bpj.2015.08.040 (2015).
354 Kim, D. K. & Poudel, B. Tools to detect influenza virus. *Yonsei Med J* **54**, 560-566, doi:10.3349/ymj.2013.54.3.560 (2013).
355 Kim, J. H. *et al.* High cleavage efficiency of a 2A peptide derived from porcine teschovirus-1 in human cell lines, zebrafish and mice. *PLoS One* **6**, e18556, doi:10.1371/journal.pone.0018556 (2011).
356 Hoffmann, E., Neumann, G., Kawaoka, Y., Hobom, G. & Webster, R. G. A DNA transfection system for generation of influenza A virus from eight plasmids. *Proc Natl Acad Sci U S A* **97**, 6108-6113, doi:10.1073/pnas.100133697 (2000).
357 Niwa, H., Yamamura, K. & Miyazaki, J. Efficient selection for high-expression transfectants with a novel eukaryotic vector. *Gene* **108**, 193-199 (1991).
358 Chlanda, P. *et al.* Structural Analysis of the Roles of Influenza A Virus Membrane-Associated Proteins in Assembly and Morphology. *J Virol* **89**, 8957-8966, doi:10.1128/JVI.00592-15 (2015).
359 Martinez-Sobrido, L. & Garcia-Sastre, A. Generation of recombinant influenza virus from plasmid DNA. *Journal of visualized experiments : JoVE*, doi:10.3791/2057 (2010).
360 Morrill, J. C. *et al.* Rapid accumulation of virulent rift valley Fever virus in mice from an attenuated virus carrying a single nucleotide substitution in the m RNA. *PLoS One* **5**, e9986, doi:10.1371/journal.pone.0009986 (2010).
361 Hughes, C. S. *et al.* Ultrasensitive proteome analysis using paramagnetic bead technology. *Mol Syst Biol* **10**, 757, doi:10.15252/msb.20145625 (2014).
362 Cox, J. & Mann, M. MaxQuant enables high peptide identification rates, individualized p.p.b.-range mass accuracies and proteome-wide protein quantification. *Nat Biotechnol* **26**, 1367-1372, doi:10.1038/nbt.1511 (2008).
363 Tyanova, S. *et al.* The Perseus computational platform for comprehensive analysis of (prote)omics data. *Nat Methods* **13**, 731-740, doi:10.1038/nmeth.3901 (2016).
364 Zaro, B. W., Batt, A. R., Chuh, K. N., Navarro, M. X. & Pratt, M. R. The Small Molecule 2-Azido-2-deoxy-glucose Is a Metabolic Chemical Reporter of O-GlcNAc Modifications in Mammalian Cells, Revealing an Unexpected Promiscuity of O-GlcNAc Transferase. *ACS chemical biology* **12**, 787-794, doi:10.1021/acschembio.6b00877 (2017).

365 Schnaar, R. L. & Needham, L. K. Thin-layer chromatography of glycosphingolipids. *Methods Enzymol* **230**, 371-389 (1994).
366 Laemmli, U. K. Cleavage of structural proteins during the assembly of the head of bacteriophage T4. *Nature* **227**, 680-685 (1970).
367 Dyballa, N. & Metzger, S. Fast and sensitive colloidal coomassie G-250 staining for proteins in polyacrylamide gels. *Journal of visualized experiments : JoVE*, doi:10.3791/1431 (2009).
368 Thiele, C. *et al.* Tracing fatty acid metabolism by click chemistry. *ACS chemical biology* **7**, 2004-2011, doi:10.1021/cb300414v (2012).
369 Bligh, E. G. & Dyer, W. J. A rapid method of total lipid extraction and purification. *Can J Biochem Physiol* **37**, 911-917, doi:10.1139/o59-099 (1959).
370 Ozbalci, C., Sachsenheimer, T. & Brugger, B. Quantitative analysis of cellular lipids by nano-electrospray ionization mass spectrometry. *Methods Mol Biol* **1033**, 3-20, doi:10.1007/978-1-62703-487-6_1 (2013).
371 Narayanaswamy, P. *et al.* Lipidomic "deep profiling": an enhanced workflow to reveal new molecular species of signaling lipids. *Anal Chem* **86**, 3043-3047, doi:10.1021/ac4039652 (2014).

7 Supplement

- Characterisation of A549 CRISPR KOs

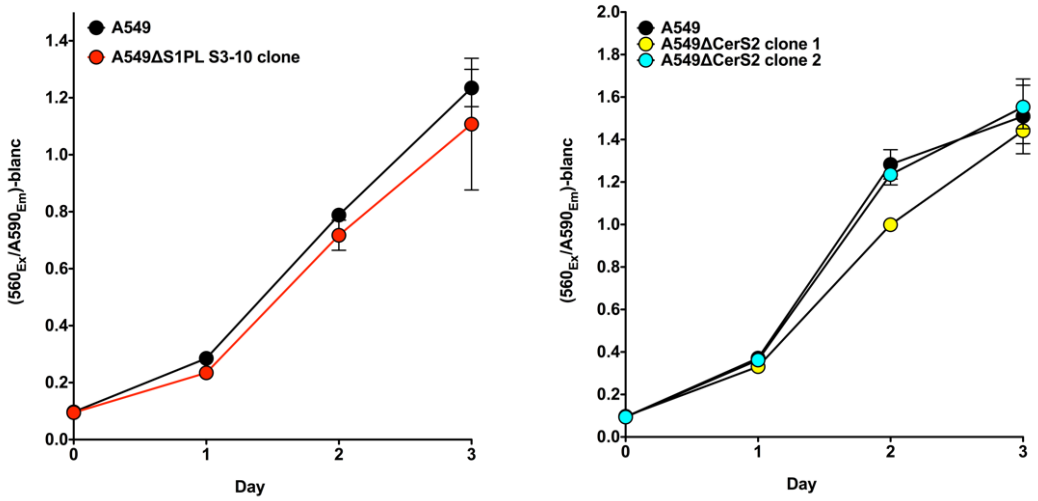

Figure 7.1: Cell viability assay of A549 wild type and CRISPR-KO clones.

A549 WT and KO cells in the same passage were seeded at $0.25*10^4$ cells/96-well plate. Cell viability was determined using the CellTiter®-Blue Cell Viability Assay which is based on the reduction of resazurin to resorufin by viable cells. Note that this assay is an end-point measurement (no kinetic curve). Shown: mean, ±SEM; n=4.

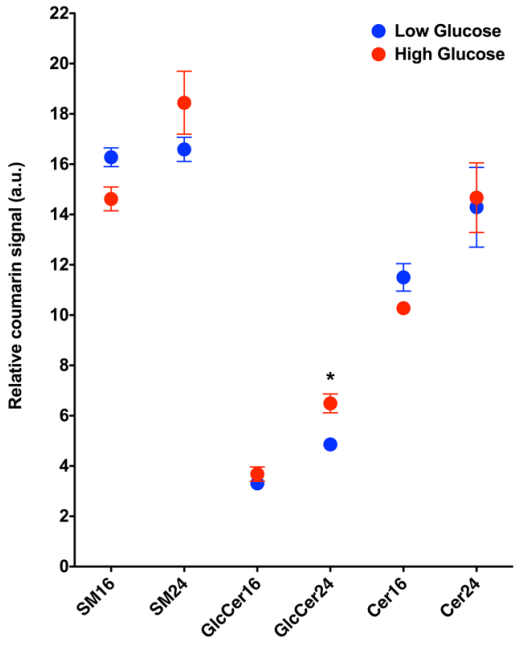

Figure 7.2: Incubation of A549ΔS1PL cells in either low or high glucose DMEM affects pacSph-metabolisation.

A549ΔS1PL cells were incubated in low glucose DMEM (1 mg/mL, standard culturing condition) and high glucose DMEM (4.5 mg/mL, same concentration as in SILAC media). The incorporation of pacSph (3 µM, 6 h labelling, coumarin-CLICK) into C16 and C24 SL-species was determined via TLC. The coumarin signal/species (C16 and C24) was calculated relative to the total coumarin signal detected (a.u.) in the two conditions. It was observed that the presence of high glucose (4.5 mg/mL) induces an enhanced incorporation of pacSph into C24 SL species compared to low glucose conditions (1 mg/mL). Shown: mean, ±SEM; unpaired, two-tailed *t* test performed; n=3. SM= sphingomyelin, GlcCer= Glucosylceramide, Cer= ceramide.

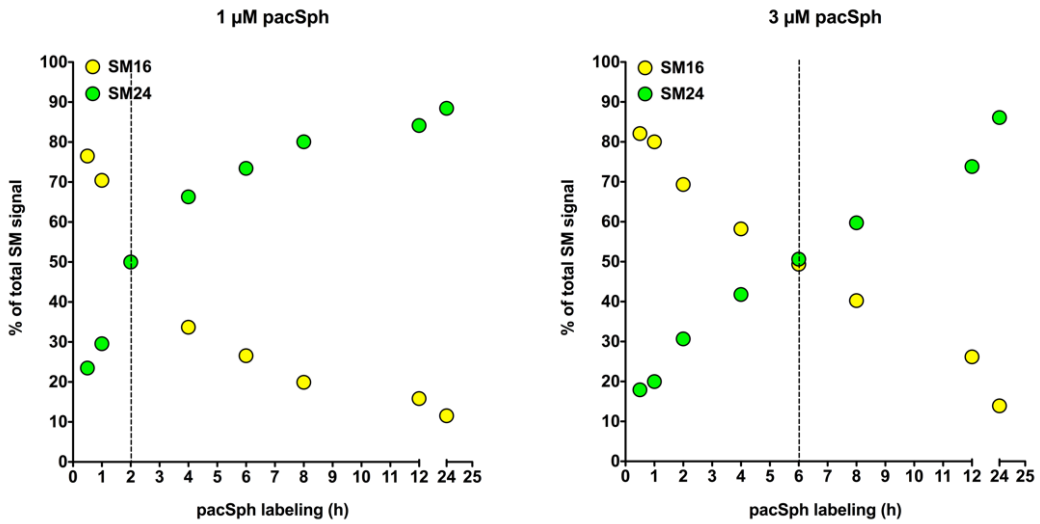

Figure 7.3: The velocity of pacSph-metabolisation is affected by the molar amount used for cell labelling.

A549ΔS1PL cells were pulsed with either 1 or 3 µM pacSph for 30 min and samples collected after different time points. Cells were subjected to lipid extraction, coumarin-clicked and analysed via TLC. The relative coumarin signal of SM16 or SM24 species was calculated relative to the total SM signal; n=1. Dotted lines indicate the "equilibrium" of pacSph-labelled C16 and C24 species.

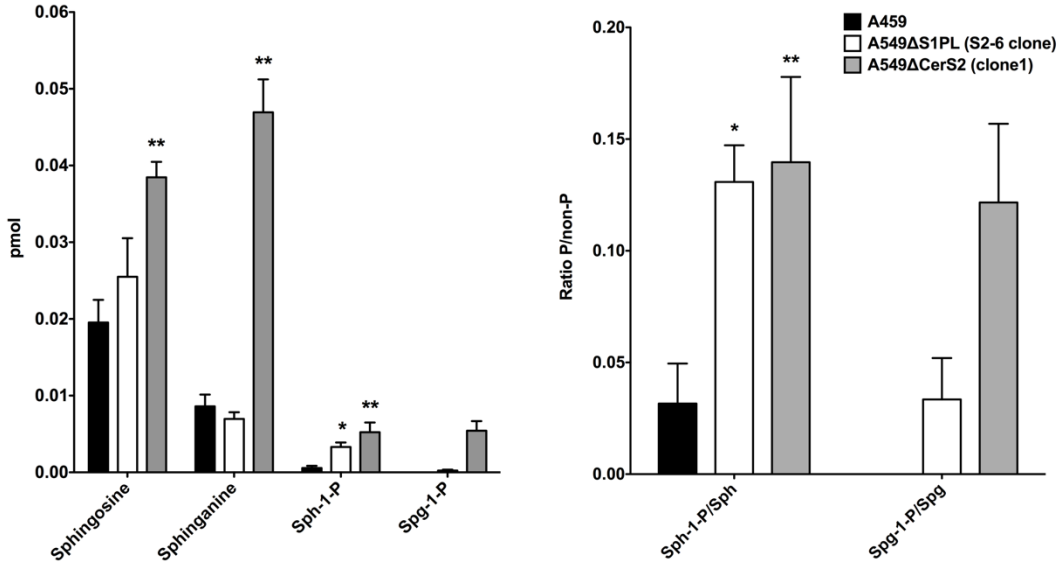

Figure 7.4: Lipid levels of sphingoid bases in A549 wild type and CRISPR KO cells.

Cells were collected from a 10 cm dish. The amounts of free sphingoid backbones and the corresponding phosphorylated molecules are either depicted separately (in pmol, left panel) or as ratio of phosphorylated vs. non-phosphorylated base (right panel). In HeLa *SGPL1*[254] and *SGPL1/CERS2*-deficient (D. Ostkotte, Brügger lab) cells, a similar increase in the ratio of P/non-P sphingoid backbones was observed compared to WT cells. Ceramide (Cer) and ceramide-1-phosphate (Cer-1-P) are also bioactive SL derivatives[58]. Cer was not affected by the *SGPL1* KO in A549 cells, but Cer levels were significantly increased in CerS2-depleted A549 cells compared to WT cells (Figure 7.5). Cer-1-P amounts were not determined. Shown: mean, ±SEM; unpaired, two-tailed *t* test (WT vs. KO) performed; n=3. Sample derivatisation conducted and data provided by T. Sachsenheimer, Brügger lab.

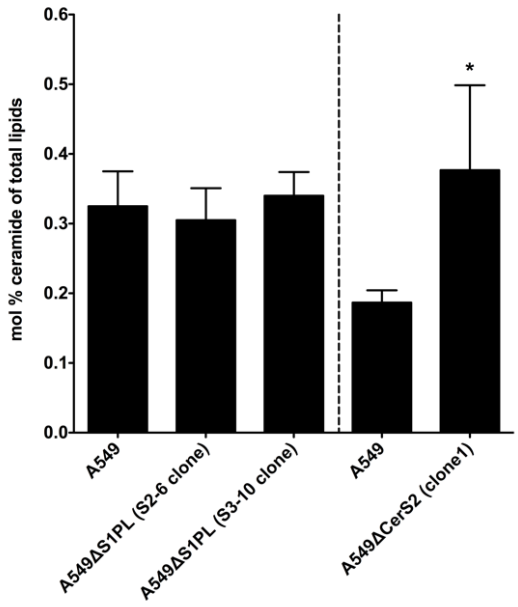

Figure 7.5: Ceramide levels in A549 wild type and CRISPR KO cells.

A549 and respective CRISPR-generated KO cells were collected from a 6-well plate and prepared for lipidomic analysis. The amount of ceramide compared to total lipidomes is depicted in mol%. Shown: mean, ±SEM; unpaired, two-tailed *t* test (WT vs. KO) performed; n=3. The dotted line indicates two different experiments. Lipidomic samples prepared and data provided by I. Leibrecht and C. Lüchtenborg, Brügger lab.

- **Gene expression data of SILAC proteomic screens**

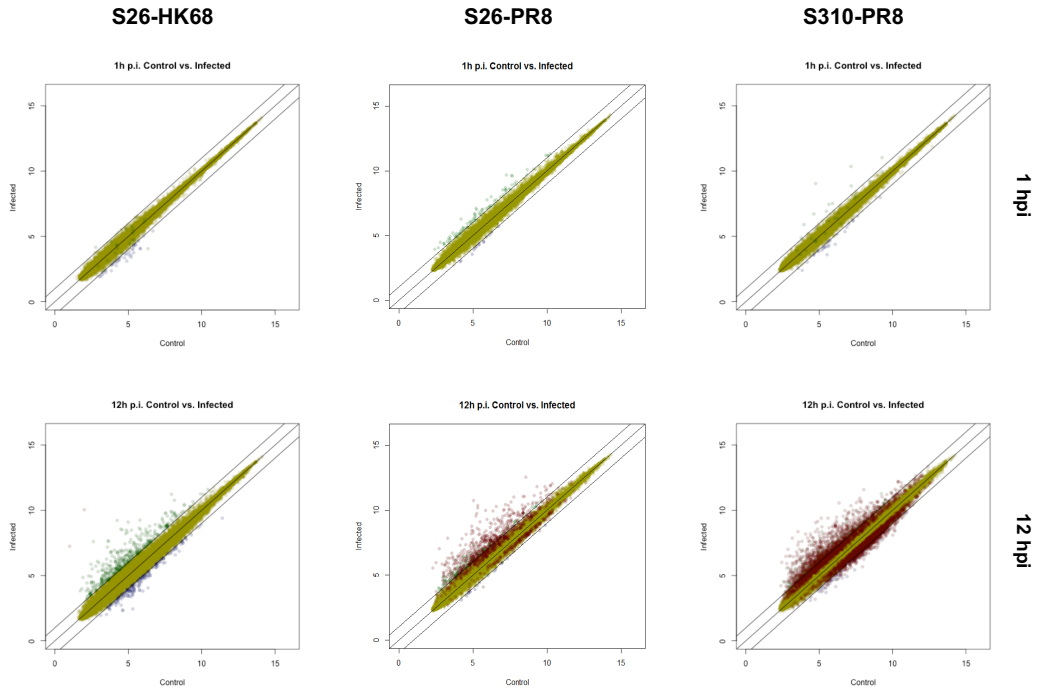

Figure 7.6: Gene expression intensities of microarray data from SILAC proteomic screens.

The average log_2-fold changes (log_2FC) of three biological replicates from infected over control (=non-infected) sample gene expression intensities were illustrated as scatter plot. Black lines indicate a cut off of 1 or -1 (genes 2-fold enriched in infected or mock samples). Dark blue dots indicate genes which are enriched in mock samples, lime green dots those enriched in infected samples; in purple are those genes with a p-value <0.05. Analysis done by R, Bioconductor package. S26= A549ΔS1PL S2-6 clone; S310= A549ΔS1PL S3-10 clone. Samples analysed and data provided by Genomics Core facility, EMBL.

Table 7.1: Top 20 genes up- or downregulated in IAV infected cells at 1 and 12 hpi (SILAC proteomic screens).

The log_2FC(infected/mock) average gene expression of three biological replicates is depicted in the "log2FC" column. The first 20 genes up- or downregulated are separated by the double-line. Genes showing a 2-fold enriched gene transcription activity in infected cells (log2FC>1) are highlighted in red, those enriched in the mock condition (<-1) in yellow. Samples were analysed with the R Bioconductor package. Notably, the same set of genes was analysed in each screen (Affymetrix Human Gene Chip 2.0 array). Log2FC= log 2-fold change; AvExp= average expression; t= t-statistics; p.Val= p-value; adj.PVal= adjusted p-value, B= posterior odds of differential expression. Samples were analysed and data provided by Genomics Core facility, EMBL.

GENENAME	UNIPROT	Log FC	Av Exp	t	P. Val	adj. P Val	B
HK68 SCREEN-S26 clone							
1 hpi							
early growth response 1	P18146, Q546S1	0.8	6.5	1.3	0.2	1.0	-4.5
nuclear receptor subfamily 4 group A member 1	P22736, F5GXF0, Q6ZMM6, A0A024R126	0.8	5.9	2.8	0.0	1.0	-4.0
nidogen 2	Q14112	0.8	8.5	2.5	0.0	1.0	-4.1
small nucleolar RNA, H/ACA box 15	NA	0.8	2.5	3.5	0.0	1.0	-3.8
interleukin 6	B4DVM1, P05231, Q75MH2, B5MC21, B4DNQ5	0.8	6.6	2.4	0.0	1.0	-4.1
integrin subunit beta 3	P05106	0.7	9.6	1.7	0.1	1.0	-4.4
nuclear receptor subfamily 4 group A member 2	F1D8N6, P43354, Q53EL4	0.7	7.6	3.7	0.0	1.0	-3.7
microRNA 3126	NA	0.7	5.9	2.8	0.0	1.0	-4.0
microRNA 487b	NA	0.7	3.5	3.5	0.0	1.0	-3.8
GRAM domain containing 3	Q96HH9	0.7	7.5	2.6	0.0	1.0	-4.1
microRNA 200c	NA	0.7	3.4	5.6	0.0	1.0	-3.4
interleukin 7 receptor	P16871	0.7	6.4	3.7	0.0	1.0	-3.8
cystatin SA	P09228	0.7	7.8	1.3	0.2	1.0	-4.5
connective tissue growth factor	P29279, Q5M8T4	0.7	9.8	3.1	0.0	1.0	-3.9
fibroblast growth factor 5	Q8NBG6, P12034	0.7	9.2	2.0	0.1	1.0	-4.3
cell migration inducing hyaluronan binding protein	Q8WUJ3	0.7	6.0	1.0	0.4	1.0	-4.6
metallothionein 1J, pseudogene	NA	0.6	4.1	3.7	0.0	1.0	-3.8
signal regulatory protein gamma	Q9P1W8	0.6	4.0	5.4	0.0	1.0	-3.5
T-cell receptor alpha constant	NA	0.6	3.6	2.0	0.1	1.0	-4.3
microRNA 3144	NA	0.6	2.7	2.8	0.0	1.0	-4.0
small nucleolar RNA, C/D box 114-10	NA	-0.6	2.7	-1.6	0.1	1.0	-4.4
uncharacterized LOC105371281	NA	-0.6	5.0	-2.8	0.0	1.0	-4.0
microRNA 3116-1	NA	-0.6	5.6	-3.2	0.0	1.0	-3.9

zinc finger protein 716	A6NP11	-0.6	4.0	-3.5	0.0	1.0	-3.8
glutathione S-transferase alpha 2	A0A140VKE2, A8K987, P09210	-0.6	3.8	-2.2	0.1	1.0	-4.2
uncharacterized LOC105376050	NA	-0.6	4.0	-3.7	0.0	1.0	-3.8
aldo-keto reductase family 1 member C2	P52895, B4DK69	-0.6	9.6	-1.5	0.2	1.0	-4.4
ST6 beta-galactoside alpha-2,6-sialyltransferase 2	Q96JF0	-0.6	6.0	-1.6	0.2	1.0	-4.4
uncharacterized LOC105376438	NA	-0.6	3.9	-4.3	0.0	1.0	-3.6
microRNA 181a-2	NA	-0.7	3.9	-2.1	0.1	1.0	-4.2
interferon alpha 13	A0A087WWS6, P01562	-0.7	3.5	-2.3	0.0	1.0	-4.1
cyclin Y-like 2 (pseudogene)	NA	-0.7	4.6	-3.0	0.0	1.0	-3.9
small nucleolar RNA, C/D box 113-8	NA	-0.7	4.9	-1.7	0.1	1.0	-4.4
keratin associated protein 4-11	Q9BYQ6	-0.7	3.9	-3.8	0.0	1.0	-3.7
carbamoyl-phosphate synthase 1	P31327, Q6PEK7, B7ZAW0, A0A024R454	-0.7	8.4	-0.8	0.4	1.0	-4.7
progestagen associated endometrial protein	B4E3C0, P09466, A0A024R8D8, B2R4F9, A6XNE0	-0.7	4.5	-5.0	0.0	1.0	-3.5
small nucleolar RNA, C/D box 114-2	NA	-0.7	4.0	-1.5	0.2	1.0	-4.5
cytochrome P450 family 1 subfamily B member 1	Q16678, Q53TK1	-0.7	8.6	-1.3	0.2	1.0	-4.5
keratin associated protein 13-2	Q52LG2	-0.8	2.7	-3.6	0.0	1.0	-3.8
microRNA 4279	NA	-0.8	3.9	-1.9	0.1	1.0	-4.3
	12 hpi						
interferon induced protein with tetratricopeptide repeats 1	P09914	4.6	6.8	6.8	0.0	0.2	1.0
interferon induced protein with tetratricopeptide repeats 2	P09913, Q05DN2	4.0	6.7	5.2	0.0	0.2	-0.5
interferon induced protein 44	Q8TCB0	3.9	5.7	6.1	0.0	0.2	0.4
MX dynamin like GTPase 1	P20591	3.8	6.6	4.5	0.0	0.2	-1.1
interferon lambda 2	Q8IZJ0	3.7	6.7	2.9	0.0	0.4	-3.2
C-X-C motif chemokine ligand 10	A0A024RDA4, P02778	3.5	5.4	3.1	0.0	0.3	-2.8
interferon induced protein with tetratricopeptide repeats 3	O14879, Q5T765	3.4	7.3	4.8	0.0	0.2	-0.9
interferon induced with helicase C	Q9BYX4	3.4	6.8	4.5	0.0	0.2	-1.2

domain 1							
2'-5'-oligoadenylate synthetase 2	P29728, Q7Z6D0	3.3	6.9	4.2	0.0	0.2	-1.5
interferon alpha inducible protein 6	P09912	3.2	9.5	6.2	0.0	0.2	0.5
interferon beta 1	P01574	2.9	5.8	6.2	0.0	0.2	0.5
sterile alpha motif domain containing 9 like	Q8IVG5	2.8	7.3	4.0	0.0	0.3	-1.7
interferon induced protein 44 like	Q53G44, B4E019	2.8	5.6	4.2	0.0	0.2	-1.5
2'-5'-oligoadenylate synthetase like	Q15646	2.7	7.2	4.9	0.0	0.2	-0.7
C-X-C motif chemokine ligand 8	A0A024RDA5, P10145	2.6	6.3	3.5	0.0	0.3	-2.4
DEXD/H-box helicase 58	O95786	2.6	9.4	4.9	0.0	0.2	-0.7
HEAT repeat containing 9	A2RTY3	2.4	6.5	3.7	0.0	0.3	-2.1
interleukin 24	Q13007	2.4	6.6	5.6	0.0	0.2	0.0
interleukin 6	B4DVM1, P05231, Q75MH2, B5MC21, B4DNQ5	2.4	7.4	2.8	0.0	0.4	-3.3
cytidine/uridine monophosphate kinase 2	Q5EBM0	2.4	6.3	3.0	0.0	0.3	-3.0
matrix metallopeptidase 24	Q86VV6, Q9Y5R2	-1.0	7.1	-3.8	0.0	0.3	-2.0
phospholipase C epsilon 1	Q9P212, B7ZM61	-1.0	8.1	-6.3	0.0	0.2	0.6
small nucleolar RNA, C/D box 19B	NA	-1.1	5.7	-4.4	0.0	0.2	-1.3
aldo-keto reductase family 1 member C2	P52895, B4DK69	-1.1	9.4	-2.7	0.0	0.4	-3.4
GATS protein like 2	A6NHX0	-1.1	7.9	-3.7	0.0	0.3	-2.1
versican	P13611, Q86W61, A0A024RAL1, Q6MZK8, A0A024RAP3, A0A024RAQ9, Q59FG9	-1.1	7.1	-5.6	0.0	0.2	0.0
inhibitor of DNA binding 1, HLH protein	P41134	-1.1	9.1	-4.9	0.0	0.2	-0.8
6-phosphofructo-2-kinase/fructose-2,6-biphosphatase 3	B7Z8A0, Q16875	-1.2	8.6	-2.8	0.0	0.4	-3.3
cyclin E1	P24864, A0A0G3DHS8, V5W5X2	-1.2	8.0	-3.9	0.0	0.3	-1.8
BTB domain containing 11	A6QL63, B3KVD0, B3KXB0	-1.2	6.3	-4.3	0.0	0.2	-1.3
neuropilin 2	O60462, Q7LBX6,	-1.2	8.3	-4.1	0.0	0.2	-1.6

	Q7Z3T9, X5D2Q8, A0A024R412, A0A024R3W6						
calcium voltage-gated channel auxiliary subunit gamma 4	A0A024R8J8, Q9UBN1	-1.2	7.7	-5.1	0.0	0.2	-0.5
snail family transcriptional repressor 2	O43623	-1.2	8.0	-2.5	0.0	0.4	-3.7
glycine cleavage system protein H	P23434	-1.2	4.5	-7.8	0.0	0.2	1.7
family with sequence similarity 111 member B	Q6SJ93	-1.3	7.9	-4.9	0.0	0.2	-0.7
contactin 1	Q12860, A0A024R104	-1.3	6.3	-1.6	0.1	0.5	-4.8
SLIT and NTRK like family member 6	Q9H5Y7	-1.5	5.1	-2.3	0.1	0.4	-3.9
protocadherin 9	B7ZM79, Q9HC56, A7E2D9, Q5VT82, X5D7N0	-1.6	7.6	-5.7	0.0	0.2	0.1
dehydrogenase/reductase 3	O75911	-1.6	7.4	-4.4	0.0	0.2	-1.3
cytochrome P450 family 24 subfamily A member 1	Q07973	-2.0	10.2	-4.2	0.0	0.2	-1.5
PR8 SCREEN I-S26 clone							
1 hpi							
early growth response 1	P18146, Q546S1	2.5	9.0	4.9	0.0	1.0	-2.6
interferon induced protein with tetratricopeptide repeats 1	P09914	2.1	6.2	1.5	0.2	1.0	-4.4
prostaglandin-endoperoxide synthase 2	P35354	2.0	9.0	4.8	0.0	1.0	-2.7
nuclear receptor subfamily 4 group A member 2	F1D8N6, P43354, Q53EL4	1.9	9.0	4.5	0.0	1.0	-2.8
nuclear receptor subfamily 4 group A member 1	P22736, F5GXF0, Q6ZMM6, A0A024R126	1.7	7.1	5.2	0.0	1.0	-2.5
MX dynamin like GTPase 1	P20591	1.7	6.0	1.3	0.2	1.0	-4.5
C-X-C motif chemokine ligand 8	A0A024RDA5, P10145	1.7	7.8	5.5	0.0	1.0	-2.4
interferon induced protein with tetratricopeptide repeats 2	P09913, Q05DN2	1.6	6.7	1.2	0.3	1.0	-4.6
interferon induced protein 44	Q8TCB0	1.5	5.5	1.4	0.2	1.0	-4.5
2'-5'-oligoadenylate synthetase 2	P29728, Q7Z6D0	1.5	6.5	1.2	0.3	1.0	-4.6
interferon alpha inducible protein 6	P09912	1.4	9.7	1.7	0.1	1.0	-4.3
interferon induced with helicase C domain 1	Q9BYX4	1.4	6.3	1.5	0.2	1.0	-4.4
tripartite motif containing 41	Q8WV44	1.4	5.3	1.4	0.2	1.0	-4.5

long intergenic non-protein coding RNA 616	NA	1.4	5.2	1.2	0.2	1.0	-4.6
interferon induced protein with tetratricopeptide repeats 3	O14879, Q5T765	1.3	7.4	1.3	0.2	1.0	-4.5
succinate receptor 1	Q9BXA5	1.3	5.5	1.2	0.3	1.0	-4.6
vault RNA 1-3	NA	1.3	8.6	3.7	0.0	1.0	-3.1
FosB proto-oncogene, AP-1 transcription factor subunit	P53539, A0A024R0P6, K7EKC1	1.2	7.6	5.1	0.0	1.0	-2.6
C-C motif chemokine ligand 2	P13500	1.2	10.8	4.0	0.0	1.0	-3.0
C-C motif chemokine ligand 5	D0EI67, P13501	1.2	7.9	1.4	0.2	1.0	-4.5
ankyrin 2	Q01484	-0.5	7.4	-1.9	0.1	1.0	-4.1
microRNA 3671	NA	-0.5	6.7	-1.4	0.2	1.0	-4.4
aldo-keto reductase family 1 member C2	P52895, B4DK69	-0.5	9.6	-1.4	0.2	1.0	-4.5
C-C motif chemokine ligand 8	P80075	-0.5	3.1	-4.2	0.0	1.0	-2.9
microRNA 643	NA	-0.5	5.8	-2.0	0.1	1.0	-4.1
microRNA 4500	NA	-0.5	7.0	-1.7	0.1	1.0	-4.3
NOP2/Sun RNA methyltransferase family member 5 pseudogene 1	NA	-0.5	9.7	-1.5	0.2	1.0	-4.4
microRNA 503	NA	-0.5	7.3	-2.6	0.0	1.0	-3.7
cytochrome P450 family 3 subfamily A member 4	P08684, Q6GRK0	-0.5	3.6	-3.9	0.0	1.0	-3.0
taste 2 receptor member 10	Q9NYW0	-0.5	6.4	-2.2	0.1	1.0	-3.9
microRNA 548t	NA	-0.5	5.0	-1.8	0.1	1.0	-4.2
microRNA 4263	NA	-0.5	4.8	-1.9	0.1	1.0	-4.1
collagen type XII alpha 1 chain	Q99715	-0.5	8.1	-2.3	0.0	1.0	-3.9
versican	P13611, Q86W61, A0A024RAL1, Q6MZK8, A0A024RAP3, A0A024RAQ9, Q59FG9	-0.5	8.9	-1.3	0.2	1.0	-4.5
microRNA 1252	NA	-0.6	3.1	-2.7	0.0	1.0	-3.7
RNA binding motif	Q6XE24, C9JIJ9	-0.6	7.0	-1.4	0.2	1.0	-4.4

single stranded interacting protein 3							
long intergenic non-protein coding RNA 858	NA	-0.6	5.9	-2.5	0.0	1.0	-3.8
microRNA 1206	NA	-0.6	7.3	-3.1	0.0	1.0	-3.4
ATP binding cassette subfamily A member 1	B2RUU2, B7XCW9, O95477	-0.6	7.9	-1.4	0.2	1.0	-4.5
microRNA let-7a-2	NA	-0.8	7.0	-4.2	0.0	1.0	-2.9
	12 hpi						
interferon induced protein with tetratricopeptide repeats 1	P09914	5.6	9.1	32.4	0.0	0.0	12.7
MX dynamin like GTPase 1	P20591	5.0	8.4	24.4	0.0	0.0	11.6
2'-5'-oligoadenylate synthetase 2	P29728, Q7Z6D0	4.8	8.4	21.1	0.0	0.0	10.8
interferon induced protein with tetratricopeptide repeats 2	P09913, Q05DN2	4.5	8.0	19.8	0.0	0.0	10.4
interferon induced protein 44	Q8TCB0	4.3	7.6	14.1	0.0	0.0	8.2
interferon lambda 2	Q8IZJ0	3.7	6.2	11.7	0.0	0.0	6.8
interferon induced protein with tetratricopeptide repeats 3	O14879, Q5T765	3.7	8.5	19.0	0.0	0.0	10.2
interferon induced protein 44 like	Q53G44, B4E019	3.6	6.8	11.9	0.0	0.0	6.9
interferon induced with helicase C domain 1	Q9BYX4	3.5	8.0	16.2	0.0	0.0	9.1
cytidine/uridine monophosphate kinase 2	Q5EBM0	3.5	7.7	12.3	0.0	0.0	7.1
succinate receptor 1	Q9BXA5	3.4	7.2	9.3	0.0	0.0	4.9
2'-5'-oligoadenylate synthetase like	Q15646	3.3	8.4	17.7	0.0	0.0	9.7
C-X-C motif chemokine ligand 10	A0A024RDA4, P02778	3.3	6.4	9.8	0.0	0.0	5.4
interleukin 1 alpha	P01583	3.0	7.4	5.1	0.0	0.0	0.1
C-C motif chemokine ligand 5	D0EI67, P13501	3.0	8.8	12.1	0.0	0.0	7.0
sterile alpha motif domain containing 9 like	Q8IVG5	2.9	9.0	11.6	0.0	0.0	6.7
chromosome 1 open reading frame 189	Q5VU69	2.8	7.0	7.2	0.0	0.0	2.8
interferon induced transmembrane protein 1	A0A024R210, P13164	2.6	8.7	8.9	0.0	0.0	4.5
ubiquitin specific peptidase 18	Q9UMW8	2.6	10.1	21.2	0.0	0.0	10.8
phosphorylase, glycogen, muscle	P11217	2.6	7.2	9.7	0.0	0.0	5.3
lengsin, lens protein with glutamine synthetase domain	Q5TDP6	-0.7	6.2	-3.5	0.0	0.1	-2.3
collagen type XII alpha 1 chain	Q99715	-0.7	8.0	-2.8	0.0	0.2	-3.6
sorting nexin 29	Q8TEQ0	-0.7	7.0	-4.1	0.0	0.1	-1.4

microRNA 604	NA	-0.7	7.6	-4.2	0.0	0.1	-1.1
taste 2 receptor member 31	P59538	-0.8	5.4	-3.0	0.0	0.2	-3.1
insulin receptor	P06213	-0.8	7.4	-4.3	0.0	0.1	-1.0
microRNA 4263	NA	-0.8	4.8	-2.9	0.0	0.2	-3.3
glutaminase	O94925, Q68D38	-0.8	10.0	-3.6	0.0	0.1	-2.2
leukotriene B4 receptor 2	B4E292, Q9NPC1	-0.8	5.8	-4.2	0.0	0.1	-1.1
neurobeachin	Q8NFP9, B3KXQ8, Q5T321	-0.8	8.6	-3.5	0.0	0.1	-2.3
GATS protein like 2	A6NHX0	-0.8	5.2	-3.2	0.0	0.2	-2.9
NHS actin remodeling regulator	Q6T4R5	-0.8	7.2	-3.8	0.0	0.1	-1.8
microRNA 1206	NA	-0.8	6.7	-4.1	0.0	0.1	-1.4
ankyrin 2	Q01484	-0.8	7.1	-5.2	0.0	0.0	0.3
long intergenic non-protein coding RNA 993	NA	-0.8	5.5	-2.6	0.0	0.2	-3.9
zinc finger protein 469	NA	-0.9	7.6	-6.5	0.0	0.0	2.0
microRNA 4441	NA	-0.9	4.0	-7.3	0.0	0.0	2.9
hect domain and RLD 2 pseudogene 9	NA	-0.9	8.8	-7.7	0.0	0.0	3.4
versican	P13611, Q86W61, A0A024RAL1, Q6MZK8, A0A024RAP3, A0A024RAQ9, Q59FG9	-0.9	8.4	-2.4	0.0	0.3	-4.1
taste 2 receptor member 14	Q9NYV8	-1.0	6.5	-4.0	0.0	0.1	-1.5
PR8 SCREEN II-S310 clone							
1 hpi							
early growth response 1	P18146, Q546S1	2.2	8.3	9.6	0.0	0.3	-1.1
neurotensin	P30990, Q6FH20	2.0	6.2	8.1	0.0	0.4	-1.3
nuclear receptor subfamily 4 group A member 1	P22736, F5GXF0, Q6ZMM6, A0A024R126	1.9	7.0	12.1	0.0	0.1	-0.9
nuclear receptor subfamily 4 group A member 2	F1D8N6, P43354, Q53EL4, F1DAL2	1.8	8.0	8.5	0.0	0.4	-1.2

mucin 5B, oligomeric mucus/gel-forming	Q9HC84	1.3	8.4	3.8	0.0	0.9	-2.7
mucin 5AC, oligomeric mucus/gel-forming	P98088	1.3	9.5	4.5	0.0	0.9	-2.3
nuclear receptor subfamily 4 group A member 3	A0A024R168, Q92570	1.2	6.9	5.3	0.0	0.8	-2.0
tandem C2 domains, nuclear	Q8N9U0	1.2	6.0	7.5	0.0	0.5	-1.4
connective tissue growth factor	P29279, Q5M8T4	1.2	10.0	4.1	0.0	0.9	-2.5
carcinoembryonic antigen related cell adhesion molecule 6	P40199	1.1	10.2	4.1	0.0	0.9	-2.5
keratin 4	B4DRS2	1.1	7.5	3.9	0.0	0.9	-2.6
sciellin	O95171	1.1	4.7	12.2	0.0	0.1	-0.9
tubulin polymerization promoting protein family member 3	A0A024R702, Q9BW30	1.0	8.3	9.2	0.0	0.3	-1.1
cadherin 17	Q12864	0.9	7.6	4.4	0.0	0.9	-2.3
G protein-coupled receptor 37	O15354	0.9	6.9	5.3	0.0	0.8	-2.0
trefoil factor 1	P04155	0.9	8.5	3.0	0.0	1.0	-3.2
fibrinogen beta chain	P02675, V9HVY1	0.9	5.4	7.8	0.0	0.4	-1.3
fibronectin leucine rich transmembrane protein 3	Q9NZU0	0.9	7.8	7.4	0.0	0.5	-1.4
schlafen family member 11	Q7Z7L1	0.9	8.1	3.4	0.0	1.0	-3.0
small nucleolar RNA, H/ACA box 12	NA	0.9	5.3	3.3	0.0	1.0	-3.0
formin 2	Q9HBL1, Q9NZ56	-0.6	5.6	-4.9	0.0	0.8	-2.1
leucine rich repeat containing 37 member A3	J3QTJ5, O60309	-0.6	6.3	-2.4	0.0	1.0	-3.7
RAB3B, member RAS oncogene family	P20337	-0.6	8.3	-3.3	0.0	1.0	-3.0
hyaluronan and proteoglycan link protein 3	A8K7T8, H3BTH8, Q96S86, A0A024RC58	-0.6	7.9	-4.8	0.0	0.8	-2.1
SPARC (osteonectin), cwcv and kazal like domains proteoglycan 1	Q08629	-0.6	8.0	-5.6	0.0	0.8	-1.9
family with sequence similarity 196 member B	A6NMK8	-0.6	5.9	-2.5	0.0	1.0	-3.6
iodothyronine deiodinase 2	A8K845, Q92813, Q9HCP7	-0.7	6.6	-2.6	0.0	1.0	-3.6
ADP ribosylation factor like GTPase 4D	P49703	-0.7	8.1	-4.5	0.0	0.9	-2.3
microRNA 924	NA	-0.7	3.9	-3.5	0.0	1.0	-2.9
microRNA 4481	NA	-0.7	4.8	-2.3	0.1	1.0	-3.8
myocardin	Q8IZQ8	-0.7	5.7	-2.3	0.1	1.0	-3.8
neuronal pentraxin 1	Q15818	-0.7	7.3	-2.8	0.0	1.0	-3.4

microRNA 3189	NA	-0.7	6.9	-1.5	0.2	1.0	-4.4
solute carrier family 51 beta subunit	Q86UW2	-0.7	8.2	-4.0	0.0	0.9	-2.6
collagen and calcium binding EGF domains 1	Q6UXH8	-0.8	6.1	-5.2	0.0	0.8	-2.0
solute carrier family 16 member 2	P36021	-0.8	8.6	-4.3	0.0	0.9	-2.4
snail family transcriptional repressor 2	O43623	-0.9	7.3	-4.3	0.0	0.9	-2.4
DNA damage inducible transcript 3	P35638, Q53YD1	-1.1	6.3	-2.4	0.0	1.0	-3.7
atypical chemokine receptor 3	P25106	-1.1	6.9	-4.1	0.0	0.9	-2.5
insulin like growth factor binding protein 7	Q16270	-1.2	8.8	-10.8	0.0	0.2	-1.0
12 hpi							
tripartite motif containing 41	Q8WV44	4.0	6.7	15.2	0.0	0.0	6.6
glycogen phosphorylase, muscle associated	P11217	3.8	7.2	20.4	0.0	0.0	8.2
early growth response 1	P18146, Q546S1	3.3	8.6	7.4	0.0	0.0	1.8
retinal pigment epithelium-derived rhodopsin homolog	O14718	3.2	6.2	27.2	0.0	0.0	9.5
fibronectin type III domain containing 7	Q5VTL7	3.2	6.3	9.6	0.0	0.0	3.6
long intergenic non-protein coding RNA 616	NA	3.1	5.7	9.4	0.0	0.0	3.4
chromosome 1 open reading frame 189	Q5VU69	3.1	6.3	6.9	0.0	0.0	1.3
succinate receptor 1	Q9BXA5	3.1	6.4	7.3	0.0	0.0	1.7
DEAQ-box RNA dependent ATPase 1	Q8TE96	3.0	7.1	26.1	0.0	0.0	9.3
long intergenic non-protein coding RNA 672	NA	3.0	7.1	24.1	0.0	0.0	9.0
microRNA 4753	NA	2.9	4.2	7.6	0.0	0.0	2.0
long intergenic non-protein coding RNA 1729	NA	2.9	6.9	7.1	0.0	0.0	1.6
glycogen synthase 2	P54840	2.9	5.8	14.0	0.0	0.0	6.0
F-box and WD repeat domain containing 10	Q5XX13	2.8	7.5	11.4	0.0	0.0	4.7
uncharacterized LOC105374653	NA	2.7	6.6	11.5	0.0	0.0	4.8
NME/NM23 family member 5	A0A0S2Z4L9, P56597	2.7	4.9	12.4	0.0	0.0	5.3
lymphocyte antigen 6 family member G6C	A0A1U9X7Z1, O95867	2.7	7.0	12.1	0.0	0.0	5.1
DNA damage inducible transcript 3	P35638, Q53YD1	2.7	8.3	6.0	0.0	0.0	0.4
lactate dehydrogenase C	A0A140VKA7, P07864	2.6	5.5	8.4	0.0	0.0	2.6

integrin subunit beta 1 binding protein 2	Q9UKP3	2.6	7.1	17.4	0.0	0.0	7.4
glycogen synthase 1	P13807	-1.4	6.6	-7.3	0.0	0.0	1.7
myosin heavy chain 9	A0A024R1N1, P35579	-1.4	8.9	-9.4	0.0	0.0	3.4
sec1 family domain containing 2	Q8WU76	-1.5	7.7	-6.2	0.0	0.0	0.6
tensin 3	Q68CZ2	-1.5	9.0	-10.7	0.0	0.0	4.3
lengsin, lens protein with glutamine synthetase domain	Q5TDP6	-1.5	6.4	-4.5	0.0	0.0	-1.4
NHS actin remodeling regulator	Q6T4R5	-1.5	7.2	-10.2	0.0	0.0	4.0
calcium voltage-gated channel auxiliary subunit gamma 4	A0A024R8J8, Q9UBN1	-1.5	8.0	-5.2	0.0	0.0	-0.5
RAB3B, member RAS oncogene family	P20337	-1.5	7.7	-6.3	0.0	0.0	0.7
solute carrier family 46 member 1	A0A024QZ44, Q96NT5, A0A024QZ15	-1.5	8.6	-7.2	0.0	0.0	1.6
atypical chemokine receptor 3	P25106	-1.5	6.6	-7.2	0.0	0.0	1.6
BicC family RNA binding protein 1	Q9H694	-1.5	8.3	-10.6	0.0	0.0	4.3
KIAA1549 like	Q12914, Q6ZVL6	-1.5	7.3	-9.3	0.0	0.0	3.4
family with sequence similarity 230 member C	NA	-1.5	6.0	-6.0	0.0	0.0	0.4
solute carrier family 16 member 2	P36021	-1.6	7.7	-6.9	0.0	0.0	1.3
heparan sulfate proteoglycan 2	P98160	-1.6	7.9	-4.8	0.0	0.0	-1.0
CXADR like membrane protein	B4E3S3, Q9H6B4	-1.6	8.4	-3.7	0.0	0.1	-2.6
solute carrier family 29 member 3	Q9BZD2	-1.6	9.1	-11.8	0.0	0.0	5.0
GLI family zinc finger 2	P10070, Q1PSW9, Q59FV5	-1.7	8.1	-7.1	0.0	0.0	1.6
matrix metallopeptidase 24	Q86VV6, Q9Y5R2	-1.8	8.3	-10.0	0.0	0.0	3.9
tensin 4	Q6PJP3, Q8IZW8	-1.9	8.9	-5.1	0.0	0.0	-0.6

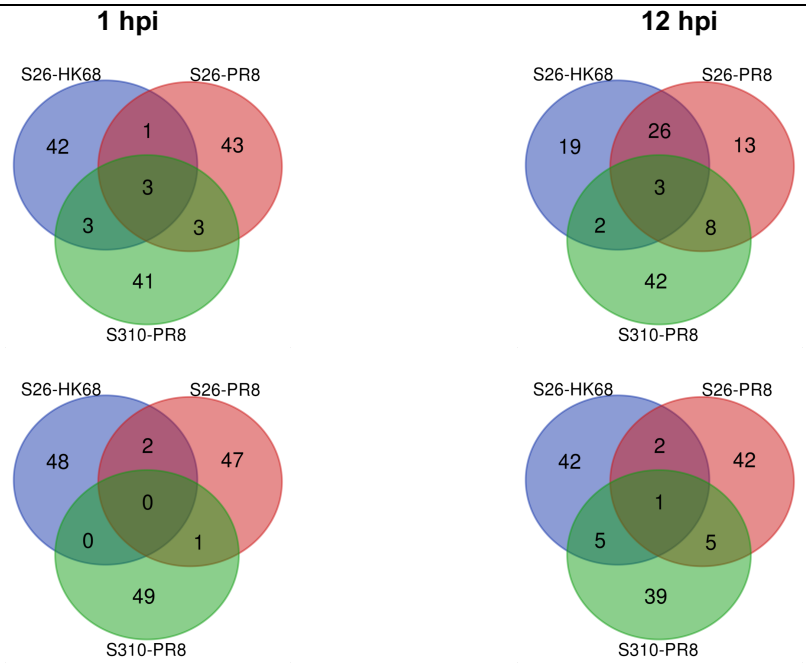

Figure 7.7: Alignment of the Top 50 of up-or downregulated genes of all three SILAC-proteomic screens conducted.

The 50 genes showing the highest (upper panel) or lowest (lower panel) log_2FC(infected/mock) ratio were aligned with http://bioinformatics.psb.ugent.be/cgi-bin/liste/Venn/calculate_venn.htpl. Notably, the same set of genes was analysed in each screen (Affymetrix Human Gene Chip 2.0 array). Overlapping proteins in: **lowest ratio, 12 hpi**= matrix metallopeptidase 24; **highest ratio, 1 hpi**= nuclear receptor subfamily 4 group A member 2, early growth response 1, nuclear receptor subfamily 4 group A member 1; **highest ratio, 12 hpi**= succinate receptor 1, C-X-C motif chemokine ligand 8, nuclear receptor subfamily 4 group A member 1. S26= A549ΔS1PL S2-6 clone; S310= A549ΔS1PL S3-10 clone. Samples were analysed and data provided by Genomics Core facility, EMBL.

Table 7.2: Differential gene expression data of protein candidates identified in SILAC-proteomic screens (depicted Table 3.3 and in Table 3.5).

Values for each protein represent the mean of log_2FC(infected/mock) from three biological replicates. For ITGB1, only gene expression data of integrin subunit beta 1 binding protein 1 & 2 (ITGB1BP1/2) was available. No gene expression data were available for VMP1 and ANXA2. Proteins which have been tested in transient knock-down experiments are highlighted in grey. S26= A549ΔS1PL S2-6 clone; S310= A549ΔS1PL S3-10 cloneSamples were analysed and data provided by Genomics Core facility, EMBL.

	HK68-S26		**PR8-S26**		**PR8-S310**	
Protein	**1 hpi**	**12 hpi**	**1 hpi**	**12 hpi**	**1 hpi**	**12 hpi**
ITGB1BP1/2 (O14713/ Q9UKP3)*	-0.028/0.187	-0.326/0.751	0.012/0.517	-0.005/1.546	0.026/-0.029	-0.323/2.62
SLC1A5	0.013	0.209	-0.006	0.143	0.002	0.275
CD63	0.058	0.195	0.072	0.205	0.098	0.508
ELOVL1	0.015	-0.120	-0.069	-0.127	0.043	-0.304
TRAM1	0.035	-0.136	0.051	0.147	-0.064	0.002
NCL	0.080	0.134	-0.007	0.033	-0.086	-0.279
VMP1						
LAMP1	0.006	-0.137	-0.054	-0.032	-0.093	-0.287
SCARB2	-0.028	0.228	0.014	0.159	0.000	-0.057
CD81	0.015	-0.109	-0.052	-0.111	0.020	-0.160
CAV1	-0.010	-0.008	-0.010	-0.008	-0.042	-0.071
VIM	0.032	0.141	-0.002	0.018	-0.017	0.083

ANXA2						
VDAC1	-0.048	-0.313	-0.078	0.051	-0.010	-0.025
SLC46A1	0.064	-0.151	0.106	0.188	0.008	0.262
TMEM41B	-0.046	-0.684	-0.071	-0.491	-0.088	-1.500
RAB11(A)	0.004	0.019	-0.033	-0.146	0.031	0.262
TM9SF3	0.068	0.262	0.005	-0.014	-0.063	-0.080
UGCG	0.122	0.036	0.041	0.199	0.088	0.756
SLC25A11	-0.091	-0.364	-0.115	-0.121	-0.081	-0.586
PCYOX1	0.021	-0.281	-0.021	-0.303	0.013	-0.455

- Proteomic screens

Table 7.3: Alignment of protein hits from Replicate 3 of the HK68 SILAC-screen.

High confidence master proteins identified at 1 and 12 hpi (irrespective of infection) were aligned (http://bioinformatics.psb.ugent.be/cgi-bin/liste/Venn/calculate_venn.htpl). Only proteins unique to the 1 or 12 hpi condition are depicted. Rep= Replicate.

Sample	**Nr. of proteins**	**Proteins**
1hpi_Rep3	3	60S ribosomal protein L15 (RPL15)
		Propionyl-CoA carboxylase alpha chain, mitochondrial (PCCA)
		78 kDa glucose-regulated protein (HSPA5)
12hpi_Rep3	39	ADP/ATP translocase 2 (SLC25A5)
		Plectin (PLEC)
		Isoform 3 of Calumenin (CALU)
		Serine hydroxymethyltransferase, mitochondrial (SHMT2)
		78 kDa glucose-regulated protein (HSPA5)
		Surfeit locus protein 4 (SURF4)
		Epoxide hydrolase 1 (EPHX1)
		Heat shock cognate 71 kDa protein (HSPA8)
		Non-POU domain-containing octamer-binding protein (NONO)
		Isoform 3 of Coronin-1C (CORO1C)
		Endoplasmin (HSP90B1)
		Voltage-dependent anion-selective channel protein 1 (VDAC1)
		Heterogeneous nuclear ribonucleoprotein L (HNRNPL)
		Sodium/potassium-transporting ATPase subunit alpha-1 (ATP1A1)
		Cytoskeleton-associated protein 4 (CKAP4)
		Protein disulfide-isomerase (P4HB)
		Isoform 2 of Fatty aldehyde dehydrogenase (ALDH3A2)
		Protein jagunal homolog 1 (JAGN1)
		Serine palmitoyltransferase 1 (SPTLC1)

	Heterogeneous nuclear ribonucleoprotein Q (SYNCRIP)
	Isoform 2 of Ras-related protein Rab-4B (RAB4B)
	Probable ATP-dependent RNA helicase DDX5 (DDX5)
	60S ribosomal protein L27 (Fragment) (RPL27)
	Delta(3,5)-Delta(2,4)-dienoyl-CoA isomerase, mitochondrial (ECH1)
	Plasma membrane calcium-transporting ATPase 1 (ATP2B1)
	Basigin (BSG)
	Sarcoplasmic/endoplasmic reticulum calcium ATPase 2 (ATP2A2)
	Propionyl-CoA carboxylase alpha chain, mitochondrial (PCCA)
	Vacuole membrane protein 1 (VMP1)
	Serine/arginine-rich splicing factor 3 (SRSF3)
	Isoform 4 of 4F2 cell-surface antigen heavy chain (SLC3A2)
	Nucleolin (NCL)
	Large neutral amino acids transporter small subunit 1 (SLC7A5)
	Desmoplakin (DSP)
	Neutral amino acid transporter B(0) (SLC1A5)
	Myoferlin (MYOF)
	Phosphate carrier protein, mitochondrial (SLC25A3)
	Acyl-Coenzyme A dehydrogenase, C-4 to C-12 straight chain, isoform CRA_a (ACADM)
	Hemagglutinin Influenza A virus (strain A/Hong Kong/1/1968 H3N2) (HA)

Table 7.4: Protein alignment of run 1 and run 2 (SILAC PR8 screen I, PR8-I) of protein hits identified at 1 and 12 hpi

High confidence master proteins identified at 1 and 12 hpi (irrespective of infection) in run 1 and 2 were aligned with http://bioinformatics.psb.ugent.be/cgi-bin/liste/Venn/calculate_venn.htpl. Only proteins with a 2-fold enrichment over the background sample were considered for analysis. Proteomic screen was conducted in A549ΔS1PL S2-6 clone cells. MS analysis performed and data provided by S. Föhr (Krijgsveld lab).

Runs	**Nr. of pro-teins**	**Proteins**
		1 hpi
run1 & run2	6	Cleft lip and palate transmembrane protein 1 OS=Homo sapiens GN=CLPTM1 PE=1 SV=1
		Annexin A1 OS=Homo sapiens GN=ANXA1 PE=1 SV=2
		Moesin OS=Homo sapiens GN=MSN PE=1 SV=3
		Isoform 8 of Filamin-B OS=Homo sapiens GN=FLNB
		Retinal dehydrogenase 1 OS=Homo sapiens GN=ALDH1A1 PE=1 SV=2

		Actin, cytoplasmic 1 OS=Homo sapiens GN=ACTB PE=1 SV=1
run1	17	Secretory carrier-associated membrane protein 2 OS=Homo sapiens GN=SCAMP2 PE=1 SV=2
		Protein disulfide-isomerase A4 OS=Homo sapiens GN=PDIA4 PE=1 SV=2
		Protein disulfide-isomerase A3 OS=Homo sapiens GN=PDIA3 PE=1 SV=4
		Lysosome membrane protein 2 OS=Homo sapiens GN=SCARB2 PE=1 SV=2
		Heterogeneous nuclear ribonucleoproteins C1/C2 OS=Homo sapiens GN=HNRNPC PE=1 SV=4
		Isoform 2 of Minor histocompatibility antigen H13 OS=Homo sapiens GN=HM13
		Paraoxonase 2, isoform CRA_a OS=Homo sapiens GN=PON2 PE=1 SV=1
		Isoform 2 of Heterogeneous nuclear ribonucleoprotein K OS=Homo sapiens GN=HNRNPK
		Plectin OS=Homo sapiens GN=PLEC PE=1 SV=3
		Polypeptide N-acetylgalactosaminyltransferase 1 OS=Homo sapiens GN=GALNT1 PE=1 SV=1
		Surfeit locus protein 4 OS=Homo sapiens GN=SURF4 PE=1 SV=3
		Neuroplastin OS=Homo sapiens GN=NPTN PE=1 SV=2
		Endoplasmin OS=Homo sapiens GN=HSP90B1 PE=1 SV=1
		Isoform 2 of 40S ribosomal protein S3 OS=Homo sapiens GN=RPS3
		Vacuole membrane protein 1 OS=Homo sapiens GN=VMP1 PE=1 SV=1
		60 kDa heat shock protein, mitochondrial OS=Homo sapiens GN=HSPD1 PE=1 SV=2
		Isoform B of Membrane cofactor protein OS=Homo sapiens GN=CD46
run2	59	Leucine-rich repeat flightless-interacting protein 1 OS=Homo sapiens GN=LRRFIP1 PE=1 SV=2
		ADP/ATP translocase 2 OS=Homo sapiens GN=SLC25A5 PE=1 SV=7
		Apoptosis-inducing factor 1, mitochondrial OS=Homo sapiens GN=AIFM1 PE=1 SV=1
		Isoform HMG-Y of High mobility group protein HMG-I/HMG-Y OS=Homo sapiens GN=HMGA1
		Isoform 2 of Annexin A2 OS=Homo sapiens GN=ANXA2
		Probable ATP-dependent RNA helicase DDX17 OS=Homo sapiens GN=DDX17 PE=1 SV=1
		Isoform 2 of Membrane-associated progesterone receptor component 2 OS=Homo sapiens GN=PGRMC2
		Elongation of very long chain fatty acids protein 1 OS=Homo sapiens GN=ELOVL1 PE=1 SV=1
		Lamina-associated polypeptide 2, isoforms beta/gamma OS=Homo sapiens GN=TMPO PE=1 SV=2
		ATP synthase F(0) complex subunit B1, mitochondrial OS=Homo sapiens GN=ATP5F1 PE=1 SV=2
		Reticulocalbin-1 OS=Homo sapiens GN=RCN1 PE=1 SV=1
		Monocarboxylate transporter 1 OS=Homo sapiens GN=SLC16A1 PE=1 SV=3
		Emerin OS=Homo sapiens GN=EMD PE=1 SV=1
		Glucosidase 2 subunit beta OS=Homo sapiens GN=PRKCSH PE=1 SV=1

Histone H1.3 OS=Homo sapiens GN=HIST1H1D PE=1 SV=2
CD81 antigen OS=Homo sapiens GN=CD81 PE=1 SV=1
Kinesin-1 heavy chain OS=Homo sapiens GN=KIF5B PE=1 SV=1
Receptor expression-enhancing protein 5 OS=Homo sapiens GN=REEP5 PE=1 SV=3
SNW domain-containing protein 1 OS=Homo sapiens GN=SNW1 PE=1 SV=1
Ras GTPase-activating protein-binding protein 1 OS=Homo sapiens GN=G3BP1 PE=1 SV=1
CAAX prenyl protease 1 homolog OS=Homo sapiens GN=ZMPSTE24 PE=1 SV=2
Phosphatidylinositol transfer protein beta isoform OS=Homo sapiens GN=PITPNB PE=1 SV=1
Glutamate dehydrogenase 1, mitochondrial OS=Homo sapiens GN=GLUD1 PE=1 SV=2
Filamin-A OS=Homo sapiens GN=FLNA PE=1 SV=4
Thioredoxin-related transmembrane protein 4 OS=Homo sapiens GN=TMX4 PE=1 SV=1
Ezrin OS=Homo sapiens GN=EZR PE=1 SV=4
Isoform 1 of Voltage-dependent anion-selective channel protein 2 OS=Homo sapiens GN=VDAC2
Calnexin OS=Homo sapiens GN=CANX PE=1 SV=1
CD9 antigen (Fragment) OS=Homo sapiens GN=CD9 PE=1 SV=1
Syntaxin-4 OS=Homo sapiens GN=STX4 PE=1 SV=2
Ribosomal biogenesis protein LAS1L OS=Homo sapiens GN=LAS1L PE=1 SV=2
Tricarboxylate transport protein, mitochondrial OS=Homo sapiens GN=SLC25A1 PE=1 SV=2
RNA-binding protein FUS OS=Homo sapiens GN=FUS PE=1 SV=1
Transitional endoplasmic reticulum ATPase OS=Homo sapiens GN=VCP PE=1 SV=4
Band 4.1-like protein 2 OS=Homo sapiens GN=EPB41L2 PE=1 SV=1
Spectrin beta chain, non-erythrocytic 1 OS=Homo sapiens GN=SPTBN1 PE=1 SV=2
Vinculin OS=Homo sapiens GN=VCL PE=1 SV=4
X-ray repair cross-complementing protein 5 OS=Homo sapiens GN=XRCC5 PE=1 SV=3
Elongation factor 1-delta OS=Homo sapiens GN=EEF1D PE=1 SV=1
Voltage-dependent anion-selective channel protein 1 OS=Homo sapiens GN=VDAC1 PE=1 SV=2
Polypeptide N-acetylgalactosaminyltransferase 5 OS=Homo sapiens GN=GALNT5 PE=1 SV=1
U3 small nucleolar RNA-associated protein 18 homolog OS=Homo sapiens GN=UTP18 PE=1 SV=3
Protein jagunal homolog 1 OS=Homo sapiens GN=JAGN1 PE=1 SV=1
Phosphatidate cytidylyltransferase 2 OS=Homo sapiens GN=CDS2 PE=1 SV=1
Caldesmon OS=Homo sapiens GN=CALD1 PE=1 SV=3
Hydroxysteroid dehydrogenase-like protein 2 OS=Homo sapiens GN=HSDL2 PE=1 SV=1
Neurabin-2 OS=Homo sapiens GN=PPP1R9B PE=1 SV=2

		Synaptic vesicle membrane protein VAT-1 homolog OS=Homo sapiens GN=VAT1 PE=1 SV=2
		Translocating chain-associated membrane protein 1 OS=Homo sapiens GN=TRAM1 PE=1 SV=3
		Basigin OS=Homo sapiens GN=BSG PE=1 SV=2
		Signal recognition particle subunit SRP72 OS=Homo sapiens GN=SRP72 PE=1 SV=3
		Clathrin heavy chain 1 OS=Homo sapiens GN=CLTC PE=1 SV=5
		Sarcoplasmic/endoplasmic reticulum calcium ATPase 2 OS=Homo sapiens GN=ATP2A2 PE=1 SV=1
		Nuclease-sensitive element-binding protein 1 (Fragment) OS=Homo sapiens GN=YBX1 PE=1 SV=1
		WD repeat-containing protein 43 OS=Homo sapiens GN=WDR43 PE=1 SV=3
		NAD(P)H dehydrogenase [quinone] 1 OS=Homo sapiens GN=NQO1 PE=1 SV=1
		Isoform F of Constitutive coactivator of PPAR-gamma-like protein 1 OS=Homo sapiens GN=FAM120A
		Heat shock protein HSP 90-beta OS=Homo sapiens GN=HSP90AB1 PE=1 SV=4
		Elongation factor 1-alpha 1 OS=Homo sapiens GN=EEF1A1 PE=1 SV=1
		12 hpi
run1	18	Isoform 2 of Membrane-associated progesterone receptor component 2 OS=Homo sapiens GN=PGRMC2
		Tetraspanin-3 OS=Homo sapiens GN=TSPAN3 PE=2 SV=1
		Dolichyl-diphosphooligosaccharide--protein glycosyltransferase subunit STT3A OS=Homo sapiens GN=STT3A PE=1 SV=2
		Epithelial membrane protein 3 OS=Homo sapiens GN=EMP3 PE=2 SV=1
		Isoform 4 of Inhibitor of nuclear factor kappa-B kinase-interacting protein OS=Homo sapiens GN=IKBIP
		Non-POU domain-containing octamer-binding protein OS=Homo sapiens GN=NONO PE=1 SV=4
		Histone H2B OS=Homo sapiens GN=HIST2H2BF PE=1 SV=1
		Lysosome-associated membrane glycoprotein 1 OS=Homo sapiens GN=LAMP1 PE=1 SV=3
		Synaptogyrin OS=Homo sapiens GN=SYNGR2 PE=1 SV=1
		Very-long-chain (3R)-3-hydroxyacyl-[acyl-carrier protein] dehydratase 3 OS=Homo sapiens GN=PTPLAD1 PE=1 SV=1
		PRA1 family protein 3 OS=Homo sapiens GN=ARL6IP5 PE=1 SV=1
		Isoform 2 of Neutral alpha-glucosidase AB OS=Homo sapiens GN=GANAB
		Isoform LAMP-2C of Lysosome-associated membrane glycoprotein 2 OS=Homo sapiens GN=LAMP2
		Cystine/glutamate transporter OS=Homo sapiens GN=SLC7A11 PE=1 SV=1
		Transmembrane protein 97 OS=Homo sapiens GN=TMEM97 PE=1 SV=1
		Trans-Golgi network integral membrane protein 2 OS=Homo sapiens GN=TGOLN2 PE=1 SV=2
		Methylcrotonoyl-CoA carboxylase subunit alpha, mitochondrial OS=Homo sapiens GN=MCCC1 PE=1 SV=3
		Monocarboxylate transporter 4 OS=Homo sapiens GN=SLC16A3 PE=1 SV=1

run2	75	Protein disulfide-isomerase TMX3 OS=Homo sapiens GN=TMX3 PE=1 SV=2
		Prohibitin-2 OS=Homo sapiens GN=PHB2 PE=1 SV=1
		Zinc finger RNA-binding protein OS=Homo sapiens GN=ZFR PE=1 SV=2
		DNA topoisomerase 1 OS=Homo sapiens GN=TOP1 PE=1 SV=2
		Isoform 3 of Calumenin OS=Homo sapiens GN=CALU
		Heterogeneous nuclear ribonucleoprotein U OS=Homo sapiens GN=HNRNPU PE=1 SV=6
		Matrin-3 OS=Homo sapiens GN=MATR3 PE=1 SV=1
		Protein disulfide-isomerase A3 OS=Homo sapiens GN=PDIA3 PE=1 SV=4
		Splicing factor U2AF 65 kDa subunit OS=Homo sapiens GN=U2AF2 PE=1 SV=4
		Ras-related protein Rab-1B OS=Homo sapiens GN=RAB1B PE=1 SV=1
		Early endosome antigen 1 OS=Homo sapiens GN=EEA1 PE=1 SV=2
		Profilin-1 OS=Homo sapiens GN=PFN1 PE=1 SV=2
		RRP15-like protein OS=Homo sapiens GN=RRP15 PE=1 SV=2
		Isoform 2 of B-cell receptor-associated protein 29 OS=Homo sapiens GN=BCAP29
		Nodal modulator 3 OS=Homo sapiens GN=NOMO3 PE=2 SV=1
		Isoform 3 of Coronin-1C OS=Homo sapiens GN=CORO1C
		Leucine-rich PPR motif-containing protein, mitochondrial OS=Homo sapiens GN=LRPPRC PE=1 SV=3
		Anoctamin-10 OS=Homo sapiens GN=ANO10 PE=1 SV=2
		Thyroid hormone receptor-associated protein 3 OS=Homo sapiens GN=THRAP3 PE=1 SV=2
		Isoform 2 of Minor histocompatibility antigen H13 OS=Homo sapiens GN=HM13
		Serine/threonine-protein kinase TAO1 OS=Homo sapiens GN=TAOK1 PE=1 SV=1
		Splicing factor 3A subunit 1 OS=Homo sapiens GN=SF3A1 PE=1 SV=1
		Nucleolar protein 58 OS=Homo sapiens GN=NOP58 PE=1 SV=1
		Nucleoprotein TPR OS=Homo sapiens GN=TPR PE=1 SV=3
		Heterogeneous nuclear ribonucleoprotein M OS=Homo sapiens GN=HNRNPM PE=1 SV=3
		ATP-dependent RNA helicase A OS=Homo sapiens GN=DHX9 PE=1 SV=4
		PC4 and SFRS1-interacting protein OS=Homo sapiens GN=PSIP1 PE=1 SV=1
		Nuclear mitotic apparatus protein 1 OS=Homo sapiens GN=NUMA1 PE=1 SV=2
		Ribosome biogenesis protein BMS1 homolog OS=Homo sapiens GN=BMS1 PE=1 SV=1
		Prohibitin OS=Homo sapiens GN=PHB PE=1 SV=1
		60S ribosomal protein L35a OS=Homo sapiens GN=RPL35A PE=1 SV=2
		Nucleolar protein 7 OS=Homo sapiens GN=NOL7 PE=1 SV=2
		CKLF-like MARVEL transmembrane domain-containing protein 6 OS=Homo sapiens GN=CMTM6 PE=1 SV=1
		Histone H1x OS=Homo sapiens GN=H1FX PE=1 SV=1

LETM1 and EF-hand domain-containing protein 1, mitochondrial OS=Homo sapiens GN=LETM1 PE=1 SV=1
Protein transport protein Sec61 subunit beta OS=Homo sapiens GN=SEC61B PE=1 SV=2
Dihydrolipoyllysine-residue succinyltransferase component of 2-oxoglutarate dehydrogenase complex, mitochondrial OS=Homo sapiens GN=DLST PE=1 SV=4
Golgi integral membrane protein 4 OS=Homo sapiens GN=GOLIM4 PE=1 SV=1
Desmoplakin OS=Homo sapiens GN=DSP PE=1 SV=3
MKI67 FHA domain-interacting nucleolar phosphoprotein OS=Homo sapiens GN=NIFK PE=1 SV=1
Transmembrane and coiled-coil domain-containing protein 1 OS=Homo sapiens GN=TMCO1 PE=1 SV=1
39S ribosomal protein L47, mitochondrial OS=Homo sapiens GN=MRPL47 PE=1 SV=2
Splicing factor 3B subunit 1 OS=Homo sapiens GN=SF3B1 PE=1 SV=3
Isoform 5 of Splicing factor 1 OS=Homo sapiens GN=SF1
DNA-dependent protein kinase catalytic subunit OS=Homo sapiens GN=PRKDC PE=1 SV=3
Bcl-2-associated transcription factor 1 OS=Homo sapiens GN=BCLAF1 PE=1 SV=2
Probable ATP-dependent RNA helicase DDX27 OS=Homo sapiens GN=DDX27 PE=1 SV=2
ATP-dependent RNA helicase DDX3X OS=Homo sapiens GN=DDX3X PE=1 SV=3
Leucine zipper protein 1 OS=Homo sapiens GN=LUZP1 PE=1 SV=2
Isoform 4 of Putative ribosomal RNA methyltransferase NOP2 OS=Homo sapiens GN=NOP2
Nucleolar GTP-binding protein 1 OS=Homo sapiens GN=GTPBP4 PE=1 SV=3
Neuroplastin OS=Homo sapiens GN=NPTN PE=1 SV=2
Spectrin alpha chain, non-erythrocytic 1 OS=Homo sapiens GN=SPTAN1 PE=1 SV=2
Isoform 2 of Chromodomain-helicase-DNA-binding protein 4 OS=Homo sapiens GN=CHD4
Ribosome biogenesis protein BRX1 homolog OS=Homo sapiens GN=BRIX1 PE=1 SV=2
Glutaminase kidney isoform, mitochondrial OS=Homo sapiens GN=GLS PE=1 SV=1
Heme oxygenase 1 OS=Homo sapiens GN=HMOX1 PE=1 SV=1
60S ribosomal protein L13a (Fragment) OS=Homo sapiens GN=RPL13A PE=1 SV=2
Podocalyxin OS=Homo sapiens GN=PODXL PE=1 SV=1
Torsin-1A-interacting protein 2 OS=Homo sapiens GN=TOR1AIP2 PE=1 SV=1
CD97 antigen OS=Homo sapiens GN=CD97 PE=1 SV=4
Splicing factor 3B subunit 2 OS=Homo sapiens GN=SF3B2 PE=1 SV=2
CCAAT/enhancer-binding protein zeta OS=Homo sapiens GN=CEBPZ PE=1 SV=3
Heterogeneous nuclear ribonucleoprotein D-like OS=Homo sapiens GN=HNRNPDL PE=1 SV=3
Protein disulfide-isomerase OS=Homo sapiens GN=P4HB PE=1 SV=3

KH domain-containing, RNA-binding, signal transduction-associated protein 1 OS=Homo sapiens GN=KHDRBS1 PE=1 SV=1
Ribosome biogenesis protein NSA2 homolog OS=Homo sapiens GN=NSA2 PE=1 SV=1
Non-histone chromosomal protein HMG-17 OS=Homo sapiens GN=HMGN2 PE=1 SV=3
Pre-mRNA-processing-splicing factor 8 OS=Homo sapiens GN=PRPF8 PE=1 SV=2
Vacuole membrane protein 1 OS=Homo sapiens GN=VMP1 PE=1 SV=1
Isoform 2 of 39S ribosomal protein L30, mitochondrial OS=Homo sapiens GN=MRPL30
Isoform 4 of 4F2 cell-surface antigen heavy chain OS=Homo sapiens GN=SLC3A2
Isoform Beta of Nucleolar and coiled-body phosphoprotein 1 OS=Homo sapiens GN=NOLC1
Chloride channel CLIC-like protein 1 OS=Homo sapiens GN=CLCC1 PE=1 SV=1
Heterochromatin protein 1-binding protein 3 OS=Homo sapiens GN=HP1BP3 PE=1 SV=1

Table 7.5: Protein hitlist from the SILAC PR8 screen II (PR8-II)

Proteins with a 4-fold enrichment over the background ("medium" SILAC, infected, non-UV irradiated) in at least 2 out of 3 biological replicates are indicated with a "+" in each condition (mock or infected at 1 or 12 hpi). Proteomic screen was conducted in A549ΔS1PL S2-6 clone cells. H= "heavy"= infected condition, L= "light"= mock condition; hpi= hours post infection; R= replicate; U.p.= unique peptides. Red= likely contaminants; bold= protein hits validated for SL-interaction and in siRNA assays (see **section** Error! Reference source not found. and **3.2.5**). The total protein hits/condition are depicted at the table bottom (yellow). MS analysis performed and data provided by G. Sigismondo (Krijgsveld lab).

Protein	**Gene**	**Mock 1 hpi**	**Inf 1 hpi**	**Mock 12 hpi**	**Inf 12 hpi**	**Log2 H/L 1 hpi R1**	**Log2 H/L 1 hpi R2**	**Log2 H/L 1 hpi R3**	**Log2 H/L 12 hpi R1**	**Log2 H/L 12 hpi R2**	**Log2 H/L 12 hpi R3**	**U.p. 12 hpi R1**	**U.p. 12 hpi R2**	**U.p. 12 hpi R3**	**U.p. 1 hpi R1**	**U.p. 1 hpi R2**	**U.p. 1 hpi R3**
Fatty aldehyde dehydrogenase;Aldehyde dehydrogenase	ALDH3A2	+	+	+	+	0.27	0.12	-0.41	-0.10	-0.26	0.66	7	10	8	5	7	9
Aspartyl/asparaginyl beta-hydroxylase	ASPH	+		+	+	-0.38	NaN	-4.32	-0.39	-4.32	0.38	1	2	9	1	0	1
Sodium/potassium-transporting ATPase subunit alpha-1	ATP1A1	+		+	+	0.12	-0.55	-0.70	-1.05	-0.48	-0.75	9	6	18	4	5	12
Plasma membrane calcium-transporting ATPase 1	ATP2B1	+	+	+	+	0.05	-0.27	-0.46	-0.97	-0.53	-0.28	6	10	15	3	4	11
B-cell receptor-associated protein 31	BCAP31	+	+	+		0.09	0.18	-0.35	NaN	-4.32	0.39	0	2	13	1	2	6
BRI3-binding protein	BRI3BP	+	+	+	+	-0.28	NaN	5.64	NaN	NaN	0.34	0	1	5	2	1	1
Solute carrier family 35 member F6	SLC35F6	+	+	+	+	-0.16	-0.60	-0.65	-0.49	-1.02	-0.34	1	1	2	1	1	1
Caveolin;Caveolin-1	CAV1	+	+	+	+	-0.12	-0.64	-0.68	0.04	-0.79	0.34	1	1	2	2	2	2

Caveolin;Caveolin-1	CAV1	+	+	+	+	0.01	-0.40	-0.58	0.13	-0.80	0.26	1	3	5	2	3	3
Coiled-coil domain-containing protein 47	CCDC47	+			+	-0.38	-4.32	NaN	5.64	5.64	0.45	1	1	2	2	1	0
Calicin	CCIN	+		+		-1.96	-5.19	-4.91	-4.36	-5.30	NaN	1	1	0	1	1	1
CD151 antigen	CD151	+	+	+		0.40	-0.27	-0.37	-0.32	-4.32	-0.89	2	1	2	1	3	3
CD44 antigen	CD44	+	+	+	+	0.57	-0.20	-0.30	0.24	-0.05	-0.30	3	4	5	1	2	4
Membrane cofactor protein	CD46	+		+	+	NaN	-4.32	-0.27	-4.32	NaN	0.08	2	2	2	1	1	1
CD63 antigen	CD63	+	+	+		0.24	-0.52	NaN	-0.01	-0.72	NaN	1	1	0	1	1	0
CD9 antigen	CD9, BTCC-1	+			+	NaN	NaN	-4.32	5.64	NaN	0.11	2	2	2	0	2	1
CD97 antigen;CD97 antigen subunit alpha;CD97 antigen subunit beta	CD97	+	+	+	+	0.32	NaN	-0.27	NaN	NaN	-0.64	1	1	1	2	1	1
Cytoskeleton-associated protein 4	CKAP4	+	+	+	+	-0.07	0.21	-0.07	0.00	-0.09	1.37	6	9	20	3	5	5
Cleft lip and palate transmembrane protein 1	CLPTM1	+	+	+	+	-1.47	0.50	-0.42	0.04	0.15	0.00	1	1	6	5	2	4
	CSF2RB	+		+		NaN	-9.63	-9.73	-9.68	NaN	-4.32	1	0	1	0	1	1
Cathepsin D;Cathepsin D light chain;Cathepsin D heavy chain	CTSD	+	+	+	+	-0.26	-0.40	0.19	0.74	-0.25	2.22	5	7	6	3	2	2
Desmoglein-1	*DSG1*	+		+		*NaN*	*-3.38*	*-2.22*	*-3.01*	*-0.91*	*NaN*	*1*	*1*	*0*	*0*	*5*	*1*
Desmoplakin	*DSP, DSP variant protein*	+				*-4.72*	*-3.13*	*-3.19*	*NaN*	*-3.01*	*NaN*	*1*	*3*	*0*	*5*	*7*	*2*
Emerin	EMD	+		+	+	-4.32	NaN	-4.32	NaN	-0.14	-0.02	0	1	1	1	0	1
Epoxide hydrolase 1	EPHX1	+	+	+	+	0.42	0.20	0.27	1.03	0.01	1.71	5	9	10	3	4	3

G-protein coupled receptor 56;GPR56 N-terminal fragment;GPR56 C-terminal fragment	GPR56	+				NaN	NaN	-4.32	-4.32	NaN	NaN	1	0	0	1	0	1
Retinoic acid-induced protein 3	GPRC5A	+	+	+	+	-0.04	-0.15	-0.39	-1.05	-0.41	-1.22	1	1	2	1	1	1
Basigin	hEMMPRIN, BSG	+	+	+	+	*0.31*	*-0.23*	*-0.35*	*-0.38*	*-0.44*	*-0.11*	*3*	*6*	*8*	*3*	*2*	*7*
Integrin alpha-3;Integrin alpha-3 heavy chain;Integrin alpha-3 light chain	ITGA3	+	+	+	+	0.41	-4.32	-0.35	-0.36	-0.35	-0.29	4	4	6	2	2	5
Junction plakoglobin	*JUP*	+		+		*-3.71*	*-4.32*	*-4.32*	*NaN*	*-4.32*	*-1.76*	*0*	*1*	*2*	*2*	*1*	*1*
Keratinocyte proline-rich protein	*KPRP*	+		+		*-3.66*	*NaN*	*NaN*	*-4.32*	*-4.32*	*NaN*	*2*	*2*	*0*	*2*	*2*	*0*
Keratin, type I cytoskeletal 18	*KRT18*	+	+	+	+	*-0.12*	*0.08*	*0.12*	*0.44*	*0.20*	*2.08*	*9*	*13*	*20*	*9*	*7*	*11*
Kinectin	KTN1	+		+	+	-0.42	-4.32	-0.96	-0.75	-0.20	0.08	2	2	5	2	1	1
Lysosome-associated membrane glycoprotein 2	LAMP2	+				-4.32	-4.32	NaN	NaN	NaN	NaN	1	1	0	1	1	0
Leucine-rich repeat-containing protein 59	LRRC59	+	+	+	+	-0.23	0.08	-0.48	-0.36	-0.17	0.05	2	3	3	3	1	2
Protein LYRIC	MTDH	+	+	+	+	-0.27	0.20	-0.68	-0.74	0.03	-0.26	3	2	6	3	2	4
Myeloid-associated differentiation marker	MYADM	+	+	+	+	0.53	-0.17	-0.43	-1.04	-0.34	-0.62	3	3	1	2	3	3
Membrane-associated progesterone receptor component 2	PGRMC2	+		+	+	-0.44	-4.32	NaN	-0.25	-0.28	0.14	2	1	2	2	1	0
Plakophilin-1	PKP1	+	+			1.49	4.01	-4.32	2.71	NaN	NaN	3	2	0	1	3	2

Serum paraoxonase/arylesterase 2	PON2	+	+	+	+	0.05	0.06	-0.40	0.13	-0.42	0.26	2	4	3	3	4	2
Serum paraoxonase/lactonase 3	PON3	+	+	+	+	NaN	-0.01	0.04	0.49	-4.32	1.00	1	1	3	0	1	1
NADPH--cytochrome P450 reductase	POR	+	+	+	+	-0.18	-0.05	-0.38	0.18	-0.35	0.34	3	2	12	2	2	3
Lipid phosphate phosphohydrolase 3	PPAP2B	+				NaN	-4.32	-4.32	NaN	NaN	-4.32	0	0	2	0	1	1
Presenilin-2;Presenilin-2 NTF subunit;Presenilin-2 CTF subunit	PSEN2	+	+	+	+	NaN	-0.37	-0.30	-4.32	-0.82	0.09	2	1	1	0	2	2
Very-long-chain (3R)-3-hydroxyacyl-[acyl-carrier protein] dehydratase 3	PTPLAD1	+	+	+	+	NaN	-0.30	-0.64	NaN	-0.60	-0.08	0	2	5	0	1	1
Reticulon-3	RTN3	+		+		NaN	0.06	-0.61	-0.87	-0.66	-0.23	1	1	1	0	1	1
Reticulon-4	RTN4	+	+	+	+	5.64	-0.16	-0.88	-0.72	-0.26	-0.92	1	2	4	2	2	2
Suprabasin	SBSN	+				-4.32	NaN	-4.32	NaN	NaN	NaN	0	0	0	1	1	1
Secretory carrier-associated membrane protein 2	SCAMP2	+	+	+	+	0.24	-0.18	-0.30	-0.23	-0.40	0.15	3	3	3	2	3	3
Signal peptidase complex catalytic subunit SEC11A	SEC11A, SPC18	+		+	+	-0.17	-4.32	-4.32	-0.02	NaN	NaN	2	3	1	1	2	1
Solute carrier family 12 member 2	SLC12A2	+	+	+	+	1.16	0.15	0.06	1.72	0.93	0.10	7	8	13	2	4	8
Monocarboxylate transporter 1	SLC16A1	+	+	+	+	-0.11	-0.42	-0.67	-1.38	-0.59	-1.13	3	5	7	2	2	5
Monocarboxylate transporter 4	SLC16A3	+	+	+	+	NaN	-0.54	-0.24	-1.01	5.64	-0.61	1	2	3	1	2	3

Neutral amino acid transporter B(0)	**SLC1A5**	**+**	**+**	**+**	**+**	**0.55**	**-0.40**	**-0.53**	**-1.10**	**-0.90**	**-1.64**	**1**	**1**	**2**	**1**	**1**	**2**
Phosphate carrier protein, mitochondrial	SLC25A3	+			+	0.08	-0.53	-0.44	0.03	-0.63	0.65	1	2	1	1	2	2
ADP/ATP translocase 2;ADP/ATP translocase 2, N-terminally processed	SLC25A5	+	+	+	+	NaN	-0.41	-0.30	0.29	0.00	1.60	1	3	3	0	1	2
Sulfate transporter	SLC26A2	+	+	+		-0.45	-1.03	-0.96	NaN	-1.21	-1.12	0	1	3	1	1	2
Solute carrier family 2, facilitated glucose transporter member 1	SLC2A1	+	+	+	+	1.54	-0.15	-0.36	-0.87	-0.29	-0.75	3	4	5	3	2	6
Adenosine 3-phospho 5-phosphosulfate transporter 1	SLC35B2	+	+	+	+	NaN	-0.42	-0.35	NaN	-0.59	0.10	0	2	3	1	2	2
4F2 cell-surface antigen heavy chain	SLC3A2	+	+	+	+	-0.38	-0.42	-0.71	-1.25	-0.37	-0.66	3	4	12	2	3	10
Sodium- and chloride-dependent taurine transporter;Transporter	SLC6A6	+	+	+	+	NaN	NaN	-0.83	-1.32	NaN	-0.58	1	0	1	1	0	2
Large neutral amino acids transporter small subunit 1	SLC7A5	+	+	+	+	0.01	-0.76	-0.80	-1.52	-0.84	-1.17	4	5	6	5	6	6
Protein spinster homolog 1	SPNS1	+	+	+	+	-0.55	-0.76	-0.82	-4.32	NaN	-0.33	1	1	2	1	1	1
Signal recognition particle receptor subunit beta	SRPRB	+	+	+	+	-0.07	0.07	-0.46	-0.25	-0.43	0.26	2	4	9	2	3	4
MLN64 N-terminal domain homolog	STARD3NL	+	+	+	+	NaN	-0.39	-0.39	-0.51	-1.11	0.25	2	2	3	0	1	2
Syntaxin-4	STX4, STX4A	+		+	+	NaN	-0.61	-4.32	NaN	-0.62	-0.20	1	3	4	1	2	1
Surfeit locus protein 4	SURF4	+	+		+	NaN	-0.11	-0.66	-0.48	-0.18	0.98	1	1	2	0	1	1

Transducin beta-like protein 2	TBL2	+	+	+	+	0.29	NaN	-0.83	-0.05	-0.19	0.38	2	4	4	2	1	4
Transferrin receptor protein 1;Transferrin receptor protein 1, serum form	TFRC	+	+	+	+	NaN	NaN	-1.06	-2.16	-0.07	-1.04	3	2	7	1	0	3
Trans-Golgi network integral membrane protein 2	TGOLN2	+	+	+	+	NaN	NaN	-0.36	NaN	5.64	-0.24	2	1	13	2	1	1
Transmembrane protein 106B	TMEM106B	+	+			NaN	NaN	NaN	NaN	-1.39	NaN	0	2	1	1	1	1
Transmembrane protein 199	TMEM199	+	+	+	+	NaN	0.15	-0.32	NaN	-0.16	0.23	1	1	1	0	2	1
Translocating chain-associated membrane protein 1	TRAM1	+	+	+	+	-0.29	-0.37	-0.58	-0.30	NaN	0.13	1	0	1	1	1	1
Tetraspanin-3	TSPAN3	+				NaN	-0.60	-0.45	NaN	NaN	-0.24	0	1	1	0	1	1
Ubiquitin-60S ribosomal protein L40;Ubiquitin;60S ribosomal protein L40;Ubiquitin-40S ribosomal protein S27a;Ubiquitin;40S ribosomal protein S27a;Polyubiquitin-B;Ubiquitin;Polyubiquitin-C;Ubiquitin	UBB, RPS27A, UBC, UBA52, UbC, UBBP4	+		+		-0.16	-0.73	-1.07	-0.77	-1.07	-1.25	2	6	9	2	1	4
Vesicle-associated membrane protein 8	VAMP8	+				NaN	-4.32	-1.08	NaN	NaN	-1.27	0	0	1	0	1	1
Vang-like protein 1	VANGL1	+	+			NaN	-4.32	5.64	NaN	NaN	-0.41	0	0	1	1	1	1
Voltage-dependent anion-selective channel protein 1	VDAC1	+	+	+	+	-0.14	0.09	-0.32	-0.01	-0.44	0.67	5	8	17	6	5	6

Voltage-dependent anion-selective channel protein 2	VDAC2	+	+	+	+	*-0.10*	*0.09*	*-0.13*	*0.19*	*-0.41*	*0.76*	*5*	*5*	*11*	*3*	*4*	*5*
Skin-specific protein 32	XP32	+				-2.81	-2.37	-1.03	NaN	NaN	NaN	1	1	0	1	1	1
		+		+		NaN	-4.32	-4.32	-4.32	-4.32	NaN	1	1	0	0	1	1
Disintegrin and metalloproteinase domain-containing protein 10	ADAM10			+	+	NaN	NaN	-0.98	NaN	-1.02	-1.62	0	1	2	0	0	1
Type-1 angiotensin II receptor-associated protein	AGTRAP			+		NaN	NaN	-0.78	NaN	-1.47	-1.12	0	1	1	0	0	1
Apolipoprotein L2	APOL2				+	NaN	NaN	-0.70	5.64	-0.23	0.25	1	1	2	0	0	1
Platelet receptor Gi24	C10orf54			+		NaN	NaN	-4.32	-4.32	-0.32	NaN	1	1	0	0	0	1
CD99 antigen-like protein 2	CD99L2			+		NaN	NaN	-0.47	-4.32	NaN	0.26	2	1	1	1	2	1
Ceramide synthase 2	CERS2		+	+	+	3.20	NaN	-0.22	-0.07	-0.25	0.08	2	2	3	1	0	2
Battenin	CLN3			+		NaN	NaN	NaN	NaN	-1.43	-0.46	0	0	1	0	0	0
Cleft lip and palate transmembrane protein 1-like protein	CLPTM1L			+	+	NaN	NaN	5.64	NaN	-0.22	0.61	0	1	3	0	0	1
CKLF-like MARVEL transmembrane domain-containing protein 4	CMTM4			+	+	NaN	NaN	5.64	5.64	-0.52	0.47	1	1	2	0	0	1
CKLF-like MARVEL transmembrane domain-containing protein 6	CMTM6			+	+	NaN	-0.89	0.15	-0.57	NaN	-0.57	1	1	2	1	1	1

Carnitine O-palmitoyltransferase 1, liver isoform	CPT1A	+	+	NaN	NaN	NaN	NaN	NaN	0.56	1	1	1	0	1	2
	DLG2		+	NaN	NaN	NaN	7.50	5.64	NaN	1	1	0	0	0	0
DnaJ homolog subfamily C member 1	DNAJC1	+	+	NaN	NaN	5.64	-4.32	-0.84	-0.29	1	2	6	0	0	2
Delta(3,5)-Delta(2,4)-dienoyl-CoA isomerase, mitochondrial	ECH1	+	+	-0.43	NaN	NaN	0.39	0.06	1.95	1	2	4	1	0	1
Feline leukemia virus subgroup C receptor-related protein 1	FLVCR1	+		NaN	NaN	-4.32	NaN	-0.98	-0.84	0	1	2	0	0	1
G-protein coupled receptor 126	GPR126	+		NaN	NaN	NaN	-4.32	NaN	NaN	1	0	2	0	0	0
78 kDa glucose-regulated protein	HSPA5	+	+	NaN	NaN	-0.19	-0.55	-0.32	1.57	1	3	9	0	0	1
Integrin beta-1;Integrin beta	**ITGB1**	**+**		**NaN**	**NaN**	**-4.32**	**-4.32**	**NaN**	**-0.67**	**1**	**0**	**5**	**0**	**0**	**1**
ER lumen protein retaining receptor 1;ER lumen protein retaining receptor 2;ER lumen protein retaining receptor	KDELR1, KDELR2		+	NaN	-0.02	-0.23	0.29	-0.28	5.64	1	2	1	0	1	2
Lysosome-associated membrane glycoprotein 1	LAMP1	+		NaN	NaN	NaN	NaN	-1.43	0.03	0	1	2	0	0	0
Major facilitator superfamily domain-containing protein 6	MFSD6	+		NaN	NaN	NaN	NaN	-4.32	-0.23	0	1	1	0	0	1
Major facilitator superfamily domain-containing protein 8	MFSD8	+		NaN	-1.36	NaN	NaN	-4.32	-0.33	0	1	1	0	1	0

Mannose-P-dolichol utilization defect 1 protein	MPDU1, HBEBP2BPA	+	+	NaN	NaN	-0.35	NaN	0.92	0.10	0	1	1	0	1	1
	NCAM2		+	-0.11	NaN	0.09	NaN	0.31	1.43	0	1	1	1	0	1
ORM1-like protein 1;ORM1-like protein 2	ORMDL1, ORMDL2	+		NaN	NaN	-0.41	NaN	-4.32	-0.46	0	1	1	0	0	1
Prenylcysteine oxidase 1	**PCYOX1**	**+**		**NaN**	**NaN**	**NaN**	**NaN**	**-4.32**	**0.96**	**0**	**1**	**1**	**0**	**0**	**0**
Piezo-type mechanosensitive ion channel component 1	PIEZO1	+	+	NaN	NaN	-0.82	NaN	-0.42	0.03	0	1	1	0	0	1
PRA1 family protein 2	PRAF2	+	+	NaN	NaN	-0.51	NaN	-0.43	0.15	1	1	2	0	0	1
Phosphatidylserine synthase 2	PTDSS2	+	+	NaN	NaN	-4.32	NaN	NaN	-0.29	1	0	2	0	1	2
Ras-related protein Rab-10	RAB10	+	+	NaN	NaN	-0.47	NaN	-0.46	0.33	0	1	2	0	0	1
Ras-related protein Rab-11A;Ras-related protein Rab-11B	**RAB11A, RAB11B**		**+**	**NaN**	**NaN**	**NaN**	**NaN**	**-0.43**	**1.14**	**0**	**1**	**5**	**0**	**0**	**0**
Lysosome membrane protein 2	SCARB2	+	+	NaN	NaN	-0.67	NaN	-0.96	0.34	0	1	4	0	1	1
Saccharopine dehydrogenase-like oxidoreductase	SCCPDH	+	+	NaN	NaN	-0.48	0.05	-0.59	0.90	2	1	4	0	0	1
Mitochondrial 2-oxoglutarate/malate carrier protein	SLC25A11	+		***NaN***	***-0.44***	***-0.11***	***-4.32***	***-0.38***	***1.11***	***1***	***1***	***1***	***1***	***1***	***1***
ADP/ATP translocase 3	SLC25A6		+	*NaN*	*NaN*	*-0.50*	*-0.14*	*NaN*	*1.45*	*1*	*0*	*1*	*0*	*0*	*1*
Sodium-coupled neutral amino acid transporter 2	SLC38A2	+	+	NaN	NaN	-0.48	NaN	-0.72	0.25	0	2	3	0	0	1

Proton-coupled folate transporter	**SLC46A1**	**+**		**+**	**5.64**	**NaN**	**-0.97**	**NaN**	**5.64**	**-0.96**	**0**	**1**	**1**	**1**	**0**	**1**
Multidrug and toxin extrusion protein 1	SLC47A1		+		NaN	-0.74	-0.59	NaN	-4.32	-0.22	0	1	2	0	1	2
Anion exchange protein 2	SLC4A2		+	+	NaN	NaN	-1.60	-1.32	-0.69	-0.28	1	2	3	0	1	1
Solute carrier family 52, riboflavin transporter, member 2	SLC52A2, GPCR		+		NaN	-0.40	-0.58	NaN	-0.66	NaN	1	1	1	0	1	1
Y+L amino acid transporter 2	SLC7A6		+		NaN	-1.03	-1.24	-1.60	NaN	-1.06	2	0	1	0	1	1
Serine palmitoyltransferase 1	SPTLC1		+	+	NaN	-0.83	-0.43	-0.71	-0.60	0.20	1	2	6	0	1	3
Stimulated by retinoic acid gene 6 protein homolog	STRA6	+	+	+	0.73	0.02	-0.24	0.38	-0.21	0.56	3	3	4	2	4	3
Transmembrane 9 superfamily member 3	TM9SF3, SMBP			+	NaN	NaN	NaN	0.10	5.64	5.64	1	1	1	0	0	1
Transmembrane protein 41B	TMEM41B	+		+	NaN	5.64	-0.62	NaN	5.64	0.18	0	1	1	0	1	1
Transmembrane protein 97	TMEM97		+	+	-0.12	NaN	NaN	NaN	-0.52	0.10	0	2	1	1	0	0
Thioredoxin-related transmembrane protein 1	TMX1, TXNDC		+		-0.25	NaN	NaN	NaN	-0.52	0.49	0	1	3	1	1	0
Thioredoxin-related transmembrane protein 2	TMX2		+	+	NaN	NaN	NaN	NaN	NaN	-0.03	1	1	1	0	0	1
Endoplasmin	TRA1, HSP90B1		+	+	-0.13	NaN	NaN	NaN	-0.03	1.66	0	1	5	1	0	0
Ceramide glucosyltransferase	UGCG			+	NaN	NaN	NaN	NaN	-0.26	5.64	0	1	1	0	0	0
Uroplakin-1b	UPK1B		+	+	NaN	NaN	NaN	NaN	-0.81	-0.61	1	1	1	0	0	0

Vimentin	VIM			+	+	*-0.74*	*-0.46*	*-0.37*	*-0.52*	*-0.35*	*1.37*	*7*	*13*	*24*	*9*	*8*	*7*
Vacuole membrane protein 1	VMP1, TMEM49			+		NaN	NaN	NaN	-4.32	NaN	NaN	1	1	2	0	0	1
Total protein hits/condition		72	57	104	92												

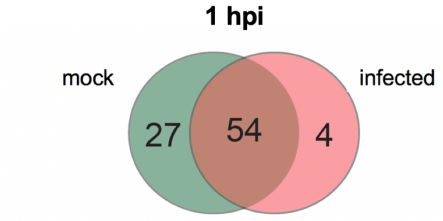

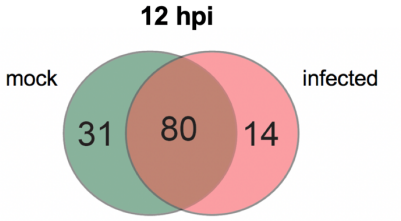

Protein IDs	Protein names	Gene names
H0YNG3	Signal peptidase complex catalytic subunit SEC11A	SEC11A;SPC18
O15173	Membrane-associated progesterone receptor component 2	PGRMC2
P05023-4	Sodium/potassium-transporting ATPase subunit alpha-1	ATP1A1
Q12797	Aspartyl/asparaginyl beta-hydroxylase	ASPH
Q12846	Syntaxin-4	STX4;STX4A
Q5HY57	Emerin	EMD
Q86UP2-2	Kinectin	KTN1
R4GN18	Membrane cofactor protein	CD46
J3QS39	Ubiquitin-60S ribosomal protein L40	UBB;RPS27A
L0R5A1		CSF2RB
P14923	Junction plakoglobin	JUP
Q02413	Desmoglein-1	DSG1
Q08499-7		
Q5T749	Keratinocyte proline-rich protein	KPRP
Q7RTN4	Reticulon-3	RTN3
Q8WX35	Calicin	CCIN
B4DPP0	CD9 antigen	CD9;BTCC-1
F8VVM2	Phosphate carrier protein, mitochondrial	SLC25A3
Q96A33	Coiled-coil domain-containing protein 47	CCDC47
B4DM06	G-protein coupled receptor 56	GPR56
B7Z2R9	Lysosome-associated membrane glycoprotein 2	LAMP2
B8ZZT4	Vesicle-associated membrane protein 8	VAMP8
H0YKJ9	Tetraspanin-3	TSPAN3
O14495	Lipid phosphate phosphohydrolase 3	PPAP2B
P15924	Desmoplakin	DSP;DSP variant protein
Q5T750	Skin-specific protein 32	XP32
Q6UWP8	Suprabasin	SBSN

Protein IDs	Protein names	Gene names
B3KR81	Stimulated by retinoic acid gene 6 protein homolog	STRA6
Q5SZE2	Ceramide synthase 2	CERS2
B4DJ17	Proton-coupled folate transporter	SLC46A1
Q5BJD5-3	Transmembrane protein 41B	TMEM41B

Protein IDs	Protein names	Gene names
E9PMR4	CD151 antigen	CD151
F8VNT9	CD63 antigen	CD63
P50443	Sulfate transporter	SLC26A2
Q53HT6	B-cell receptor-associated protein 31	BCAP31
J3QS39	Ubiquitin-60S ribosomal protein L40	UBB;RPS27A
L0R5A1		CSF2RB
P14923	Junction plakoglobin	JUP
Q02413	Desmoglein-1	DSG1
Q08499-7		
Q5T749	Keratinocyte proline-rich protein	KPRP
Q7RTN4	Reticulon-3	RTN3
Q8WX35	Calicin	CCIN
B3KRY3	Lysosome-associated membrane glycoprotein 1	LAMP1
B4DSK4	G-protein coupled receptor 126	GPR126
E9PKE4	Solute carrier family 52, riboflavin transporter, member 2	SLC52A2;GPCR
F6WST4	ORM1-like protein 1;ORM1-like protein 2	ORMDL1;ORMDL2
F8W8W4	Prenylcysteine oxidase 1	PCYOX1
H7C284	Major facilitator superfamily domain-containing protein 6	MFSD6
O95090	Battenin	CLN3
P05556	Integrin beta-1;Integrin beta	ITGB1
Q02978-2	Mitochondrial 2-oxoglutarate/malate carrier protein	SLC25A11
Q59E53		
Q6RW13	Type-1 angiotensin II receptor-associated protein	AGTRAP
Q8NHS3	Major facilitator superfamily domain-containing protein 8	MFSD8
Q8TCZ2-6	CD99 antigen-like protein 2	CD99L2
Q92536	Y+L amino acid transporter 2	SLC7A6;DKFZp686K14185
Q96FL8	Multidrug and toxin extrusion protein 1	SLC47A1
Q96GC9	Vacuole membrane protein 1	VMP1;TMEM49
Q9H3N1	Thioredoxin-related transmembrane protein 1	TMX1;TXNDC
Q9Y5Y0	Feline leukemia virus subgroup C receptor-related protein 1	FLVCR1
R4GNB4	Platelet receptor Gi24	C10orf54

Protein IDs	Protein names	Gene names
O15260-2	Surfeit locus protein 4	SURF4
B4DPP0	CD9 antigen	CD9;BTCC-1
F8VVM2	Phosphate carrier protein, mitochondrial	SLC25A3
Q96A33	Coiled-coil domain-containing protein 47	CCDC47
B4DJ17	Proton-coupled folate transporter	SLC46A1
Q5BJD5-3	Transmembrane protein 41B	TMEM41B
L0R512		NCAM2
L8E8R0		DLG2
P24390-2	ER lumen protein retaining receptor 1	KDELR1;KDELR2
P62491-2	Ras-related protein Rab-11A;Ras-related protein Rab-11B	RAB11A;RAB11B
Q16739	Ceramide glucosyltransferase	UGCG
Q5TB53	Transmembrane 9 superfamily member 3	TM9SF3;SMBP
Q6I9V5	ADP/ATP translocase 3	SLC25A6
Q9BQE5	Apolipoprotein L2	APOL2

Figure 7.8: Proteins unique to the infected or mock condition at 1 or 12 hpi (SILAC PR8 screen II)

"Valid" protein candidates (4-fold enriched over the background in at least two biological replicates) of the mock and infected condition were aligned separately for the 1 and 12 hpi condition. Proteins unique to mock condition are shown in green, those unique to the infected condition in red. Venn diagrams and tables produced by G. Sigismondo (Krijgsveld lab).

Table 7.6: List of unique, putative SL-binding proteins identified in only the mock or infected cells (SILAC PR8 screen II).

Non-infected		**Infected**	
Gene name	**Protein name**	**Gene name**	**Protein name**
WHSC1L1	Histone-lysine N-methyltransferase NSD3	GRAMD1C	GRAM domain-containing protein 1C
ANO6	Anoctamin-6, Anoctamin	TMEM194A	Transmembrane protein 194A
PPAP2B	Lipid phosphate phosphohydrolase 3	CD47	Leukocyte surface antigen CD47
EEF1D	Elongation factor 1-delta	FAM162A	Protein FAM162A
TRGC1, TRGC2	T-cell receptor gamma chain C region 1, T-cell receptor gamma-2 chain C region	NUP210	Nuclear pore membrane glycoprotein 210
NRP1	Neuropilin-1	CLDND1	Claudin domain-containing protein 1
FAM8A1	Protein FAM8A1	TOMM22, MST065	Mitochondrial import receptor subunit TOM22 homolog
LAMP2	Lysosome-associated membrane glycoprotein 2	GOLIM4	Golgi integral membrane protein 4
STX18	Syntaxin-18		
SGMS1, TMEM23	Phosphatidylcholine: ceramide cholinephosphotransferase 1		
CYB5A	Cytochrome b5		
TMEM245	Transmembrane protein 245		
POF1B	Protein POF1B		
PCDH9	Protocadherin-9		
MARCH6	E3 ubiquitin-protein ligase MARCH6		
SBSN	Suprabasin		
SLC25A10	Mitochondrial dicarboxylate carrier		
CLCC1	Chloride channel CLIC-like protein 1		
RNF5	E3 ubiquitin-protein ligase RNF5		
SDK2	Protein sidekick-2		
SLC35D2	UDP-N-acetylglucosamine/UDP-glucose/GDP-mannose transporter		

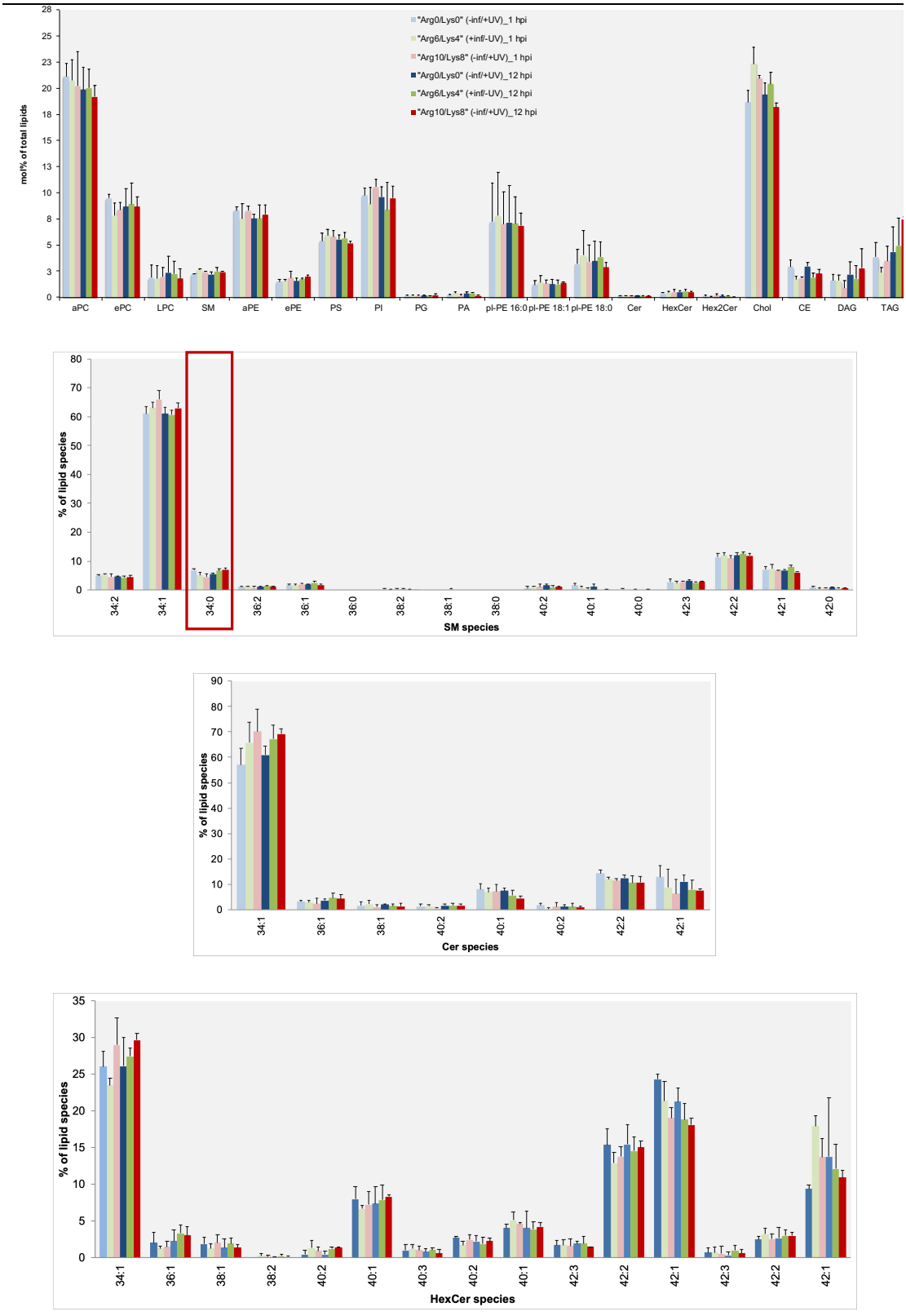

Figure 7.9: Lipidome analysis of samples from the SILAC PR8 screen II.

Approximately 10% of the collected cells from the proteomic screen were subjected to lipidomic analysis. The species profiles of sphingomyelin (SM), ceramide (Cer) and hexosylceramide (HexCer) are shown separately. The first number indicates the total amount number of C-atoms, including the C18 sphingoid backbone; the second indicates the number of double bonds. Red frame= SM(d18:0/16:0) or dihydrosphingomyelin (DHSM) C16. a= even, e= ether, pl= plasmalogen. Shown: mean, ±SD; n=3.

- Metabolic labelling of cells with paclipids

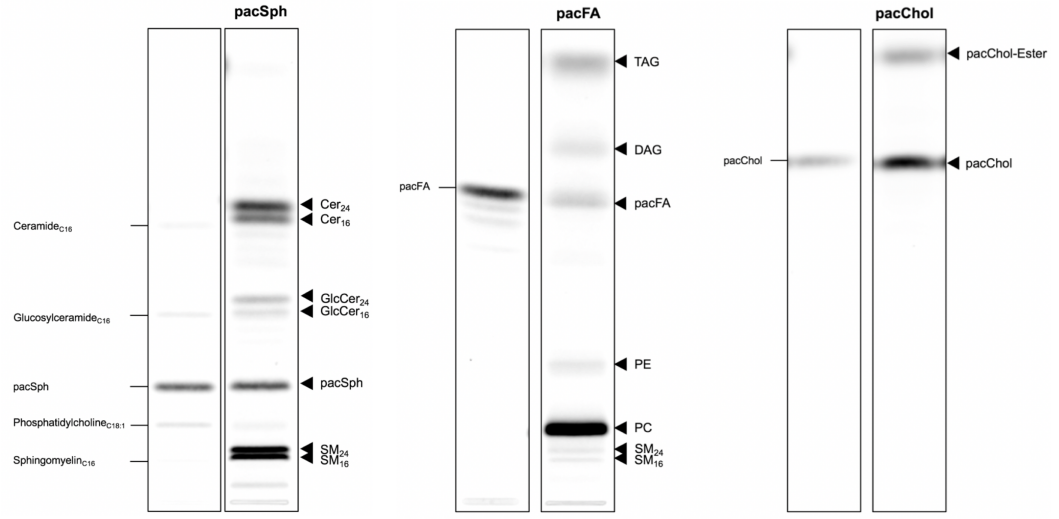

Figure 7.10: TLC analysis of paclipid metabolisation.

The incorporation of paclipids after 6 hours labelling with either pacSph (3 µM) or pacFA (40 µM) was investigated in A549ΔS1PL cells (S3-10 clone) via coumarin-CLICK and subsequent TLC analysis. Although pacFA is also a substrate for serine palmitoyl transferase[293], only a very low amount is incorporated into SM (middle panel). The major pacFA-incorporated glycerolipid class is PC, which is the bulk lipid of mammalian cells, and to lesser extent PE, DAG and TAG[293]. Cells were only fed for 30 min with pacChol (6 µM) because the molecule is cleaved at the ester bond by intracellular esterases and thus would separate the synthetic cholesterol molecule from the clickable alkyne group[249].

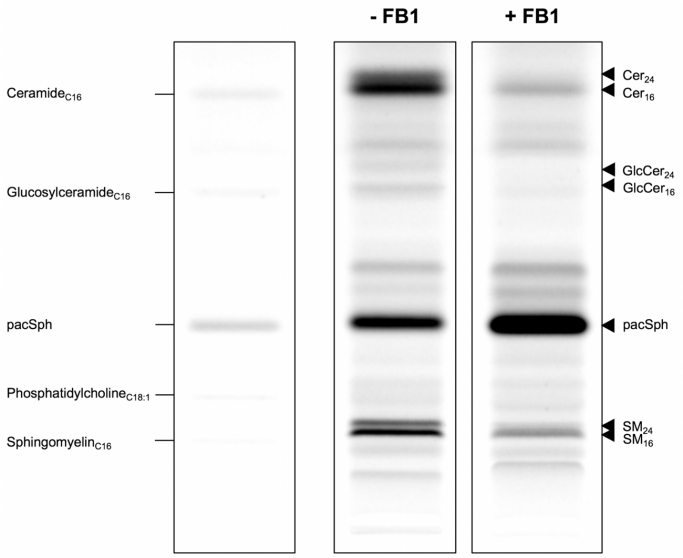

Figure 7.11: FB1-treatment of A549ΔS1PL cells (S3-10 clone).

A549ΔS1PL cells were labelled with 3 µM pacSph for 6 h in presence or absence of the Sph-analogue FB1 (1 day pre-treatment, 100 µM) and subjected to coumarin-CLICK followed by TLC analysis. Treatment with the inhibitor leads to an increase of free pacSph due to competitive inhibition of CerS[311] and a concomitant decrease in pac-incorporated SL species. As a result, incorporation of pacSph into complex SLs and ceramide is reduced.

- IFITM3 expression in S1PL-deficient A549 cells

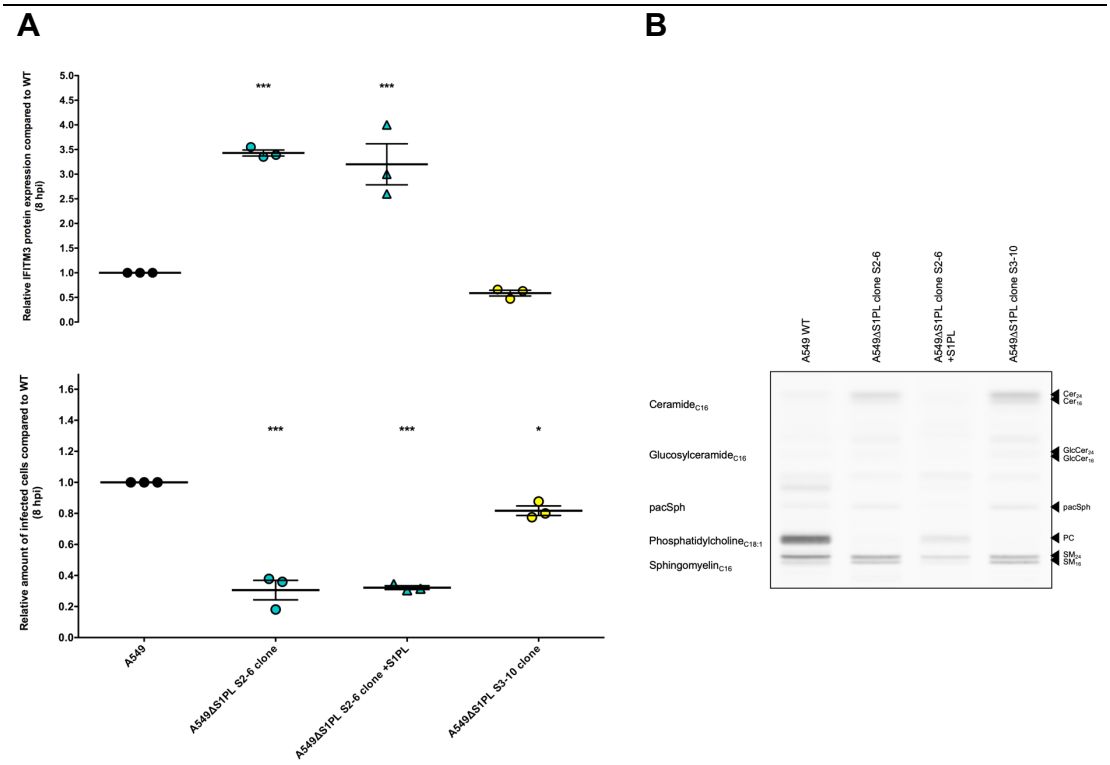

Figure 7.12: IFITM3 expression is increased in A549ΔS1PL S2-6 clone cells independent of the SGPL1 KO.

(A) Basal IFITM3 protein expression levels (35 µg of membrane fraction loaded, normalized to CXN) were determined in *SGPL1* KOs (clone S2-6 and S3-10) relative to the A549 WT (upper panel). A549ΔS1PL S2-6 clone cells were additionally transfected with a vector encoding for the S1PL protein (2 µg pDNA, electroporation, 48 h). In parallel, A549 WT and KO cells were infected with IAV PR8 strain (MOI of 1 for 8 h) and the number of infected cells determined via anti-NP stain (lower panel). Data represents the mean ± SEM of three independent experiments; ONE-way ANOVA and Dunnett's multiple comparison test performed (A549 as reference). (B) S1PL complementation in the S2-6 clone was verified by TLC (3 µM pacSph, 6 h, 6-well plate). The presence of the PC band in transfected cells appears due to the incorporation of fed pacSph into glycerolipids as a result of the S1PL enzymatic reaction[254]

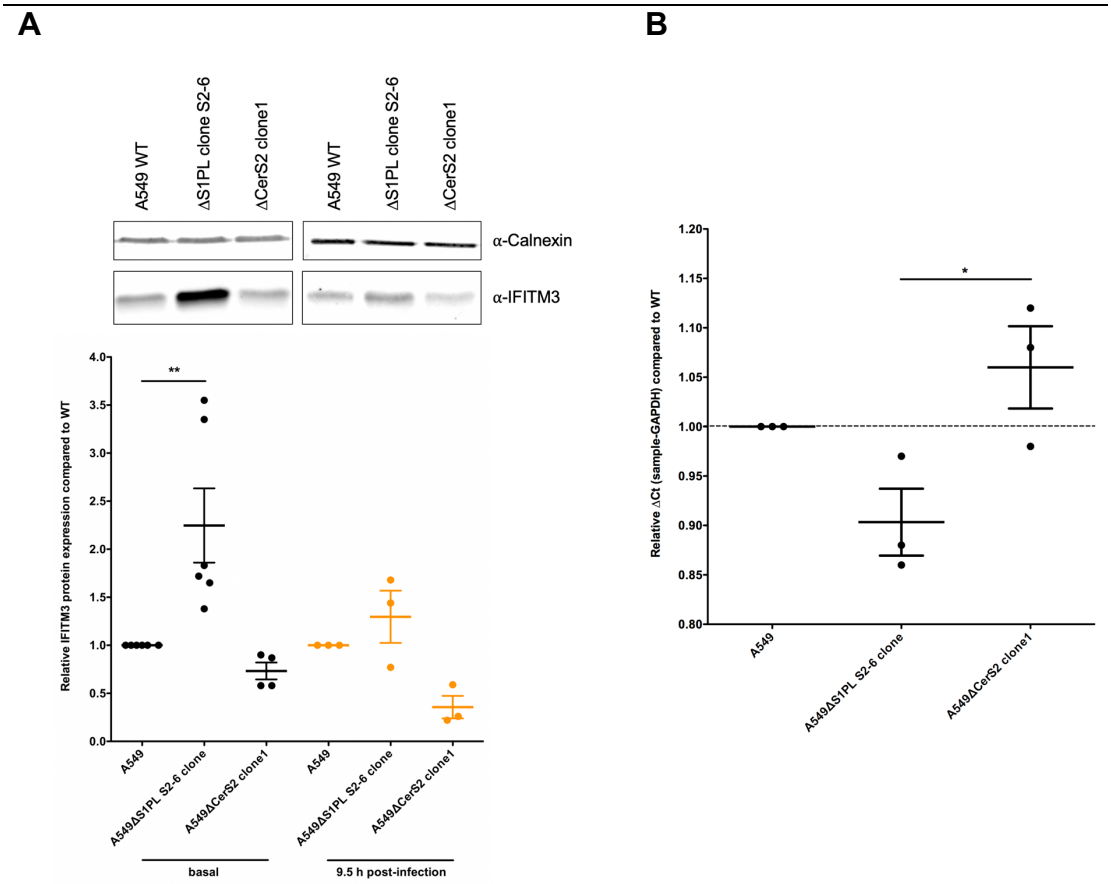

Figure 7.13: IFITM3 protein and gene expression levels in A549 wild type versus A549ΔS1PL (S2-6 clone) and A549ΔCerS2 (clone 1) cells.

(A) Cells were infected with the IAV PR8 strain (MOI 1) for 9.5 h, lysed and 35 µg membrane fraction loaded on SDS-PAGE. IFITM3 levels were normalised to CXN and the IFITM3 protein expression of *SGPL1* and *CERS2* KO clones calculated relative to A549 WT cells in infected and non-infected (basal protein level) samples. In non-infected samples, IFITM3 levels are strongly elevated in the *SGPL1* KO S2-6 clone compared to WT cells. Upon infection, IFITM3 expression levels in WT cells are comparable to those in the S1PL KO, whereas IFITM3 protein expression is (slightly) reduced in *CERS2* KO clone 1 cells compared to A549 WT/ΔS1PL cells. Shown: mean, ±SEM; ONE-way ANOVA and Dunnett's multiple comparison test performed; each dot represents one replicate. (B) IFITM3 gene expression levels were analysed in A549 WT, *SGPL1* and *CERS2* KO clones. The Ct from GAPDH (housekeeping gene) was subtracted from the Ct of each cell probe (ΔCt). The ΔCt of KO cells was calculated relative to the ΔCt of WT cells. Gene expression of IFITM3 was significantly higher in A549ΔS1PL cells, but lower in A549ΔCerS2 cells. Ct= threshold cycle. Shown: mean, ±SEM; ONE-way ANOVA and Dunnett's multiple comparison test performed (A549 as reference); n=3.

Danksagung

Hiermit möchte ich mich zunächst bei Frau Prof. Dr. Britta Brügger bedanken, die mir die Möglichkeit gab, meine Doktorarbeit im Rahmen dieses Projektes zu verfassen, und trotz ihrer vielen Verpflichtungen stets mit Rat zur Seite stand. Zudem möchte ich mich bei allen meinen TAC Mitgliedern bedanken, die sich bereit erklärt haben, diese Doktorthese mit zu betreuen und konstruktiv zu gestalten. Ich möchte mich auch bei Prof. Dr. Hans-Georg Kräusslich bedanken, denn ohne den SFB1129 würde dieses Forschungsprojekt nicht existieren.

Ganz besonderen Dank möchte ich auch Dr. Susann Kummer für ihren umfassenden Beitrag an diesem Projekt, sowie ihre ausgesprochene Unterstützung aussprechen. Die Zusammenarbeit habe ich lediglich in guter Erinnerung ☺
Des Weiteren gilt mein Dank Prof. Dr. Jeroen Krijgsveld für die Zusammenarbeit hinsichtlich der Proteomscreens. Hier möchte ich mich auch insbesondere bei Sophia Föhr und Dr. Gianluca Sigismondo für die Präparation, Messung und Prozessierung der SILAC Daten bedanken.

Innerhalb der Gruppe danke ich selbstverständlich auch Iris Leibrecht für die Aufbereitung der Lipidproben, sowie Timo Sachsenheimer und Christian Lüchtenborg für Lipidmessungen und Bereitstellung der Lipidomdaten, von denen in den Jahren meiner Doktorarbeit doch recht viele produziert wurden ☺
Meinen lieben Kollegen möchte ich auch danken, für die Unterstützung und Hilfsbereitschaft, sowie die gemeinsame Zeit. Ehemalige Mitglieder möchte ich ebenfalls adressieren, insbesondere Mathias Gerl, der mir eine große Hilfe am Anfang meines PhDs war, mich in mein Thema einzufinden und mir die Bedeutung von paclipids (stets in Ruhe und Gelassenheit) näher zu bringen; sowie Cagacan Özbalci, einfach nur weil es Cagacan ist ☺

Zu aller Letzt danke ich meiner Familie und Freunden; ohne sie wäre ich nicht dort, wo ich jetzt bin, in vielerlei Hinsicht.
Zuletzt möchte ich den Erfindern von Netflix meinen Dank aussprechen.